Experimental investigation on the influence of rotation on thermal convection

Dissertation

for the award of the degree
"Doctor rerum naturalium" (Dr.rer.nat.)
of the Georg-August-Universität Göttingen

within the doctoral program
Physics of Biological and Complex Systems (PBCS)
of the Göttingen Graduate School of Neurosciences, Biophysics and Molecular Biosciences (GGNB)
of the Georg-August University School of Science (GAUSS)

submitted by

Marcel Frederik Wedi

from München, Germany

Göttingen, 2021

Thesis reviewer:

Dr. Stephan Weiss
Department for Experimental Methods
Deutsches Zentrum für Luft- und Raumfahrt, Göttingen

Prof. Dr. Stefan Dreizler
Institute for Astrophysics
Georg-August-Universität Göttingen

Additional members of the examination board:

Dr. Olga Shishkina
Department of Fluid Physics, Pattern Formation and Biocomplexity
Max-Planck-Institute for Dynamics and Self-Organization, Göttingen

Prof. Dr. Jörg Enderlein
Third Institute of Physics
Georg-August-Universität Göttingen

Prof. Dr. Stefan Klumpp
Institute for the Dynamics of Complex Systems
Georg-August-Universität Göttingen

Prof. Dr. Andreas Tilgner
Institute of Geophysics
Georg-August-Universität Göttingen

Date of oral examination: 14.02.2022

Abstract

We report on experimental measurements of rotating Rayleigh-Bénard convection to study the influence of the Coriolis force on the heat transport and the flow structure. Two experimental setups were used. The first is a 2.24 m tall cylindrical cell with an aspect ratio between its diameter (D) and its height H, $\Gamma = D/H = 0.5$. It is filled with either nitrogen or pressurized gaseous sulfur hexafluoride to achieve Rayleigh numbers $7.5 \times 10^9 \leq Ra \leq 7.5 \times 10^{14}$, while the Prandtl number Pr remained fairly constant at $0.72 \leq Pr \leq 0.96$. We performed heat flux measurements (i.e. the Nusselt number Nu) and obtain scaling relations as function of Ra and the rotation rate in form of the inverse Rossby number $1/Ro$. We find $Nu_0 \propto Ra^{0.315}$ for the non-rotating and a collapse of $Nu/Nu_0(1/Ro)$ for the rotating case. For sufficiently large $1/Ro$, we find $Nu/Nu_0 \propto 1/Ro^{-0.42}$. Three regimes were determined, with increasing influence of rotation. Their transitional values $1/Ro_1^* = 0.8$ and $1/Ro_1^* = 4$ could be found in numerous quantities throughout the analysis, where we relied on point-wise temperature measurements distributed throughout the cell. $1/Ro_1^*$ was found as the onset of a travelling temperature wave around the circumference close to the sidewall, referred to as *boundary zonal flow* (BZF). This structure with wave number $k_{BZF} = 1$ drifts in counter-rotating direction with a frequency $\omega/\Omega \propto 1/Ro^{-3/4}$.

In the smaller, optically accessible setup, we performed particle image velocimetry (PIV). It consists of a $H = 0.196$ m, $\Gamma = 1$, transparent setup made out of acrylic glass. With mixtures of water and glycerol at different mass concentrations we achieved $6.55 \leq Pr \leq 76$ at various combinations of Ra and the dimensionless rotation rate (Ekman number - Ek). We focussed on an horizontal layer at half-height, where we investigated the BZF in the velocity field. We found a thickness scaling relation $\delta_0 \propto Ek^{1/2}$, while the distance from the sidewall to the maximum azimuthal velocity was found to scale as $\delta_\phi^{max} \propto Ek^{3/2} Ra^{1/2} Pr^{-0.8}$.

Contents

Often used fluid and experimental parameters

symbol	dimension	description
ν	m^2/s	kinematic viscosity
μ	Pa s	dynamic viscosity
ρ	kg/m^3	fluid density
α	1/K	isobaric expansion coefficient
κ	m^2/s	thermal diffusivity
λ	W/m·K	thermal conductivity
$\boldsymbol{u}$	m/s	flow velocity vector
ω	1/s	flow vorticity
Ω	rad/s	rotation rate
T_{top}	°C	top plate temperature
T_{bot}	°C	bottom plate temperature
Δ	K	temperature difference between top and bottom plate
T_m	°C	mean temperature
T_c	°C	temperature at mid-height
P	bar	experimental pressure
g	m/s^2	Earth's gravitational acceleration
H	m	height of the experimental cell
D	m	diameter of the experimental cell
Q_{BP}	W	heating power at the bottom of the cell
ϵ_u	J/kg·s	average kinetic dissipation rate
ϵ_θ	K^2/s	average thermal dissipation rate
τ_{ff}	s	free-fall time
u_{ff}	m/s	free-fall velocity
δ_{BL}	m	boundary layer thickness
δ_0	m	width of the boundary zonal flow
ϕ	rad	azimuthal angle
u_r	m/s	radial velocity
u_ϕ	m/s	azimuthal velocity
u_ϕ^{max}	m/s	maximum azimuthal velocity
δ_{max}	m	radial position of u_ϕ^{max}

Dimensionless quantities

symbol	formula	description
$\tilde{T}$	$(T - T_m)/\Delta$	normalized temperature
Θ	$(\langle T \rangle - T_m)/\Delta$	normalized average temperature
Ra	$g\alpha\Delta H^3/(\nu\kappa)$	Rayleigh number
Nu	$Q_{BP}H/(\lambda\Delta)$	Nusselt number
Ta	$4\Omega^2 H^4/\nu^2$	Taylor number
Ek	$\nu/(H^2\Omega)$	Ekman number
Ro	$\sqrt{\alpha g\Delta/H}/(2\Omega)$	Rossby number
Pr	ν/κ	Prandtl number
Re	UH/ν	Reynolds number
Fr	$\Omega^2 D/g$	Froude number
Γ	D/H	aspect ratio
Ra_c	$8.7Ek^{-4/3}$	critical Ra for convection onset in rotating RBC
Ra_w	$\pi^2\sqrt{6\sqrt{3}}Ek^{-1} + 46.5Ek^{-2/3}$	critical Ra for onset of wall modes
$\widetilde{Ra}$	$RaEk^{4/3}$	reduced Ra for rotating RBC

Common abbreviations

term	description
RBC	Rayleigh-Bénard convection
LSC	large scale circulation
OB	Oberbeck-Boussinesq
BZF	boundary zonal flow
DNS	direct numerical simulation
PIV	particle image velocimetry
pdf	probability density function

1 Introduction

Everyone enjoys the feeling of a warm house, when the heating makes one forget about the freezing cold winter. But how does the warmth actually distribute throughout the room? If you push hot liquid through the heater elements, they heat up because the energy is conducted through the metal by collisions of the atoms. It turns out, however, that this process is quite inefficient when it comes to gases or liquids. Also on large distances, where the temperature gradients become smaller and smaller, conduction is a rather slow process. Other ways of heat transport become much more effective, in both, transporting heat from the inner core of stars to the outer shell and eventually to us on Earth, and transporting the heat from our heater through the living room. These processes are *radiation* and *convection*. This thesis examines the latter.

Since typically warmer fluid is less dense, it ascends, while cold fluid parcels descent. This process, the flow driven by temperature differences, is called *thermal convection*. It causes large-scale fluid flows, for example in the Earth's atmosphere, its inner core as well as the interior of giant gas planets, the sun or other stars. These flows on celestial bodies take place in a rotating frame, where additionally Coriolis forces influence the movement, creating phenomena such as hurricanes, Rossby waves or zonal flows. But how exactly do these forces influence the heat transport and the flow structure of thermal convection? This is the question we want to adress in the present thesis by using laboratory experiments and analytical investigations.

Thermal convection is of upmost importance in numerous natural systems and industrial applications. Topics range from small-sized processes such as in metal production (Brent et al. [1988]) or fluid flow in buildings (Hunt and Linden [1999]) to large-scale atmospheric convection on Earth or other planets. On Earth, the temperature difference between the solar-heated surface and the upper parts of the atmosphere lead to an updraft, resulting in a low-pressure area. Understanding the role of convection is therefore crucial for weather modelling and climate research (Newton [1963], Maddox [1980], Rahmstorf [2000], Popke et al. [2013]). In the oceans, currents are subject to convective and rotational forces additionally to a density gradient due to salinity (Marshall and Schott [1999], Gascard et al. [2002]). Convection within Earth's liquid outer core creates the Earth's magnetic field via the Dynamo effect (see e.g. Cardin and Olson [1994], Glatzmeier and Roberts [1995], Glatzmaier [2002], Buffett [2000], Jones [2000],

Aubert et al. [2017]). Beyond our home planet, similar convective motion helps to explain phenomena like the layered cloud composition on Jupiter-like gas planets (Ingersoll [1990], Sanchez-Lavega et al. [2000], Heimpel et al. [2005], Reuter et al. [2007]) or inside stars (Spiegel [1971], Busse and Carrigan [1976], Cattaneo et al. [2003], Hindman et al. [2020]) such as the sun (a schematic is shown in fig. 1.2a). On most celestial bodies, the Coriolis force inflicted by the rotation around their axes influences the convective flow. An often used example on Earth are hurricanes, where heated moist air ascends to the upper parts of the atmosphere and is twisted by Earth's rotation such that it creates the typical spiral form observable from space (Smith [2000], Ruf et al. [2016]).

These natural processes are often at scales up to hundreds or thousands of kilometers and thus unachievable to reproduce in laboratory experiments. At these large scales and high velocities, flows are turbulent, meaning that the velocity and temperature fields fluctuate randomly and large-scale structures typically transfer kinetic energy to ever smaller scales, where it is eventually dissipated into heat. This requires resolving also the smallest scales in numerical simulations, and applying such fully resolved direct numerical simulations on natural scales is impossible with computer systems available nowadays. Techniques that can be used to better understand natural convective flows are numerical simulations focussed on the large scales, e.g. large-eddy simulations, where the smallest scales are approximated by suitable parametric models (Deardorff [1970]), field experiments (e.g. Richardson [1921], Fitzjarrald [1976], Roth [2000], Renno et al. [2004]) or idealized model systems, in which scaling arguments are found which extend to the largest imaginary systems. An example of such a system is the Rayleigh-Bénard convection (RBC), first investigated experimentally by Bénard [1900] and theoretically described by Rayleigh [1916]. Including the Coriolis force into the model system, i.e. rotating RBC, has been investigated for several decades, where either rotation is applied to the experimental setup such as in studies by Rossby [1969], or is numerically included in the governing equations, e.g. in Julien et al. [1996a].

Rayleigh-Bénard convection

Over a century ago, French physicist Henri Bénard performed an experiment where he heated up a thin layer of various liquids from underneath, while the top surface was open and thus cooled by the surrounding air. He found hexagon patterns created by the convective motion, where the fluid rises at the centre and descends back to the bottom at the edges of the hexagons (fig. 1.1). These structures were later investigated theoret-

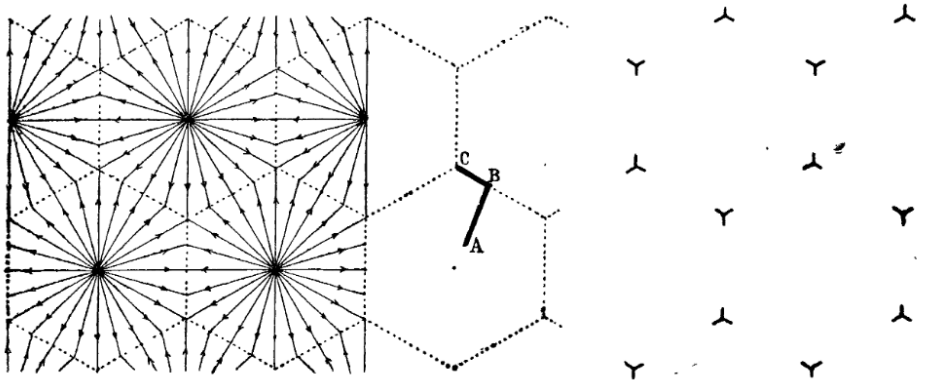

Figure 1.1: Observed hexagon structures by Bénard [1900], where the heated fluid rises up in the center of the hexagon, descending at the edges.

ically by Rayleigh [1916] in a stability analysis based on governing equations given by Boussinesq [1903]. He found that a finite, not too small viscosity is required for the stable modes to form the patterns observed by Bénard. The investigation of such systems heated from below continued in the following decades, nowadays known as Rayleigh-Bénard convection (RBC). An RBC setup consists of a fluid layer contained between rigid top and bottom surfaces, where the bottom side is warmer than the upper one (see schematic in fig. 1.2b). Typical fluids such as gases or water above $\approx 4°$ expand with increasing temperature. Due to its lower density compared to its surrounding, a heated fluid parcel rises from the bottom to the top, while cold, denser fluid descends from the top towards the bottom, creating the convective motion within the cell. In most experiments and numerical simulations, the temperature at the top (T_{top}) and the bottom (T_{bot}) surfaces are kept at a constant value at all time, resulting in a temperature difference of $\Delta = T_{bot} - T_{top}$ and a fixed mean temperature of $T_m = (T_{bot} + T_{top})/2$. The gravity vector is commonly pointed in vertical direction, although inclined RBC at various angles up to vertical convection at a tilt angle of 90° is also a subject of ongoing research (e.g. Clever [1973], Daniels et al. [2000], Zwirner and Shishkina [2018]). The cell size varies a lot from experiment to experiment, for example a height of up to 4 meters (Cheng et al. [2020]) or rather small heights such as 0.52 mm (Bodenschatz et al. [1991]) have been investigated in the past. A relevant parameter describing the shape of cylindrical cells is the aspect ratio $\Gamma = D/H$. It is the ratio of the cell's diameter D to its height H and it varies greatly depending on the use case, e.g. $\Gamma = 1/5$ in Zwirner and Shishkina [2018] as well as down to 1/10 in de Wit et al. [2020], where multiple convection roles can be stacked on top of each other. For pattern formation research, typically large aspect ratios are chosen, such as $\Gamma = 86$ in Bodenschatz et al. [1991]. Setups focussed on the measurement

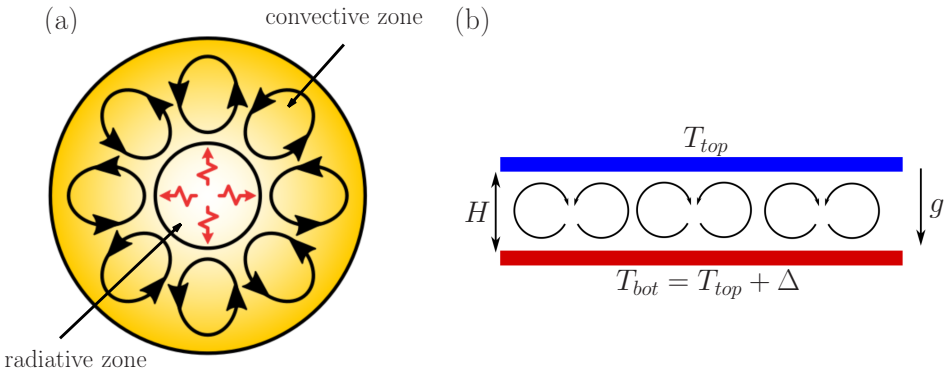

Figure 1.2: (a) Schematic of the two dominating processes of transporting heat in stars similar to the sun: In the dense core, radiation dominates, whereas in the outer layers convection transports the heat towards the surface (Wikimedia [2005]). (b) Schematic of an RBC setup: A fluid is confined between two horizontal plates that are separated by a distance H, the gravity g acts in vertical direction. The bottom side is heated to a temperature $T_{bot} = T_{top} + \Delta$, while the top remains at T_{top}. For large enough Δ, convection rolls start to form in the fluid between the two plates, which, e.g. create the hexagon patterns observed by Bénard in fig. 1.1.

of turbulent convection are most often at Γ around unity such as in this investigation, where we are using cells with $\Gamma = 1$ and $\Gamma = 1/2$. In cells with these aspect ratios, one expects a single large-scale convection role, whereas multiple rolls in vertical direction reduce the overall heat transport (Verzicco and Camussi [2003], Nikolaenko et al. [2005]).

2 Background

To describe the underlying theory, we will first derive the governing equations, which are then simplified using the Oberbeck-Boussinesq approximation to obtain the relevant control parameters. In the derivation we mostly follow the notation in Pope [2000], however, it is comparably found in any introductory book on fluid mechanics.

2.1 Governing equations

We assume a flow with a velocity vector $\boldsymbol{u}(\boldsymbol{x}, t)$ and a density $\rho(\boldsymbol{x}, t)$. Considering a continuous flow, where no sources or sinks of mass are present, the net flux inside and outside of a fluid parcel must be identical to its change of density. This is expressed

with the continuity equation:

$$\frac{\partial \rho}{\partial t} + \nabla \cdot (\rho \boldsymbol{u}) = 0. \tag{2.1}$$

For a non-compressible fluid, the density does not change with respect to spatial direction and can be treated as a constant, i.e. $\rho(t, \boldsymbol{x}) = \rho$ everywhere, anytime. Thus eq. (2.1) becomes $\nabla \cdot \boldsymbol{u} = 0$.

From Newton's second law $F = m \cdot a$ we can relate the acceleration $D\boldsymbol{u}/Dt$ to surface and body forces within the fluid. We introduce here the notation of the material derivative, since the description of a fluid parcel depends on its acceleration by differentiating in time, but also on advection of the surrounding fluid (see e.g. Pope [2000])

$$\frac{D}{Dt} = \frac{\partial}{\partial t} + u_i \frac{\partial}{\partial x_i} = \frac{\partial}{\partial t} + \boldsymbol{u} \cdot \nabla. \tag{2.2}$$

Surface forces are generally described by a stress tensor $\tau_{i,j}$ (for a more basic derivation, see e.g. Wieghardt [2005]), while the body force for our case is the gravity in vertical direction g. Then the momentum equation reads as

$$\rho \frac{Du_j}{Dt} = \frac{\partial \tau_{ij}}{\partial x_i} - \rho g. \tag{2.3}$$

We are only interested in Newtonian fluids here, for which the viscosity remains constant independent of the working stresses. This is a widely used good approximation for many common fluids like gases or water. Counterexamples for this would be for example shear-thinning fluids such as blood, where the observed viscosity decreases under increased strain. In the case of Newtonian fluids, the stress tensor becomes

$$\tau_{ij} = -P\delta_{ij} + \mu \left(\frac{\partial u_i}{\partial x_j} + \frac{\partial u_j}{\partial x_i} \right), \tag{2.4}$$

with P the pressure, δ_{ij} the Kronecker-delta and μ the dynamic viscosity of the fluid. We introduce a reduced pressure term $p = P + \rho g z$, which includes the hydrostatic pressure $\rho g z$, and the kinematic viscosity $\nu = \mu/\rho$. Inserting (2.4) and $\nabla \cdot \boldsymbol{u} = 0$ from the continuity equation into (2.3), we obtain the Navier-Stokes equations (2.6), and the

governing equations for an incompressible Newtonian fluid become:

$$\nabla \cdot \boldsymbol{u} = 0, \tag{2.5}$$

$$\partial_t \boldsymbol{u} + (\boldsymbol{u} \cdot \nabla)\boldsymbol{u} = -\frac{1}{\rho}\nabla p + \nu \nabla^2 \boldsymbol{u}. \tag{2.6}$$

In addition to the kinetic equations, also energy needs to be conserved. Ignoring effects like viscous dissipation of kinetic energy, radiation or phase transitions, heat is either advected away or dissipated with a constant thermal diffusivity κ. Thus, with ∇^2 the Laplacian, $\kappa \nabla^2 T = D/D_t T$, and with (2.2):

$$\partial_t T + \nabla \cdot (\boldsymbol{u} T) = \kappa \nabla^2 T. \tag{2.7}$$

Equations (2.5)-(2.7) now fully describe the evolution of a thermal convective system for an incompressible Newtonian fluid, neglecting other body forces which act on a fluid element. The latter can be gravitational acceleration, which would add a term $\boldsymbol{g}$ to the right side of (2.6). Unfortunately, the equations can generally not be solved analytically because it is highly non-linear and non-local.

2.2 Oberbeck-Boussinesq approximation

For small enough Δ, it can be assumed that density only varies linearly with temperature (Oberbeck [1879], Boussinesq [1903]) around a mean density ρ_0 like $\rho = \rho_0(1-\alpha\theta)$, where $\theta = T - T_0$ is the deviation of the temperature from its mean value T_0 and α represents the isobaric expansion coefficient

$$\alpha = \frac{1}{\rho_0}\frac{\partial \rho}{\partial T}. \tag{2.8}$$

We assume density variations are of relevance only in the buoyancy term, otherwise we approximate it by ρ_0. All other parameters (ν, κ, α, ...) are assumed to be constant throughout the flow field and only evaluated once at mean temperature. This is of course a strong simplification of the underlying dynamics as the fluid parameters usually depend on the temperature and in most natural systems change significantly, for example in the atmosphere where the ground can be at about 300 K, while in the upper troposphere the temperature is usually ≈ 200 K. Thus, the Oberbeck-Boussinesq (OB) approximation for RBC demands relatively low Δ and a fluid relatively far away from its critical point or from phase transitions, where fluid properties can change rather quickly

with small temperature variations. All effects that are based on deviations from this approximation are summarized as *non-Oberbeck-Boussinesq* (NOB) effects.

Considering a fluid in the OB approximation, we can expand the pressure term around the hydrostatic pressure p_0 with a variation p':

$$p = p_0 + p' \quad \rightarrow \quad \frac{\nabla p}{\rho} = \nabla p \left(\frac{1}{\rho} - \frac{\alpha\theta\rho_0}{\rho_0^2} + \dots \right) \tag{2.9}$$

$$\approx \frac{\nabla p_0}{\rho_0} - \frac{\nabla p_0 \alpha\theta\rho_0}{\rho_0^2} + \frac{\nabla p'}{\rho_0} - \underbrace{\frac{\nabla p' \rho_0 \alpha\theta}{\rho_0^2}}_{\approx 0, \text{ since } \theta \text{ and } p' \text{ small}} . \tag{2.10}$$

The derivative of the hydrostatic pressure is $\nabla p_0 = g\rho_0\hat{z}$. The momentum equation, with gravity as a body force, then reads as

$$\partial_t \boldsymbol{u} + (\boldsymbol{u}\cdot\nabla)\boldsymbol{u} = -\frac{1}{\rho_0}\nabla p' + \nu\nabla^2\boldsymbol{u} + g\alpha\theta\hat{z}. \tag{2.11}$$

Non-dimensional parameters are introduced in RBC by performing a dimensional analysis using convenient scales for the physical units. As a length scale the distance between the plates H is suitable, for the temperature its difference between bottom and top plate Δ. Thus, spatial derivations scale as $\partial/\partial_x \sim 1/H$ and $\partial^2/\partial_x^2 \sim 1/H^2$. A typical time unit in thermal convection is the free-fall time, the time a parcel of cold fluid requires to descend from the top to the bottom of the container, assuming frictionless constant acceleration. This depends on Δ and H, as well as α like $\tau_{ff} = \sqrt{H/(\alpha\Delta g)}$. In it, a typical velocity scale is identified, the free-fall velocity $u_{ff} = H/\tau_{ff} = \sqrt{\alpha\Delta g H}$. The derivative with respect to time is expressed as $\partial_t \sim 1/\tau_{ff}$. Pressure has dimensions mass$\times$length$^{-1}\times$time^{-2}, so we non-dimensionalise it with $\tilde{p} = p/(\rho_0 u_{ff}^2)$. Replacing the dimensional parameters with their non-dimensional counterparts like $\tilde{\boldsymbol{u}} = \boldsymbol{u}/u_{ff}$ and $\tilde{\nabla} = H\nabla$, the equations (2.5),(2.7) and (2.11) are reformulated and we yield

$$\frac{u_{ff}}{H}\tilde{\nabla}\cdot\tilde{\boldsymbol{u}} = 0, \tag{2.12}$$

$$\frac{u_{ff}^2}{H}\tilde{\partial}_t\tilde{\boldsymbol{u}} + \frac{u_{ff}^2}{H}\tilde{\boldsymbol{u}}\cdot\tilde{\nabla}\tilde{\boldsymbol{u}} = -\frac{u_{ff}^2}{H}\tilde{\nabla}\tilde{p'} + \frac{u_{ff}\nu}{H^2}\tilde{\nabla}^2\tilde{\boldsymbol{u}} + g\alpha\tilde{\theta}\Delta\hat{z}, \tag{2.13}$$

$$\frac{u_{ff}\Delta}{H}\tilde{\partial}_t\tilde{\theta} + \frac{u_{ff}\Delta}{H}\tilde{\nabla}\cdot(\tilde{\boldsymbol{u}}\tilde{\theta}) = \frac{\kappa\Delta}{H^2}\tilde{\nabla}^2\tilde{\theta}. \tag{2.14}$$

By reordering the constants we obtain the *Oberbeck-Boussinesq equations*

$$\tilde{\nabla} \cdot \tilde{\boldsymbol{u}} = 0, \tag{2.15}$$

$$\tilde{\partial}_t \tilde{\boldsymbol{u}} + \tilde{\boldsymbol{u}} \cdot \tilde{\nabla} \tilde{\boldsymbol{u}} = -\tilde{\nabla} \tilde{p} + \sqrt{Pr/Ra} \tilde{\nabla}^2 \tilde{\boldsymbol{u}} + \tilde{\theta} \hat{z}, \tag{2.16}$$

$$\tilde{\partial}_t \tilde{\theta} + \tilde{\nabla} \cdot (\tilde{\boldsymbol{u}} \tilde{\theta}) = 1/\sqrt{Pr Ra} \tilde{\nabla}^2 \tilde{\theta} \tag{2.17}$$

where two new non-dimensional parameters are defined, the Rayleigh number Ra and the Prandtl number Pr. With the time derivative and the Laplacian, the momentum and energy equations still suffer from the closure problem and can not be solved analytically, the system has, however, the enormous advantage of only having two independent control parameters, i.e.

$$Ra = \frac{g\alpha \Delta H^3}{\nu \kappa} \qquad Pr = \frac{\nu}{\kappa}. \tag{2.18}$$

Now, Ra describes the convective driving of the flow, while Pr is a parameter describing the ratio of viscous forces to thermal dissipation. Pr is heavily dependent on the choice of fluid, typical values are $Pr = \mathcal{O}(10^{-2})$ for liquid metals (Aurnou and Olson [2001], Frick et al. [2015]), $Pr \approx 0.8$ for most gases, $Pr \approx 4-7$ for water, or $Pr = \mathcal{O}(10^4 - 10^6)$ for more viscous fluids such as glycerol (Sugiyama et al. [2007], Horn et al. [2013]) or sugar syrup (Manga and Weeraratne [1999]). In geophysical settings, Pr can be much higher such as $\mathcal{O}(10^{23})$ for convection in Earth's mantle.

For very low temperature differences, a fluid parcel has not enough buoyancy to overcome the viscosity of the fluid and heat is transported by conduction only. Then the equations (2.15)-(2.17) have the trivial solution of $\boldsymbol{u} = 0$. The heat diffusion equation becomes $\sqrt{Pr Ra} \tilde{\partial}_t \tilde{\theta} = \tilde{\nabla}^2 \tilde{\theta}$, solved by a linear temperature distribution $\tilde{\theta}(z) = 1 - z$ and a linear pressure gradient $\tilde{\partial}_z \tilde{p} = \sqrt{Ra/Pr}(1 - z)$.

Assuming infinitely extended upper and lower plates, the critical value Ra_{conv} where the fluid layer becomes unstable, i.e. where a fluid parcel is accelerated without bounds, can be computed semi-analytically using linear stability analysis. The calculation depends on the type of boundary condition at the top and bottom, in our case we assume rigid boundaries which have the no-slip condition $u|_{plate} = 0$. It leads to a set of algebraic equations, which solvability condition forms an equation, which roots lead to $k = k_n(Ra)$, $n = 1, 2, \ldots$ (Landau and Lifshitz [1959]). The inverse $Ra = Ra_n(k)$ is minimized, the smallest one yields $Ra_{\text{conv}} \approx 1708$ at a wave number $k_c = 3.12$ (for details,

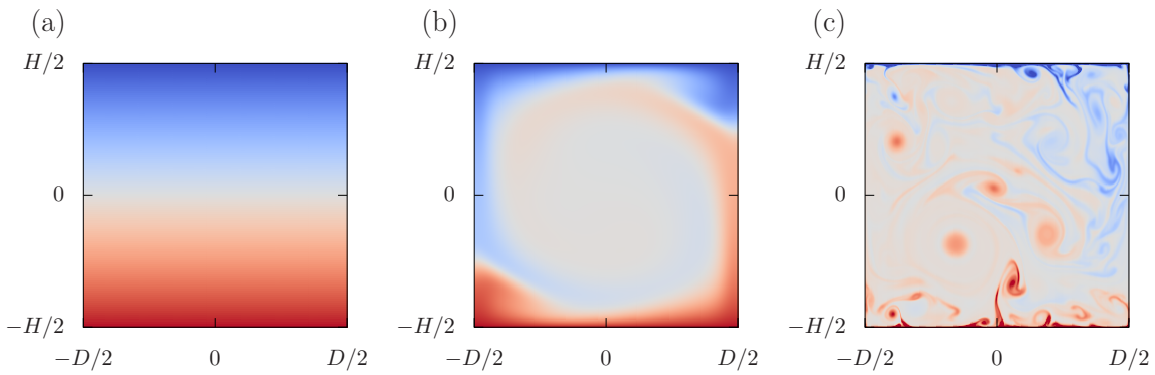

Figure 2.1: Examplary snapshots of the temperature field of a two-dimensional RBC realization using DNS, where (2.15)-(2.17) are solved numerically. Hot fluid with temperature above T_m is coloured red, colder fluid is marked blue on an arbitrary scale. (a) no convection at $Ra = 10^3$, (b) non-turbulent convection roll at $Ra = 10^6$ and (c) $Ra = 10^{10}$ turbulent convection with small vortices and plumes ejecting from the top and bottom surfaces. $Pr = 1$ and no-slip walls are considered at all sides for all cases.

see e.g. Pellew and Southwell [1940], Malkus and Veronis [1958], Landau and Lifshitz [1959], Cross and Hohenberg [1993]). For $Ra > Ra_{\text{conv}}$ hence periodic convection rolls start to form. Turbulent motion, however, sets in at much larger Ra and with it at larger velocities.

An example for a two dimensional RBC flow in a laterally confined box is shown in fig. 2.1, where the governing equations are solved for $Ra = 10^3 < Ra_{\text{conv}}$(a), compared to $Ra = 10^6 > Ra_{\text{conv}}$(b), where a convection roll known as *large scale circulation* (LSC) spans the entire domain. In fig. 2.1c for $Ra \gg Ra_{\text{conv}}$, turbulent motion occurs and one observes stretched fluid patches of hot or cold fluid that are ejected from the region close to the bottom and top plates (so-called "plumes").

As seen in the example images, simulations seem to be an easy way to study RBC, so why do we still perform experiments? With increasing Ra, the velocity in the system increases due to larger thermal driving. The velocity for fluid mechanical applications is incorporated in the *Reynolds number* $Re = UL/\nu$ with L a suitable lengthscale, for RBC again usually $L = H$. In RBC the temperature and subsequent density differences introduce potential energy into the system, which is transformed into kinetic energy within the LSC at the largest scales $\sim H$. In a turbulent flow (at sufficient Ra), the kinetic energy in the three-dimensional system is transferred from this scale H to the

smaller scales via the energy cascade. This continues until at the smallest scales, the Kolmogorov microscale (Kolmogorov [1941]), viscous forces dominate and transfer momentum to heat via dissipation. Note that the total energy dissipation is exactly the introduced potential energy. This process happens at a rate of ϵ, the *energy dissipation rate*. If we want to model this energy cascade using DNS, we need to model the entire range of scales. With increasing Re this Kolmogorov microscale becomes increasingly smaller, thus increasing Ra in DNS requires above proportional processing time $\propto Ra^{3/2} \ln Ra$ (Ahlers et al. [2009b]), limiting the available $Ra \leq 10^{13}$ for state of the art computers. Experiments on the other hand can reach larger Ra for much longer time, increasing the statistical power of time-averaged quantities.

2.3 Vertical heat transport

As we have introduced in sec. 1 using the example of a heater element, one major question in RBC research is how and how efficiently the flow transfers heat. Energy can be transported from the warmer bottom to the cooler top side either by conduction or by convection. Heat transport by conduction is a diffusive process, which depends on the thermal conductivity of the fluid λ and the temperature difference Δ between the plates. The heat flux density by conduction is expressed by $q_{cond} = \lambda\Delta/H$. λ strongly depends on the material, for high-conductive metals like copper it can reach $\lambda_{Cu} = 394\,\mathrm{W/m{\cdot}K}$ at room temperatures (Hust and Lankford [1984]), for typical working fluids in convection experiments it is smaller by several orders of magnitude, e.g. for water $\lambda_{H_2O} = 0.61\,\mathrm{W/m{\cdot}K}$ and sulfur hexafluoride $\lambda_{SF_6} = 0.013\,\mathrm{W/m{\cdot}K}$ at atmospheric pressures (Bell et al. [2014]). Owing to these low values, heat transport by conduction is a very slow process and in convective systems at sufficient driving only plays a minor role for the overall heat transport. As a brief comparison to highlight the importance of convection let us compare the relevant time scales: for conduction, the typical diffusion time scale is H^2/κ, which for a setup with a height of one meter in air at atmospheric pressures is about 45,600 s or 13 hours. Convection takes place close to free-fall time scales, which in a similar setup remains below one second. Therefore, for example for many heating elements, conduction is negligible.

To express the heat transport in dimensionless form, the *Nusselt number* Nu is defined. It contains the ratio of the total heat transport q and the heat transport q_{cond}

apparent in a purely conduction-driven system

$$Nu = \frac{q}{q_{cond}} \approx \frac{qH}{\lambda\Delta}. \tag{2.19}$$

A lot of theoretical work has been performed to obtain a description of the heat transport $Nu(Ra, Pr)$, usually in form of simple power-laws $Nu \sim Ra^{\alpha} Pr^{\beta}$ (for an overview of scaling laws, see e.g. Ahlers et al. [2009b] and references therein). Depending on the choice of Ra and Pr the exponents do not remain constant for all combinations. For example, according to a review by Siggia [1994], already Davis [1922a,b] proposed $\alpha = 1/4$ for small Ra.

Let us look at the area close to the bottom plate: due to the no-slip boundary condition at the rigid surfaces, boundary layers (BL) build up. These are the limiting factor in vertical heat transport in RBC since they are laminar at low enough velocity (low enough Ra) with negligible velocity u_z and hence little heat transport $\langle u_z T \rangle$ in z direction, while the turbulent flow above the BL is very effective at moving heat. Malkus [1954] argued the boundary layers to be marginally stable at large Ra_{BL}, such that $Ra_{BL,c} \propto Ra_{\text{conv}}$ within the BL. Assuming the bulk is well mixed and has no significant vertical gradient $\partial T/\partial z$, the temperature drop across each BL is $\Delta/2$. For Ra_{BL} then follows

$$1 = \frac{Ra_{BL}}{Ra_{BL,c}} \propto \frac{1}{2}\left(\frac{\delta_{BL}}{H}\right)^3 \frac{Ra}{Ra_{\text{conv}}} \tag{2.20}$$

with δ_{BL} the BL width. At the same time, $Nu_{BL} = 2(\delta_{BL}/H)Nu = 1$ and thus

$$Nu \propto \frac{1}{2}\left(\frac{Ra}{2Ra_{\text{conv}}}\right)^{1/3}. \tag{2.21}$$

Since $Ra_{\text{conv}} = const$, $Nu \sim Ra^{1/3}$ according to Malkus [1954].

Later, $\alpha = 2/7$ was proposed by different groups, e.g. see Castaing et al. [1989], Shraiman and Siggia [1990], Cioni et al. [1997], the last one was reported for $Pr \ll 1$ in liquid mercury. Castaing et al. [1989] argued with a mixing zone above the BL, in which plumes accelerate until they merge with the LSC flow velocity. Dimensional analysis then leads to the exponent $\alpha = 2/7$. Experiments in the last decades were generally in accordance with the predicted classical scaling exponents. However, the question remains what happens at asymptotically $Ra \to \infty$? In 1962, Kraichnan [1962]

approached this question and performed an scaling analysis for "extremely high Ra". He proposed a dependence $\sim Ra^{1/2}(\ln Ra)^{-3/2}$, i.e. $\alpha = 1/2$ with logarithmic corrections at this limiting case due to the viscous sublayer within a turbulent BL. Similarly, Spiegel [1971] argued with a 1/2 scaling. Assuming Ra is sufficiently large that also the BL becomes turbulent, then the bottleneck of a laminar temperature BL is circumvented. If we write out the heat transport by convection q_{conv} as a function of the fluid parameters

$$q_{conv} \propto \frac{\kappa\Delta}{H}\left(\frac{g\alpha\Delta H^3}{\kappa\nu}\right)^{\alpha}\left(\frac{\nu}{\kappa}\right)^{\beta} \tag{2.22}$$

and assume in the turbulent bulk flow the dissipation is only subdominant, then q_{conv} should become independent of ν and κ. Since

$$q_{conv} \propto \kappa^{1-\alpha-\beta}\nu^{\beta-\alpha}, \tag{2.23}$$

this requires $\alpha + \beta = 1$ and $\beta - \alpha = 0$, thus $\alpha = \beta = 1/2$.

That the maximal reachable heat transport by convection does in fact scale as $\sim Ra^{1/2}$, can be shown by a simple consideration, as well: In an imaginary cylinder without any rigid walls or boundary layers, imagine a fluid parcel with temperature T_{bot} rising upwards with free-fall velocity u_{ff}. It thus takes the time $\tau_{ff} = 1/\sqrt{\alpha\Delta g/H}$ to reach the upper plate and transports an energy of $dq = \Delta c_p \rho dV$ with c_p the heat capacity of the fluid, and dV the infinitesimal volume. At the same time, conduction in the same column transports $dq_{cond} = \tau_{ff}\Delta\lambda dA/H$. Comparing both contributions, we obtain

$$Nu \sim dq/dq_{cond} \sim \frac{\Delta c_p H^2 \rho}{\Delta\lambda\tau_{ff}} = \frac{(\Delta\alpha g H^3)^{1/2}}{\kappa} = Ra^{1/2}\sqrt{\nu/\kappa} = Ra^{1/2}Pr^{1/2},$$

with $\kappa = \lambda/c_p\rho$ the thermal diffusivity. Looking at the last expression, this is equal to $Ra^{1/2}$ despite a factor of $\sqrt{\nu/\kappa} = Pr^{1/2}$, hence $Nu \sim Ra^{1/2}$, which was supposed to be shown. If no viscous BL develops where diffusion remains dominant, then one should observe this 1/2 scaling. And indeed, experiments where the fluid was not heated at the bottom plate but by absorption of radiation within the bulk flow show this "ultimate" scaling behaviour (Bouillaut et al. [2019]).

The Grossmann-Lohse (GL) theory (Grossmann and Lohse [2000], Stevens et al. [2013]) predicts power-law dependences of Nu on Ra and Pr, with varying scaling expo-

nents depending on areas in the *Ra*-*Pr* parameter space, and thus combines the different scaling ideas. Since it is currently the most widely used model to compare results with, we will shortly explain the idea of the theory and derive scaling laws for $Nu(Ra, Pr)$ and $Re(Ra, Pr)$ in the following, which is mainly obtained from the original publication (Grossmann and Lohse [2000]).

First, the kinetic $\tilde{\epsilon}_u$ and thermal $\tilde{\epsilon}_\theta$ dissipation rates are defined as

$$\tilde{\epsilon}_u(\boldsymbol{x}, t) = \nu \left(\partial_i u_j(\boldsymbol{x}, t)\right)^2, \tag{2.24}$$

$$\tilde{\epsilon}_\theta(\boldsymbol{x}, t) = \kappa \left(\partial_i \theta(\boldsymbol{x}, t)\right)^2. \tag{2.25}$$

θ denotes the non-dimensional temperature, u_j are the velocity components. Inserting the equations of motion (2.15)-(2.17) into the definitions and averaging over the entire volume leads to

$$\epsilon_u = \langle \tilde{\epsilon}_u(\boldsymbol{x}, t) \rangle_V = \frac{\nu^3}{H^4}(Nu - 1) Ra Pr^{-2} \tag{2.26}$$

$$\epsilon_\theta = \langle \tilde{\epsilon}_\theta(\boldsymbol{x}, t) \rangle_V = \kappa \frac{\Delta^2}{H^2} Nu, \tag{2.27}$$

where $\langle \cdot \rangle_V$ is the volume average. The boundary layers close to the horizontal plates are divided into a thermal and a kinetic BL with thicknesses δ_θ and δ_u, respectively (compare fig. 2.2). In the schematic, it is shown that depending on the control parameters these two boundary layers are generally not of similar thickness or even in a fixed relation. In case of turbulent convective transport, these can be expressed by *Nu* and *Re* like

$$\delta_\theta = \frac{1}{2} H Nu^{-1} \qquad \text{and} \qquad \delta_u \sim H Re^{-1/2}. \tag{2.28}$$

The global dissipation rates ϵ_u, ϵ_θ are divided into contributions of the bulk flow and in the boundary layers like $\epsilon_i = \epsilon_{i,BL} + \epsilon_{i,bulk}$. In this way, four regimes come to mind immediately, where one or both dissipation rates are dominated by either the bulk or the BL contributions. For example, for large *Ra*, where the boundary layers are very thin, the dissipation is dominated by the bulk. If, however, *Pr* is increased sufficiently, $\delta_u \gg \delta_\theta$ and thus ϵ_u is dominated by the BL contributions while ϵ_θ is still dominated by $\epsilon_{\theta,bulk}$.

From the equations of motion the contributions now need to be expressed as function of the non-dimensional parameters *Nu*,*Ra*,*Ek*, and *Pr*. For this, let us assume that the

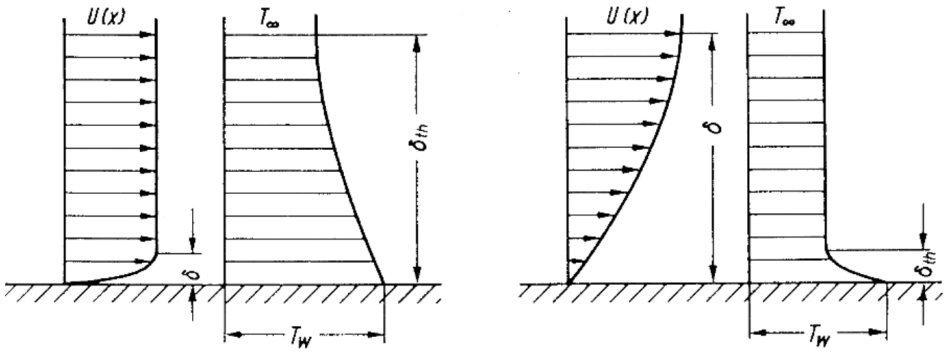

Figure 2.2: Velocity and temperature boundary layers for low $Pr \to 0$ (left) and high $Pr \to \infty$ (right), obtained from Schlichting and Gersten [2017].

RBC inhibits a large-scale circulation, a convection role which spans the entire width of the cell with a velocity U. Sufficiently far away from the BL we assume a turbulent flow, where the large scale rolls break down in smaller ones, transferring energy and momentum (turbulent energy cascade). For an isotropic environment, from dimensional analysis it is shown that the kinetic dissipation rate scales as U^3/H. If we assume the fluctuations to scale with the LSC velocity U we obtain with $Re = UH/\nu$:

$$\epsilon_{u,bulk} \sim \frac{U^3}{H} = \frac{\nu^3}{H^4} Re^3. \tag{2.29}$$

For the thermal bulk dissipation it follows for small Pr, where the kinetic BL is nested within the thermal BL

$$\epsilon_{\theta,bulk} \sim \frac{U\Delta^2}{H} = \kappa \frac{\Delta^2}{H^2} PrRe. \tag{2.30}$$

For larger Pr, the kinetic BL reaches into the thermal bulk, hence the velocity in the thermal bulk is not U, but smaller. If the velocity in the kinetic BL is linear, this reduction factor is δ_θ/δ_u and one takes this reduced velocity in the typical time scale:

$$\epsilon_{\theta,bulk} \sim \frac{\delta_\theta}{\delta_u} \frac{U\Delta^2}{H} = \kappa \frac{\Delta^2}{H^2} PrRe^{3/2} Nu^{-1}. \tag{2.31}$$

The boundary layer contributions can be expressed using dimensional analysis. The lengthscale within the BL is δ_u, thus $\partial_i u_j \sim U/\delta_u$ and due to the volume averaging the value is reduced by the volume fraction δ_u/H. Similar considerations apply to the

thermal dissipation rate. Inserting these into the definitions (2.24) and (2.25) yields

$$\epsilon_{u,BL} \sim \nu \frac{U^2}{{\delta_u}^2} \frac{\delta_u}{H} \sim \frac{\nu^3}{H^4} Re^{5/2}, \tag{2.32}$$

$$\epsilon_{\theta,BL} \sim \kappa \frac{\Delta^2}{\delta_\theta H} \sim \kappa \frac{\Delta^2}{H^2} Nu. \tag{2.33}$$

Finally we approximate the energy equation (2.17) by the dominant terms

$$u_x \partial_x \theta + u_z \partial_z \theta = \kappa \partial_z^2 \theta, \tag{2.34}$$

where for $\delta_u < \delta_\theta$ the horizontal velocity is the LSC velocity $u_x \sim U$ and for $\delta_u > \delta_\theta$ it is $u_x \sim U\delta_\theta/\delta_u$. With the previous typical scale $\partial_x \sim 1/H$ and $\partial_z \sim {\delta_\theta}^2$, one obtains

$$Nu \sim Re^{1/2} Pr^{1/2} \qquad \text{for} \quad \delta_u < \delta_\theta, \tag{2.35}$$

$$Nu \sim Re^{1/2} Pr^{1/3} \qquad \text{for} \quad \delta_u > \delta_\theta. \tag{2.36}$$

Scaling relations of the form $Nu \sim Ra^\alpha Pr^\beta$ are now calculated depending on the choice of Ra. Most notably for our large experiment, at very large Ra, when both dissipations are dominated by the bulk contributions, one obtains

$$Nu \sim Ra^{1/2} Pr^{1/2}. \tag{2.37}$$

This is the same 1/2 scaling as found by Kraichnan [1962] and Spiegel [1971]. For similarly large Ra, but larger Pr, (2.31) has to be used and with it

$$Nu \sim Ra^{1/3}, \tag{2.38}$$

which is the regime identified by Malkus [1954]. In the phase diagram (fig. 2.3), the Kraichnan scaling corresponds to regime IV_l, while the 1/3-scaling is found in regime IV_u. With the same arguments other regimes with different scalings of Nu are identified, listed in the table of figure 2.3.

The GL theory derived above can be expressed by two coupled equations as shown in

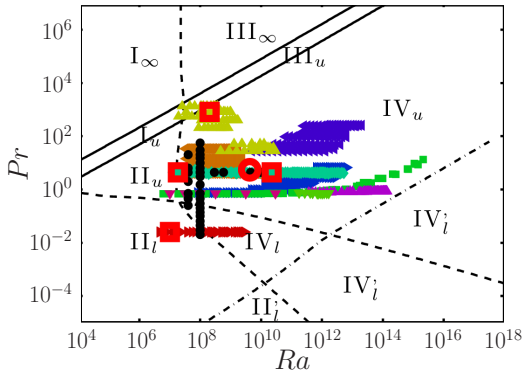

regime	scaling of Nu
I_l	$0.27Ra^{1/4}Pr^{1/8}$
I_u	$0.33Ra^{1/4}Pr^{-1/12}$
II_l	$0.97Ra^{1/5}Pr^{1/5}$
III_l	$6.43 \cdot 10^{-6}Ra^{2/3}Pr^{1/3}$
III_u	$3.43 \cdot 10^{-3}Ra^{3/7}Pr^{-1/7}$
IV_l	$4.43 \cdot 10^{-4}Ra^{1/2}Pr^{1/2}$
IV_u	$0.038Ra^{1/3}$

Figure 2.3: Left: *Ra-Pr* phase diagram from Stevens et al. [2013] (their fig. 1) based on the Grossmann-Lohse theory (Grossmann and Lohse [2000]), where the different symbols show experimental and numerical data points for $\Gamma = 1$ from studies as found in the original publication. Right: predictions of exponents and prefactors for the scaling of $Nu(Ra, Pr)$ in the different regimes (compare left figure) from the original GL-theory publication Grossmann and Lohse [2000].

Stevens et al. [2013]:

$$(Nu-1)RaPr^{-2} = c_1 \frac{Re^2}{g\left(\sqrt{Re_H/Re}\right)} + c_2 Re^3, \tag{2.39}$$

$$Nu - 1 = c_3 Re^{1/2} Pr^{1/2} \left(f\left[\frac{2aNu}{\sqrt{Re_H}} g\left(\sqrt{\frac{Re_H}{Re}} \right) \right] \right)^{1/2} + c_4 PrRe f\left[\frac{2aNu}{\sqrt{Re_H}} g\left(\sqrt{\frac{Re_H}{Re}} \right) \right]. \tag{2.40}$$

g and f are crossover functions, which model the transition of a nested thermal BL inside the kinetic one into the opposite case. a is a prefactor corresponding to the amplitude parameter of the Prandtl-Blasius BL thickness, where $\delta_u = aH/\sqrt{Re}$, and the constant Re_H is chosen such that $\delta_u = aH/\sqrt{Re_H} = L/2 \rightarrow Re_H = (2a)^2$. The coefficients c_i and a were fitted to mostly experimental data in Stevens et al. [2013] and are $c_1 = 8.05$, $c_2 = 1.38$, $c_3 = 0.487$, $c_4 = 0.0252$, $a = 0.922$, though it has to be noted that these values are based on $\Gamma = 1$. The stability of the boundary layers should not strongly depend on the lateral extend for a constant heat input density, given $\Gamma H \gg \delta_{u,\theta}$. Hence the influence of Γ on the heat transport remains quite weak as confirmed by, e.g., Funfschilling et al. [2005], Stevens et al. [2018]. In the latter study, Stevens et al. found a maximum heat transport for $\Gamma = 0.75$, with a decrease to $\approx 0.93Nu(\Gamma = 1)$ for $\Gamma \geq 4$ and a sharp decrease for $\Gamma < 0.5$. At our investigated $\Gamma = 1/2$, $Nu/Nu(\Gamma = 1) \approx 0.98$.

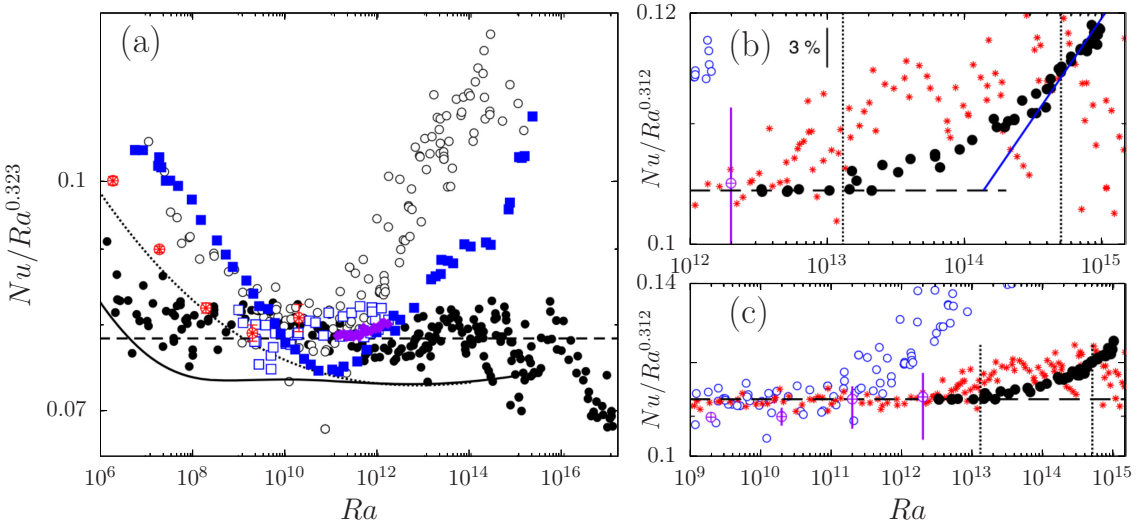

Figure 2.4: (a) Data of $Nu/Ra^{0.323}$ versus Ra, adapted from Ahlers et al. [2009b]. Solid circles data from Niemela et al. [2000] after corrections in Niemela and Sreenivasan [2006], open circles Chavanne et al. [2001], solid blue squares Niemela and Sreenivasan [2003], solid purple diamonds Nikolaenko et al. [2005], open blue squares Fleischer and Goldstein [2002], red stars in circles Stevens et al. [2010b]. The solid and dashed lines show the Grossmann-Lohse predicition (with the prefactors availabe at publication of the review in 2009) for $Pr = 0.8$ and $Pr = 29$, respectively. (b) Reduced $Nu/Ra^{0.312}$ as function of Ra, adapted from He et al. [2012b]. Black filled spheres show data obtained within the study, red stars Niemela et al. [2000], open blue circles Chavanne et al. [2001], circles with pluses and errorbars show DNS data from Stevens et al. [2011]. Blue line indicates a scaling of $Ra^{0.38}$, dashed vertical black lines suggested transitional values of $Ra_1^* = 1.3 \times 10^{13}$ and $Ra_2^* = 5 \times 10^{14}$. (c) Same data, but for a larger Ra range.

The debate of where the crossover from 1/3 to 1/2 occurs is not settled. Kraichnan [1962] estimated an increase in the scaling behaviour at moderate Pr around unity to set in at some $Ra \sim 10^{24}$, however with great uncertainty. Chavanne et al. [2001] reported a $Nu \propto Ra^{2/7}$ up to $Ra = 2 \times 10^{11}$, with an increased scaling of $Ra^{0.375}$ for higher Ra in gaseous helium. Also using helium as a working gas, Niemela and Sreenivasan [2003] found a transition to a 1/3 scaling at $Ra = 10^{13}$, but no further increase in the exponent, although the authors already point out some degree of non-Oberbeck-Boussinesq influence for high Ra in their setup. In the last decades, several experiments claimed having observed a transition to the so called "ultimate" regime. E.g. Chavanne et al. [1997] reported a scaling compatible with $\sim Ra^{1/2}$ for $Ra > 10^{11}$ and He et al. [2012b] found $\alpha = 0.312$ using SF_6 at large pressures for $Ra \leq 1.3 \times 10^{13}$, which gradually increases to $\alpha = 0.38$ for $Ra \geq 5 \times 10^{14}$, also see fig. 2.4. In the last years also numerical simulations reach very large Ra, e.g. for two-dimensional RBC Zhu et al. [2018] reported a transition in scaling behaviour at some $Ra \geq 5 \times 10^{13}$. Despite the recent findings and ever higher Ra the transition is still a vivid and ongoing debate in the field. A selection of data recorded or accumulated in Ahlers et al. [2009b] and He et al. [2012b] is shown in fig. 2.4 as function of Ra.

2.4 Including rotation into the equations

To explain the theory behind rotation-influenced systems as the beforementioned hurricanes, we need to include rotation in our theoretical description. It introduces two external forces into the flow by changing the reference frame: the *Coriolis* force and the *centrifugal* force. On large dimensions such as the Earth, centrifugal forces are not significant compared to Coriolis forces, such that in numerical simulations, usually only the Coriolis force is modeled and in experiments one tries to keep the centrifugal forces as low as possible. To describe fluid flows in a rotating reference frame, we apply a Galilean transformation to the governing equations. Time derivatives of any vector $\boldsymbol{f}$ in the rotating frame are then written as

$$\left.\frac{d\boldsymbol{f}}{dt}\right|_{rot} = \left.\frac{d\boldsymbol{f}}{dt}\right|_{lab} + \boldsymbol{f} \times \boldsymbol{\Omega} \tag{2.41}$$

with $\boldsymbol{\Omega}$ being the constant rotation rate of the system. Applying this relation twice on the position vector leads to the description of acceleration

$$\left.\frac{d^2\boldsymbol{r}}{dt^2}\right|_{lab} = \left.\frac{d^2\boldsymbol{r}}{dt^2}\right|_{rot} + 2\boldsymbol{\Omega}\times\boldsymbol{u} + \boldsymbol{\Omega}\times(\boldsymbol{\Omega}\times\boldsymbol{r}). \tag{2.42}$$

Here we find the Coriolis force term $2\boldsymbol{\Omega}\times\boldsymbol{u}$ and the centrifugal term $\boldsymbol{\Omega}\times(\boldsymbol{\Omega}\times\boldsymbol{r})$. Using only the perpendicular projection $\boldsymbol{r}_\perp$ of $\boldsymbol{r}$ with regard to $\boldsymbol{\Omega}$ and using the identity $\boldsymbol{\Omega}\times(\boldsymbol{\Omega}\times\boldsymbol{r}) = -\Omega^2\boldsymbol{r}_\perp$, the centrifugal term can be incorporated into the pressure gradient term $\nabla p = \nabla(P - \frac{1}{2}\Omega^2 r_\perp^2)$. The momentum equation (2.6) becomes

$$\partial_t\boldsymbol{u} + \boldsymbol{u}\cdot\nabla\boldsymbol{u} + 2\Omega z\times\boldsymbol{u} = -\frac{1}{\rho}\nabla p + \nu\Delta\boldsymbol{u} + g\alpha\theta\hat{z}. \tag{2.43}$$

A similar non-dimensionalization as before introduces next to Ra and Pr also a parameter describing the rotation rate: the convective Rossby number

$$Ro = \frac{\sqrt{\alpha g\Delta/H}}{2\Omega}. \tag{2.44}$$

Alternative parameters can be defined which are closely linked to each other, such as the *Ekman* number Ek

$$Ek = \frac{\nu}{H^2\Omega} = 2Ro\sqrt{\frac{Pr}{Ra}} \tag{2.45}$$

or the Taylor number

$$Ta = \frac{4\Omega^2H^4}{\nu^2} = \frac{1}{Ek^2}. \tag{2.46}$$

Most numerical studies neglect any influence of so-called centrifugal buoyancy. A denser fluid parcel experiences greater acceleration by centrifugal forces than a less dense one, in a rotating RBC setup effectively pushing colder fluid towards the sidewall, while warmer fluid accumulates around the rotating axis. To estimate the strength of the centrifugal force $\sim\Omega\times(\Omega\times\boldsymbol{r})$ compared to the Coriolis force $\sim\Omega\times\boldsymbol{u}$, the *Froude number* is defined as $Fr = \Omega^2D/g$ (with the diameter $D = H\Gamma$). For many astro- and geophysical applications Fr is usually very small[1], justifying the negligence of the centrifugal forces and one thus tries to minimize their influence in experiments and numerical simulations as well. It has been shown (Horn and Aurnou [2018, 2019]) that only for $Fr > \Gamma$ centrifugal forces become dominant over Coriolis forces. In a proper environment using a suitable Pr a very high Fr leads to the formation of tornado-like structures in rotating

[1]With Earth's rotation at $\Omega \approx 7\times10^{-5}$rad/s, $R \approx 6$ km this results in $Fr \approx 0.003$.

RBC (Horn and Aurnou [2021]). In our experiments we limit the rotation rate such that $Fr < \Gamma$ to keep the influence on the flow field small.

Flows on Earth or inside stars are heavily influenced by the Coriolis force and hence, Ek is usually used as the relevant parameter for these systems. As example, the length-scale in geodynamo applications is $\mathcal{O}(10^6\text{m})$ and Gubbins [2001] estimates $Ek \approx 10^{-16}$, with Ra between $10^{21} - 10^{29}$. On Jupiter, studies suggest $Ek \approx 10^{-19}$, $Ro \approx 10^{-10}$ (Schubert and Soderlund [2011]) with Ra somewhere at 10^{17}. Values in experiments have reached down to $Ek = \mathcal{O}(10^{-9})$ (Cheng et al. [2020], Wedi et al. [2021]) and much smaller Ek are only achievable by dramatically increasing H, which quickly becomes experimentally unfeasible and cost-intensive. In order to estimate the influence of Ek on the flow patterns and heat transfer in astrophysical settings we need to extrapolate our knowledge at comparatively low Ek towards these large scales.

2.5 Geostrophic balance

Let us assume a flow with large time scales, where we can neglect the time derivative term in the governing equations. Additionally we look at the bulk convection where viscosity plays no important role. Then, the momentum equation (2.43) simplifies to

$$2\Omega\hat{z} \times \boldsymbol{u} = -\frac{1}{\rho}\nabla p + g\alpha\theta\hat{z}. \tag{2.47}$$

This describes the *geostrophic balance*: looking at the horizontal components

$$2\Omega\rho u_y = \partial_x p \tag{2.48}$$

$$2\Omega\rho u_x = -\partial_y p \tag{2.49}$$

we see that the horizontal velocities u_x and u_y are balanced purely by the pressure gradients. Streamlines in this balance are thus aligned with regions of equal pressure, the isobars. This result is counter-intuitive at first, as in a non-rotating system, flow is in general parallel to the pressure gradient, leading to a flow from high-pressure regions to low-pressure ones. In the geostrophic balance, however, the Coriolis forces divert the tracks around the low-pressure center. Even though this balance is an ideal model case hardly reached in nature, it helps to explain the different rotational directions around high or low pressure regions between the northern and southern hemisphere.

The vertical component of eq. (2.47),

$$\partial_z p = g\alpha\rho\theta, \tag{2.50}$$

describes the hydrostatic balance within the Boussinesq approximation. If we now take the derivative ∂_y of (2.48) and ∂_x of (2.49) and substract them, we yield $-2\Omega(\partial_y u_y + \partial_x u_x) = 0$. Combined with the continuity equation $\nabla \boldsymbol{u} = 0$, this means that

$$\partial_z u_z = 0, \tag{2.51}$$

i.e. a constant vertical velocity along the vertical axis. Derivating both (2.48) and (2.49) with respect to z and exploiting the hydrostatic balance (2.50), we obtain the *thermal wind balance*

$$2\Omega\partial_z \boldsymbol{u} = g\alpha\hat{z} \times \nabla\theta. \tag{2.52}$$

Assuming a barotropic environment with $\nabla\theta = \partial_z\theta\hat{z}$ this leads to the *Taylor-Proudman theorem* (Taylor [1923])

$$\partial_z \boldsymbol{u} = 0. \tag{2.53}$$

Note that this is a much stronger statement than the constant vertical velocity, since this implies that all vertical velocity fluctuations become 0, essentially rendering the flow at a given height quasi-twodimensional.

2.6 The Ekman and Stewartson layers

Let's compare this to the flow close to the plates, inside the Ekman boundary layer (Ekman [1905]). There, viscosity plays a dominating role and we must not discard it from the equations, but since velocity derivations are predominantly in the vertical direction, we may approximate the Laplacian with the second derivative ∂_z^2. Neglecting any influence of the convective term, we obtain

$$2\Omega\hat{z} \times \boldsymbol{u}_{Ek} = -\frac{1}{\rho}\nabla p_{Ek} + \nu\partial_z^2 \boldsymbol{u}_{Ek}. \tag{2.54}$$

Due to the incompressibility condition $\nabla \boldsymbol{u} = 0$ and the irrelevance of the horizontal derivatives of $\boldsymbol{u}_{Ek}$, we conclude that $u_{Ek,z} \ll u_{Ek,(x,y)}$. We yield an important feature of

the Ekman layer: the pressure is constant in vertical direction.

$$-\frac{1}{\rho}\partial_z p_{Ek} + \nu\partial_z^2 u_{Ek,z} = 0 \quad \rightarrow \quad \partial_z p_{Ek} = 0 \tag{2.55}$$

We can now match the pressure p_b of the bulk equations in geostrophic balance (2.48), (2.49) at the edge of the Ekman layer to the pressure within the Ekman layer p_{Ek}.

$$2\Omega\rho u_y = \partial_x p_b = \partial_x p_{Ek} \qquad 2\Omega\rho u_x = -\partial_y p_b = -\partial_y p_{Ek} \tag{2.56}$$

The following coupled differential equation

$$2\Omega u_y = \nu\partial_z^2 u_{Ek,x} + 2\Omega u_{Ek,y} \quad \text{and} \quad 2\Omega u_x = -\nu\partial_z^2 u_{Ek,y} + 2\Omega u_{Ek,x} \tag{2.57}$$

can be solved analytically by applying a general exponential ansatz to

$$\frac{\partial^2(u_{Ek,x} - iu_{Ek,y})}{\partial z^2} = \frac{2\Omega}{\nu}\left(u_y + iu_x - u_{Ek,y} - iu_{Ek,x}\right). \tag{2.58}$$

Within the solution, we obtain two remarkable results. First, the lengthscale $\delta_{Ek} = \sqrt{\nu/\Omega}$ of the Ekman layer, which with the definition of Ek (2.45) reads as $\delta_{Ek}/H = Ek^{1/2}$. In the rotation-dominated regime we thus expect an Ekman layer of thickness δ_{Ek} which decreases in size with rotation. Secondly, we find a relation for the vertical flow velocity in the bulk by matching the velocities at the interface from the boundary layer to the bulk flow:

$$u_z = \frac{\delta_{Ek}}{2}\omega. \tag{2.59}$$

This is the beforementioned Ekman pumping, where due to the existence of an Ekman layer the vorticity in the bulk ω leads to a change in vertical velocity. For $\omega < 0$ we get $u_z < 0$, which is called Ekman suction, for $\omega > 0$ it is referred to as Ekman pumping. This leads to a mass flux through the Ekman layer whenever $\omega \neq 0$ with magnitude $\delta_{Ek} = \mathcal{O}(Ek^{1/2})$, which creates a compensating flux at the lateral sidewalls in the so-called *Stewartson layers* (Stewartson [1957, 1966]). Within this Stewartson boundary layer, the velocity increases from 0 due to the no-slip condition at the walls to u_y in the bulk flow. It has been shown (Greenspan and Howard [1963]) that the thickness δ_{St} has to obey $\sim Ek^{1/4}$ to carry the necessary flux. Additionally, the condition of $u_y|_{r=R} = 0$ demands an additional sub-layer with $\delta_{St2} \propto Ek^{1/3}$.

2.7 Influence of rotation on Nu

Applying rotation to the RBC system influences the flow structure in RBC, for example the mentioned Ekman layer build up. It is thus to assume that Ek has an effect on the heat transport as well, and we raise the question what the functional dependence $Nu = f(Ra, Pr, Ek)$ is. Similar to the non-rotating case, one hopes to find simple power-law relations that includes Ek like

$$Nu \propto Ra^{\alpha} Pr^{\beta} Ek^{\gamma}, \tag{2.60}$$

where rotation is just another dependency described by an additional exponent. This has proven to be a hard task, since depending on the choice of Pr, Ra, and Ek the exponent γ differs substantially. Most basically, three regimes have been agreed on:

- rotation-unaffected regime
- rotation-affected (but buoyancy-dominated)
- rotation-dominated regime

In the first regime, at slow rotation (large Ek), Nu remains constant and the flow structure is not or only very little influenced by Coriolis forces. For larger Ra one needs to decrease Ek to smaller values to leave this rotation-unaffected regime, while at small Ra convection may be supressed fast by rotation at even low rotation rates. Thus there has to be a functional dependence on the onset of convection $Ra_c = f(Ek)$, which was found to be (Chandrasekhar [1961])

$$Ra_c \propto Ek^{-4/3}. \tag{2.61}$$

The coefficient depends on the geometry of the system, for $\Gamma = 1$ the relation becomes $Ra_c = 3(\pi^2/2)^{2/3} Ek^{-4/3} \approx 8.7 Ek^{-4/3}$. The relation indicates that in rotating RBC, the faster the rotation, the higher Ra is needed to force convective motion.

In the intermediate rotation-affected regime, depending on Pr, different effects are dominating. Already very early in researching rotation effects, Rossby [1969] observed a non-monotonic behaviour of the heat transport when rotation was applied, see figure 2.5. For $Nu = const$, he measured Ra necessary to keep the heat flux constant for every Ek and he observed a decrease in the needed Ra at small rotation rates. The other way around, this means that for constant Ra at large Ek one observes a larger heat transport

than in the non-rotating case. Rossby used water with $Pr = 6.8$ for his measurements, and as it later turned out, this enhancement depends strongly on Pr, and for $Pr < 1$ no such heat transport enhancement was found (Zhong et al. [2009]). However, for $Pr > 1$, several studies supported the findings of an increased Nu at low rotation rates of up to some 30% (Liu and Ecke [1997], Stevens et al. [2009, 2010a], Weiss et al. [2016]).

In rotation-affected RBC, the rising and descending plumes get twisted by the Coriolis force, which locally introduces a vorticity $\omega = \nabla \times \boldsymbol{u}$. If Ekman layers (sec. 2.6) exist close to the top and bottom plates, they force a vertical movement on the flow and *Ekman suction/pumping* occurs. Since the fluid in the boundary layer has considerably larger (at the bottom plate) or smaller (at the top plate) temperature than the surrounding fluid, this leads to a larger heat transport since $Nu \propto \langle u_z T \rangle$. For low-$Pr$ fluids, the absence of this enhancement is commonly explained by the larger diffusion of plumes into the surrounding and since they do not extend through the vertical height of the cell, no Ekman pumping can develop.

Due to the Ekman layer and its resulting Stewartson layers at the sidewall, there exists an inwards-directed recirculation of vertical moving fluid in the central region of the cell (Stewartson [1957], Greenspan and Howard [1963]). This results in a net azimuthal movement due to deviations caused by the Coriolis force.

The rotation dominated regime finally appears at very large rotation rates, i.e. low Ek, and is seen most easily in the rapid decrease of Nu at constant Ra. Coriolis forces dominate over buoyancy, suppressing vertical movement and leading to the disappearance of the LSC. At sufficiently fast rotation rates, i.e. small Ek, the *Taylor-Proudman* (2.53) theorem applies, according to which vertical velocity is largely suppressed, and with it heat transport by convection $\langle u_z T \rangle$ has to asymptotically become zero (Vallis [2017]).

If the scaling laws are valid over a wide range of parameters, one could now with (2.61) replace the dependence on Ra^α by $(Ra/Ra_c)^\alpha$ in (2.60) and expect

$$Nu \propto Ra^\alpha Pr^\beta Ek^{4\alpha/3}. \tag{2.62}$$

Then, the determining factor to describe the convective motion is replaced by a reduced

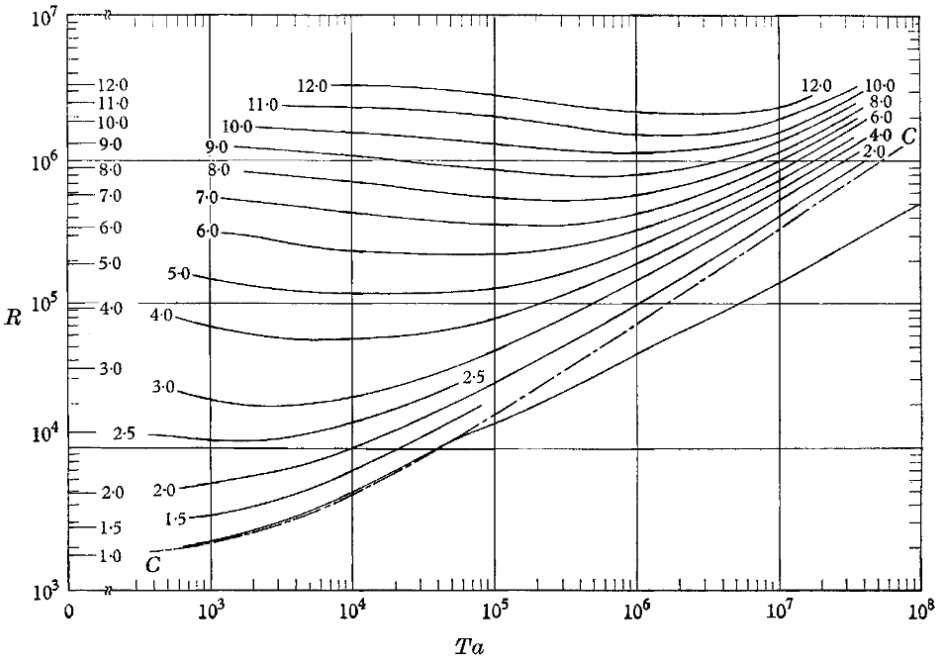

Figure 2.5: From Rossby [1969]: Lines represent $Nu = const$ as function of Ra (y-axis) and Ta (x-axis) for water with $Pr = 6.8$. The dashed-dotted line titled "C" shows the marginal stability curve according to Chandrasekhar [1961]. For any $Nu > 3$ one sees a drop of the necessary Ra at intermediate Ta, a first indication of heat transport enhancement at slow rotation rates.

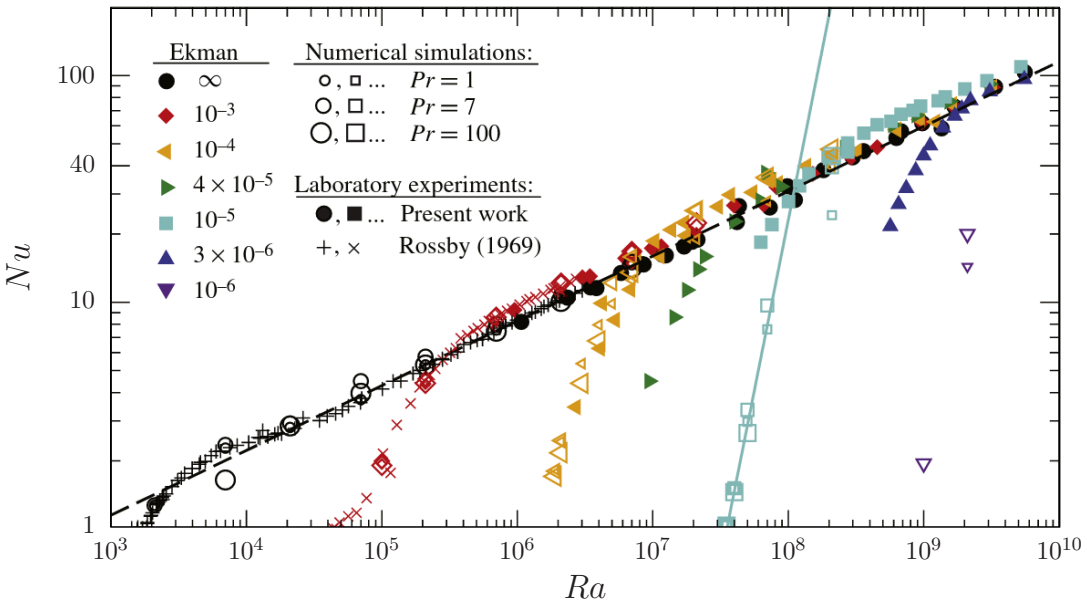

Figure 2.6: Adapted from King et al. [2012]: Nusselt number Nu as function of Ra for several $Ek = const$. Filled symbols show experimental results, open ones show numerical simulations. The crossover from the rotation dominated (strongly decreasing Nu) towards the buoyancy dominated regime is clearly visible for each Ek.

Rayleigh number $\widetilde{Ra} = RaEk^{4/3}$. In the limiting case of $\widetilde{Ra} \leq \mathcal{O}(1)$, convection in the bulk flow is completely suppressed, and with it $Nu = 1$.

A comprehensive overview of Nu as function of relatively low $Ra < 10^{10}$ and various Ek is given in fig.2.6, as published in King et al. [2012]. The non-rotating data follows a scaling of $Nu \propto Ra^{2/7}$, shown as dashed black line. For each $Ek = const$, the Rayleigh number was decreased far into the rotation-dominated regime, where the crossover from the rotation-(un)affected to the rotation-dominated regime appears at larger Ra if the rotation is increased (low Ek). At the fastest rotation rates, convection is completely suppressed. Then, regardless of Ra, one observes $Nu = 1$.

Of especially high interest in heat transport research is the geostrophic regime (sec 2.5). Long time scales such as in the Earth's atmosphere or oceans lead to a quasi-steady description, therefore the understanding of the geostrophic regime is crucial for understanding relations of Nu on planetary scales (compare e.g. Vallis [2017]).
Within the geostrophic regime $Nu \propto Ra^{3/2}Ek^2$ is expected (Julien et al. [2012]), but it is a challenge to reach this regime in both, DNS and experiments, due to the high Ra and simultaniously needed low Ek. There is ambiguity of where the transition to geostrophic turbulence should occur, for example Julien et al. [2012] set the limit to $RaEk^{4/3} \geq 1$, whereas King et al. [2012] argues with thermal boundary layer scalings and suggests a transition at $RaEk^{3/2} = \mathcal{O}(1)$.

2.8 Flow morphologies in rotating RBC

Depending on the control parameters Ra, Pr, and Ek, within the rotation-dominated regime various subregimes with different flow morphologies have been found. For convection with stress-free or periodic lateral boundaries, convection is completely suppressed for $Ra < Ra_c$. Increasing Ra just above the onset creates stable structures known as cellular convection, where hot fluid rises to the top at rather fixed positions, while cold fluid descends constantly at others, compare fig. 2.7a. These stationary cellular structures are similar to the ones found in beforementioned experiments by Bénard [1900] (fig. 1.1). Increasing Ra leads to so-called convective Taylor columns (fig. 2.7b), where hot ascending fluid is surrounded by a sheet of cold descending fluid. With further increase in thermal driving, the flow structures become less organized, creating plumes (fig. 2.7c) or large-scale vortices (LSVs) (fig. 2.7d) far away from the convective onset.

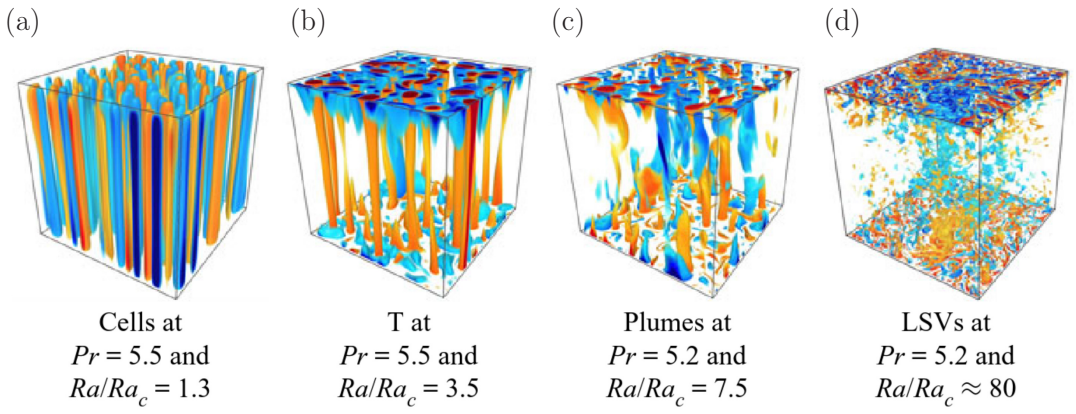

Figure 2.7: Temperature distributions for different flow morphologies for rotating RBC at $Pr \approx 5$ from Aguirre Guzmán et al. [2021]. From (a) to (d) Ra increases, $Ek = const = 10^{-7}$ for all cases. (a) cellular convection just above the convective onset, (b) convective Taylor columns, (c) plumes, (d) large-scale vortices at rather large Ra.

In experimental settings we are bound by solid lateral sidewalls with the no-slip condition. This is in contrast to most models which assume infinite horizontal extent and thus $\Gamma \to 0$ or periodic sidewall conditions. It has been observed that even before the onset of convection, wall modes occur in cells with finite extents (fig. 2.8). These are convective structures which appear way below Ra_c (2.61) (Zhong et al. [1991]), forming a travelling wave at the sidewall and precess in counter-rotating direction (Buell and Catton [1983b,a], Bajaj et al. [2002], Zhong et al. [1993], Goldstein et al. [1993, 1994]). Performing an asymptotic analysis for the cricital Ra for the onset of wall modes for RBC leads to (Herrmann and Busse [1993], Kuo and Cross [1993], Zhang and Liao [2009], Favier and Knobloch [2020])

$$Ra_w = \pi^2 \sqrt{6\sqrt{3}} Ek^{-1} + 46.5 Ek^{-2/3}. \tag{2.63}$$

In first order we expect the wall modes to occur thus with Ek^{-1} for rapid rotation, which we will investigate in the context of the heat transport measurements.

The wall-bounded flows are not only important at onset of convection, but also in the highly turbulent state with $Ra \gg Ra_{\text{conv}}$ (and therefore also $Ra \gg Ra_w$). With applied rotation Ekman layers build up at the no-slip top and bottom boundaries. This condition leads to the azimuthal velocity to vanish at the plate's surfaces, leading to a stress term, building the boundary layer (Vallis [2017]). Within this Ekman layer, the

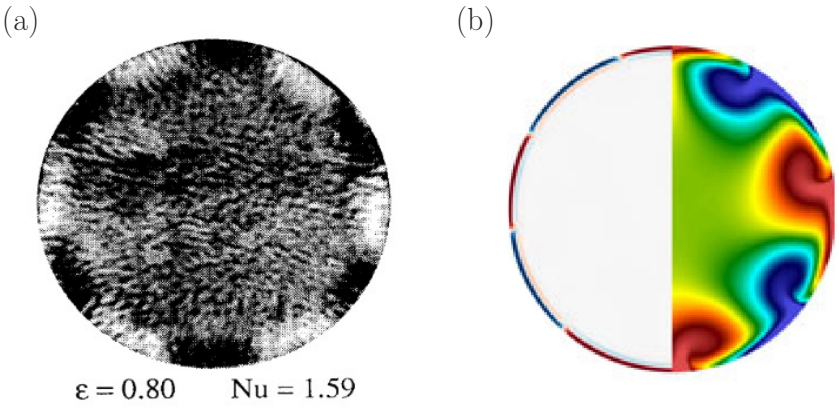

Figure 2.8: (a) shadowgraph image of rotating RBC, showing the appearing wall modes at the side walls below onset according to criterion (2.61), adapted from Zhong et al. [1991]. (b) vertical velocity u_z (left half) and temperature (right half) of a DNS at $z = H/2$, $Ra = 2 \times 10^8$, $Ek = 10^{-6}$, $Pr = 1$ from Favier and Knobloch [2020].

Coriolis forces are balanced not by pressure as in the geostrophic bulk, but by these stress terms. Suppose the flow to be in geostrophic balance one finds the pressure to be constant in the Ekman layer and the momentum equation there becomes

$$2\Omega z \times \boldsymbol{u}_E = \frac{\partial \boldsymbol{\tau}}{\partial z} \tag{2.64}$$

with τ the stress tensor. At the wall the stress is written as the *shear stress* $\tau = \nu \partial \boldsymbol{u}/\partial z$ and hence the viscous term can be written as $\partial \boldsymbol{\tau}/\partial z = \nu \partial^2 \boldsymbol{u}/\partial z^2$. Then,

$$2\Omega z \times \boldsymbol{u}_E = Ek \frac{\partial^2 \boldsymbol{u}_E}{\partial z^2}. \tag{2.65}$$

This is similar to the derivation in section 2.6, but instead of assuming the vertical derivation dominates, we assume the wall stress to dominate. Since the result is the same, here we also obtain $\delta_E \sim Ek^{1/2}$, i.e. a boundary layer that decreases in size with increased rotation at constant Pr, Ra.

3 Measurements in RBC at large *Ra*

During the work on this project, two different experimental RBC setups were used with focus on two different experimental methods. The first setup used a large cell, filled with pressurized gas, where local temperatures were measured at individual points, with strong focus on the vertical heat transport Nu as function of the input parameters Ra and Ek. Pr was almost constant throughout the experiments. The second setup (sec. 4.1.1), smaller in size, was filled with different liquids to vary Pr. Its velocity in a two-dimensional sheet at half-height was recorded using particle image velocimetry (PIV). This gives information on the flow structures again as function of Ra, Ek and Pr. Both experiments are located at the Max-Planck-Institute for Dynamics and Self-Organization in Göttingen.

This section contains the measurements at high Ra, where first the heat flux is evaluated, followed by a wide range of analysis of the temperature readings from individual thermistors. Parts of the experimental setup have been described before for non-rotating (Ahlers et al. [2009a]) and rotating RBC (Wedi [2018], Wedi et al. [2021]). Some parts of the analysis in this chapter have been published in Wedi et al. [2021], in particular much of the analysis and figures in sections (3.2.2, 3.4, 3.5, 3.7 and 3.9-3.11)[2]. Data especially from chapter 3.5 were also part of the publication Zhang et al. [2020].

3.1 Large-scale setup *HPCF*

For the measurements at large Ra, the high pressure convection facility (HPCF) was used. Its cell II (then called HPCF-II) consists of a cylindrical cell with height $H = 2.24\,\mathrm{m}$ and diameter $D = 1.112\,\mathrm{m}$, thus has an aspect ratio of $\Gamma = D/H = 1/2$, see fig. 3.1a. It has been investigated in multiple non-rotating studies before (see e.g. Ahlers et al. [2009c], He et al. [2012a]). The sidewalls of the cell consist of 9.5 mm thick acrylic, which has a low heat conductivity of roughly $0.2\,\mathrm{W/m{\cdot}K}$. Top and bottom plates were made out of high-purity copper with a heat conductivity of $\lambda_{Cu} = 394\,\mathrm{W/m{\cdot}K}$. The horizontal bottom plate forms a sandwich, consisting of two of such copper plates, 35 mm and 25 mm thick, respectively. To measure the heat flow into the cell, they

[2]For the publication, the author of this thesis performed the experiments and the analysis. The first version of the manuscript was also written by the author, most improvements on the manuscript that followed towards the finished publication have been done together with Dr. Stephan Weiss.

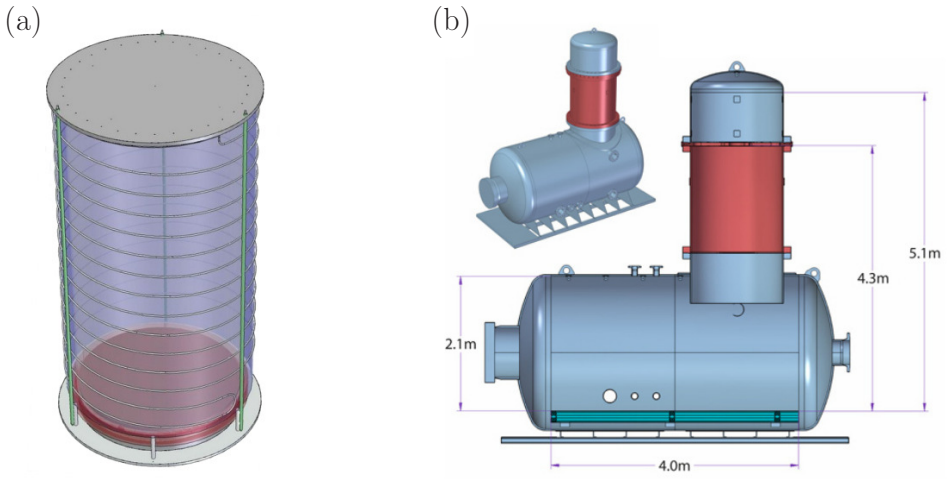

Figure 3.1: (a) Schematic of HPCF-II cell with its side shield consisting of two intertwined water pipes running around its circumference. (b) Schematic of the pressure vessel "U-Boot" with an entrance on the left and the turret extension in red. It is designed to withstand working pressures up to 19 bar with SF_6 or N_2. The cell was lowered into the vessel from the top, after which the turret and the lid were screwed onto the vessel.

are separated by a layer of $d_{lex} = 5\,\text{mm}$ thin Lexan with $\lambda_{lex} = 0.192\,\text{W/m·K}$. This low conductivity results in a temperature drop across the Lexan layer ΔT_{lex}. It was measured using five embedded thermistors in each of the copper plates, over which the mean temperature of the bottom side of the sandwich T_{BPb} and of the top side T_{BPt} was measured, $\Delta T_{lex} = T_{BPb} - T_{BPt}$. The heat flow into the cell was determined by

$$Q = A_{bot}\lambda_{lex}\Delta T_{lex}/d_{lex}, \tag{3.1}$$

where $A_{bot} \approx 0.97\text{m}^2$ is the surface area of the bottom plate.

The bottom side of the sandwich was heated from underneath by a heating wire, which was embedded in grooves at its underside. The grooves were filled with thermally highly conductive epoxy to ensure good heat transfer between the wire and the plate, while ensuring an electrical insulation to prevent a short circuit. The resistance of the heating wire was $R_{heat} = 4.5\Omega$ and power was supplied by an Agilent 6675A with a maximum power output of 2160 W. With the maximum current output of $I_{max} = 18\,\text{A}$, the maximum usable heating power was limited to $P_{max} = I^2 R_{heat} = 1458\,\text{W}$. The top plate was cooled by a circulated water bath, which temperature was controlled with a precision of 0.02 K by Thermo Scientific AC150, NESLAB RTE-7 and ThermoFlex

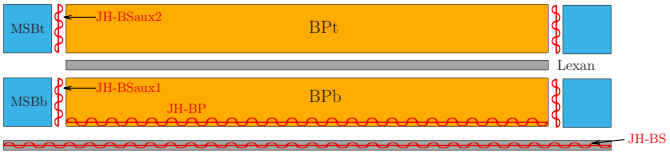

Figure 3.2: Cross section of the bottom sandwich. On the bottommost part the bottom shield with a heater JH-BS, above it the bottom plate bottom (BPb) copper plate, separated by a Lexan layer from the bottom plate top (BPt) plate. Around the circumference of each plate, an auxiliary ohmic heater (JH-BSaux1 and JH-BSaux2) as well as microshields MSBb and MSBt were installed, which are temperature-controlled with a coolant.

2500 circulators, connected to the main control computer using the RS-422 standard. A thermal shield around the sidewall, fig. 3.1a, and insulation with thick porous foam minimized the heat loss through the sides. This shield was kept at the mean temperature $T_m = (T_{top} + T_{bot})/2$ again using circulated water baths. This approximates the conditions of an adiabatic sidewall, i.e. no heat exchange towards the sides. Due to wall effects, the fluid's temperature at the sidewalls close to the bottom (top) plate increases (decreases) relative to T_m which would cause a heat transfer from the fluid through the sidewall (Ahlers [2000], Stevens et al. [2014]). To suppress this, additional micro shields were installed, as well as two micro shields to reduce heat flow from the bottom plates into the surrounding. An additional ohmic heater JH_{BS} below the supporting bottom plate even below the sandwich ensured no heat flow from the main ohmic heater into the structure below the cell. Two additional ohmic heaters JH_{aux} were applied around each of the bottom sandwich plates to further minimize heat loss out of the sandwich to the sides. Each was powered by a Keysight E3634A power supply unit.

A fourth power supply was used to regulate a valve, which allowed surrounding gas to enter or exit the cell for pressure equilibration through a hole located at the side of the cell at $H/2$. During measurements, it was closed to suppress secondary flows and interference with the convective structure.

To rotate the setup, the cell was mounted on a rotating table (fig. 3.3a) that could sustain an axial load up to 2800 kg. The table was driven by a direct drive motor (Siemens 1FW6150 SIMOTICS T Torque-motor), able to deliver a torque of up to 1000 Nm even at very low rotation rates down to 1 rad/min, ensuring smooth rotation even at such low speeds. Inside the table, a water distribution system was installed, which brought the water lines from the laboratory into the rotating frame via water feedthroughs (red

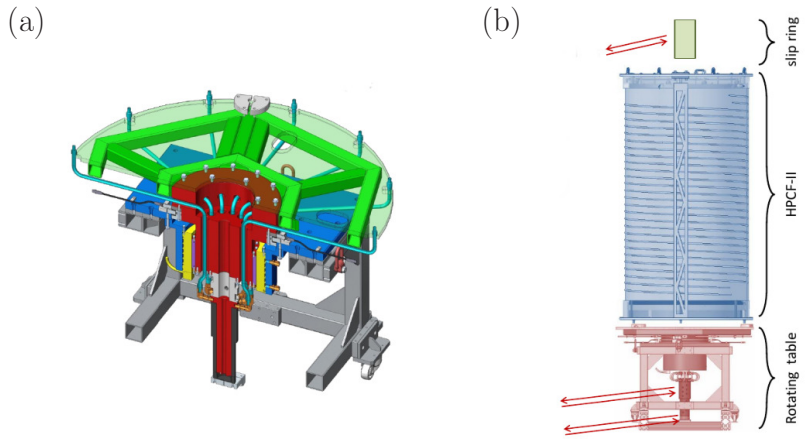

Figure 3.3: (a) Schematic of the rotating table with support structure (grey and green) and the water distribution (red), which transfers the water from the laboratory into the rotating frame. (b) The cell HPCF-II on top of the rotating table from (a). On the top the slip ring provides electrical connections for readouts of the thermistors, on the bottom additional slip rings are attached for power input and water connections to the thermal shields and the top plate.

coloured part in fig. 3.3a). Slip rings at the top and bottom (fig. 3.3b) allowed electrical signal readout as well as power input into the rotating frame to heat the total of four ohmic heaters at the bottom sandwich. For comparison with DNS results, where the centrifugal forces are generally omitted, its influence on the experiment had to be minimized. Thus we set the maximal rotation rate to 2 rad/s, such that $Fr < Fr_c = 0.5$, obeying the suggestion in Horn and Aurnou [2018, 2019].

The rotating table and cell were installed into the *U-Boot of Göttingen*, fig. 3.1b, a 4 m long and up to 4.3 m high pressure vessel (see Ahlers et al. [2009c]), which can be filled with either nitrogen or sulfur hexafluoride (SF_6). The pressure inside the U-Boot could be increased up to 19 bar. At these high pressures, SF_6 has a density of ≈ 157 kg/m^3 and a kinematic viscosity of only $\approx 1 \times 10^{-7}$ m^2/s. This results in a substantial increase in available Ra compared to other working fluids. As comparison, at $T_m = 22.5°$ C, $\Delta = 10$ K and pressure of 19 bar, if we had filled the cell HPCF-II with nitrogen we would have $Ra_{N_2} \approx 4.2 \times 10^{12}$, whereas SF_6 as a working gas resulted in $Ra_{SF_6} \approx 1.0 \times 10^{15}$. All fluid parameters in this thesis are calculated using CoolProp (Bell et al. [2014]), a library for calculating physical properties of pure liquids and certain mixtures. A comparison with the Reference Fluid Thermodynamic and Transport Properties Database (REFPROP) by the National Institute of Standards and Technol-

ogy has been conducted for the relevant pressures and temperatures, finding no or only negligible differences.

Thermistor readouts

Probing the flow structure within the cell is done by measuring temperatures at various locations inside the sidewall and the fluid. As measurement devices thermistors, fig. 3.4c, are used which consist of semi-conductor material with a negative temperature coefficient, i.e. the specific resistance decreases with increasing temperature. Compared to other used methods such as resistance temperature detectors (RTDs), for example PT100 sensors, thermistors have faster response time and are much cheaper while offering a comparable temperature resolution. Additionally, the thermistor's resistance is rather large with $\mathcal{O}(10^4 - 10^5\,\Omega)$, which allows us to read the resistance without separate test leads, which would require additional cabling and measurement devices.
The electrical resistance R_t is measured by applying a test current and measuring the voltage drop across the thermistor. The temperature T was then calculated from the measured R_t based on a previously conducted calibration, where R_t was measured at fixed temperatures across a range between 10 and 70°C. A calibration curve of the form

$$\begin{aligned} \Delta T &= T - T_0, \\ R_t(T) &= R_0 \cdot \exp\left[\left(a_0\Delta T + a_1\Delta T^2 + a_2\Delta T^3 + a_3\Delta T^4\right)/(T + 273.15)\right] \end{aligned} \tag{3.2}$$

was fitted with T_0 an arbitrary fixpoint somewhere in the middle of the calibration, typically at 25°C with a resistance of R_0. a_i are fit parameters individual for each thermistor. To obtain the inverse $T(R_t)$ given a measured resistance, a simple divide-and-conquer algorithm is used.

In total, 116 thermistors are read out in the experiment, 30 of them for control of the heating/cooling inside the shields or the top and bottom plates. Of the 86 thermistors measuring the temperature of the flow field, three rows of eight thermistors distributed azimuthally at equal distance were sunk into blind holes in the sidewall at heights $H/4$, $H/2$ and $3H/4$. Within the flow, an additional 62 thermistors were arranged in vertical columns close to the sidewall at four radii $r = 0.73R, 0.93R, 0.96R$ and $0.98R$. An overview of the radial and azimuthal locations of these thermistors is given in fig. 3.4.

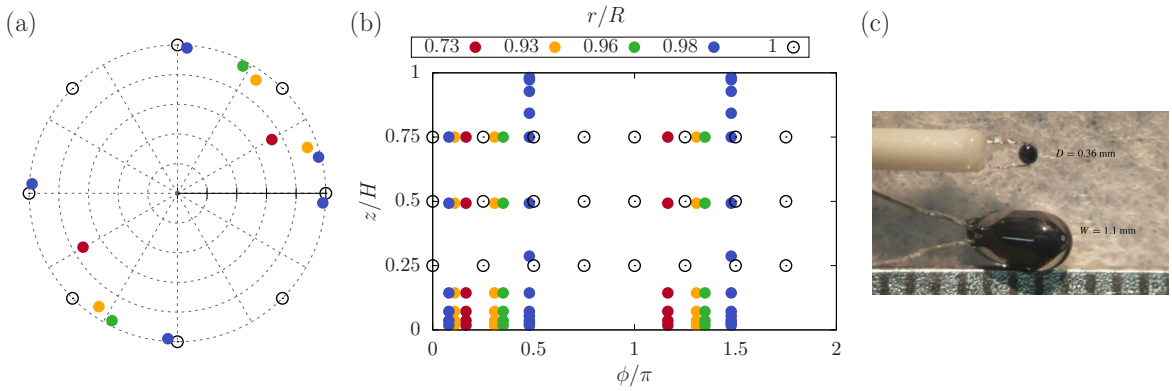

Figure 3.4: (a): Radial and azimuthal positions of the thermistors, colours mark the radial location, equal to the legend of (b). (b): Vertical z/H and azimuthal ϕ/π position of the thermistors. The black open circles mark thermistors that are embedded inside the acrylic sidewall at $r/R = 1$. Filled circles mark thermistors inside the fluid. The colour code reflects the radial position. Adapted from Wedi et al. [2021]. (c) Image of two thermistors used in the HPCF cell with diameters of 0.36 mm (top) and 1.1 mm (bottom) from Ahlers et al. [2014].

The resistance signal of the thermistors are read out by three Keysight 34970A multimeters, which can read out up to 60 independent channels consecutively. Since we are mostly interested in average values or in processes on large time scales, the non-simultaneous readout of the thermistors with a spacing of $\approx 1/60\,\mathrm{s}$ in between consecutive channels is unproblematic. Connection to the controlling computer was established using a General Purpose Interface Bus (GPIB, IEEE-488), which connected the power supplies for the Joule heaters as well. A converter to USB is used and the signals are read using a custom Python program with National Instrument's implementation of the GPIB interface. The power input of the Joule heaters was controlled with a proportional-differential control loop within the same control program, while simpler proportional feedback loops set the desired temperature of the water baths for the side shield and microshields.

Experimental realisations

For a typical rotating RBC experimental series, Ra was kept constant by setting T_{top} and T_{bot} as well as the pressure P to a constant value. After an equilibration time of approximately four hours, data was taken for typically a total of additional eight hours to obtain sufficient statistics. With a typical free-fall time in our setup of $\tau_{ff} \approx 3\,\mathrm{s}$, we average over almost $10{,}000\tau_{ff}$, for the highest pressures and temperature difference we still cover some $5{,}000\tau_{ff}$. The rotation rate was altered between two measurements in the range of $0 \leq \Omega \leq 2\mathrm{rad/s}$. An example of the temperatures T_{bot} and T_{top} is given in

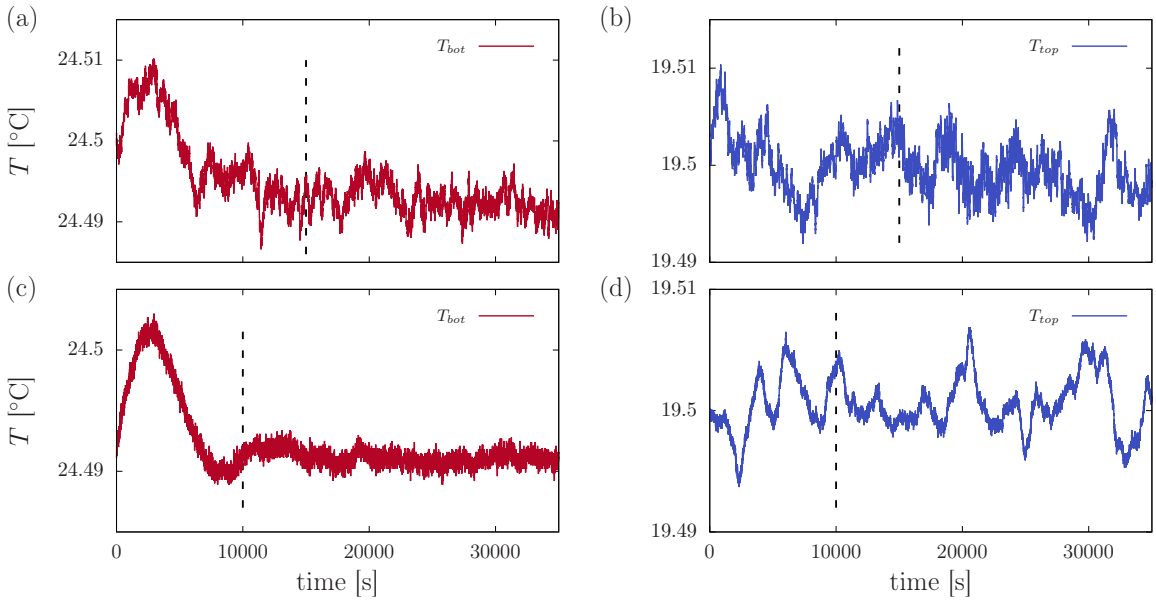

Figure 3.5: Plots of the temperature at the bottom plate T_{bot} (a) and (c) and the top plate (b) and (d) as function of time for typical runs, here $Ra = 3.7 \times 10^{14}$, $1/Ro = 1.4$ ((a) and (b)) as well as $Ra = 1.9 \times 10^{11}$, $1/Ro = 5.29$ ((c),(d)). Data before the vertical dashed lines were discarded in the analysis. When rotation is increased from the previous run at $Ra = const$, due to decreasing Nu less heat on the bottom side is required for $T_{bot} = const$, thus the temperature initially increases until the power input is adjusted. This effect can be clearly seen in (c) exemplarily.

plot fig. 3.5. During the measurement time the rotation rate Ω was held constant while the thermistors were read out approximately every 5 sec. Ra was changed in between different sets by changing either Δ or the pressure of the working gas SF_6. The latter resulted in a slight change of Pr from 0.78 at 1 bar to 0.97 at 19 bar. While the U-Boot temperature T_U, thanks to the side shield, was found to have only little impact on the results at the here presented mean temperatures, we still kept it close to T_m. A list of all measurements is given in table 1, a plot of the parameter space in figure 3.6a.

Run	P (bar)	Δ (K)	Pr	Ra	$1/Ro$	Ek	T_m (°C)	Fluid
E1a	1.0	7.0	0.718	7.5×10^9	≤ 13.0	$\geq 1.5 \times 10^{-6}$	25.0	N_2
E1b	1.0	9.6	0.718	1.0×10^{10}	≤ 11.1	$\geq 1.5 \times 10^{-6}$	25.0	N_2
E1c	1.0	19.2	0.718	2.0×10^{10}	≤ 7.9	$\geq 1.5 \times 10^{-6}$	24.8	N_2
E2a	0.9	5.0	0.784	1.9×10^{11}	≤ 15.1	$\geq 2.7 \times 10^{-7}$	22.0	SF_6
E2b	1.3	11.6	0.786	9.8×10^{11}	≤ 9.9	$\geq 1.8 \times 10^{-7}$	22.0	SF_6
E2c	5.0	5.0	0.804	8.2×10^{12}	≤ 10.4	$\geq 6.0 \times 10^{-8}$	22.0	SF_6
E2d	5.0	15.0	0.804	2.4×10^{13}	≤ 6.0	$\geq 6.1 \times 10^{-8}$	22.0	SF_6
E2e	10.0	5.0	0.836	4.7×10^{13}	≤ 12.3	$\geq 2.1 \times 10^{-8}$	22.0	SF_6
E2f	10.0	8.0	0.836	7.6×10^{13}	≤ 6.8	$\geq 3.1 \times 10^{-8}$	22.0	SF_6
E2g	10.0	15.0	0.836	1.4×10^{14}	≤ 7.1	$\geq 2.1 \times 10^{-8}$	22.0	SF_6
E2h	17.8	5.0	0.941	3.7×10^{14}	≤ 9.3	$\geq 1.1 \times 10^{-8}$	22.0	SF_6
E2i	18.7	5.0	0.966	4.8×10^{14}	≤ 6.2	$\geq 1.4 \times 10^{-8}$	22.0	SF_6
E2j	18.7	8.0	0.966	7.5×10^{14}	≤ 4.9	$\geq 1.4 \times 10^{-8}$	22.0	SF_6
E2k	17.8	10.0	0.941	7.5×10^{14}	≤ 6.6	$\geq 1.1 \times 10^{-8}$	22.0	SF_6

Table 1: Overview of the conducted rotational experiments. The U-Boot temperature T_U was close to the mean temperature $T_m = (T_{top} + T_{bot})/2$, i.e., $T_m - T_U < 3.0\,\mathrm{K}$, for all measurements. From Wedi et al. [2021].

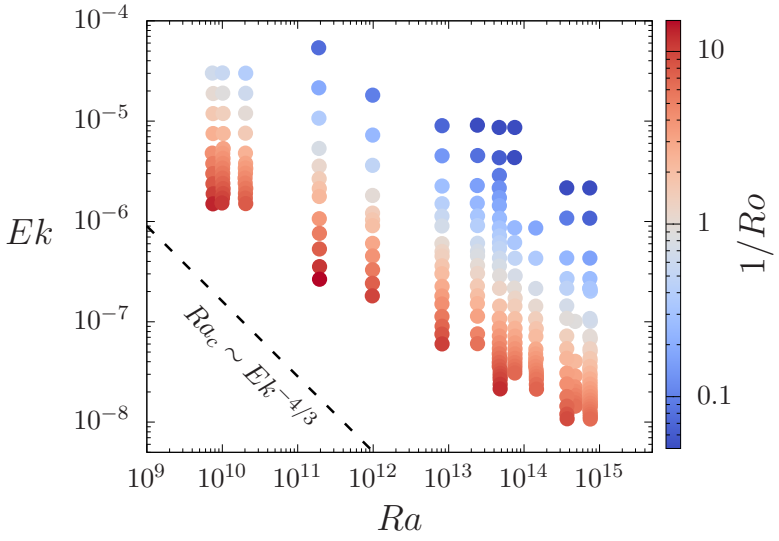

Figure 3.6: Investigated parameter space for the rotating experiments under Oberbeck-Boussinesq conditions, colour symbolizes $1/Ro$. For each Ra, also non-rotating experiments were conducted to compare the results with. The dashed line marks the onset of convection according to (2.61).

3.2 Heat transport measurements

Let us first focus on the vertical heat transport throughout the cell. As explained in the setup section above, the input power Q_{BP} (3.1) was measured via the temperature drop across the bottom plate sandwich. Heat transported by conduction is simply calculated by $Q_{cond} = \Delta\lambda A/H$ with A the area of the plates and λ the heat conductivity of the working gas. All fluid parameters are here assumed to be constant within the Oberbeck-Boussinesq approximation (sec. 2.1) and are evaluated at the mean temperature $T_m = (T_{bot}+T_{top})/2$. The Nusselt number is then calculated as $Nu = \langle Q_{BP}/Q_{cond}\rangle_t$, averaged over the entire measurement time.

3.2.1 Without rotation

Even though the setup and the layout of the experiments are focussed on the rotating case with only a few different Ra, it is interesting to perform a quick check how Nu behaves as function of Ra and whether it agrees with previous publications. To that regard, in fig. 3.7 Nu is plotted as a function of Ra for all non-rotating cases in a log-log representation. The data follow a fitted power-law scaling of $0.094Ra^{0.315\pm0.002}$ over about five order of magnitudes in Ra, which resembles the simple Malkus scaling rather well and follows the solution of the GL theory (2.39) and (2.40) very closely. Our results fall in line with previous studies such as in Ahlers et al. [2009c] or He et al. [2012b] using the same cell. A similar relation $0.11Ra^{0.308}$ was found experimentally at larger Pr (Cheng et al. [2020]). Unfortunately, we do not have any points for $Ra > 10^{15}$, where He et al. [2012b] suggested a larger scaling of 0.38 using the same cell in a comparable configuration and are therefore unable to test this transition to the ultimate regime.

3.2.2 With rotation

For each of the previously mentioned Ra, several Ro were achieved by increasing the rotation rate as listed in tab. 1. Since for our experiments we always have $Pr < 1$, we do not expect any Nu-enhancements as observed for larger Pr in experiments with water, for example in Rossby [1969] or Weiss et al. [2016].

Nu is plotted as function of $1/Ro$ in fig. 3.8, normalized by Nu_0, the Nusselt number measured without rotation, i.e. $Nu_0 = Nu(1/Ro = 0)$. Thus, for a given Ra,

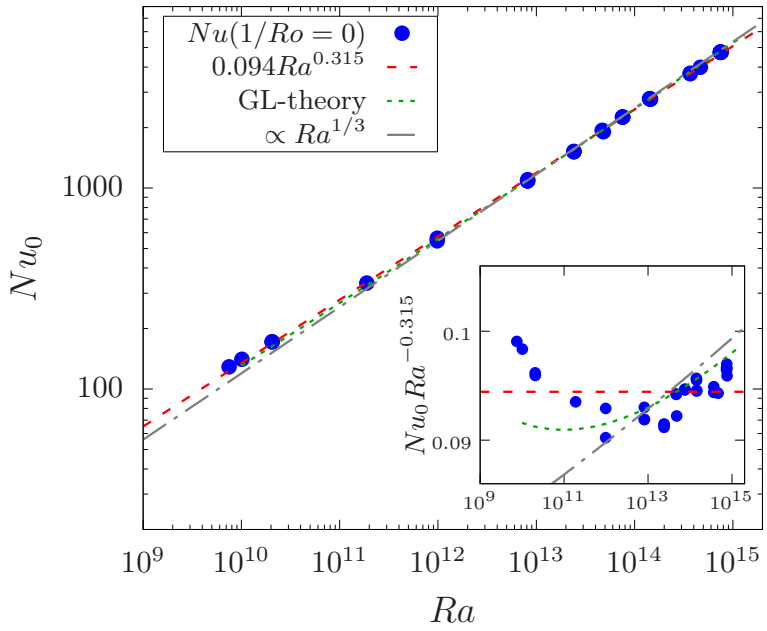

Figure 3.7: Nu for no rotation (Nu_0) as function of Ra in log-log plot (blue bullets). Red dashed line is a power-law fit to the data, yielding $0.094 \pm 0.004 Ra^{0.315 \pm 0.002}$, green dotted line is the solution according to the Grossmann-Lohse equations (eqs. (2.39) and (2.40)), while the grey dot-dashed line shows $Ra^{1/3}$ as proposed by Malkus [1954]. Inset shows the same data reduced by the fitted $Ra^{-0.315}$ to highlight the differences between the predictions and the observations. Adapted from the supplemental material in Wedi et al. [2021].

$\lim_{Ro \to \infty} Nu/Nu_0 = 1$ for very small rotation rates. The data for all Ra collapse rather well when plotted this way. From this plot, we can distinguish immediately three rotational regimes. For low rotation rates, $1/Ro < 1/Ro_1^*$, we do not see any influence of rotation on the vertical heat transport and Nu/Nu_0 remains around unity. For larger rotation rates, convection becomes less effective in transporting heat, observable in a reduction in Nu/Nu_0. We will see later that this rotation rate is a significant transitional point and thus it is marked with $1/Ro_1^* = 0.8$. After a transitional phase in the range of $1/Ro_1^* \leq 1/Ro \leq 1/Ro_2^* = 4$, Nu/Nu_0 decreases rapidly, below $0.5 Nu_0$ for our highest $1/Ro$. The decrease is fitted by a power-law A/Ro^B, where $A = 1.70 \pm 0.06$ and $B = -0.42 \pm 0.02$, however, we note that a logarithmic function of the form $N \log(M/Ro)$ (with parameters $N = -0.33 \pm 0.02$, $M = 0.015 \pm 0.002$) fits the data equally well and the parameter range in $1/Ro$ does barely cover one decade. Therefore, a power-law behaviour is not necessarily deductible from our data alone. It seems logical that in the first regime the flow is dominated by buoyancy, whereas the third is at least strongly influenced by the rotation and the occurring Coriolis forces. This suppresses vertical motion in the bulk, i.e. leads to the Taylor-Proudman effect (see sec. 2.5). In fig. 3.8a

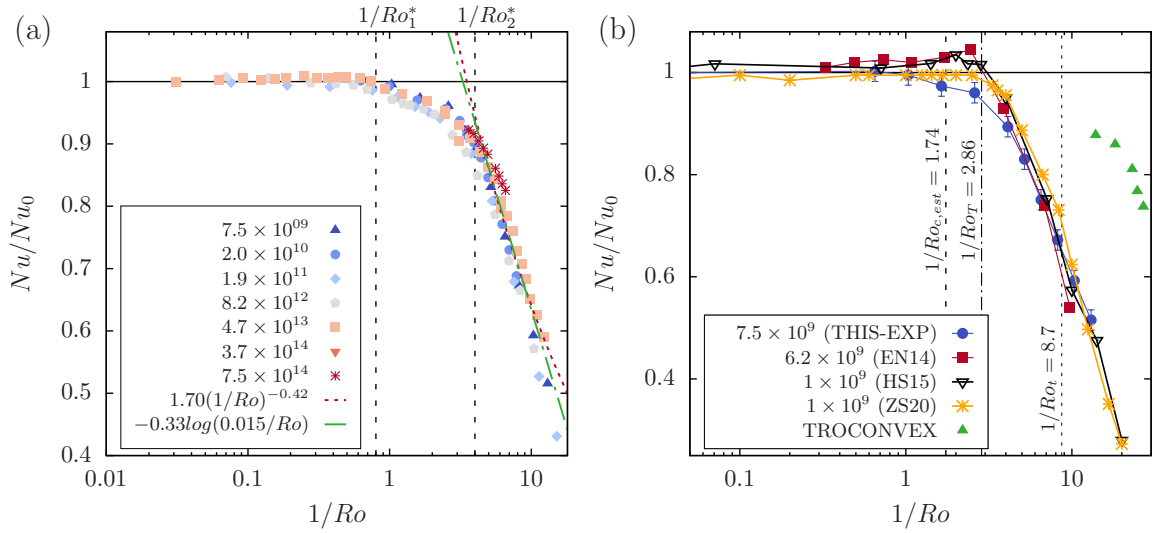

Figure 3.8: (a) Nu/Nu_0 as function of $1/Ro$ in semi-logarithmic representation of a selection of runs with Ra symbolized by different shape/colour as specified in the legend. Vertical lines mark the points $1/Ro_1^* = 0.8$, where Nu/Nu_0 begins to decrease and $1/Ro_2^* = 4$, marking a transition to a possible power-law decrease. Dashed red line is a fitted power-law to data with $1/Ro > 1/Ro_2^*$, green dot-dashed line is a logarithmic fit to the same data. (b) shows a comparison of our data for the lowest $Ra = 7.5 \times 10^9$ (blue bullets) with data for $Ra = 6.2 \times 10^9$ (red squares) experimentally obtained in helium with $Pr = 0.7$ (Ecke and Niemela [2014]). Open black down-facing triangles mark DNS results for $Ra = 10^9$, $Pr = 0.8$ (Horn and Shishkina [2015]), orange stars as well $Ra = 10^9$ (Zhang et al. [2021]). Green up-facing triangles show experimental results for $Pr \approx 5.2$, $1.12 \times 10^{10} \leq Ra \leq 3.5 \times 10^{11}$ with $1/Ro \leq 30$ (Cheng et al. [2020]). Dashed vertical line shows the estimated cricital $1/Ro_{c,est}$ from Weiss et al. [2010], dot-dashed and dotted two transition points $1/Ro_t$ and $1/Ro_T$ from Ecke and Niemela [2014]. From Wedi et al. [2021].

one might speculate that within the rotation affected regime data at higher Ra, but constant $1/Ro$, show an increased Nu/Nu_0. While these differences are within the margin of uncertainty, Nu for two separate runs can differ by about 1% or so, we can not exclude such a Ra dependency. Another possible explanation is the increasing centrifugal effect at larger Ra since then, for $1/Ro = const$ one needs larger rotation rates, increasing Fr.

Our results are in general consistent with experiments and simulations conducted at comparable Ra and Pr. In fig. 3.8b we show experiments in cryogenic helium (red squares) by Ecke and Niemela [2014] and DNS at $Ra = 10^9$ (black triangles) by Horn and Shishkina [2015]. Looking closely at the intermediate regime $0.8 < 1/Ro < 4$ highlights some differences, where both studies show a small increase in Nu/Nu_0. Opposed to that, our experiment shows a significant decrease in heat transport already at this rotation rate at similar Pr and Ra. This difference is within the margin of uncertainty, especially since this enhancement is only clearly seen for one data point in both, Horn and Shishkina [2015] and Ecke and Niemela [2014]. In fact, in more recent DNS (Zhang et al. [2021]), again at $Ra = 10^9$, where finer computational grids and longer simulation time were used, this increase is not found. The dashed lines in fig. 3.8b marked with $1/Ro_T$ and $1/Ro_t$ show suggested values for the transition from buoyancy-dominated to rotation-affected ($1/Ro_T$) and from the rotation-affected to the rotation-dominated ($1/Ro_t$) regime, according to Ecke and Niemela [2014]. Clearly we do not capture these transitional values, our respective transitional rotation rates $1/Ro^*_{1,2}$ are considerably lower. How influential the Prandtl number on $Nu/Nu_0(1/Ro)$ is, shows data from Cheng et al. [2020] (green triangles in fig. 3.8b), obtained at $Pr = 5 - 6$ in a $\Gamma = 1/2$ cell. The decrease with rotation is found at substantially increased $1/Ro$.

Compared to measurements e.g. in water or even higher Pr, Nu is not affected by weak rotation rates, and we find $Nu/Nu_0 \approx 1$ for $1/Ro < 0.8$ for all Ra. Nevertheless, it is interesting to see where the predicted heat transport enhancement is expected to occur and where it falls within our detected changes of scaling behaviour. Therefore, the empirical law suggested by Weiss et al. [2016] is used, for which the Nu/Nu_0 enhancement sets in at $1/Ro_c = K_1 Pr^\alpha$ with $K_1 = 0.75$ and $\alpha = -0.41$. This result was obtained for a $\Gamma = 1$ cell, and while it is unclear how K_1 and α depend on Γ, it was previously found that $1/Ro_c = a/\Gamma(1 + b/\Gamma)$ for $Pr = 4.38$, where $a = 0.381, b = 0.061$ (Weiss et al.

[2010]). This could be combined to a rough estimate

$$\frac{1}{Ro_c} = \frac{K_1 Pr^{\alpha}}{\Gamma(1+b)} \left(1 + b/\Gamma\right). \tag{3.3}$$

For the experiment investigated in this section it was $\Gamma = 0.5$. Assuming an average $Pr = 0.8$ we calculate with eq. (3.3) $1/Ro_{c,est} = 1.74$, hence somewhere between $1/Ro_1^*$ and $1/Ro_2^*$. No significant changes can be observed at $1/Ro_{c,est}$ as seen in fig. 3.8b. This suggests that the mechanisms leading to a heat transport enhancement at larger Pr are absent for $Pr < 1$ and are not just counteracted by suppression of vertical velocity (Wedi et al. [2021]).

As introduced in the theory section (3.2.2), one goal in RBC research is to find simple scaling behaviours of $Nu(Ra, Ro, Pr)$ in the geostrophic regime. In it, the flow is affected heavily by rotation but still in a turbulent state. There is still uncertainty in which combinations of control parameters geostrophic convection is present, Julien et al. [2012] suggested a necessary condition to be $RaEk^{4/3} \gg 1$ and that this is also the only relevant parameter describing the flow, thus the relation $Nu \propto \left(RaEk^{4/3}\right)^{\alpha}$ was proposed. This is tested in fig. 3.9a, where Nu is plotted against $Ra/Ra_c = RaEk^{4/3}$. As seen, no collapse onto a single power-law between the different Ra is found. While this was expected for large $RaEk^{4/3}$, since we are far away from the geostrophic regime there, the data for smaller values all decrease for faster rotation. The data are compared to DNS results by Plumley et al. [2016] (green triangles) for large values of $RaEk^{4/3}$. In that study, the full equations for the quasi-geostrophic model were solved and the resulting data are thus defined to be within the geostrophic regime. A solid green line in fig. 3.9 shows the proposed scaling $\alpha = 3/2$. Clearly our data are still in transition from the rotation-affected towards a geostrophic regime, the fully developed regime is seemingly not achievable with the experimental setup, since for even smaller Ek also the centrifugal forces would become significant.

Ecke and Niemela [2014] found a good collapse of Nu/Nu_0, when plotted against a reduced $RaEk^{-7/4}$. This scaling was proposed by King et al. [2009, 2012] by matching the thickness of the thermal boundary layer and the Ekman layer, which marks the transition from the rotation-influenced to the rotation-dominated regime. We therefore plot our data in this way in fig. 3.9b. The data for lower Ra, measured with the working gas N_2, collapse rather well, as do the data at large Ra, measured with SF_6. Two

intermediate Ra runs lie somewhere inbetween. The reason for this shift is unknown, a Pr influence seems unlikely, since it changes only barely from the lowest $Ra = 7.5 \times 10^9$ ($Pr \approx 0.72$) to the highest $Ra = 7.5 \times 10^{14}$ ($Pr \approx 0.97$). Increasing the exponent to $RaEk^{8/4}$ collapses the data again since $Ro^2 \propto Ek^2 Ra$, which we have seen in fig. 3.8.

As we have seen in the previous analysis, our data are not represented well by $RaEk^{4/3}$. Let us remember that this $Ra_c \sim Ek^{-4/3}$ is the critical Rayleigh number for convective onset in an infinitely extended system. Here, we have a finite cell with $\Gamma = 1/2$, where wall modes (see sec. 2.8) occur even before the bulk convective onset. Their onset scales as $Ra_w \sim Ek^{-1}$. For rapid rotation it is thus interesting to test whether remnants of this scaling can be found in the heat measurements. For this, in fig. 3.9c we plot Nu as function of $RaEk$, separated between low rotation (open symbols) and fast rotation ($1/Ro > 4$) as closed symbols. Indeed we find for the rapidly rotating data a nice collapse of Nu as function of $RaEk$. A power-law through this fastest rotating data returns as a best fit $Nu \sim (RaEk)^{0.615}$ over three decades in $RaEk$. This suggests a strong influence from the wall even in the turbulent regime, where usually its influence is assumed to be weak.

Assuming Pr dependence to be weak enough in our case, one can fit the Nu data to Ra and Ek independently with a simple fit of the form $Nu \sim Ra^a Ek^b$. This is done within the rotation-dominated regime, i.e. $1/Ro \geq 1/Ro_2^* = 4$. The best fit yields $a = 0.54$ and $b = 0.45$. However, we note these values lie in an extended residual minima valley for the fit parameters a, b, see fig. 3.10a. There, blue colour symbolizes low residuals for the fit, while red show high residuals. One finds that all combinations $b = 0.83a$ exhibit similar residuals, thus are equally good fits to the data. For $a = 1, b = 0.83$, the fit is plotted in fig. 3.10b with a resulting power-law $Nu \sim \left(RaEk^{0.83}\right)^{0.54}$. These exponents are used to reduce Nu in fig. 3.9d, where we see no satisfying collapse of the data for this scaling. Hence this simple two-dimensional fit does not allow statements about the underlying physical relations.

3.3 Vertical temperature gradient

At high Ra and thus turbulent convection in the bulk flow, the BLs are the bottle neck in the heat transport, which presents itself in the temperature distribution along the vertical axis. In a fully conductive state T is a linear function of z, $T(z/H) = T_{bot} - \Delta z/H$,

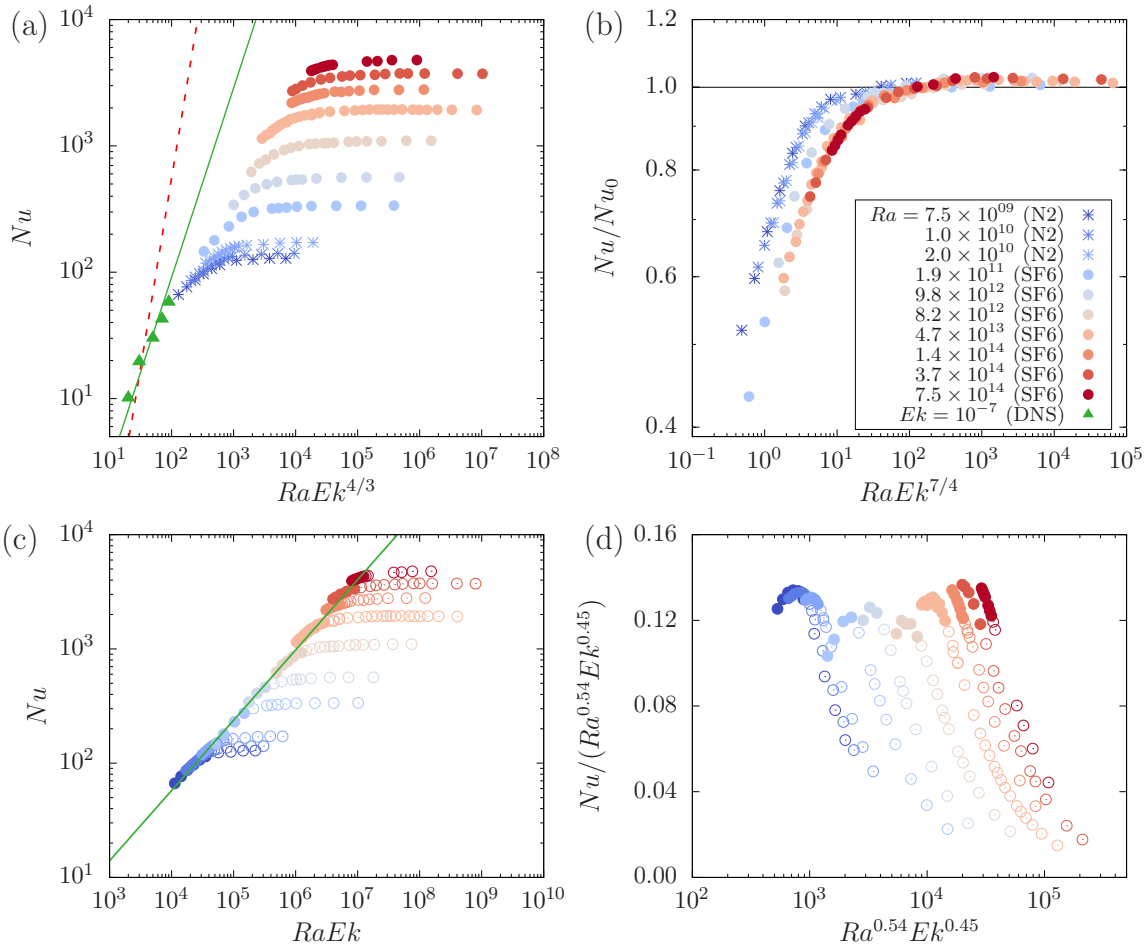

Figure 3.9: (a) Nu as function of $RaRa_c$ with $Ra_c \sim Ek^{-4/3}$ (Chandrasekhar [1961]). Differently coloured bullets show data with different Ra as in the legend of (b). Green triangles show data with $Ek = const$ from Plumley et al. [2016] in the geostrophic regime, green line the corresponding scaling $\sim (RaEk^{4/3})^{3/2}$ for large values of $RaEk^{4/3}$. Dashed red line shows the scaling behaviour from the same study for small $RaEk^{4/3}$ with exponent 3. The coefficients for both power-laws are chosen so that they intersect at $RaEk^{4/3} = 30$ as estimated from figure 2 of Plumley et al. [2016]. (b) Experimental data of Nu normalized by the value for no rotation Nu_0 as function of $RaEk^{7/4}$ as suggested in Ecke and Niemela [2014]. (c) Nu as function of $RaEk$, where colour again shows the same data as in the legend of (b). Filled spheres are data $1/Ro \geq 4$, while open are $1/Ro < 4$. The solid line is a power-law fit with exponent 0.62, which was fitted through all available data with $1/Ro \geq 4$. (d) Nu compensated by $Ra^{0.54}Ek^{0.45}$. The exponents were obtained from a two-dimensional fit to all data with $1/Ro \geq 4$ (filled spheres, also see fig. 3.10). Adapted from Wedi et al. [2021].

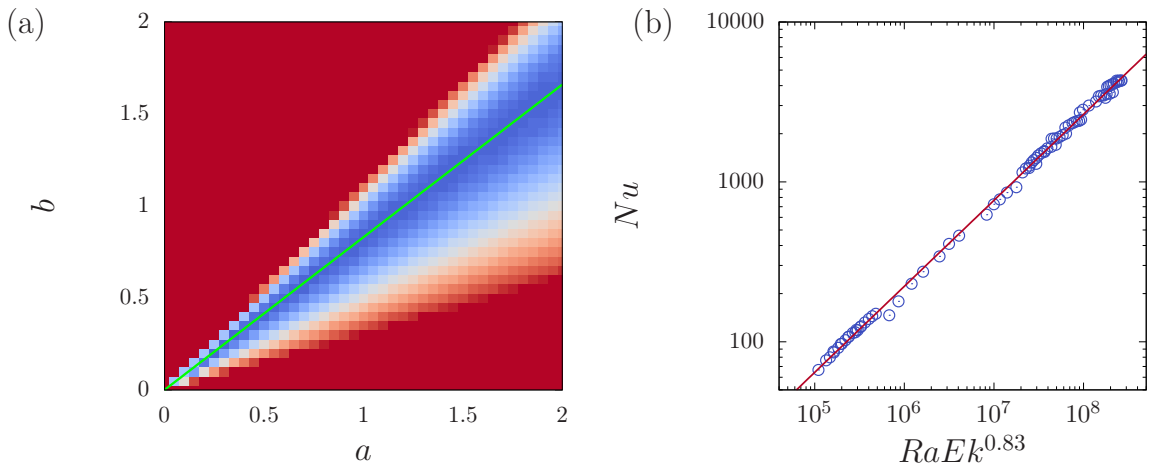

Figure 3.10: (a) fitted exponents a and b from $Nu \propto Ra^a Ek^b$ for data with $1/Ro > 4$ on a residual heatmap, where bluer colour corresponds to lower residual in the fit. Residuals are the X^2 values of the fits $X^2 = \sum \left(\left(Nu - Nu_{\text{fit}}(Ra^a Ek^b) \right) / \left(Nu - \langle Nu \rangle \right) \right)^2$. The green line symbolizes $b = 0.83a$, for which residuals are equally at a minimum. (b) best fit for Nu as function of $RaEk^{0.83}$, corresponding to a point on the minima curve of (a). Red line is a power law fit to the data with $Nu \propto (RaEk^{0.83})^{0.54}$. Adopted from Wedi et al. [2021].

whereas at high Ra, $T(z)$ has a sharp decrease at both the bottom ($z = 0$) and top ($z = H$) plates and is close to constant at $T_m = (T_{bot} + T_{top})/2$ in the majority of the bulk flow. Rotation affects this almost constant T distribution, which we analyse here in this section. From here on, we introduce

$$\Theta(z) = \frac{\langle T(z) \rangle - T_m}{\Delta} \tag{3.4}$$

as a normalized temperature, where $\langle \cdot \rangle$ denotes the temporal average.

One of the easiest quantitative investigations of the temperature profile in the bulk is done by fitting a linear function to measurements in the vicinity of $z = H/2$. This yields the central gradient $\partial\Theta/\partial z|_{z=H/2}$. With increased rotation we observe a larger gradient in the center of the bulk, returning an increased fitted slope. We determine $\partial\Theta/\partial z|_{z=H/2}$ by a linear fit to the azimuthal averaged measurements $\langle \Theta(z) \rangle_\phi$ as defined in (3.4) at $z = H/4$, $H/2$ and $3H/4$ within the sidewall, fig. 3.11e. The resulting gradients are shown in figure 3.11a. We see an increase in $|\partial\Theta/\partial z|$, which resembles the decrease in Nu in the previous section. The gradient starts to decrease around $1/Ro_1^* = 0.8$, though the change at $1/Ro_2^*$ is less pronounced. In fig. 3.11c we show measurements of

$\partial\Theta/\partial z|_{z=H/2}$ obtained within the fluid at radial distance $r = 0.93R$ from the cylinder axis. It exhibits a very similar behaviour to the case within the sidewall, with slightly stronger deviation due to rotation at $r = 0.93R$. There, however, the setup does not possess a thermistor at $z = 0.25H$, hence we use $z = 0.144H$ for the linear fit. Considering the non-linear $T(z)$ above the plates (see below) this introduces a systematic difference, i.e. somewhat larger gradients. At our innermost measurement $r = 0.73R$, we do not have working thermistors at $z = 3H/4$ for most of our runs unfortunately and we can not determine the gradient around $z = H/2$.

Omitting the measurement at half-height, one could also measure the difference between $z = H/4$ and $z = 3H/4$ at the sidewall as done by Stevens et al. [2009]. At $Pr = 4.38$ the study found a non-monotonic dependence on $1/Ro$ with a minimum temperature difference at $1/Ro \approx 0.34$. We can not reproduce this minimum, as the temperature difference between $H/4$ and $3H/4$ increases steadily with $1/Ro$. Liu and Ecke [2011] found a linear dependence $\Theta(z)$ even close to the plates in the central bulk in a cell with square cross section. The suggested relation $\partial_z\Theta$ with $1/Ro$ and Ra though does not follow some monotonic behaviour to compare with. The measurements in fig. 3.11c can, for large rotation rates $1/Ro \geq 1/Ro_2^*$, be approximated by a logarithmic function of $1/Ro$, which is plotted for reference as a black line. Note that logarithmic dependences on the input parameters are often found for decaying or spreading processes, but hardly expected in the present context. Nevertheless, data in other publications (Horn and Shishkina [2014], Wei et al. [2015]) also follow a logarithmic dependence of the form $\partial\Theta/\partial z|_{z=H/2} = A\log(1/Ro) + B$ rather closely.

Trying to find a more general scaling behaviour, we try to collapse the data at the wall by reducing it with $RaEk^{\alpha_w}$. For fast rotation, we find the best result with $\alpha_w = 7/4$, and while a power-law dependence over the whole $1/Ro$ range is not viable, a best fit for the rotation-dominated regime ($1/Ro > 4$) yields $\partial_z\Theta = (-0.22 \pm 0.01)(RaEk^{7/4})^{-0.40\pm0.02}$. The overlapping results for both distances from the sidewall agree with Cheng et al. [2020], where for the rotation-affected regime the gradient was found to be similar at the wall and the central axis. Contrary to our findings, in that study a relation $-\partial_z\Theta \sim Ra^{-0.21}$ as function of a reduced $RaEk^{8/5}Pr^{-3/5}$ was proposed at the transition from geostrophic turbulence to buoyancy dominated convection. Using this dependence for our data does not result in a satisfying collapse. This does not mean that the findings are necessarily in disagreement though. The experiments in Cheng et al. [2020] were

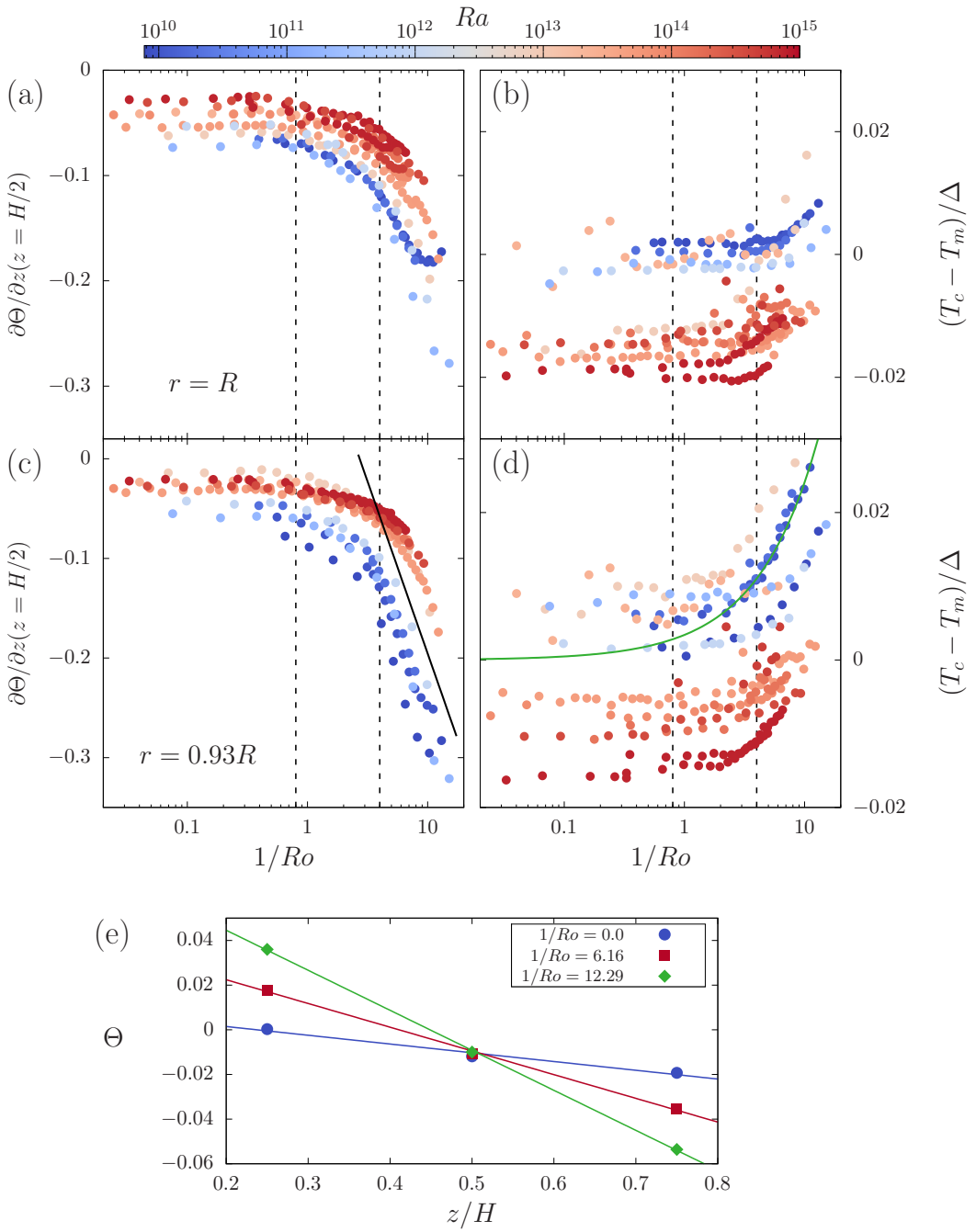

Figure 3.11: (a) linear gradient $\partial\Theta/\partial z$ between $H/4$ and $3H/4$, fitted to measurements there and at $H/2$ for all Ra (colour-coded) as function of $1/Ro$ at the sidewall $r = R$. (b) reduced central temperature at the wall from the fit $T(z)$ of (a). (c) temperature slope at $r = 0.93R$ as function of $1/Ro$ with a logarithmic slope $-0.15\log(1/Ro) + 0.15$ as black line. (d) reduced central temperature at $r = 0.93R$. Green line is a power-law $0.0034/Ro^{0.85}$, vertical dashed lines show $1/Ro^*_{1,2}$. (e) examples for gradient fits to reduced temperature data Θ for $Ra = 4.7 \times 10^{13}$ and three $1/Ro$ as in the legend.

performed at and beyond the geostrophic turbulence onset, while ours does not reach this point. Similarly, King et al. [2013] measured $\partial_z\Theta$ for rapid rotation and found a collapse of the central temperature gradient with $\widetilde{Ra}$ resulting in a power-law behaviour across all rotating data. Again here, the answer for the different behaviour lies in the lower values in $\widetilde{Ra}$ reached by the study compared to our setup.

In a similar manner the central temperature T_c is obtained by the linear fit through the adjacent measurements, which reduces the measurement error compared to just considering the data exactly at half-height. Fig. 3.11(b and d) shows T_c again at radial distances $r = R$ and $r = 0.93R$. Noticeable is a decrease in $(T_c - T_m)/\Delta$ for higher Ra at constant rotation rate like it has been observed in previous studies for NOB effects, such as Wu and Libchaber [1991] or Ahlers et al. [2007]. The influence here is small, at maximum, at our highest Ra, we see a decrease of $\approx 0.02\Delta$. At higher pressures, the fluid properties of SF_6 depend stronger on temperature, leading also to an increased NOB effect at higher pressures and therefore higher Ra, assuming $\Delta = const$.

With increased rotation for $1/Ro \geq 4$, the central temperature starts to increase by some 0.01Δ for the highest rotation rate with respect to the weakly-rotating case. We note that in a perfect Oberbeck-Boussinesq system, this deviation should not occur. There, the boundary layer at the plates resides at approximately the same temperature independent of rotation, hence for $\Delta = const$, $Ra = const$, also the thickness of the BLs remains constant. The central temperature for this ideal system for all $1/Ro$ is $T_c = T_m$, see e.g. Horn and Shishkina [2014]. For a constant deviation from the OB conditions, for example by setting a high Δ, increasing the rotation also changes T_c, as the same study showed for $Pr = 4.38$. There, $(T_c - T_m) \propto 1/Ro^{0.66}$ was found for $1/Ro \geq 2.8$. The variations in our data are rather large for different Ra and not sufficient for a comprehensive analysis, but a fitted power-law to the data with $Ra = 10^{10}$ (green line in fig. 3.11d) returns a relation $\propto 1/Ro^{0.85\pm0.05}$.

3.4 Logarithmic temperature profiles above the plates - $\Theta(z)$

Let us now consider not only mid-height, but the temperature profile along the entire vertical axis. For a first picture, in fig. 3.12a, vertical profiles $\Theta(z/H)$ are shown for $Ra = 4.7 \times 10^{13}$ and various $1/Ro$. We find a larger local gradient close to the plates and a rather small central gradient. For non-rotating RBC, using the same cell, a logarithmic

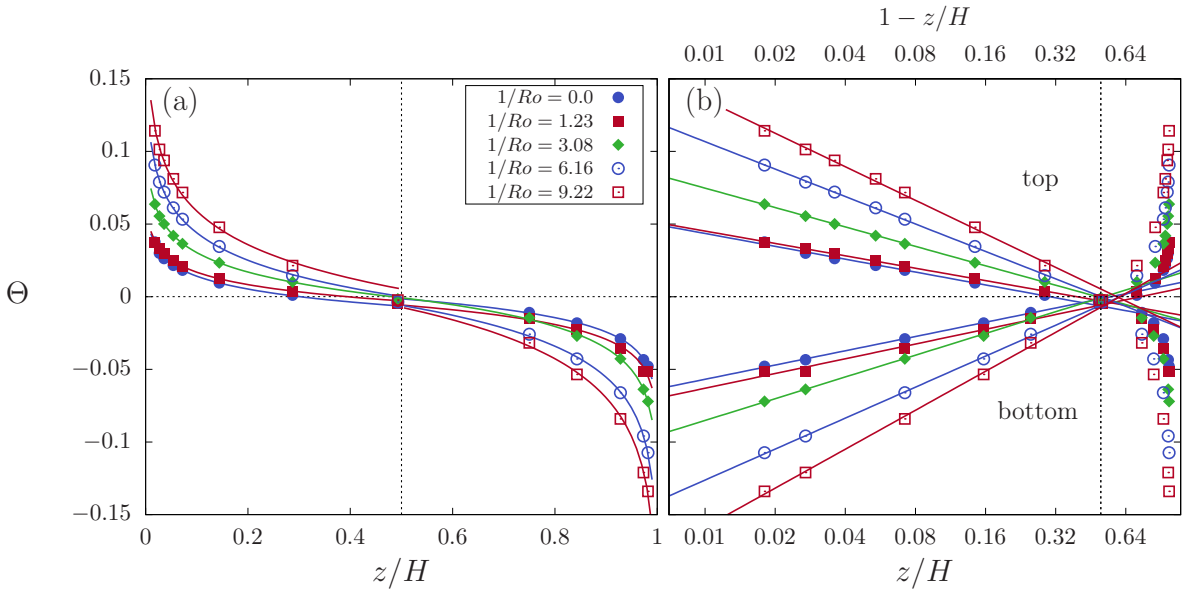

Figure 3.12: Vertical profiles of the reduced temperature $\Theta = (\langle T \rangle - T_m)/\Delta$ with height z/H for different rotation rates as in the legend and at $Ra = 4.7 \times 10^{13}$. (a) linear representation, lines are corresponding logarithmic fits to the data according to eq. (3.5) and (3.6). (b) Same data, but plotted semi-logarithmically as function of $1 - z/H$ in the upper half (upper part) and lower half as function of z/H of the cell (lower part). Adapted from Wedi et al. [2021].

temperature profile as function of height z above the heated bottom plate was found to fit the data quite well (Ahlers et al. [2014]). In order to characterise our temperature profiles, we pick up on that result and fit functions of the form

$$\Theta(z) = -a_b \log(2z/H) + b_b \qquad \text{for} \quad z < H/2 \tag{3.5}$$

$$\Theta(z) = a_t \log(1 - 2z/H) + b_t \qquad \text{for} \quad z > H/2 \tag{3.6}$$

to the measurement data. $a_{t,b}$ now represent the logarithmic slopes of the temperature gradient in the upper and lower half of the convection cell, respectively.

The steady decrease in a with Ra (fig. 3.13) for all r/R translates into smaller gradients in the bulk as seen before and is to be expected, as with increasing Ra the turbulence and mixing in the bulk is enhanced. The absolute value of the slope is smallest at the well-mixed bulk flow and increases towards the sidewall. One can speculate that this is due to corner rolls which develop close to the bottom and top plates, which counteract the LSC. This leads to a stronger gradient in the vertical direction far above the boundary layer.

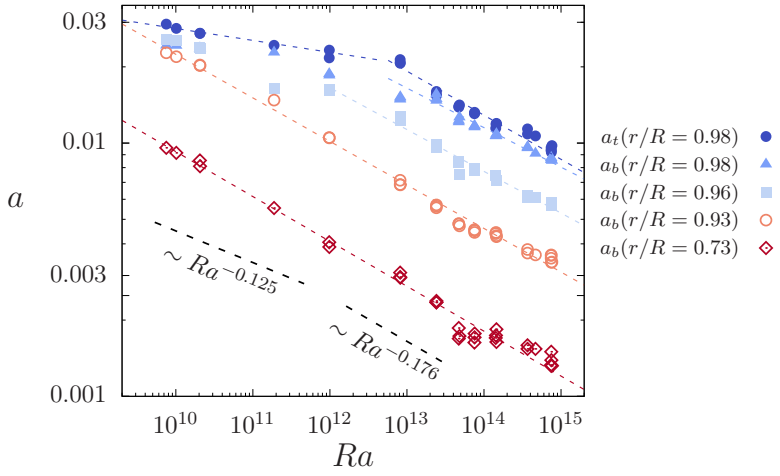

Figure 3.13: Double-logarithmic plot of the change of a from eq. (3.5),(3.6) for no rotation $1/Ro = 0$ as function of Ra at different $r/R = 0.98$ (blue bullets and up-facing triangles), $r = 0.96R$ (light blue squares), $r = 0.93R$ (light red open circles) and $r = 0.73R$ (red open diamonds). For comparison lines following $Ra^{-0.125}$ and $Ra^{-0.176}$ are shown as dashed lines. The dashed coloured lines are power-law fits through the data, for $r/R = 0.98$ to data with $Ra \geq 10^{13}$, and for $r/R = 0.93$ for $Ra \geq 10^{12}$.

Ahlers et al. [2014] observed a dependence $a_{t,b} \propto Ra^{\eta}$ for the non-rotating case, where η depends slightly on the radial distance r/R. It was differentiated between low $Ra = \mathcal{O}(10^{12})$ ("classical" state) and high $Ra = \mathcal{O}(10^{15})$ ("ultimate" state). In fig. 3.13 we show the two suggested dependences with the respective $\eta = -0.125$ and $\eta = -0.176$. Compared to the previous study, we cover more decades in Ra but have less resolution. Similar to Ahlers et al. [2014] we see a different behaviour for relatively low Ra and high Ra, however, only close to the wall for $r/R \geq 0.96$. For $Ra \geq 10^{13}$ we find $\eta_t = -0.174 \pm 0.008$ and $\eta_b = -0.156 \pm 0.008$ at $r = 0.98R$. Further away from the sidewall, we find $\eta(r = 0.96R) = -0.165 \pm 0.005$, $\eta(r = 0.93R) = -0.172 \pm 0.003$, and $\eta(r/R = 0.73) = -0.177 \pm 0.003$. This means that the slope further inside the bulk increases slightly, but with notably worse resolution close to the wall as there only two decades in Ra were considered. For $r/R \leq 0.93$, the scaling remains constant for lower Ra, while further outwards a depends less on Ra for small $Ra < 10^{13}$.

What is the cause of this? Possibly the temperature gradient at this radius is already too large to sustain and heat is moved from the lateral sides towards the bulk. However, diffusive transport is still too slow compared to the convective timescales. This suggests a boundary layer at the wall, which becomes increasingly smaller with Ra until it is thinner than $0.02R$ for $Ra \geq 10^{13}$. Viscous sidewall boundary layers were measured e.g. by Qiu and Xia [1998], who found a relation of the BL thickness $\delta_\nu/H = 3.6Ra^{-0.26}$

for a cubic cell. This relation underestimates the needed BL thicknesses to explain our results by about a factor of two. Lam et al. [2002] suggested $\delta_\nu/H = 0.65 Ra^{-0.16} Pr^{0.24}$ for the thickness of the viscous BL at the top and bottom plate. Assuming the Ra dependence at the sidewall is similar, we reproduce the changes in scaling behaviour in fig. 3.13 exactly, i.e. the viscous BL reaches down to $r/R = 0.98$ at some $Ra = 10^{13}$, and to $r/R = 0.96$ at $Ra = 10^{11}$. For even smaller $Ra \approx 5 \times 10^9$ we then expect the values for a at $r = 0.93R$ to overlap with the ones closer to the sidewall, which in fact is where our fitted power-laws for $r/R = 0.93$ and $r/R \geq 0.96$ meet.

Vertical temperature profiles with rotation

We now investigate the change of the vertical temperature profile as function of the rotation rate. Similar to above we quantify it here via the logarithmic fit parameters from eq. (3.5),(3.6) as function of $1/Ro$. For $Ra = 4.7 \times 10^{13}$ the temperature profiles as well as the fitted functions are plotted in fig. 3.12 for a selection of $1/Ro$. It can be seen that for faster rotation the convective bulk is less well mixed and the temperature gradient in the center therefore increases. When plotted in semi-logarithmic representation (fig. 3.12b), the logarithmic profile can clearly be seen also for the highest rotation rates. The bottom half of the cell is shown on the bottom part of fig. 3.12b as function of z/H, with the top half on the top plot as function of $1 - z/H$. The two halves of the cell are rather symmetric on first glance.

The fitted $a_{t,b}$ are shown as function of $1/Ro$ in fig. 3.14 for $Ra = 4.7 \times 10^{13}$. For $1/Ro < 1/Ro_1^*$, the values for $a_{t,b}$ are not influenced by the increased rotation. Afterwards, the slope increases according to a power-law $a_t \sim Ro^{0.51\pm0.02}$ and $a_b \sim Ro^{0.50\pm0.02}$. At our second transitional value $1/Ro_2^*$, we do not observe any notable changes in scaling behaviour. Values for the temperature offset b do not change drastically, representing that the central temperature remains very close to T_m even for the largest rotation rates. In plot 3.14c, the residuals from the fit to the temperature profiles show that the logarithmic fit works very well across all $1/Ro$. Only for $1/Ro > 10$ the residuals substantially increase, suggesting a deviation from the logarithmic profile.

While our focus before lay on one single Ra, the results for $a_{t,b}$ are summarized in plot 3.15 for all Ra. There, the slope value a_t for the upper half of the cell relative to the slope for no rotation $a_t/a_t(1/Ro = 0)$ is plotted as function of $1/Ro$. What this

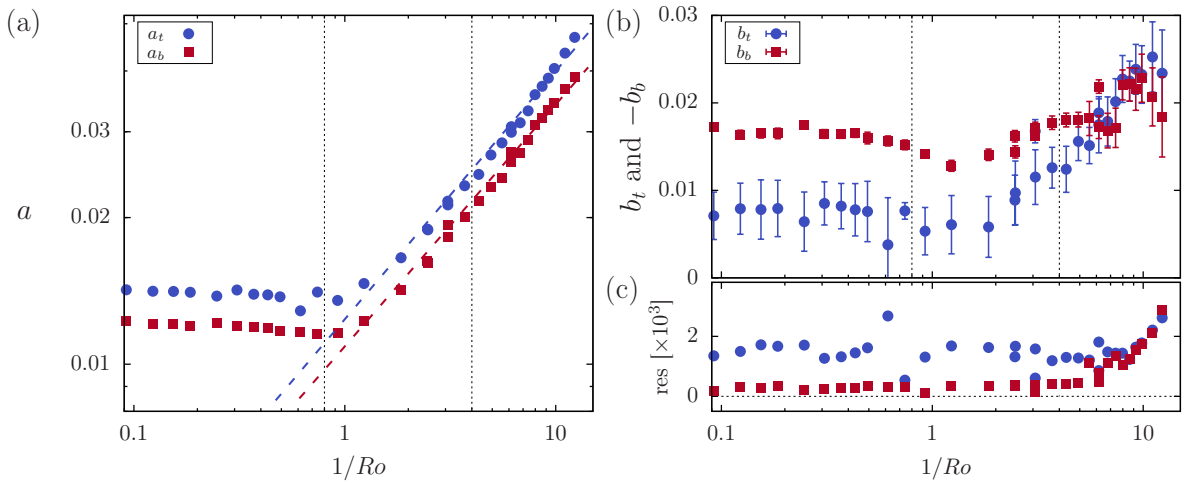

Figure 3.14: (a) fit parameter $a_{t,b}$ for the bottom half (subscript b, red squares) and the top half (subscript t, blue bullets) of the cell to the functions (3.5),(3.6) as function of $1/Ro$ for $Ra = 4.7 \times 10^{13}$. Dotted vertical lines show $1/Ro_1^* = 0.8$ and $1/Ro_2^* = 4$. (b) similarly to (a), fit parameters $b_{t,b}$ to the same functions and settings. (c) fit residuals for the same settings. Adopted from Wedi et al. [2021].

shows is that for higher Ra the gradient of the temperature profile increases faster with $1/Ro$ than for lower Ra, suggesting that the suppression of mixing through rotation is more effective at large Ra. This came as a surprise, as at similar $1/Ro$, but higher Ra, the convective term in the governing equations is stronger, while the Coriolis force remains the same. The different power-law fits can be collapsed onto a single master curve by plotting $a_t/a_t(0)$ against $1/Ro^{0.031\ln(Ra)-0.43}$ (fig. 3.15b), which is a purely empirical finding and not based on any theory. The exponents of $a_t/a_t(0) \sim 1/Ro^{\eta(Ra)}$ are plotted in the insert as function of Ra, which shows that $\eta(Ra) = 0.031\ln(Ra) - 0.43$. A similar analysis can be done by using Ek instead of Ro, which results in fig. 3.15c. It is evident that for sufficient rotation rates $a_t/a_t(0)$ closely follows a power-law behaviour $\propto Ek^\zeta$. Such a fit is applied to each Ra, the resulting exponents ζ are shown in the inset of fig. 3.15c. Note that some of the fitted exponents are not shown as data points in the main plot. At small $Ra < 10^{12}$, Ek is not low enough to reach this steady power-law, as seen by a curvature of the data in the log-log representation. Hence, ignoring these data points with $Ra < 10^{12}$, we obtain an averaged Ek^ζ with $\zeta = -0.55 \pm 0.02$. For all data with $1/Ro \geq 4$ we fit $a_t Ek^\zeta(Ra)$ with a power-law. Combined, for fast rotation $1/Ro > 1/Ro_2^*$ and large $Ra \geq 10^{12}$ we yield $a_t \sim Ra^{-0.355} Ek^{-0.55}$, see figure 3.16. Close to the wall this suggests that the slope of the vertical temperature profile decreases with increased thermal driving, but increases with rotation, like we could have assumed from the derivation of the thermal wind balance (2.52).

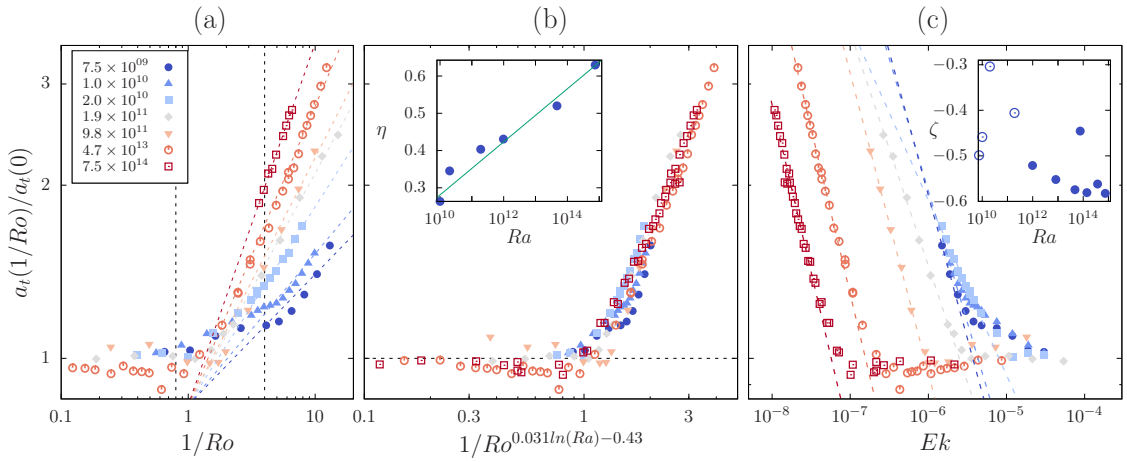

Figure 3.15: (a) fitted logarithmic slope a_t to eq. (3.6) as function of $1/Ro$, normalized by their non-rotating value $a_t(1/Ro = 0)$. Dashed vertical lines show $1/Ro_1^*$ and $1/Ro_2^*$. In colour and shapes are different Ra as specified in the legend. Power-laws of the form $m \cdot 1/Ro^\eta$ are fitted to each $Ra = const$, displayed as coloured dashed lines. (b) Collapsed plot of $a_t/a_t(0)$ by plotting it as function of the best-fit $1/Ro^{0.031\,\ln(Ra)-0.43}$. Shown in the inset are the fit parameters η (dashed lines in (a)). (a),(b) adapted from Wedi et al. [2021]. (c) Same data, plotted as function of Ek. Fits are power-laws to data with Ek sufficiently low where the slope remains constant. Inset shows these fitted exponents ζ, open circles for $Ra < 10^{12}$, filled bullets for $Ra \geq 10^{12}$.

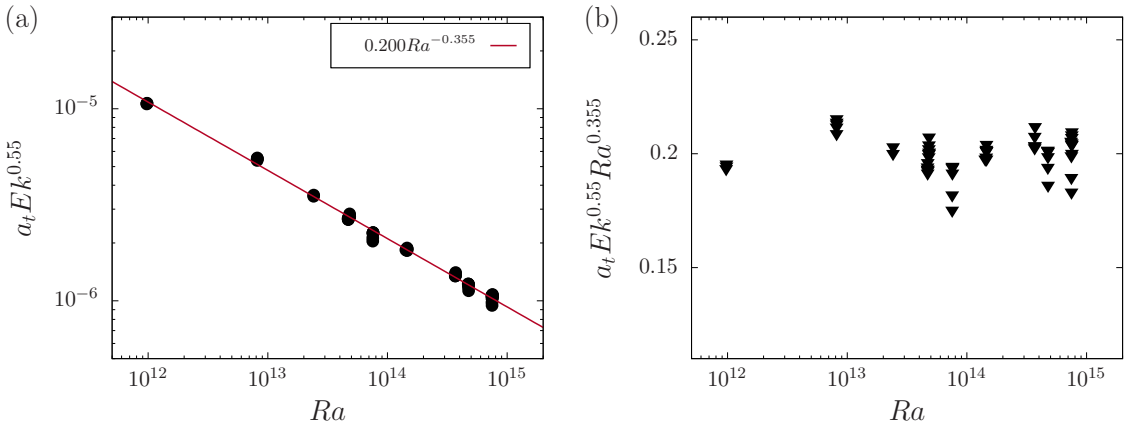

Figure 3.16: (a) logarithmic slope a_t of the temperature profile at $r/R = 0.98$ for the top half of the cell reduced by $Ek^{0.55}$ for data $1/Ro > 4$. Fitted is a power-law $0.199Ra^{-0.355\pm0.004}$. (b) Same data, reduced as well by the fit of (a).

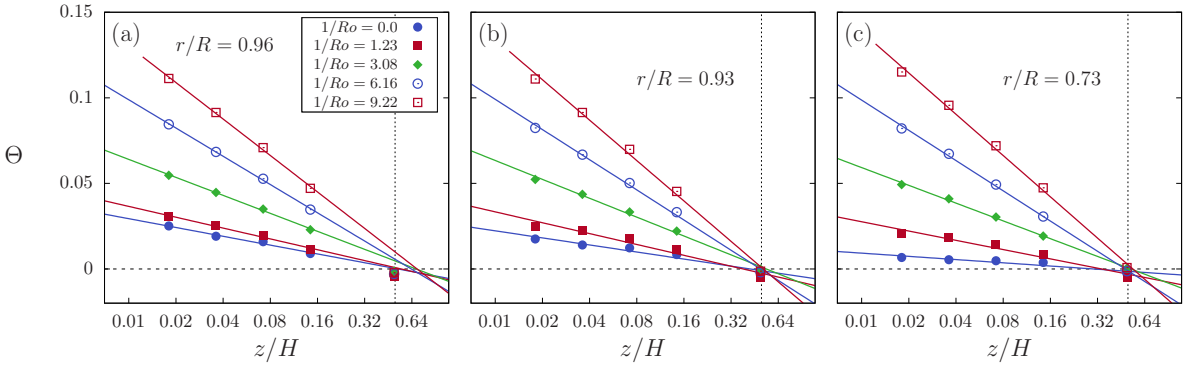

Figure 3.17: Profiles for the reduced temperature $\Theta = (\langle T \rangle - T_m)/\Delta$ for different $1/Ro$ as given in the legend of (a) at $Ra = 4.7 \times 10^{13}$. Plots show different r/R: (a) $r/R = 0.96$, (b) $r/R = 0.93$, and (c) $r/R = 0.73$.

For a more detailed look into the entire temperature field, we also consider the thermistor columns located further away from the sidewall at $r/R = 0.96, 0.93$ and 0.73. There, a similar logarithmic profile is found (fig. 3.17). Since within the bulk flow, no thermistors are placed at $z/H > 0.75$, we focus on the bottom measurements and its slopes a_b from similar fits as performed on the $r/R = 0.98$-measurements. In fig. 3.18, the resulting a_b are plotted against $1/Ro$ for $Ra = 4.7 \times 10^{13}$ at the four different radial locations. For low rotation rates, the values for the slopes a_b are very different between different r/R with a much more pronounced temperature gradient closer to the sidewall compared to the bulk flow. This is in accordance with the non-rotating case discussed above. However, at $1/Ro \approx 1/Ro_1^*$, also the slopes at $r/R = 0.96, 0.93$ and 0.73 increase rather quickly, before they join in magnitude at $1/Ro \approx 1/Ro_2^*$ and then increase as $a_b \propto 1/Ro^{0.63 \pm 0.02}$, at least for this Ra-Ro combination (black dashed line in the plot). The behaviour was found to be identical for all $Ra \geq 10^{12}$, for smaller Ra values for a_b close to the wall $r/R = 0.98$ and 0.96 remained below the slopes observed further away from the sidewall. As seen before, this suggests a boundary layer close to the lateral wall, which for $Ra \geq 10^{12}$ is too thin to observe at our measured radial positions.

Values for the temperature offset b_b (fig. 3.18b) collapse for fast rotation rates, as well. They are of largest magnitude at the sidewall and almost 0 within the bulk flow for no/low rotation. For large rotation rates above $1/Ro_2^*$, b_b for the different r/R become very similar. This suggests a temperature structure stretching from the location of our innermost thermistor $r/R = 0.73$ towards the sidewall, which was very surprising to see.

It is not obvious that we should observe logarithmic temperature profiles, at all. They

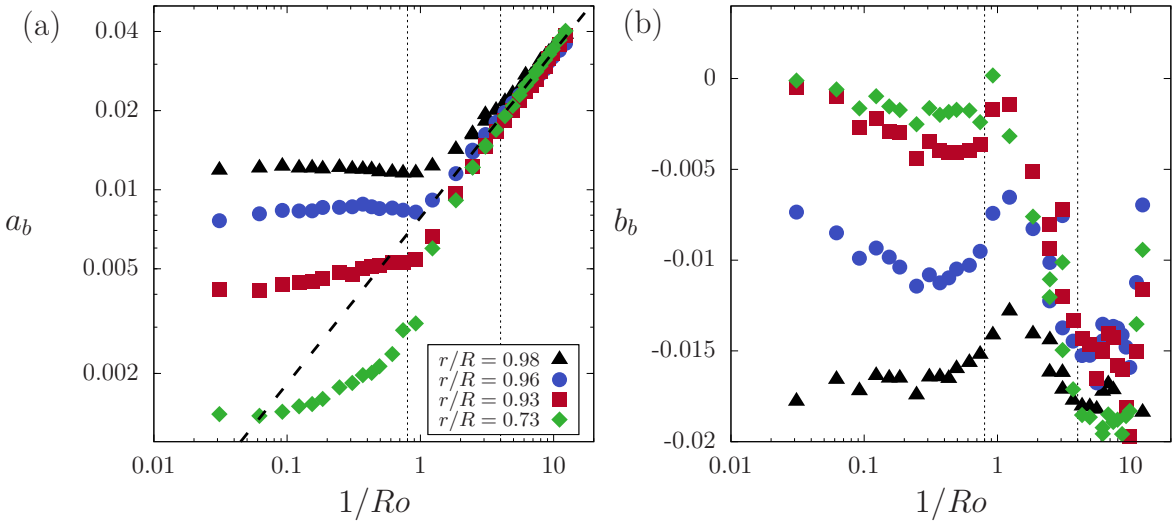

Figure 3.18: (a) logarithmic slopes a_b from the fit eq. (3.5) as function of $1/Ro$ for the four thermistor columns located at $r/R = 0.98$ (black triangles), $r/R = 0.96$ (blue bullets), $r/R = 0.93$ (red squares), and $r/R = 0.73$ (green diamonds). The black dashed line shows a power-law fit with exponent 0.63 to data with $1/Ro \geq 3$, where the values of a_b overlap. (b) offset values b_b from the fit eq. (3.5). for the same data set. Dotted vertical lines show $1/Ro_1^*$ and $1/Ro_2^*$. For all data $Ra = 4.7 \times 10^{13}$. Adapted from Wedi et al. [2021].

are often found in other fluid mechanical applications, a common example is the time-averaged velocity in a wall-bounded turbulent shear flow (Prandtl [1925], von Kármán [1930]). While logarithmic profiles of the temperature have been observed (e.g. Kader and Yaglom [1972], Landau and Lifshitz [1959]), the underlying assumption was that of a shear driven flow. Several studies of non-rotating RBC suggested a comparable behaviour, where the shear is created by the LSC, which has a predominantly horizontal velocity at the BLs (Grossmann and Lohse [2011], Ahlers et al. [2014]). As the LSC vanishes at larger rotation rates (see, e.g. Kunnen et al. [2008]), we still observe near-perfect logarithmic scaling $\propto \log(z/H)$. Even if at faster rotation the Ekman layers lead to a radial inward velocity, the transition from the origin of this shear flow would be very smooth as the low residuals in fig. 3.14c suggest.

3.5 Temperature PDFs

In the section above we have only considered time-averaged values. For a more complete view, we look at the entire temperature probability density functions (*pdfs*) at different rotation rates. In fig. 3.19 the *pdf* of the non-dimensionalized temperature $\tilde{T} = (T - T_m)/\Delta$ within the sidewall ($r/R = 1.0$) again for $Ra = 4.7 \times 10^{13}$ are shown

for four different $1/Ro$. We look at the three heights $z = H/4, H/2$, and $3H/4$. At each height eight thermistors are installed, over which the temperature data are averaged. For no rotation, fig. 3.19a, $p(\tilde{T})$ shows a skewed distribution for no rotation at $H/4$ and $3H/4$. The measurement at mid-height (green diamonds) exhibits a symmetric form with slightly wider tails than expected for a Gaussian distribution, which for comparison is fitted to the data as green line. This observation is commonly explained by the two influences of the temperature signal: the turbulent background, which exhibits a Gaussian distribution, and the signals of the thermal plumes ejected from the top (falling) and bottom (rising) plates. The latter are characterised by exponential distributions as suggested by e.g. Castaing et al. [1989], Kadanoff [2001]. If the plumes do not sufficiently mix with the surrounding fluid, we should see this as skewed Gaussian distributions close to the bottom and the top. Further analysis lead to the suggestion that the exponential distribution can be explained by a convolution of Gaussian-like dynamic modes based on the local thermal dissipation rate (He et al. [2018], Wang et al. [2019]). While we can not test this due to the lack of resolving the dissipation rate locally, qualitatively our measured exponential distributions at $z = H/2$ are consistent with such a superposition. Increasing the rotation rate slightly to $1/Ro = 0.74$ (fig. 3.19b) leads to a less skewed $p(\tilde{T})$ for $H/4$ and $3H/4$ and narrower tails for all heights. In particular at mid-height the distribution almost resembles a perfect Gaussian. This suggests the plumes ejected from the plates are better mixed with the environment and hence do not contribute to the shape of the *pdf* anymore, since particularly hot and cold temperatures build up the tails of the distribution.

At larger $1/Ro > 1/Ro_1^*$, $p(\tilde{T})$ splits into a bimodal Gaussian (fig. 3.19c, d) at all three heights. While the mean temperature at the respective z/H remains fairly similar, the signals seemingly consist of two very distinct temperature distributions. Further increase in $1/Ro$ (fig. 3.19d) leads to a significant widening of $p(\tilde{T})$, highlighted in the increased separation of the peaks. Thus, with increased rotation, even less mixing occurs between the hot and the cold regions. Both follow a Gaussian distribution, so we fit a bimodal Gaussian *pdf*

$$p(\tilde{T}) = \frac{A}{\sqrt{2\pi\sigma_1^2}} \exp\left(-\frac{(\tilde{T}-\mu_1)^2}{2\sigma_1^2}\right) + \frac{1-A}{\sqrt{2\pi\sigma_2^2}} \exp\left(-\frac{(\tilde{T}-\mu_2)^2}{2\sigma_2^2}\right), \tag{3.7}$$

to the $\tilde{T}$ data. Eq. (3.7) has five independent fit parameters, A, representing the relative amplitude of the two peaks, their expectation values $\mu_{1,2}$ and standard deviations $\sigma_{1,2}$.

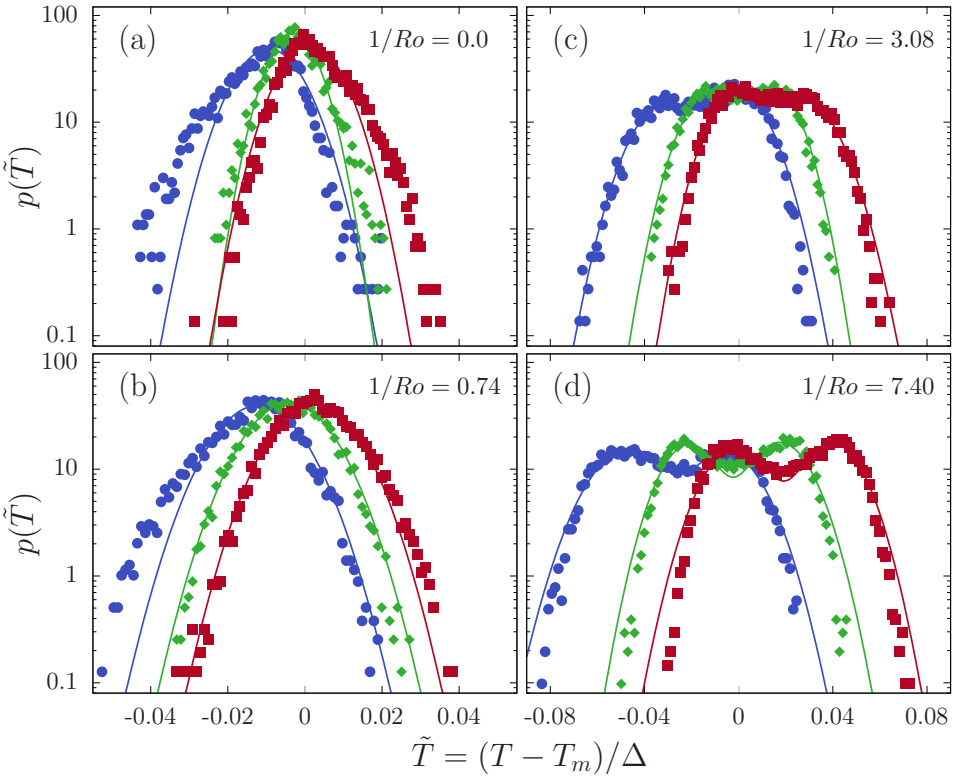

Figure 3.19: Probability density functions $p(\tilde{T})$ of the dimensionless temperature $\tilde{T} = (T - T_m)/\Delta$ for $Ra = 4.7 \times 10^{13}$, $1/Ro = 0$ (a), 0.74 (b), 3.08 (c) and 7.40 (d), measured inside the sidewall at $r = R$. Plotted are the *pdf* of $z = H/4$ (red squares), $z = H/2$ (green diamonds) and $z = 3H/4$ (blue bullets), together with respective plots of bimodal Gaussian distributions, eq. (3.7). For no or small rotation rates we see a skewed Gaussian distribution, while for higher rotation this transforms into a bimodal Gaussian. Adapted from Wedi et al. [2021].

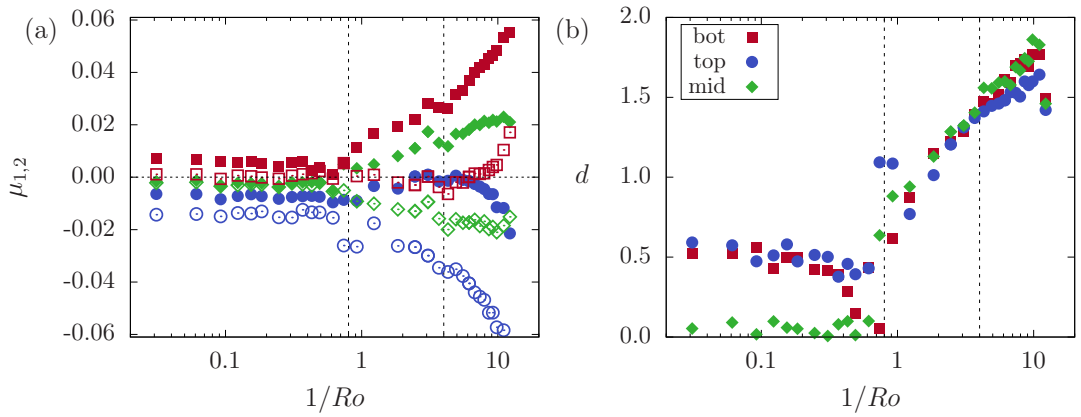

Figure 3.20: Distribution of the expectation values $\mu_{1,2}$ (a) and the standard deviations $\sigma_{1,2}$ (b) of the fits according to eq. (3.7) to the data for $r = R$, $Ra = 4.7 \times 10^{13}$ as function of $1/Ro$. Red squares are $z = H/4$, green diamonds $z = H/2$, blue bullets $z = 3H/4$, open and closed symbols are the two Gaussian contributions with $\mu_{1,2}$. Vertical dashed lines show $1/Ro_1^*$ and $1/Ro_2^*$. From Wedi et al. [2021].

For a consistent notation, we will refer to μ_1 as the colder part of the distribution and μ_2 to the hotter, so that always $\mu_1 \leq \mu_2$.

Fitting eq. (3.7) to a unimodal distribution results either in the amplitude A of one peak close to 0 or $\mu_{1,2}$ very close to each other. For $Ra = 4.7 \times 10^{13}$, the distribution of the expectation values is shown as function of $1/Ro$ in fig. 3.20a for each of the heights $H/4$ ('bot'), $H/2$ ('mid') and $3H/4$ ('top'). For $1/Ro < 1/Ro_1^*$, at each z we find $\mu_1 \approx \mu_2$, hence no bimodal distribution and all values are centered around the 0 mean, showing a well-mixed flow at each height. After $1/Ro_1^*$, the distribution widens: The cold (hot) part of the top (bottom) gets increasingly colder (hotter). Until $1/Ro_2^*$, the secondary peak with the hot (cold) fluid at the bottom (top) remains around the mean temperature $\mu = 0$. For the measurement at $z = H/2$ the values remain $\mu \approx 0$, then split up as well at $1/Ro_1^*$ and increase in distance up to our largest rotation rate. Only beyond $1/Ro > 4$ also the hot part at the bottom and the cold part at the top increases/decreases in temperature, without the two peaks getting closer due to an increased temperature change there as well. This is shown in fig. 3.20b, where the parameter

$$d = \frac{|\mu_1 - \mu_2|}{2\sqrt{\sigma_1 \sigma_2}} \tag{3.8}$$

is used as a measure of the distance of the two peaks in a bimodal distribution (Holzmann and Vollmer [2008]). For $1/Ro < 1/Ro_1^*$, d remains constant and small, but not

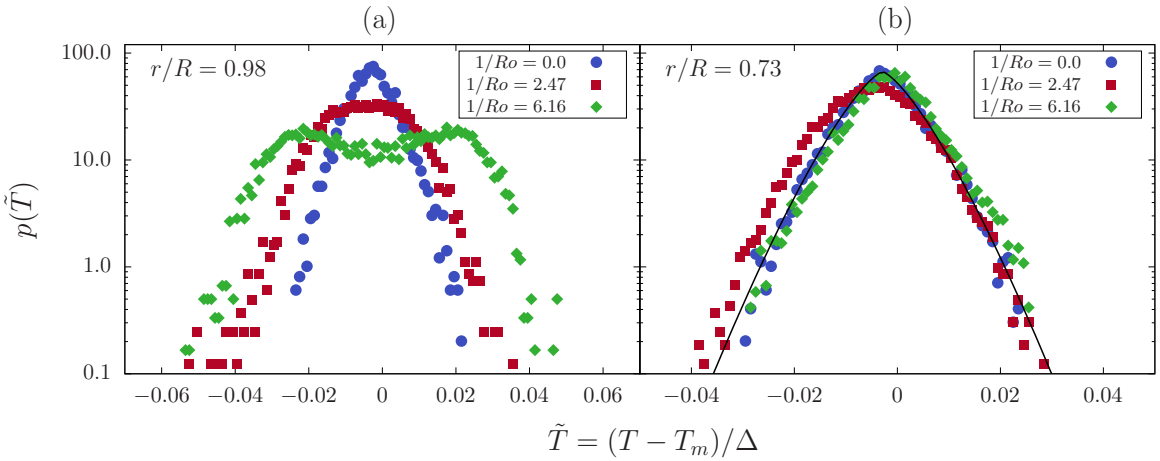

Figure 3.21: *pdf* for the reduced temperature $\tilde{T} = (T - T_m)/\Delta$ for $Ra = 4.7 \times 10^{13}$ and three rotation rates $1/Ro = 0$ (blue bullets), $1/Ro = 2.47$ (red squares), $1/Ro = 6.16$ (green diamonds). (a) shows data close to the wall, $r/R = 0.98$, (b) in the bulk, $r/R = 0.73$. In (b), we fit a stretched exponential distribution resulting in $67 \cdot \exp\left(-643 \cdot |\tilde{T} + 0.003|\right)^{1.34}$. From Wedi et al. [2021].

zero due to the skewed Gaussian distribution, where a secondary, low-amplitude Gaussian returns lower fit residuals. The distance d increases afterwards with $1/Ro$ up to the largest rotation rates, suggesting a mechanism where the mixing of the hot and cold temperature sides is increasingly suppressed.

For a better comparison how the distribution changes at the same position $z = H/2$, we show in fig. 3.21 the *pdf* for a constant $Ra = 4.7 \times 10^{13}$ with increasing rotation rate $1/Ro = 0$, 2.47, and 6.16. In fig. 3.21a, at radial distance $r/R = 0.98$, $z = H/2$, $p(\tilde{T})$ changes from a stretched exponential at no rotation to a broad Gaussian to a bimodal Gaussian distribution at large rotation rates, as seen before.

We have now seen how the *pdf* changes with rotation at the wall, but what about the measurements at the other radial distances? In fig. 3.21b, the distributions for $r/R = 0.73$ are shown, the measurements furthest away from the sidewall. The experimental settings are identical to the ones discussed above. For no rotation $1/Ro = 0$ we find a similar stretched exponential distribution, to which we fit the function $e^{-c|x|^\beta}$ and we yield as best fit the exponent $\beta = 1.34 \pm 0.03$. The decrease lies somewhere between an exponential distribution ($\beta = 1$) and a Gaussian ($\beta = 2$), as observed for temperature fluctuations in the bulk flow at relatively large Ra (Castaing et al. [1989], Ching [1991], Niemela et al. [2000]). Increasing the rotation rate to $1/Ro = 2.47$ (red squares in the plot) or even $1/Ro = 6.16$ (green diamonds) does not change the shape

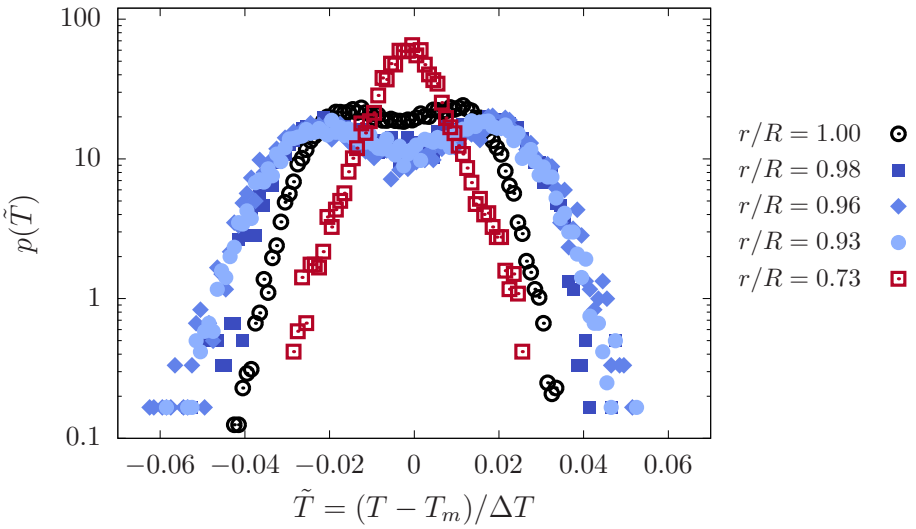

Figure 3.22: *pdf* for the reduced temperature $\tilde{T} = (T - T_m)/\Delta$ for $Ra = 4.7 \times 10^{13}$ at constant rotation rate $1/Ro = 6.16$, measured at half-height $z = H/2$. Different symbols show different radial locations as in the legend.

of the distribution and it remains a stretched exponential for all rotation rates. For the here discussed $Ra = 4.7 \times 10^{13}$, this only occurs at the innermost thermistor at $r = 0.73$, as highlighted in fig. 3.22. There, all measurements taken at different radial locations close to half-height $z \approx H/2$ are shown for a constant $1/Ro = 6.16$. We find that within the wall at $r = R$ the *pdfs* are slightly smoothed out, most likely due to the dampening effect of the surrounding sidewall. The distributions for the locations $r/R \geq 0.93$ overlap each other, all exhibiting the shape of a bimodal distribution. Only $p(\tilde{T}, r = 0.73R)$, shown as open red squares, remains at the stretched exponential form. How can this be interpreted? The results suggest the structure of the flow in our rotating experiments has to change drastically from close to the sidewall $r \geq 0.93R$ to the interior bulk flow $r \leq 0.73R$. We could not explain this behaviour, until we had DNS results to compare with, which will be discussed below in sec. 3.7.

3.6 PDFs with varying sampling frequency

Fluctuations of dimensions around their mean values often express a lot about the dynamic of the flow field. For example, in turbulence research, the deviation of the velocity u' about its mean value U defines the turbulence intensity u'/U. Due to the lack of velocity measurements in this setup, we focus on the temperature fluctuations.

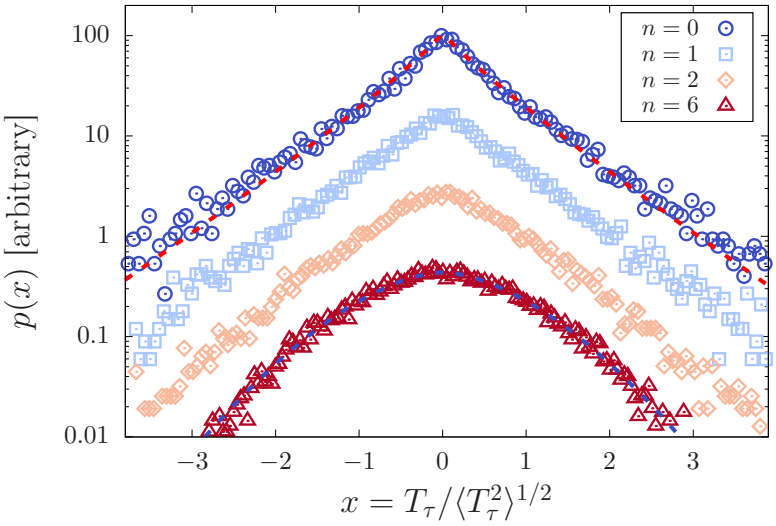

Figure 3.23: *pdf* of the temperature difference at varying sample steps $T_\tau = T(t+\tau) - T(t)$, where $\tau = 2^n \tau_0$, normalized by the rms value $\langle T_\tau^2 \rangle^{1/2}$ for $Ra = 4.7 \times 10^{13}$, $1/Ro = 0$, $z/H = 0.493$, $r = 0.73R$. Fitted to the data with $n = 0$ and $n = 6$ are stretched exponential distributions $\sim e^{-a|T_f|^\beta}$, resulting in exponents $\beta = 0.89 \pm 0.03$ ($n = 0$, blue spheres) and $\beta = 1.67 \pm 0.04$ ($n = 6$, red triangles). Light blue squares and light red diamonds show $n = 1$ and $n = 2$, respectively. The data are shifted on the y-axis for better visual separation.

Following up on the non-Gaussian distributed temperature *pdfs*, for no rotation (or in the central region), we at first compute the *pdf* of the temperature differences $p(T_\tau)$, where $T_\tau = T(t+\tau) - T(t)$. Here, τ is the separation of the measurement points, at varying sampling frequencies. Ching [1991] conducted similar measurements on this, where stretched exponential distributions were found for $p(T_\tau)$. Sticking to the same notation, we denote our base measurement frequency as τ_0, lower sampling rates are then noted as the $n-$th power of two: $\tau = 2^n \tau_0$. Stretched exponential distributions of the form $p(T_\tau) = Ae^{-c|T_\tau|^\beta}$ are used with the fitting parameters A, c, β. In the following, we focus on the exponent β. In Ching [1991], β depended on the sampling frequency, it increased from 0.51 for their τ_0 to a saturation level 1.7 ± 0.1 for increased separation at $n \geq 12$. For $Ra = 4.7 \times 10^{13}$, we show in fig. 3.23 *pdfs* for no rotation and four different sampling steps $n = 0$, $n = 1$, $n = 2$, and $n = 6$. Even though our sampling rate for the temperature measurements τ_0 is rather slow compared to Ching [1991], we do find a similar behaviour in the increase of the fitted β value with increased n.

For varying Ra and for $0 \leq n \leq 10$ we obtain values for β and plot it in fig. 3.24, against the time separation τ in units of the diffusive time scale H^2/κ for comparison.

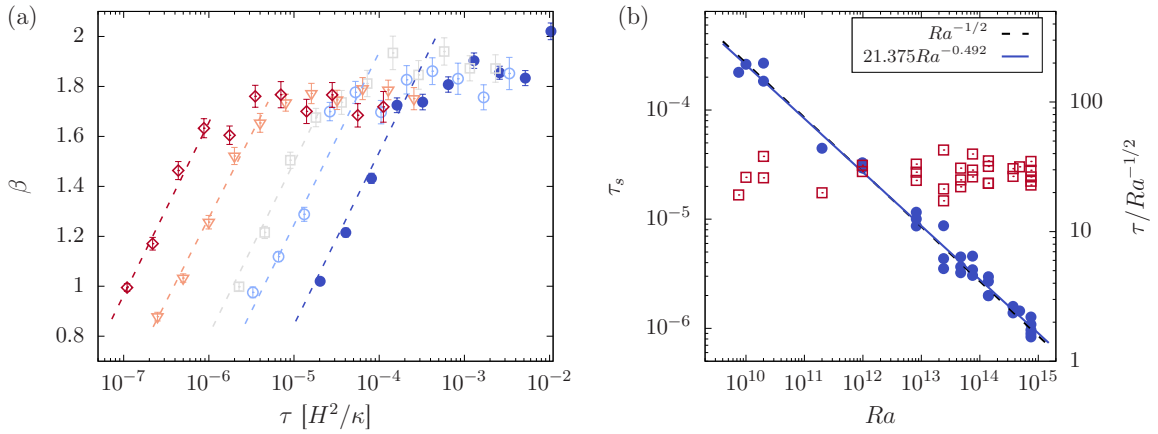

Figure 3.24: (a) Exponents β of the stretched exponential distributions of $p(T_\tau)$ for $Ra = 10^{10}$ (blue down-facing triangles), $Ra = 1.9 \times 10^{11}$ (purple bullets), $Ra = 9.8 \times 10^{11}$ (red squares), $Ra = 4.7 \times 10^{13}$ (orange up-facing triangles), and $Ra = 7.5 \times 10^{14}$ (yellow diamonds). τ is in units of diffusive time scales H^2/κ. The dashed lines are only guide to the eyes. (b) saturation time difference, where the exponent β does not increase with increased separation (blue bullets, left y-axis). Fitted is a power-law $\sim Ra^{-0.492}$ and for comparison an $Ra^{-1/2}$ is shown, as well. Red squares (right y-axis) shows the compensated diffusive time scale τ, where data at similar Ra show repeated experimental realizations.

In our data we as well see a saturation of β at higher separation τ, with slightly larger saturation level of $\beta \approx 1.8 \pm 0.1$ compared to Ching [1991]. This saturation is reached for roughly $n = 4$, while the time scale τ in units of the diffusive time scale decreases with Ra. The point where the value for β does not change anymore is associated closely to the decorrelation time, since $p(T_\tau)$ becomes independent of τ. In a non-rotating cell with $\Gamma = 1/2$ we expect a LSC to occur and a natural decorrelation time would then be one turnover time, which in turn scales with Re. Experimental studies show a relation $Re \sim Ra^\zeta$ with $\zeta = 0.41 \ldots 0.5$ (Sun and Xia [2005], Brown et al. [2007]). We test this in fig. 3.24b, where the separation time, at which the *pdf* becomes independent of τ, is plotted against Ra. We indeed find a decrease compatible with $Ra^{-1/2}$, with a fitted $21.375 Ra^{-0.492 \pm 0.02}$. It suggests the decorrelation time and thus the turnover time of the LSC to scale as such. Note, however, this scaling can be explained by the simple scaling of the diffusive time scale $H^2/\kappa \sim Ra^{-1/2}$ due to the dependence of κ on the pressure. This is shown as red squares in fig. 3.24b. Because of the similar behaviour of β between different conditions this dominates the $\tau_s \sim Ra^{-1/2}$. More points for $P = const$ and $T_m = const$ are needed for a better differentiation, since then also $\kappa = const$ and hence $\tau = const$.

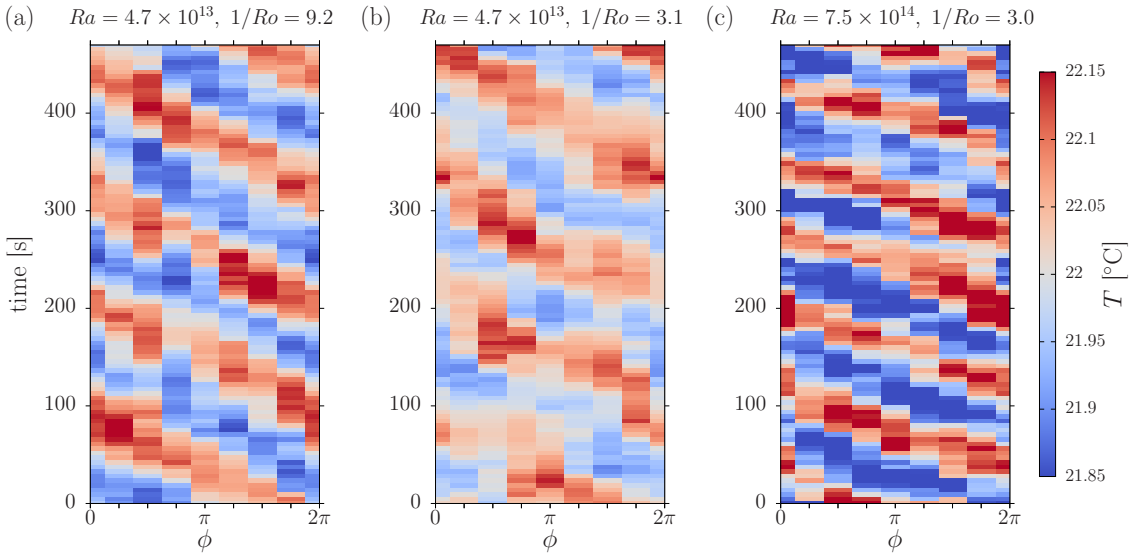

Figure 3.25: Time-angle plots of the temperature measurements in the sidewall $r = R$ at half-height $z = H/2$. Azimuthal angle is shown on the x-axis, where the data at $\phi = 0$ is shown at 2π, as well. (a) $Ra = 4.7 \times 10^{13}$, $1/Ro = 9.2$, (b) same Ra, but smaller rotation rate with $1/Ro = 3.1$. (c) Similar $1/Ro$ as in (b), but larger $Ra = 7.5 \times 10^{14}$. The temperature scale is the same for each plot.

3.7 The BZF in the temperature field

As we have seen in sec. 3.5, the bimodal distribution close to the wall compared to the unimodal in the interior bulk could not be explained, since typically one expects a rather well-mixed flow throughout the whole cell for large Ra. So let us look again at this region and see if we can draw any conclusions from a qualitative image of the temperature field.

To get a first impression, we consider a time-angle plot, for which we use the eight thermistors at $z = H/2$ at equal azimuthal spacing $\phi = (0,\ \pi/4,\ \pi/2,\ 3\pi/4,\ \pi,\ 5\pi/4,\ 3\pi/2,\ 7\pi/4)$. We plot the measured instantaneous temperature at $z = H/2$ for different times (y-axis) for three settings in fig. 3.25. The most striking result is the band-like structure we find in each case. At all times, we find one half of the circumference as a cold region, where flow must be drafting downwards and one warm side, which we interpret as an updraft region. This structure seems to be very stable across different Ra and all shown $1/Ro$. We see that the temperature signal drifts in retrograde direction, i.e. opposite to the enclosing cell. For smaller rotation rates with $1/Ro = 3$ at similar $Ra = 4.7 \times 10^{13}$ (fig. 3.25b) compared to $1/Ro = 9.2$ (a), the temperature signal is weaker, displayed in the lower colour saturation. For similar $1/Ro$, but higher $Ra = 7.5 \times 10^{14}$ (fig. 3.25c), the drift rate of the temperature structure increases.

This explains our found temperature distribution above: for sufficiently fast rotation, we measure this very distinct hot-cold pattern, where each mode of the bimodal distribution reflects one of these regions. Since we observe the effect only close to the outer sidewall, this suggests these temperature bands are also only found in vicinity of it. To exclude that this phenomenon is not just an experimental result, coworkers started to perform DNS with comparable $1/Ro$ (although at lower Ra) and rigid sidewalls to study this effect. Within the simulation, the temperature at $r = R$ was considered, which is shown for one case in fig. 3.26b. We found remarkable qualitative agreement to our results. This led us to believe this is a new flow morphology, from now on referred to as *boundary zonal flow* (BZF).

The DNS also revealed the BZF only occurs close to the sidewall, just as our measurements suggested. A schematic of this flow structure is found in fig. 3.26c. The hot updrafting region and the cold downdrafting regions are shown in the temperature field in the central region of the image. At the top the time-averaged azimuthal velocity field at half-height is projected. It exhibits an outer ring of co-rotating azimuthal velocity close to the sidewall (within the BZF), surrounding a radial center region with counter-rotating azimuthal velocity. With the here presented experimental setup we can not measure the velocity field, but measuring that will be the main topic of the second setup in sec. 4.3. Here, we only want to highlight the main findings of this zone: a drifting temperature field in retrograde direction and a co-rotating time-averaged azimuthal velocity field close to the wall.

The BZF could also explain the collapse of $Nu(RaEk)$ discussed above (fig. 3.9c). The mechanisms leading to wall modes scaling with Ek^{-1} prevail in the highly convective regime, which may transition into the BZF as suggested in Favier and Knobloch [2020]. The collapse suggests the BZF plays a crucial role in the global heat transport, which was observed and confirmed in DNS already (Zhang et al. [2020, 2021]).

Drift rate of the BZF

Naturally, we wanted to measure the temperature field's drift rate $\partial\phi/\partial t$. For this we adopted a method from previous studies, which focussed on determining the position of the large scale circulation (LSC) in non-rotating RBC. There, at least for $\Gamma = 1/2$, one has a distinct updrafting region and one down-drafting region (Verzicco and Camussi

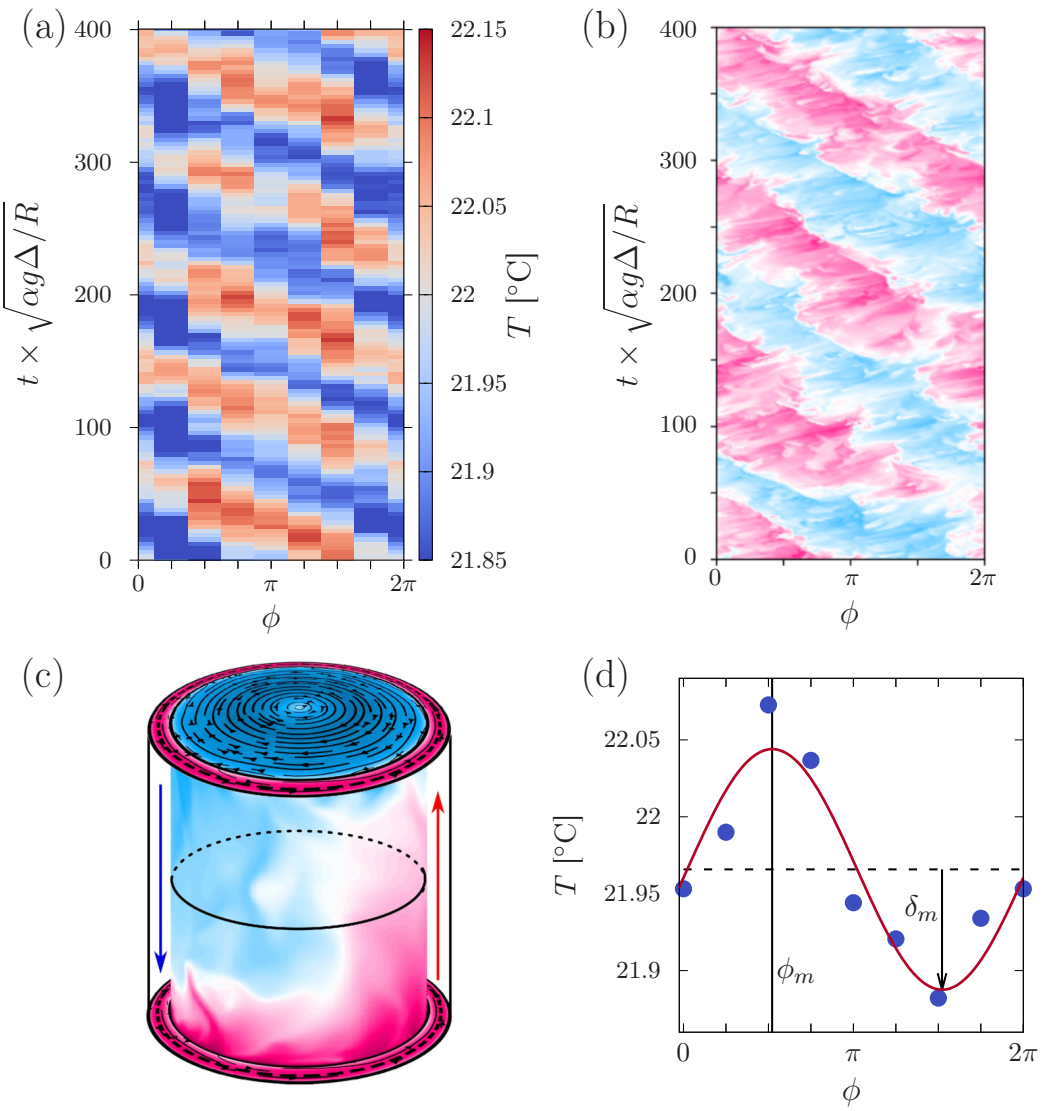

Figure 3.26: (a): Azimuthal temperature distribution for $Ra = 4.7 \times 10^{13}$, $1/Ro = 9.22$, $r/R = 1.0$, $z/H = 0.5$ as a function of time, normalized by the free-fall time $\sqrt{R/(\alpha g \Delta)}$. (b): Simulated dimensionless temperature at $r = R$ and $z = 0.5H$ as a function of time for $Ra = 10^9$ and $1/Ro = 10$. Note that for both plots we plot the temperature at $\phi = 0$ also for $\phi = 2\pi$ for a better visual appearance. (c): Schematic of the BZF. Top and bottom show the average azimuthal velocity at mid-height, the sidewall is colour coded with a snapshot of the simulated fluid temperature. The temperature field and the schematic were created using simulation results that were published already in Zhang et al. [2020]. The black circle marks the circumference at mid-height at which temperature was measured and plotted against time (b). (d): Temperature distribution as a function of the azimuthal angle (blue bullets) and a fit of eq. (3.9) to the data (red solid line). Conditions are as in (a). The fitted parameter ϕ_m and δ_m are also marked by a solid vertical line and a down-pointing arrow. Adapted from Wedi et al. [2021].

[2003], Brown and Ahlers [2007], Weiss and Ahlers [2011a]), as well. Also rotating systems were analyzed, tracking the changes of the LSC, such as in Zhong and Ahlers [2010], Weiss and Ahlers [2011b]. Since the BZF, like the LSC, is of wave number $k = 1$ for our $\Gamma = 1/2$ cell, we can use the exact same analyzing method to determine the hot and cold areas of the BZF. For this, we fit a harmonic function

$$T_{i,j} = T_{w,j} + \delta_j \cos\left(\frac{i\pi}{4} - \phi_j\right), \quad i = 0, \ldots, 7, \tag{3.9}$$

to the eight thermistors in azimuthal direction, denoted as index i. j denotes the vertical position, as we have the similarly distributed measurement points at three heights, thus j can take $j =$("b", "m", "t"), corresponding to the vertical locations $z =(H/4,\ H/2,\ 3H/4)$. We yield three fit parameters for each time step: the azimuthally averaged wall temperature $T_{w,j}$, the amplitude of the BZF δ_j and its orientation ϕ_j. Here, orientation is referred to as the maximum of the cosine-function, i.e. the hot updrafting region. An example of the fit onto data points at one time step is given in fig. 3.26d at $j =$"m". In fig. 3.27a we show the fitted angle ϕ for $Ra = 4.7 \times 10^{13}$, $1/Ro = 9.8$ as function of time. ϕ_m increases steadily until the best fit returns an angle shifted by 2π. To make the drift continuous we add or substract 2π each time the difference $\delta\phi_m$ is larger than π or smaller than $-\pi$ at two consecutive time steps $\phi_{m,i} - \phi_{m,i-1}$. This difference for each time step i results in plot 3.27b, where for each i the incremental drift $\delta\phi_m$ is plotted. We find that for this Ra and $1/Ro$ the BZF temperature structure moves by $\approx \pi/4$ each time step (≈ 4.7 seconds) relative to the cell. In the following we focus on this fitted angle ϕ_j, as the averaged temperature was analyzed previously in section 3.3.

If these differences $\delta\phi_m$ are added up, we obtain an accumulated angle, which curves show a rather smooth drift of $\phi_m(t)$. This is shown for multiple $1/Ro$ for $Ra = 4.7 \times 10^{13}$ in figure 3.28a. Again, note that this approach is valid for both flow states in a $\Gamma = 1/2$ cell, the BZF and the LSC. The obtained drift rate thus applies to both and it depends purely on $1/Ro$ which one we track using the fit function. From the plot, we see that for low rotation rates, ϕ_m changes only very slowly in prograde direction (positive ϕ), while for increased $1/Ro$, $|\phi_m|$ increases to negative values. This result is in accordance with the qualitative image of the temperature field in fig. 3.26a. The change of ϕ is fairly linear and smooth, so we define a drift rate based on the slope $\omega_j = \langle \partial\phi_j/\partial t \rangle_t$. With ω we now measure the drift rate of the temperature field in azimuthal direction with respect to the cylinder. We already see here that ω_m is not a monotonic function

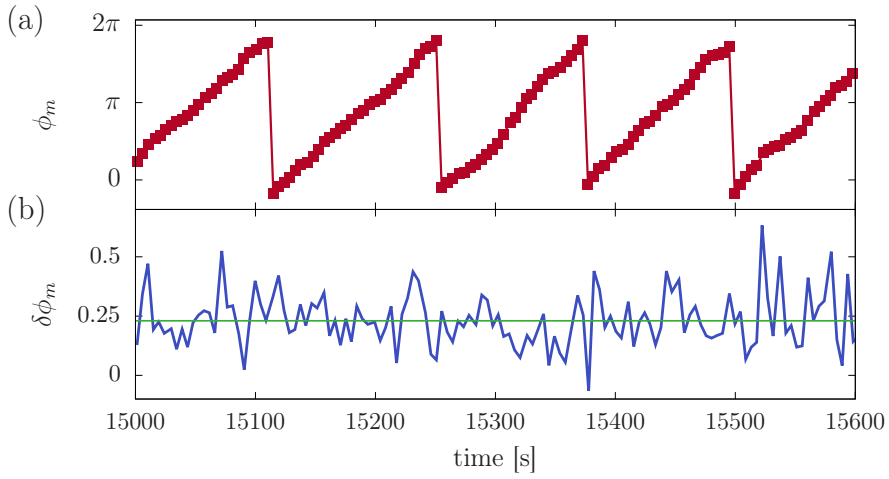

Figure 3.27: (a) Example of a time series of the fitted angle ϕ_m for $Ra = 4.7 \times 10^{13}$, $1/Ro = 9.8$ and (b) the corresponding change of angle $\delta\phi_m = \phi_{m,i} - \phi_{m,i-1}$.

of $1/Ro$: for low rotation we observe $\omega_m > 0$, with increasing rotation, ω_m decreases into a retrograde motion, while for the largest $1/Ro$ the slope again decreases slightly in amplitude.

So far, we have looked only at mid-height, but we have three rows of thermistors inside the sidewall. It is interesting to see whether the BZF is only localized around $H/2$ or if it spans the majority of the vertical axis. For relatively low Pr one usually assumes the thermal signature to diffuse relatively quickly into the surrounding, so the question is, do we still see the warmer bands at $z = 3H/4$ and the cold ones at $z = H/4$ after they travelled across 3/4 of the cell height? For this, ω_j is plotted for all three heights $z = H/4, H/2, 3H/4$ as function of $1/Ro$ for our representative $Ra = 4.7 \times 10^{13}$ in fig. 3.28b. For slow rotation, we observe what we have seen in fig. 3.28a already, the drift rate at mid-height is slightly positive and in prograde direction, i.e. faster than the cylinder. Closer to the bottom (red points) and top (blue) plates the velocity is almost equal 0. We can conclude that the temperature field is accelerated only around the mid-height. Increasing the rotation rate, ω_m crosses 0 into a retrograde drift rate at $1/Ro_1^*$, our transitional value for the BZF. For $1/Ro > 1/Ro_1^*$ the drift rates ω_j for all three heights lie exactly on top of each other, suggesting the structure of the BZF is very robust in vertical direction without differential rotation. ω_j increases in amplitude towards larger retrograde rotation rates up to $1/Ro \approx 7$, afterwards $|\omega_j|$ decreases again.

Using the same technique, Weiss and Ahlers [2011b] found a very similar behaviour

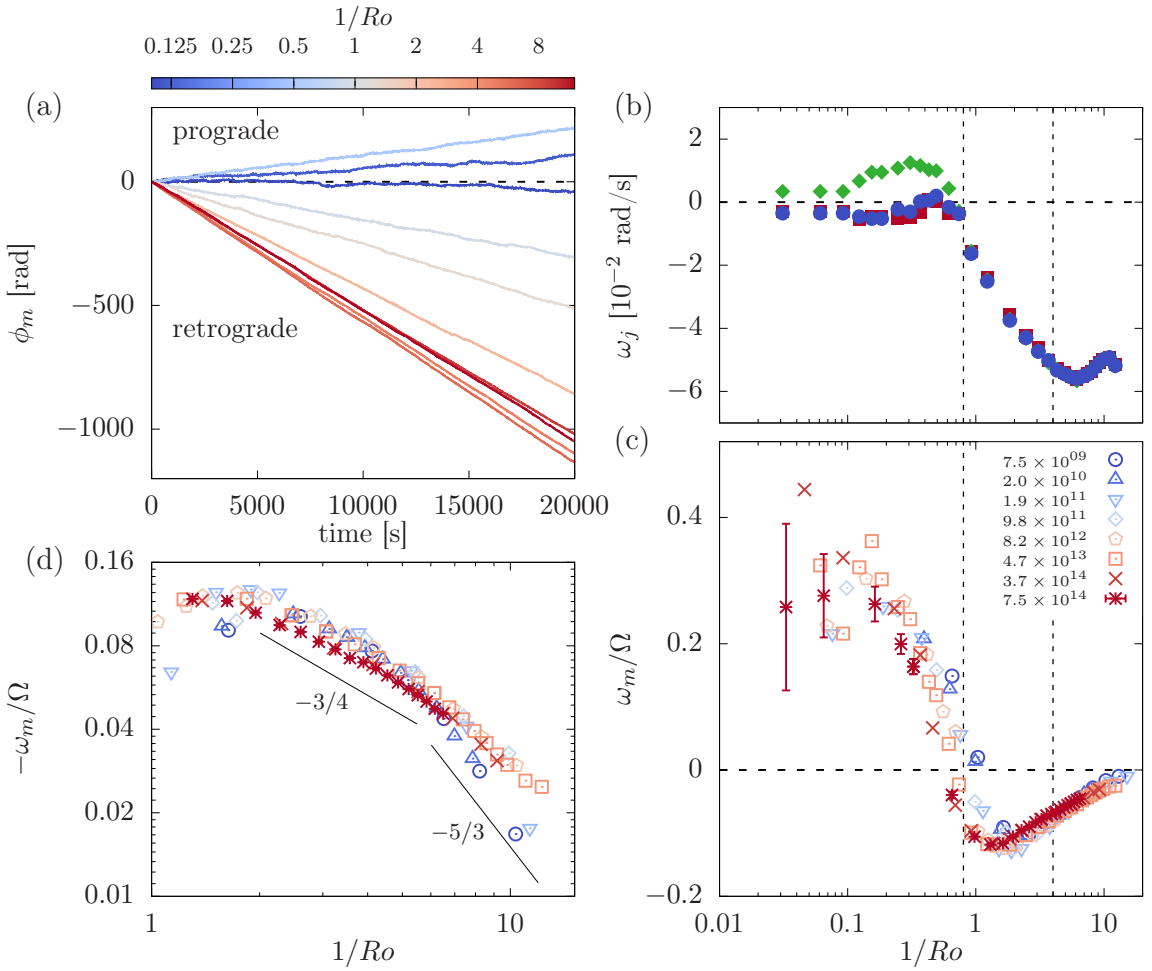

Figure 3.28: (a) Azimuthal orientation of the LSC (for small $1/Ro$) and the BZF (for large $1/Ro$) as a function of time for $Ra = 4.7 \times 10^{13}$ (Run E2e) and various $1/Ro$. (b): Average azimuthal drift velocity $\omega_{t,m,b}/\Omega$ at vertical heights $z/H = 0.75$ (blue circles), $z/H = 0.5$ (green diamonds) and $z/H = 0.25$ (red squares). (c): Average azimuthal drift velocity ω_m/Ω as a function of $1/Ro$ and for various Ra as marked in the legend. Horizontal dashed lines mark $\omega_m/\Omega = 0$. The vertical dashed lines mark $1/Ro_1^*$ and $1/Ro_2^*$. (d): Same data as in (c) multiplied by -1, only shown for $1/Ro > 1$ and plotted in a double-logarithmic representation. The black lines mark power-laws with exponents $-3/4$ and $-5/3$ for comparison. Taken from Wedi et al. [2021].

(their fig. 13), including the transitional value where ω_j changes sign, which in their publication appeared at a comparable $1/Ro \approx 0.85$. Measured at lower $Ra = 3.59 \times 10^{10}$ and higher $Pr = 4.38$, this $1/Ro$ corresponded to a local minimum in the heat transport enhancement. With higher rotation rates, Ekman pumping set in and Nu/Nu_0 increased. Even though in our setup we should not see influences of Ekman pumping due to our lower Pr, the similarity of the transitional $1/Ro_1^*$ is intriguing. Likely Weiss and Ahlers [2011b] detected the signal of the BZF for faster rotation rates, which will be discussed below in sec. 3.9. Whether the onset of both the BZF and Ekman pumping is connected or if it is coincidentally at a similar $1/Ro$ remains an open question for now.

The behaviour of $\omega_j(1/Ro)$ appears similar for all Ra we measured as seen in fig. 3.28c. Here, all ω_m for all Ra are plotted on top of each other, normalized by the drift rate of the outer cylinder Ω. For small rotation we always find $\omega_m > 0$, which decreases with increased $1/Ro$ and crosses 0 at $1/Ro \approx 1/Ro_1^*$. One might speculate that the crossover to retrograde drift sets in later for smaller Ra, the difference is however small and our resolution limited. For larger $1/Ro > 2$ all data collapses onto one curve. A zoomed in plot of this is given in fig. 3.28d, where the negative normalized $-\omega_m/\Omega$ is plotted as function of $1/Ro$. For $2 \leq 1/Ro \leq 7$ data seemingly follows a decay $\sim 1/Ro^{-3/4}$. Simulations at smaller Ra in Zhang et al. [2021] observed $\omega/\Omega \sim 1/Ro^{-5/3}$, which we show as a line in the plot as reference. We note that the behaviour for our smallest Ra and fastest rotation rates might agree with that scaling.

3.8 Correlations from singular temperature probes

Comparing two signals separated by either time or space yields information on the flow field as well. This is commonly done by correlating a signal with itself (auto-correlation) or with another signal (cross-correlation). In our case, since we have poor spatial resolution, a correlation in space is unsuitable, however, correlation in time can be done. We define the correlation between two temperature signals T_1, T_2 as

$$C_{12}(\tau) = \sum_{n=0}^{N} \tilde{T}_{1,n} \tilde{T}_{2,n-\tau+N}, \tag{3.10}$$

where $\tilde{T} = (T - \langle T \rangle)/\sigma(T)$ with $\sigma(T)$ the standard deviation of the temperature measurement. Simply put C_{12} for every time lag τ is the sum of the element-wise product

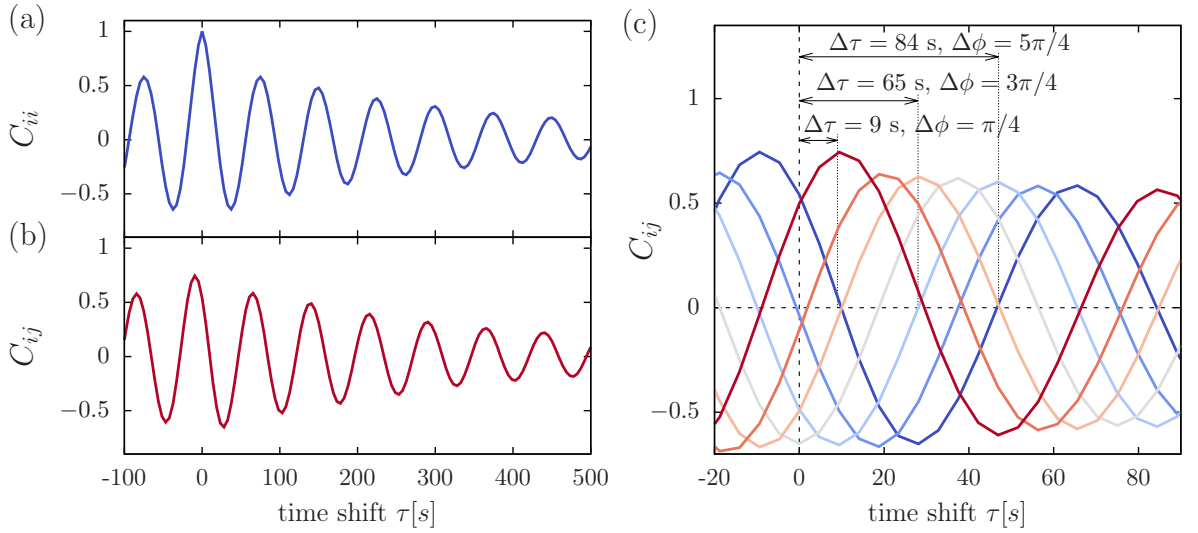

Figure 3.29: (a) Auto-correlation of the temperature signal of one thermistor located at $z/H = 0.5$, azimuthal angle $\phi = 0$, radius $r/R = 1.0$. The periods show the traveling wave of the BZF around the circumference. (b) Cross-correlation of the temperature in (a) and the signal at $\phi = \pi/4$. It is clearly shifted compared to the auto-correlation, exhibits the same structure though. (c) Cross-correlations between signal of (a) and all consecutive thermistors at the same height and r/R. From the time shift between the individual maxima and the known positions, the rotation velocity of the BZF can be estimated.

of a signal T_1 with a signal T_2 shifted by τ. If two signals are perfectly uncorrelated, $C_{12} = 0$ for all $\tau \neq 0$, whereas a constant signal would yield $C_{12} = 1$. At least for the thermistors embedded into the sidewall, we already have a strong expectation for the correlation signal at large rotation rates. The flow field exhibits a wave-like pattern with one hot and one cold region, which in turn should yield a high negative C for time lags within opposing, adjacent temperature regions and a high positive C otherwise. The BZF appears very stable in time, hence we expect a C_{ij} (and C_{ii}) which alternates in sign for long times. Indeed, this is what we see in fig. 3.29(a and b), where the correlation between thermistors embedded into the sidewall at $z = H/2$ is shown. The cross-correlations between different thermistors at $r = R$ in fig. 3.29c suggest with increasing azimuthal distance a larger time shift to the respective first maxima. This is what we expected from a uniform signal like the BZF, travelling around the circumference.

Using correlations therefore allows a determination of the existence of the BZF without fitting a function of the form $\delta_j \sin(\phi_i - \phi_j)$. This is of great advantage especially outside of our three rows of eight thermistors, since just one or two spatial points do not suffice for a sinusoidal fit. To prove that with this method we in fact capture

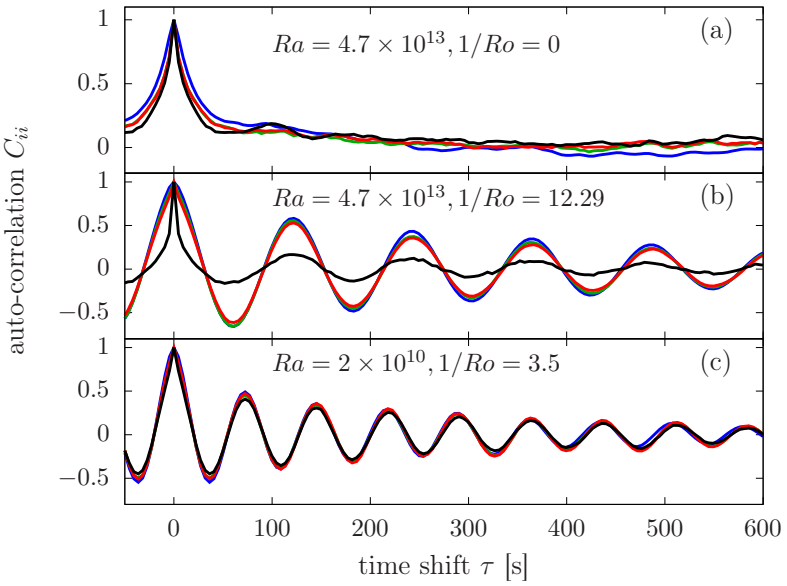

Figure 3.30: Examples of the auto-correlation C_{ii} for (a) $Ra = 4.7 \times 10^{13}, 1/Ro = 0$, (b) $Ra = 4.7 \times 10^{13}$ and $1/Ro = 12.29$, (c) $Ra = 2 \times 10^{10}$ and $1/Ro = 3.5$. The colour of the individual lines represents the radial positions $r/R = 0.98$ (blue), 0.96 (green), 0.93 (red) and 0.73 (black).

rotation-induced flow patterns is qualitatively seen in fig. 3.30a, where for no rotation, i.e. $1/Ro = 0$, the auto-correlation some time units away from its origin quickly decays and mostly consists of noise, while for high rotation rates (fig. 3.30(b and c)) we see the previously observed periodic pattern.

Correlation of single-point temperature measurements has been widely used in RBC. Qiu and Tong [2002] found a transition from chaotic temperature fluctuations to a highly correlated oscillating state for $Ra \geq 5 \times 10^7$. These oscillations were identified as the result of plume impacts at the BLs at the top and bottom plates, which excited a new detachement of a plume with opposing sign towards the second thermistor used for the cross-correlation. A local frequency $f_0 = U/(2H)$ was observed, which supported this explanation. Qiu and Tong [2002] performed non-rotating RBC experiments and the LSC was fixed in place by a slight tilt of the cell. As the LSC changes position even in absence of rotation for a non-tilted cell (Cioni et al. [1997], Weiss and Ahlers [2011a]), using a similar approach on our data should not provide a similar observation and in fact we do not see any periodic behaviour, e.g. see fig. 3.30a. King and Aurnou [2012] performed cross-correlation between thermistors at equal radial and azimuthal positions, but positioned both within the top and the bottom plates. For sufficient rotation a strong anti-correlation was found around the zero time shift for all correlation pairs. It

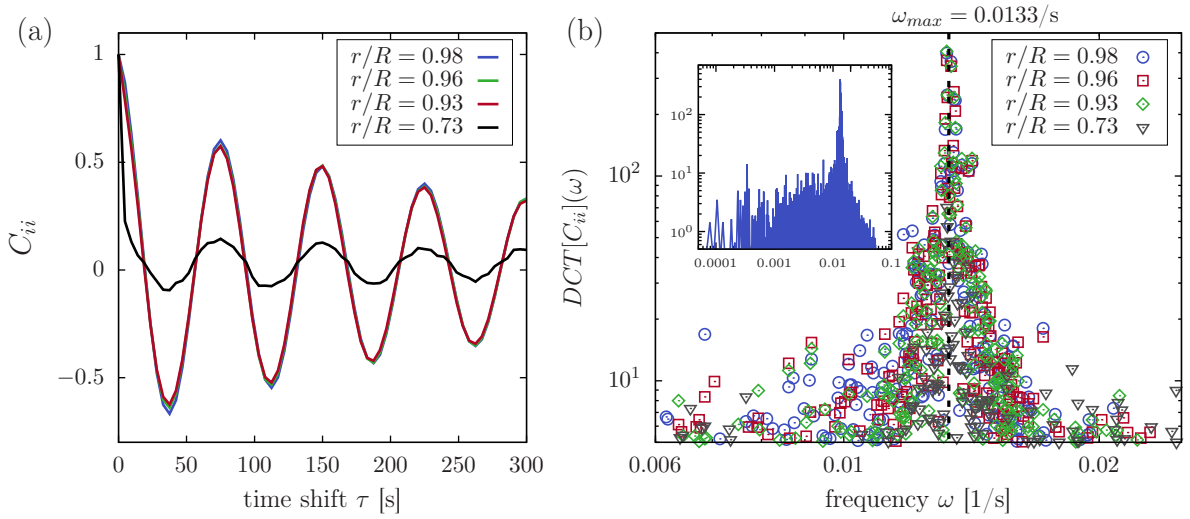

Figure 3.31: (a) Auto-correlations C_{ii} of the temperature measurements at $z/H = 0.5$ and varying radial position r/R. The signal close to the wall up to $r/R = 0.93$ show an almost identical pattern of the BZF, while at $r/R = 0.73$ the temperature imprint is still clearly visible, but C_{ii} is significantly reduced. (b) Discrete cosine transform (eq. (3.12)) of C_{ii} in (a) in log-log representation. The maximum is highlighted with a vertical dashed line at $\omega_{max} = 0.0133$/s. Inset shows a wider range of frequencies for $r/R = 0.98$. Settings are $Ra = 7.5 \times 10^{14}, 1/Ro = 4.9$ for both (a) and (b).

was interpreted as convective Taylor columns (as in fig. 2.7b) within the geostrophic regime. Since we do not reach the geostrophic regime (see sec. 3.2.2), we unfortunately can not observe this in our data.

A way to quantitatively determine the period of the BZF is by applying a Fourier-transform on the correlation functions:

$$\mathcal{F}[C_{ij}](\omega) = \int_{-\infty}^{\infty} C_{ij}(\tau) \exp(-i\omega\tau) d\tau. \tag{3.11}$$

For a symmetric and real signal one can use a discrete cosine transform (DCT) instead, which only returns real values, as well. Since auto-correlations C_{ii} are by definition symmetric and real, the DCT is chosen

$$DCT[C_{ii}](\omega) = 2 \sum_{n=0}^{N-1} C_{ii,n} \cos\left(\frac{\pi\omega(2n+1)}{2N}\right). \tag{3.12}$$

Doing this for $Ra = 7.5 \times 10^{14}$, $1/Ro = 4.9$ (fig. 3.31), we obtain a distinct maximum frequency $\omega_{max} = 0.0133$/s, and $\omega_{max}/\Omega = 0.057$. This value is nearly identical to $\omega_m/\Omega = 0.0564$, that we observed via the cosine curve fitting method, which was applied

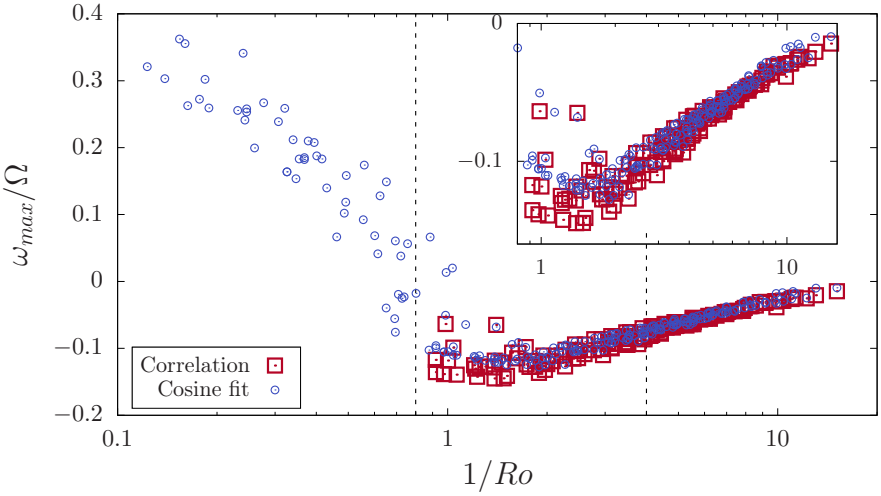

Figure 3.32: Comparison of the drift rates obtained by a Cosine fit to the eight thermistors in the sidewall (blue circles) as in fig. 3.28 and the drift rate calculated from the maximum in the frequency distribution like in fig. 3.39 (red squares) at $r/R = 0.98$. Inset shows a zoom in at the overlapping region $1/Ro \geq 0.8$.

to the temperature measurements inside the sidewall in fig. 3.28. We can thus state that auto-correlation of the temperature signature within the BZF yields the same frequency results with much simpler analysis and using only one measurement point. Of course, this is an expected result given the clearly periodic signal of the BZF. It is nevertheless reassuring to measure similar values via different techniques and measurement devices.

In general, the method of retrieving information from the auto-correlation about some large scale structure is in this form only possible due to the high periodicity of the BZF. In that case, as seen in fig. 3.32, the drift rate of the wave is almost exactly matching the one by fitting a cosine function to the eight thermistors at each time step, for all $1/Ro > 1/Ro_1^*$ and all Ra. However, it also highlights its weakness: due to the lack of spatial information, when the BZF is not present at low $1/Ro < 1/Ro_1^*$, no sensible frequency can be estimated. Thus, the azimuthal movement of the LSC remains hidden to the auto-correlation.

3.8.1 Drift rate ω at varying heights

Before (fig. 3.28b) we found that for $1/Ro > 1/Ro_1^*$, the drift rate of the BZF within the sidewall was the same for all three heights $z = H/4$, $H/2$, and $3H/4$. With the use of auto-correlations we can test ω at all measurement points in our cell and see whether

the observation is similar when we look inside the fluid and even closer to the top and bottom plates. From now on, we focus on the frequency spectrum given by the DCT of the auto-correlations. For a better visual appearance and to read off the maximum with more ease, the resulting DCT is smoothed by a convolution with a Hanning window w

$$w(n) = \frac{1}{2}\left(1 - \cos\left(\frac{2\pi n}{N-1}\right)\right) \qquad 0 \leq n \leq N-1, \tag{3.13}$$

$$\tilde{C_{ii}} = (DCT[C_{ii}] * w)(\omega) = \int_{-\infty}^{\infty} DCT[C_{ii}](\tau) w(\omega - \tau) d\tau, \tag{3.14}$$

with N the length of the window. While the smoothing alters the absolute height, this is not a problem as we are here only interested in the relative strenghts and the frequency of the maxima, which remain unchanged.

In fig. 3.33(a-c) we show this smoothed frequency spectra for three heights z/H for $Ra = 4.7 \times 10^{13}$. For the lowest rotation rate $1/Ro = 0.3$, fig. 3.33a, we observe no distinct maximum as expected in absence of the BZF for $1/Ro < 1/Ro_1^*$. Increasing rotation to $1/Ro = 3.1$ ($1/Ro = 6.2$), as shown in fig. 3.33(a and b) yields maxima at $\omega_{max} \approx 0.008\,\mathrm{Hz}$ ($\approx 0.009\,\mathrm{Hz}$). Somewhat surprisingly, we find the position of the maxima to overlap exactly at each respective height $z/H = 0.018$, 0.054, and 0.5. This means the drift rate of the temperature field of the BZF for at least these cases is independent of vertical direction. The prominence of the maxima is of similar magnitude as well, suggesting the temperature signal of the BZF is as "distinct" close to the plates as it is at mid-height. This is unexpected, as DNS have shown the BZF to be dominantly around half-height in the velocity field under strong rotations, Zhang et al. [2020, 2021].

Comparing all measured drift rates ω_{max}/Ω for $1/Ro > 1/Ro_1^*$ at all Ra between $z/H = 0.018$ and $H/2$ results in fig. 3.33d. We find the example cases above described the general trend very well, the resulting frequency is the same regardless of z/H. The same approach was used for the top half, where we have thermistors located at $z/H = 0.982$ and $r/R = 0.98$, and the temperature auto-correlation is identical to ones found at other z.

In fact, the BZF thermally couples with the bottom plate such that we can observe the temperature oscillations even in the temperature measurements inside the top half of the bottom plate sandwich (see fig. 3.34). The peaks of the auto-correlation

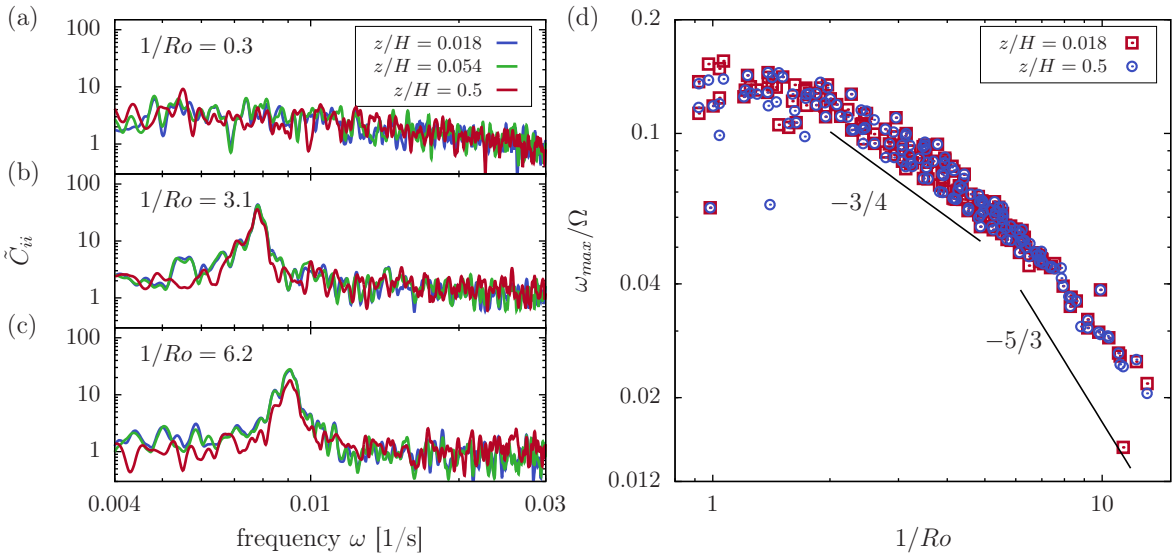

Figure 3.33: (a)-(c): frequency spectra of the auto-correlations of the signal at $r/R = 0.73$ for $Ra = 4.7 \times 10^{13}$ and increasing $1/Ro$. Shown are $z/H = 0.018$ (blue), $z/H = 0.054$ (green) and $z/H = 0.5$ (red). (b) comparison of the drift rate at $z/H = 0.018$ (red triangles) and $z/H = 0.5$ (blue circles) at $r/R = 0.98$. Lines mark the scalings of $(1/Ro)^{-3/4}$ and $(1/Ro)^{-5/3}$ for comparison.

within the bottom plate align with the ones found at $z/H = 0.493$. This is shown for $Ra = 4.7 \times 10^{13}$ and $Ra = 7.5 \times 10^{14}$ and different rotation rates. That the fluctuating temperature is not a result of an oscillating input at the bottom is tested by checking the individual temperature at the bottom side of the bottom sandwich again. There, no oscillations larger than $\delta T \approx 0.004$K were detected. Within the top plate, on the other hand, no sign of the BZF is detected in the auto-correlations, initially a surprise since both sides should be mostly symmetric. However, the boundary conditions at the respective top plate and the bottom plate are different. At the latter we have a low conductivity polycarbonate plate, whereas at the top side the temperature is almost constant due to the fast flowing cooling water. An incoming wave of higher temperature from the working fluid is quickly dissipated in the top plate and the setup acts like a short-pass filter. At the bottom side it takes a long time to restore the temperature in the adjacent polycarbonate plate, which dampens the wave only in the bottom part of the sandwich.

Even though the frequency of the temperature field is the same for all z/H, so far we have not investigated for possible phase differences. We extract these from the relative positions of the wavefronts of the temperature bands in the sidewall thermistors cross-correlations. For this, the thermistors at $r/R = 0.98$, $z/H = 0.018$ are cross-correlated

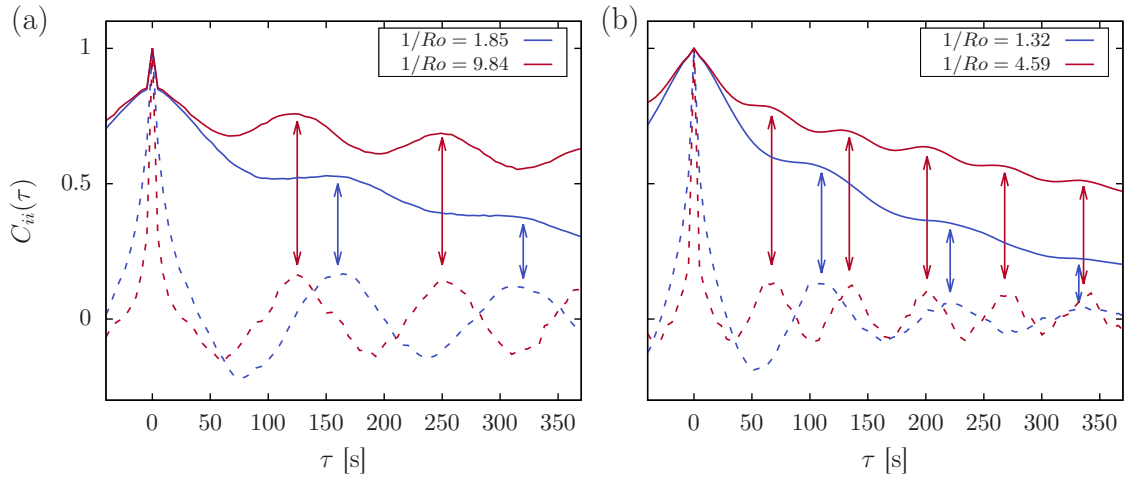

Figure 3.34: Auto-correlation for a thermistor at half-height $z/H = 0.493$, $r/R = 0.73$ (dashed lines) compared to a thermistor embedded in the top of the bottom plate sandwich (continuous lines). (a) $Ra = 4.7 \times 10^{13}$, (b) $Ra = 7.5 \times 10^{14}$. Shown are two different rotation rates at the different colours as indicated in the legend.

with every other z/H at the same azimuthal and radial position. From the first maximum in the cross-correlation (fig. 3.35), we deduce the time it takes for the wavefront to appear at the heights $z/H > 0.018$ compared to the bottommost thermistor. Since our measurements are somewhat sparse in time, a parabula is fitted around its maximum for interpolation. Then the time lag τ_{max}, the time shift of the maximum closest to 0, is plotted as function of z/H (fig. 3.35c). We find that the BZF is not a wave perfectly oriented with the gravitational axis, in which case $\tau_{max} = 0$ for all z/H. Instead, the temperature field is twisted towards the center, where it precedes the field closer to the plates at both sides. Measurements taken at different azimuthal positions ($\phi = 0.479\pi$ and $\phi = 1.479\pi$) agree rather well. For a perfect setup one would expect a symmetrical distribution around $z/H = 1/2$, which is clearly not present. Instead, τ_{max} increases towards the top plate substantially, meaning the temperature field at the top lags behind the one at the bottom. A measurement error is possible, but unlikely given the two agreeing independent measurements at opposite sides, making a slight imperfection in the setup more probable. This twisted temperature field is identical to the findings in Weiss and Ahlers [2011b], replotted in fig. 3.35d, where the breakdown of the large-scale circulation beyond $1/Ro_1^*$ was not considered.

A similar observation is made when cross-correlating the thermistors embedded into the sidewall (not shown here), as well as further within the fluid at $r = 0.96R$, $0.93R$,

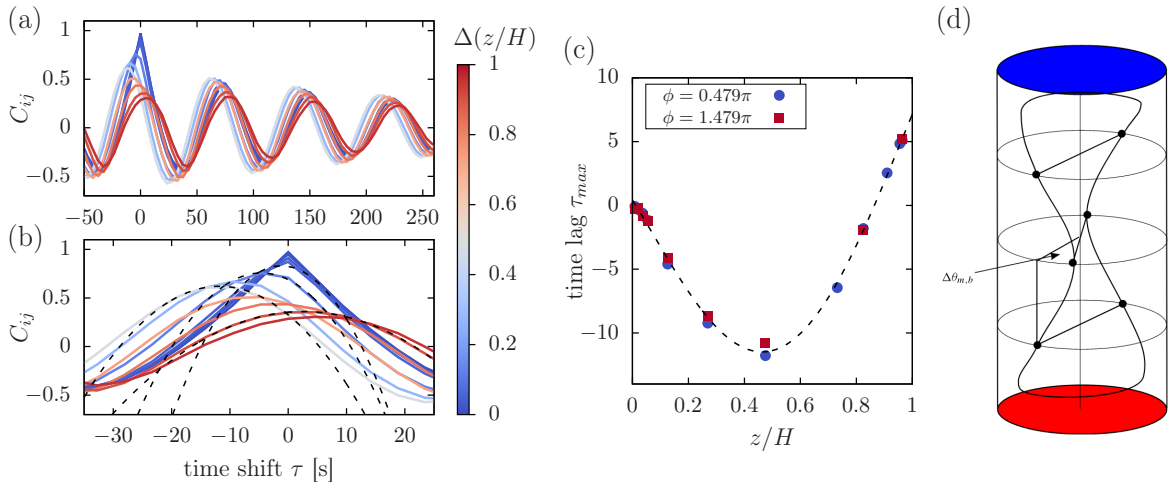

Figure 3.35: (a) Cross-correlation C_{ij} between thermistors at $r/R = 0.98$, $\phi = 0.479\pi$, $z/H = 0.018$ and thermistors located at vertically increased location as in the colour code. The strong correlation in vertical direction is visible, i.e. the BZF is stable across the full height of the cell. (b) Same data, plotted only in the range $-35\text{s} \leq \tau \leq 25\text{s}$. Parabulas are fitted to six points around the maximum for interpolation. (c) time shift of the maximum in (b) evaluated as the maximum of the fitted parabula as function of z/H of the thermistors (blue bullets). Red squares show the same analysis for the diametral opposite thermistor column $\phi = 1.479\pi$, black dashed line is a guide to the eye. (d) Bending of the LSC according to Weiss and Ahlers [2011b] due to rotation, which is qualitatively similar to the findings presented here.

and $0.73R$. Contrary, for the velocity field we know from investigations of the Stewartson layer (see, e.g. Kunnen et al. [2011]) that the rotation accelerates the fluid at mid-height in azimuthal direction. A similar acceleration was found in DNS for the BZF (Zhang et al. [2020]). Notably this does not lead to a temperature structure which lags behind at half-height. It suggests the temperature wave at the sidewall and the azimuthal velocity (which for the case of the BZF is only observed in the time-averaged fields) are rather decoupled.

This discrepancy between the angles is also observed when comparing the angles from the sinusoidal fits to the rows of thermistors inside the sidewall (fig. 3.36), where the difference in orientation between the three heights (top, mid, bot) is plotted together with their *pdf* $p(\delta\phi_{lk}) = p(\phi_l - \phi_k)$. The time plots fig. 3.36(a-c) suggest that the phase difference between different heights is rather constant in time. As could be expected from the analysis above, the angle differences top-mid $\delta\phi_{tm}$ (fig. 3.36a) and mid-bot $\delta\phi_{mb}$ (b) have a non-zero average value, also shown in the shifted *pdf* in fig. 3.36d. If the maxima of the cross-correlations are shifted with respect to each other, we can estimate the spatial difference between the measurements at different heights z/H from

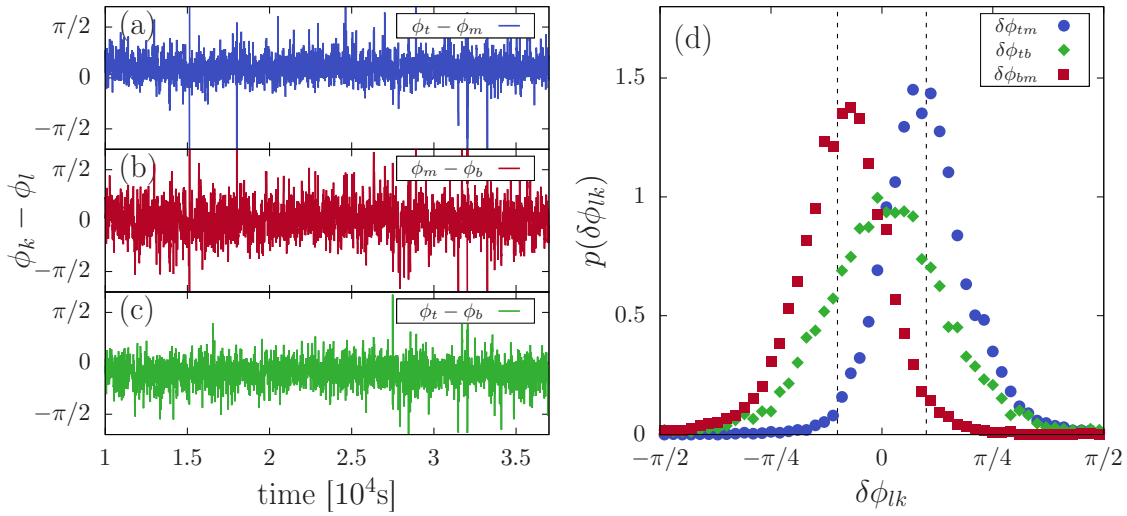

Figure 3.36: (a-c) Exemplary time series of the differences in fitted angle ϕ to the side wall thermistors at $z/H = 0.25$ (bot, b), 0.5 (mid, m), and 0.75 (top, t). (d) *pdf* of the signals $\delta\phi_{lk} = \phi_l - \phi_k$ in (a-c). Run E2j, $1/Ro = 4.9$.

fig. 3.35c. Between $z = 0.018H$ and $z = H/2$, time lag is $\Delta\tau_{max} \approx 12\,\mathrm{s}$, combined with the complete period in the cross-correlation of $\approx 70\,\mathrm{s}$, the spatial distance of the wavefront is thus $\approx 2\pi \cdot 12/70 \approx \pi/3$. Of course, since $\Delta z = 0.25H$ between the three rows of sidewall thermistors, the difference would be smaller $\approx \pi/10$ for the case $Ra = 7.5 \times 10^{14}, 1/Ro = 4.9$ in fig. 3.35. We show this as lines in fig. 3.36d and see a good agreement between the two methods and r/R.

In fig. 3.37 the mean values μ (a) and standard deviations σ (b) of $p(\delta\phi_{lk})$ are shown. A notable feature of $\mu(\phi_{lk})$ is the double-maximum in $\mu(\delta\phi_{bm})$ and $\mu(\delta\phi_{tm})$ at $1/Ro_1^* = 0.8$ and $1/Ro_2^* = 4$, respectively. What does this mean? First, for no or slow rotation, where we expect the LSC to dominate, we find that the difference of the fitted angle is close to zero, i.e. fluid ascends and descends in straight vertical trajectories. With increasing rotation, the temperature field at half-height precedes the one closer to the top/bottom. Just when we observe the occurance of the BZF at $1/Ro_1^*$, the LSC is twisted the most. This possibly explains its disappearance: the torsional forces are too large and it breaks apart around the mid-height. For the fastest rotation rates, $\mu(\phi_{lk})$ decreases again and the temperature bands of the BZF are more and more aligned in azimuthal direction.

The maximum and slow decay afterwards agrees with data published in Weiss and

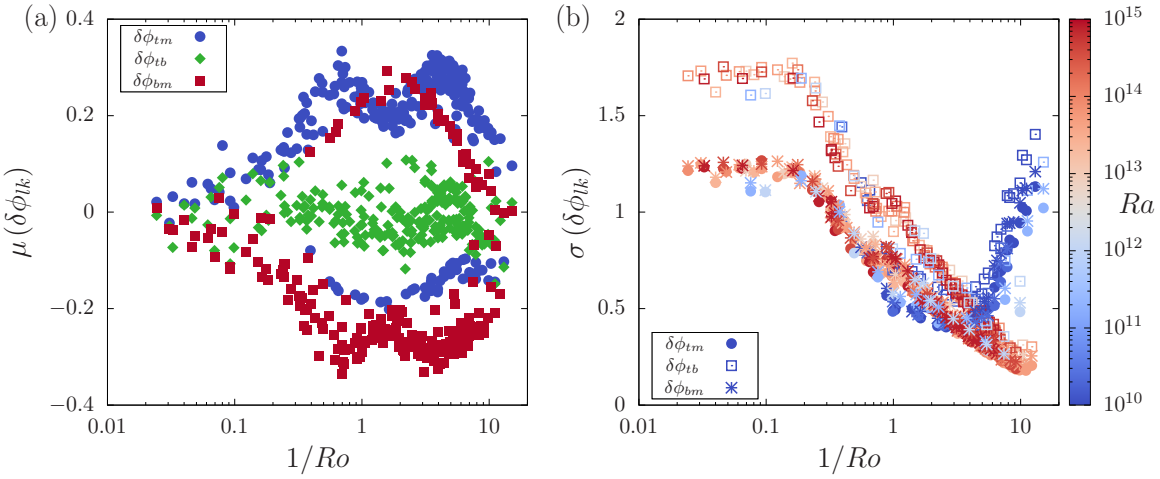

Figure 3.37: (a) Mean values μ and (b) standard deviations σ of the angle differences $\delta\phi_{lk}$ as function of $1/Ro$ of all available Ra. Different colours and shapes symbolize the three combinations of t, m, b in as displayed in the legend, while in (b) colour marks Ra.

Ahlers [2011b], where a maximum of the same quantity was observed at $1/Ro \approx 0.8$, which aligned with the maximum heat transport enhancement at $Pr > 4$. Since for larger $1/Ro$ this quantity describes the temperature structure of the BZF, it is likely the authors in Weiss and Ahlers [2011b] measured it, as well. Unfortunately, $\mu(\phi_{lk})$ was not shown at larger rotation rates to confirm also the existence of a secondary peak at our $1/Ro_2^*$.

The almost constant standard deviation $\sigma(\delta\phi_{lk})$ (fig. 3.37b) for low rotation rates $1/Ro < 0.2$ shows that the distribution remains fairly similar there. $\sigma(\delta\phi_{tb})$ is considerably larger, i.e. the distribution $p(\delta\phi_{tb})$ is wider than the deviations of the bottom and top half. Even though the LSC in average is aligned in vertical direction, shown by $\mu(\delta\phi_{tb}) \approx 0$, its alignment fluctuates quite strongly. With increased $1/Ro$, the standard deviation decreases consistently (for large Ra) or up to $1/Ro \approx 4$ (for $Ra < 10^{12}$). This suggests once more the BZF is a stable structure, which vertical alignment is rather fixed. For lower Ra, the BZF weakens for the largest rotation rates, as observed before.

3.8.2 Estimating the thickness of the BZF

With the correlation signals and their respective magnitudes, we can try to give an estimate of the BZF thickness δ_0. In fig. 3.31 we have seen that the periodicity and behaviour of the temperature signal is similar for all $r/R \geq 0.93$ and notably weaker

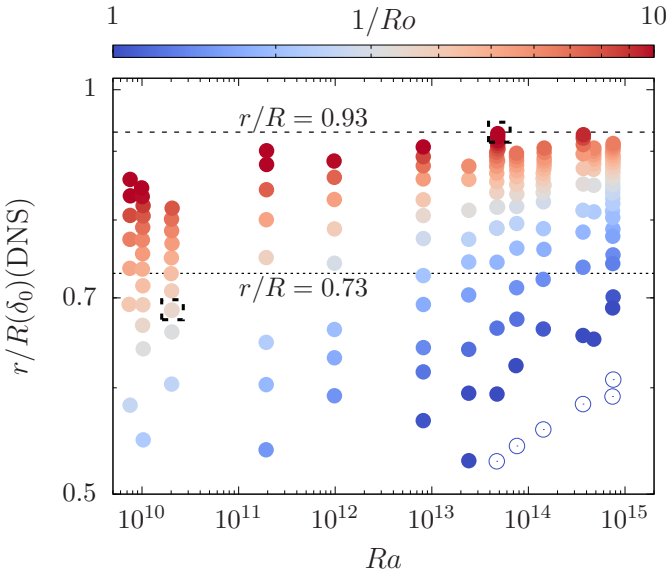

Figure 3.38: Radial position r/R of the BZF width δ_0 according to Zhang et al. [2021] calculated from control parameters as function of Ra (x-axis) and $1/Ro$ (colour code). Dashed lines are the positions of the thermistor columns $r/R = 0.73$ and 0.93. Open symbols show data with $1/Ro < 0.8$, closed $1/Ro > 0.8$. Highlighted points are the values for which C_{ii} was shown in fig. 3.30(b and c).

only for the innermost thermistor $r/R = 0.73$. This suggests that the latter does not measure the full signal of the BZF anymore. Based on DNS it was suggested that the width of the BZF δ_0 depends on all parameters Ra, Ek, Pr for $Pr < 1$ like

$$\delta_0/H \approx 0.85\Gamma^0 Pr^{-1/4} Ra^{1/4} Ek^{2/3}. \tag{3.15}$$

Unfortunately, solving this for our parameters suggests that the BZF does not vanish at $r/R > 0.93$ anywhere, see fig. 3.38. However, at $Ra = 4.7 \times 10^{13}$ and the highest rotation rate, the calculated δ_0 is close to the radial location of our thermistor. Fig. 3.30b shows the auto-correlation for this case at different radial locations. With a bit of good will, one might see a slight decrease of C_{ii} with r/R, arguably a sign of the BZF only extending up to $r/R = 0.93$. At the lowest Ra it is possible to notice the measurements at $r/R = 0.73$ coincide with those further outwards (fig. 3.30c), where all C_{ii} overlap rather nicely.

We perform the analysis at half-height by investigating the maxima of $\tilde{C}_{ii}$. Examples are shown in fig. 3.39 for $Ra = 4.7 \times 10^{13}$ (a-c) and $Ra = 2 \times 10^{10}$ (d-f) with increased rotation from top to bottom. On the one hand, for the higher Ra, the magnitude of $\max(\tilde{C}_{ii})$ at $r/R = 0.73$ is clearly smaller than the ones close to the sidewall. On the

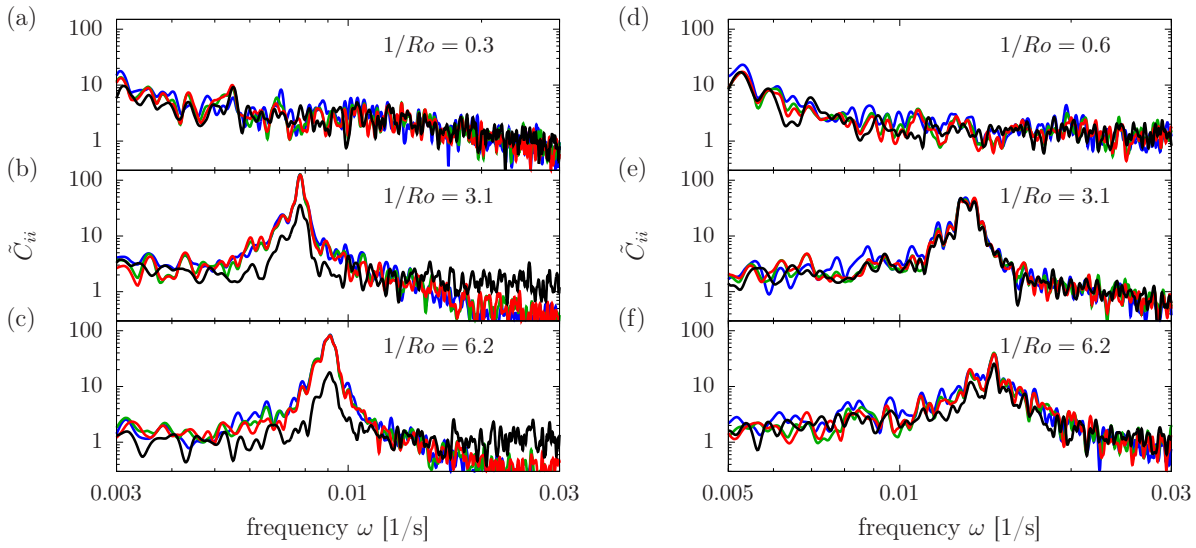

Figure 3.39: Smoothed DCT of the auto-correlations of thermistors at $z/H = 0.5$, $Ra = 4.7 \times 10^{13}$ (a)-(c) and $Ra = 2 \times 10^{10}$ (d)-(f) with varying $1/Ro$ as noted in the plots. $r/R = 0.98$ (blue), 0.96 (green), 0.93 (red), and 0.73 (black). One sees that the maximum mode for the high Ra at large rotation rates is notably lower than for the thermistors positioned further outwards, while at the lower Ra the signals overlap.

other hand, at $Ra = 2 \times 10^{10}$ and comparable $1/Ro$, the maxima are of similar height. It suggests the signal of the BZF is measured down to a radial location $r/R = 0.73$ for the lower Ra, while the zone is restricted closer to the sidewall for larger Ra.

Figure 3.40a shows the ratio of the maxima of $\tilde{C}_{ii}$ measured at radial locations $r/R = 0.73$ and 0.98 as function of $1/Ro$. With this, we want to test the prediction for the BZF width δ_0 suggested by Zhang et al. [2021]. In fig. 3.40b, we show the ratio as function of the predicted δ_0 based on eq. (3.15). One would expect the signal at $r/R = 0.73$, given $\delta_0 < 0.27R$, to be much weaker than at the wall. For $\delta_0 \geq 0.27R$, i.e. the BZF reaches far into the bulk, the magnitudes at both radial locations should exhibit a comparable magnitude. Since the influence of the bulk is always larger at the inner measurement point than at the outer edge, the ratio is very likely to almost always remain < 1, which is what we observe in fig. 3.40a. Small ratios in this plot suggest the signal of the BZF at $r = 0.73R$ is weak and therefore $0.73 < (R - \delta_0)/R < 0.98$.

The distribution of the ratio $\max(\tilde{C}_{0.73})/\max(\tilde{C}_{0.98})$ as function of the predicted δ_0 in fig. 3.40b has a Pearson correlation coefficient of 0.83. A coefficient of 0 would be no correlation and 1 is a perfect linear correlation. The high value suggests this ratio to be a good indicator of the width of the BZF in the temperature field. The exact ratio of

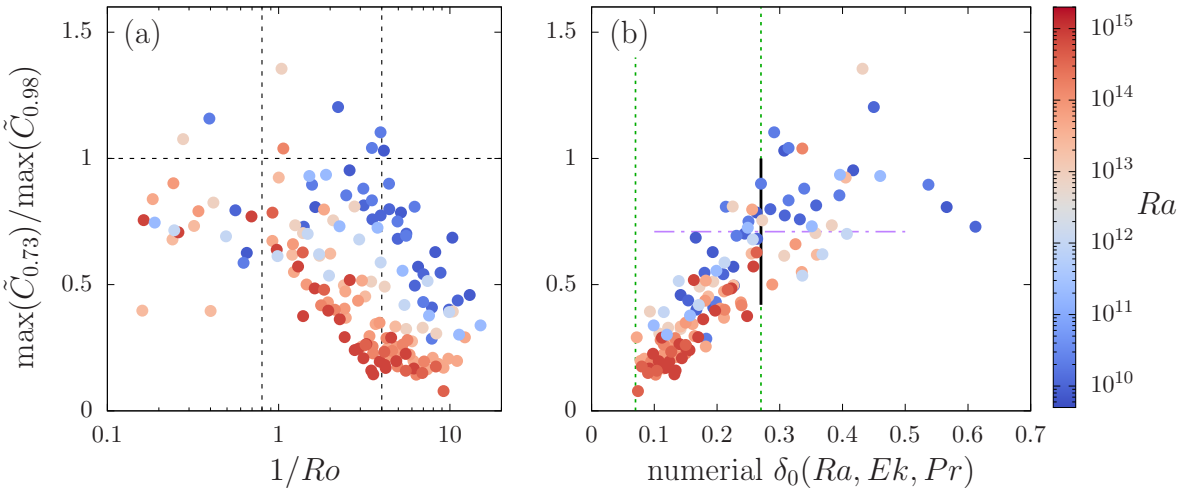

Figure 3.40: (a) ratio of the maxima of the $DCT[C_{ii}]$ at $r/R = 0.73$ and 0.98 as function of $1/Ro$. Colour code shows Ra, suggesting that the BZF is apparent at $r/R = 0.73$ for low $1/Ro$ (though larger than $1/Ro_1^*$) and low Ra. (b) same parameter as function of the expected BZF width δ_0 as in eq. (3.15). The ratio shows a Pearson correlation coefficient of 0.83 with a two-sided p-value of 1.4×10^{-37} with δ_0. Green vertical dashed lines mark the positions of two thermistor rows at $r/R = 0.73$ and 0.93, horizontal purple line is the transitional value of 0.71, above which, assuming the numerical results for δ_0, the BZF is within $r/R = 0.73$.

where to predict $\delta_0 \geq 0.27R$ is somewhat arbitrary from our data, it should be somewhere between 1/2 and below 1. Taking the average of the distribution at $\delta_0 = 0.27$, one obtains $\max(\tilde{C}_{0.73})/\max(\tilde{C}_{0.98}) = 0.71$. At larger ratios, the BZF is expected to be thicker than $0.27R$, at smaller ratios $\delta_0 < 0.27R$. Assuming the thickness scaling relation (3.15), δ_0 decreases with Ra at a constant $1/Ro$. We find the smallest values of $\max(\tilde{C}_{0.73})/\max(\tilde{C}_{0.98})$ for the largest Ra, i.e. it supports the decrease of δ_0 with Ra. To obtain a quantitative scaling relation ourselves, we would need a description how the maximum at $r = 0.73R$ depends on the radial distance to the BZF. As this is mere speculation, we refrain from such an analysis.

3.9 Fourier analysis at the sidewall

A Fourier transform $\mathcal{F}\{T(\phi)\}$ of a temperature signal $T(\phi)$ as function of the azimuthal angle ϕ (compare eq. (3.11)) can yield valuable information about the strength of individual modes of the flow. Since we only measure discrete values instead of continuous ones, we must use the (real) discrete Fourier series, which consists of a sum of harmonics. The Fourier representation of our temperature signal $T(\phi)$ is

$$T(\phi) = \sum_{i=0}^{\infty} \hat{a}_i \cos(i\phi) + \hat{b}_i \sin(i\phi). \tag{3.16}$$

Each harmonic has Fourier coefficients $\hat{a}_i$, $\hat{b}_i$, which we calculate from our temperature data by

$$\hat{a}_i = \sum_{k=1}^{N} T(\phi_k)\cos(i\phi_k) \quad \text{and} \quad \hat{b}_i = \sum_{k=1}^{N} T(\phi_k)\sin(i\phi_k), \tag{3.17}$$

where $T(\phi_k)$ is the temperature at angle ϕ_k. Since we have eight thermistors embedded within the sidewall, we can obtain the first four Fourier coefficients of the temperature signal. With these, the "energy" contained in the modes is calculated by $E_i = \hat{c}_i^2 = \hat{a}_i^2 + \hat{b}_i^2$. This is compared to the total energy $\langle E_{tot}\rangle = \sum_{i=1}^{4} E_i$ of the first four modes. The first Fourier mode refers to a sinusoidal wave spanning the entire circumference, i.e. one hot region and one cold region (eq. 3.9).

The ratio $\langle E_i\rangle/\langle E_{tot}\rangle$ is plotted as function of $1/Ro$ in fig. 3.41. Different Ra are shown: in fig. 3.41a the runs with working gas nitrogen at $7.5 \times 10^9 \leq Ra \leq 2.0 \times 10^{10}$, in (b) $Ra = 4.7 \times 10^{13}$, and in (c) $Ra = 7.5 \times 10^{14}$. The first mode $\langle E_1\rangle$ contains the most energy throughout all rotation rates and for all Ra. For low $1/Ro$, in the rotation-unaffected regime, this is caused by the LSC, since for a $\Gamma = 1/2$ cell the LSC shows itself in a $k_{LSC} = 1$ wave. Beyond $1/Ro > 1/Ro_1^*$, for high Ra, $\langle E_1\rangle$ decreases shortly due to the breakdown of the LSC and the transition into the BZF with the same wave number, which for larger rotation rates contains the dominant portion of energy.

For the fastest rotation rates at low Ra (fig. 3.41a), $\langle E_1\rangle$ decreases substantially with $1/Ro$. This is in accordance with the weakening of the other BZF signals such as the disappearance of the bimodal Gaussian temperature *pdf*, though it is difficult to interpret. We look again at the scaling relation $\delta_0 \propto Ra^{-1/12}1/Ro^{-2/3}$, suggested by Zhang et al. [2021]. We find conflictive results: for large Ra, $\langle E_1\rangle$ increases with increased

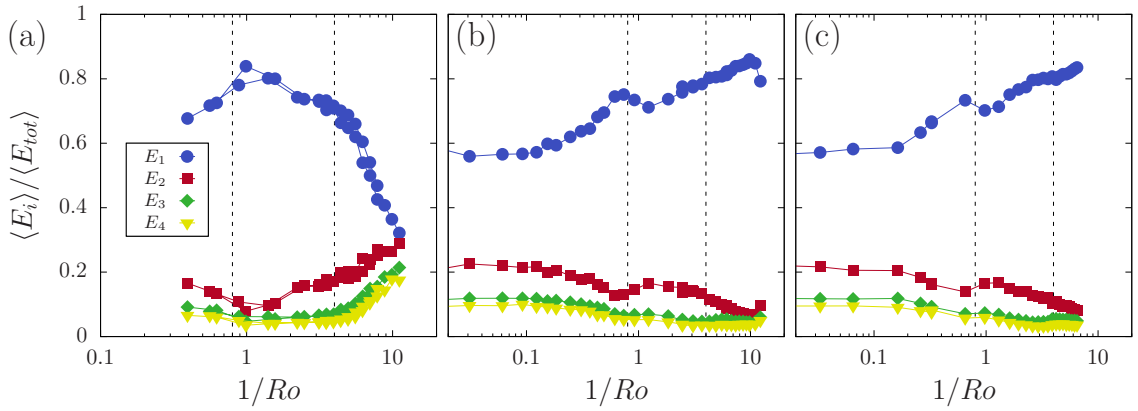

Figure 3.41: Ratio of the energy contained in the i-th Fourier mode $\langle E_i \rangle$ and the total energy in the first four Fourier modes $\langle E_{tot} \rangle$ as function of $1/Ro$. Plotted are first mode (dark blue bullets), second (purple triangles), third (dark red diamonds) and fourth (orange pentagons) for (a) $7.5 \times 10^9 \leq Ra \leq 2.0 \times 10^{10}$ (runs E1a-E1c), (b) run E2e $Ra = 4.7 \times 10^{13}$, and (c) run E2j $Ra = 7.5 \times 10^{14}$.

rotation, and there δ_0 decreases. This is rather unintuitive, as one for a thinner BZF would expect a decreased pumping efficiency and hence a decrease in $\langle E_1 \rangle$. For small Ra, however, where the BZF should be thicker at equal $1/Ro$, $\langle E_1 \rangle$ is much smaller, and decreases with $1/Ro$. This suggests a finite region of $1/Ro$, where the BZF occurs, a result not compatible with larger Ra or DNS results.

Even with our measurements at the lowest Ra, we are roughly one order of magnitude in Ra above Ra_c for the onset of bulk convection for the highest $1/Ro \approx 10$. For $Ra > 10^{13}$, this expands to at least two orders of magnitude. Still, this possibly suggests the system is simply too close to onset of convection to form the BZF and the transition from wall modes to the BZF, as suggested in Favier and Knobloch [2020], is not complete. Consider the remnants of the wall modes have the same wave number as said modes. Then the wave number in the theoretical limit $Ek \to 0$ is $\approx 3\Gamma$ (Zhang and Liao [2009]), but can be considerably higher for finite Ek like in Favier and Knobloch [2020]. As the setup does not allow measurements of any modes with $k > 4$, we can not identify such signals. Note, however, that DNS found no disappearance of the BZF, albeit measuring much closer to convective onset.

As discussed in sec. 3.7, the earlier study (Weiss and Ahlers [2011b]) likely measured the temperature signal of the BZF. We show in fig. 3.42 the energy of the first four Fourier modes from two studies: $\Gamma = 0.5$ from Weiss and Ahlers [2011b] and $\Gamma = 1$ from Zhong and Ahlers [2010], both with $Pr = 4.38$. A decrease in $\langle E_1 \rangle$ was observed for

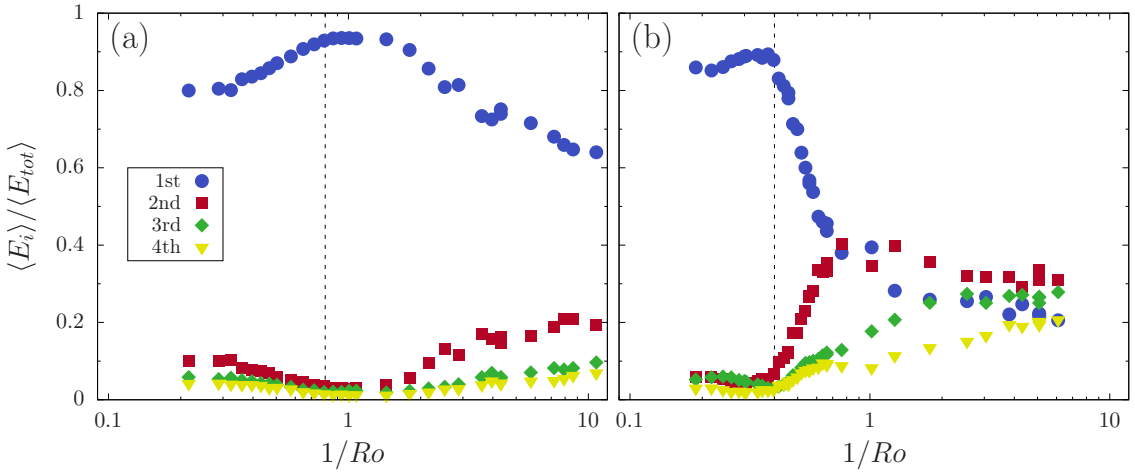

Figure 3.42: Relative energy in the first four Fourier modes of the azimuthal temperature signal at midheight of the cell from other studies. (a) $\Gamma = 0.5$ ($Ra = 1.8 \times 10^{10}$, Pr=4.38), adapted from fig. 4 of Weiss and Ahlers [2011b]. (b) $\Gamma = 1$ ($Ra = 2.25 \times 10^{9}$, Pr=4.38), adapted from fig. 19 of Zhong and Ahlers [2010]. The vertical dashed lines mark the onset of heat transport enhancement at $1/Ro_c = 0.8$ (a) and $1/Ro_c = 0.4$ (b).

rotation rates $1/Ro > 1/Ro_c$, i.e. the onset of heat transport enhancement. For the $\Gamma = 1$ measurement, the energy contained in the second mode increases simultaniously, while in the $\Gamma = 0.5$ case the decrease of $\langle E_1 \rangle / \langle E_{tot} \rangle$ is less pronounced. DNS performed at multiple Γ, Pr in Zhang et al. [2021] suggest that the BZF has a wave number of 2Γ, independent of Pr. Hence we can now explain the increase in the second mode in fig. 3.42b with the emergence of the BZF, since for $\Gamma = 1$ it is $k_{BZF} = 2$. For $\Gamma = 0.5$ the wave number of the BZF is $k_{BZF} = 1$, the same as the one of the LSC, very much like in our case. Thus the first mode remains dominant.

3.10 Standard deviation σ

As a simple measure for temperature fluctuations we use the standard deviation, which for a single measurement point we define as

$$\sigma(z,r) = \frac{\sqrt{\langle [T(t,z,r) - \langle T(t,z,r) \rangle_t]^2 \rangle_t}}{\Delta T}. \tag{3.18}$$

$\langle \dots \rangle_t$ denotes the average over time. σ is an intensively analyzed parameter in RBC, often to differentiate between areas of low σ, most notably in the boundary layers close to the horizontal plates, and the bulk flow. In the bulk for the non-rotating case, earlier investigations (Niemela et al. [2000], Daya and Ecke [2002]) suggested a relationship of

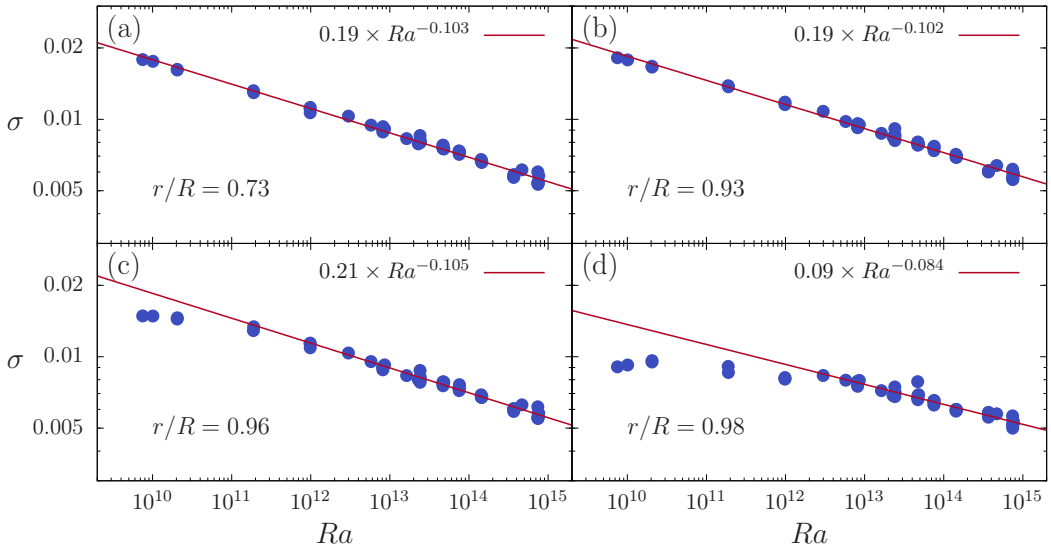

Figure 3.43: Standard deviation according to eq. (3.18) as function of Ra for non-rotating data at $T_m = 22.5°$ and different radial locations as indicated. Fitted function is a power-law to the data. All data are taken close to half-height $z/H = 0.493$.

$\sigma \propto Ra^{-\alpha_\sigma}$ with $\alpha_\sigma > 0$. The standard deviation thus decreases with increased thermal driving for sufficiently large Ra. This is commonly explained by the enhanced mixing at larger Ra. Niemela et al. [2000], for example, observed $\sigma/\Delta \sim Ra^{-0.145}$ in the center of the cell for a wide range of $10^7 \leqslant Ra \leqslant 10^{15}$ using cryogenic helium. Daya and Ecke [2002] measured a somewhat lower exponent of $\alpha \approx -0.1$ at $Pr \approx 5.5$. Other measurements, also at lower Pr, agree with these findings (e.g. -0.147 in Castaing et al. [1989]). Some theoretical predictions argue with $\alpha_\sigma = -1/9$ (Kraichnan [1962]) or, based on the assumption of a mixing zone between the boundary layer and the bulk flow, $\alpha_\sigma = -1/7$ (Castaing et al. [1989]). In our case for non-rotating data we observe $\sigma = (0.19 \pm 0.01) Ra^{-0.103 \pm 0.002}$ (fig. 3.43), consistent with previous findings though a little below the theoretically derived exponents. The scaling is similar at $r/R = 0.73$ and $r/R = 0.93$, but wall effects set in for larger r/R. Similar to the logarithmic temperature profile in fig. 3.13, σ for $Ra \leq 10^{12}$ does not follow the same scaling as for larger Ra. For $Ra > 10^{12}$ we find $\sigma \sim Ra^{-0.105}$ ($r/R = 0.96$) and $\sim Ra^{-0.084}$ ($r/R = 0.98$). This is likely the beforementioned boundary layer effect, where at the sidewall a viscous BL causes a decrease in temperature fluctuations. This BL decreases in thickness with increasing Ra.

For rotating RBC, data by other authors is sparse, for example Kunnen et al. [2010] numerically found the rms value $\Theta_{rms} \sim Ro^{-0.32}$ at $z/H = 0.5$ and 0.8 at the center

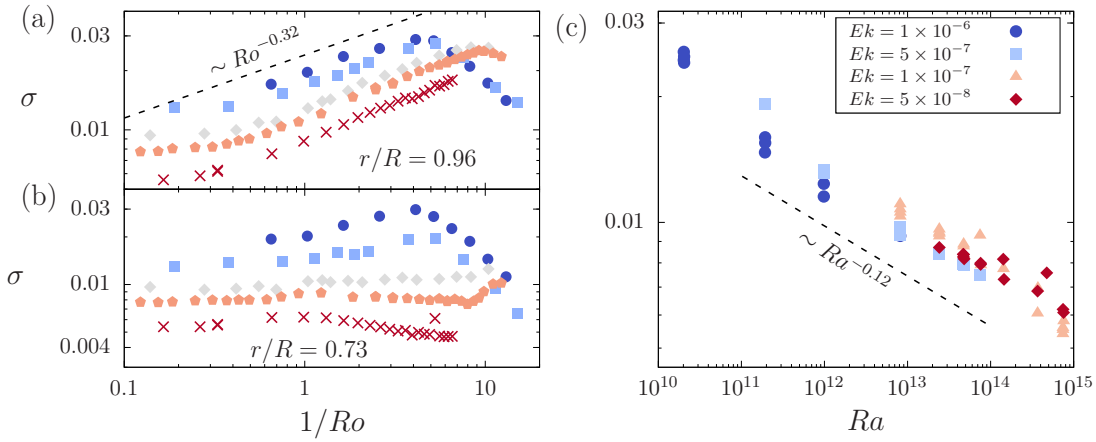

Figure 3.44: (a and b): Standard deviations σ at $z/H = 0.493$ as function of $1/Ro$ for a selection of Ra: blue bullets run E1a, violet squares E2a, purple diamonds E2c, red pentagons E2e, orange crosses E2k. (a) radial position $r/R = 0.96$, compared is the suggested scaling of the temperature rms from Kunnen et al. [2010] as dashed line $\sim Ro^{-0.32}$. (b) radial position $r/R = 0.73$, within the bulk, where we do not observe an increase in σ with $1/Ro$ for larger Ra. (c) σ as function of Ra for a selection of $Ek \approx const$ at $1/Ro_1^* \leq 1/Ro \leq 1/Ro_2^*$. Dashed line shows $\sim Ra^{-0.12}$ as a guide to the eye.

line for $Ro \geq 5$, $Ra = 10^9$. We have plotted σ as function of the rotation rate for a subset of Ra in figure 3.44 for two distances from the wall, $r/R = 0.96$, rather close to the wall, and $r/R = 0.73$, our innermost thermistor column. First we focus on measurements at roughly half-height $z/H = 0.493$. For both radial distances we first observe the increase of σ with Ra again, consistently for all but the highest rotation rates, i.e. $1/Ro < 1/Ro_2^*$. The dependence on the rotation rate, however, is ambiguous and depends on r/R. Close to the wall, fig. 3.44a, σ increases monotonically with $1/Ro$ for all Ra at $1/Ro_1^* \leq 1/Ro \leq 1/Ro_2^*$, for reference we show a power-law dependence $\sim Ro^{-0.32}$, as suggested by Kunnen et al. [2010]. In that study the dependence was observed as well at $z = H/2$, but at the center line of the cell. In the bulk flow at our innermost thermistor $r/R = 0.73$ we however observe almost no increase of σ with rotation, at least for high Ra. For the lowest $Ra = 7.5 \times 10^9$, we observe a small increase similar to the one close to the wall. For larger Ra, σ remains at a constant value at $Ra = 4.7 \times 10^{13}$, while for our largest $Ra = 7.5 \times 10^{14}$ we even observe a small decrease in σ with $1/Ro$. Thus, the power-law suggested in Kunnen et al. [2010] might only be valid at their investigated $Ra = 10^9$ in the bulk. Once more, if we want to fit a power-law dependence of σ on Ra and Ek, the exponents are likely not constant but rather a function of the input parameters.

When we remain in the regime of rotation-affected convection $1/Ro_1^* \leq 1/Ro \leq 1/Ro_2^*$ and plot data for different Ek (fig. 3.44c), data falls more or less onto one curve $\sim Ra^{-0.12}$. We do not keep Ek perfectly constant between different Ra, since we did not fix Ek but the rotation rate Ω during our experiments, so the scatter might partially be explained by slightly different Ek. The exponent is, however, close to the value of -0.103 for the non-rotating case, which suggests that the scaling with Ra is robust even under moderate rotation.

If we normalize σ by the value $\sigma(0)$ for no rotation, we obtain the relative influence of rotation on the standard deviation, shown in fig. 3.45(a, b), where the ratio is plotted as function of $1/Ro$. With increased rotation we see, as before, σ increases. Moreover, we see more clearly how changes in Ra affect how σ changes with $1/Ro$. Close to the wall at $r/R = 0.93$ (fig. 3.45a), the change of σ is similar for all Ra up to some moderate rotation $1/Ro \approx 2$, after which $\sigma/\sigma(0)$ for large Ra continues to increase. On the other side for small Ra, $\sigma/\sigma(0)$ first increases much slower and for $1/Ro > 1/Ro_2^*$ it actually decreases slightly below $\sigma(0)$ for the highest rotation rate. Notable here is the decrease in the standard deviation at all Ra which sets in for large rotation rates. The onset of this decrease is shifted towards higher $1/Ro$ with larger Ra. We observe this for the largest Ra only in a few data points, but the trend suggests this decrease is real and not some centrifugal effect.

Further away from the sidewall at $r/R = 0.73$, we observe a very different picture. $\sigma/\sigma(0)$ remains constant until $1/Ro \approx 1/Ro_1^*$, then it decreases first for high Ra, and increases for low Ra. At $1/Ro \approx 1/Ro_2^*$, also for the low Ra, $\sigma/\sigma(0)$ decreases strongly way below the value for no rotation. A general increase in σ with rotation is clearly not present. But why is the behaviour so different in the bulk compared to the flow close to the wall? Most likely the answer is again the BZF. For higher Ra, DNS tells us that the width of the BZF becomes increasingly smaller, and so it does with increasing rotation rates. We again use the suggested dependence of the thickness of the BZF (Zhang et al. [2021]), eq. 3.15, which is reformulated to $\delta_0 \sim 1/Ro^{-2/3}Ra^{-1/12}$. If we solve this for the lowest $Ra = 7.5 \times 10^9$ and at a rotation rate $1/Ro_2^*$, this estimates the BZF to reach approximately until $r/R \approx 0.7$, just so that the innermost thermistor still measures the temperature inside the BZF. There, its very distinct hot and cold areas lead to high σ due to the separation of warm updraft and cold downdrafting regions. Close to the transition of the BZF towards the bulk flow, the temperature signal of the BZF gets

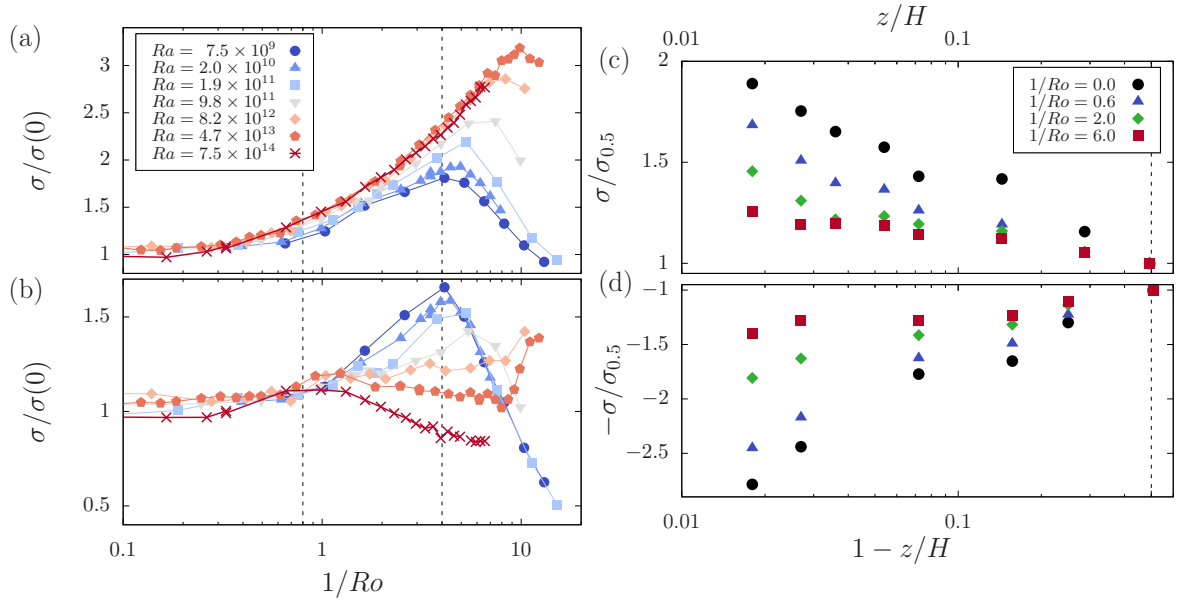

Figure 3.45: (a),(b): standard deviation σ normalized by the value $\sigma(0)$ for no rotation as function of $1/Ro$. Colours and symbols show different Ra as in the legend. (a) is for $r/R = 0.93$, (b) $r/R = 0.73$. (c),(d): Vertical profile of σ normalized by the value $\sigma_{0.5}$ at half-height $z \approx H/2$ for $r/R = 0.98$. (c) shows the upper half of the cell, (d) the lower half. $Ra = 4.7 \times 10^{13}$, run E2e, $1/Ro$ varies as in the legend. We see the value for σ increases stronger with z for no/lower rotation, while for high $1/Ro$ the values of σ are rather constant in vertical direction. Adapted from Wedi et al. [2021].

weaker, leading to a decreasing σ. This is what we observe in figure 3.45b. At the lowest Ra the BZF remains strong even at the radius of $r = 0.73R$, but as soon as it becomes thinner with increased $1/Ro$, also there mixing becomes very efficient and σ decreases rapidly.

Until now we focussed on measurements at mid-height, but we have additional measurement points in the vertical thermistor columns, where we regarded σ as well. Similar to the logarithmic profiles for the temperature, in fig. 3.45(d, e) we show the dependence of σ with height z/H. Therefore, we normalize σ by the value of the standard deviation at half-height $\sigma/\sigma_{0.5}$, and plot the resulting reduced $\sigma/\sigma_{0.5}$ for several $1/Ro$. What we observe is a much stronger increase with vertical distance from $z = H/2$ for small rotation rates (small $1/Ro$) compared to the measurements at higher rotation rates (larger $1/Ro$). While for no rotation $\sigma/\sigma_{0.5}$ is substantially larger at the lowest $z/H = 0.018$, the value for $1/Ro = 6$ is only increased by about 25% or so. Increasing rotation monotonically decreases the slope $\partial(\sigma/\sigma_{0.5})/\partial z$, all seemingly still follow a logarithmic profile. One needs to take care interpreting this observation. Note that this does not mean the fluctuations decrease with $1/Ro$, but rather that σ at different heights become more

similar with increasing $1/Ro$. This means that, close to the sidewall, the flow is much more homogeneous in vertical direction compared to the non-rotating case. In contrast to the vertical gradient of the mean temperature (see fig. 3.12), the vertical gradient of the fluctuations $\partial\sigma/\partial z$ decreases with increasing $1/Ro$.

3.11 Skewness $\gamma_1(\tilde{T})$

We have already seen that the *pdfs* of the temperature are not symmetric around $\tilde{T} = 0$ away from half-height $z = H/2$. In RBC research, the bulk flow is often shown to obey a Gaussian distribution (Julien et al. [1996b], Schumacher et al. [2018]) - the thermal background, whereas thermal plumes ejected from the top and bottom BLs are of exponential form (Wang et al. [2019]). At mid-height, plumes from both sides are of equal strength and we can expect the distribution to remain symmetric, i.e. not skewed. Closer to the top and bottom, the influence of the nearby plate is much stronger. For $z < H/2$ ($z > H/2$) we should hence effectively measure a superposition of both, the thermal background centered around T_m and the plumes emitted close by with a temperature somewhere between T_{bot} (T_{top}) and T_m. This leads to a skewed distribution, which we measure quantitatively by the definition of the skewness

$$\gamma_1 = \frac{1}{N}\sum_i^N \left[\left(\frac{T_i - \mu}{\sigma}\right)^3\right], \tag{3.19}$$

with the mean value μ and the previously investigated standard deviation σ. Far away from the horizontal plates, regardless of whether we have a Gaussian or an exponential temperature *pdf*, the distribution is symmetric around 0 and with it, we expect $\gamma_1 = 0$.

Fig. 3.46 shows γ_1 as function of $1/Ro$ at $Ra = 4.7 \times 10^{13}$. For very slow rotation, $1/Ro < 0.2$, the skewness remains constant and positive for the bottom measurement (red squares) at $z/H = 0.287$, while it is negative closer to the top plate $z/H = 0.75$. This results from the heavily skewed *pdf* $p(\tilde{T})$, which is plotted in fig. 3.46b for the two locations and very slow rotation $1/Ro = 0.12$. The measurement at $z/H = 0.287$ exhibit a larger tail towards hotter temperatures, resulting from the ejected plumes at the bottom plate drafting upwards. At that height the plumes did not have time to sufficiently mix with the environment. On the contrary, the plumes drafting downwards from the top plate through the entire cell have mixed with the turbulent background and

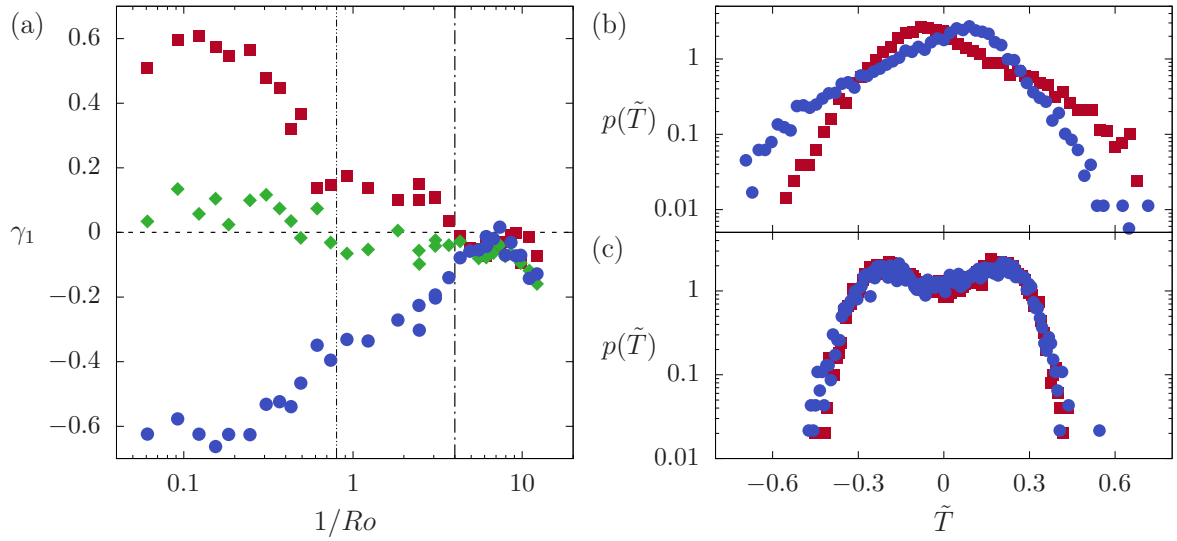

Figure 3.46: (a) skewness γ_1 as function of $1/Ro$ for $Ra = 4.7 \times 10^{13}$ at $r/R = 0.98$, $z/H = 0.287$ (red squares), $z/H = 0.493$ (green diamonds), $z/H = 0.75$ (blue bullets). Dashed vertical lines again show the transitional $1/Ro^*_{1,2}$. (b),(c) *pdf* of the reduced temperature $\tilde{T} = (T - \langle T \rangle)/\sigma$ at $1/Ro = 0.12$ (b) and $1/Ro = 9.8$ (c) for vertical position $z/H = 0.287$ (red squares) and $z/H = 0.75$ (blue bullets). Adapted from Wedi et al. [2021].

are thus invisible to the *pdf*. The distribution at the top plate, shown as blue bullets, mirrors this to the cold side and is thus consistent with this picture.

Beyond $1/Ro \approx 0.2$, $|\gamma_1|$ for both vertical locations $z/H = 0.287$ and 0.75 begins to decrease. Noteworthy is that the de-/increase in skewness happens well before $1/Ro^*_1$ found in the heat transport and the onset of the BZF as seen in the sudden increase of the peak-distance parameter d (3.8) in fig. 3.20b. This suggests that the flow structure is already affected by rotation earlier, although too weak to be recognized by other statistical quantities. We have identified the same early influence already in the phase differences at the sidewall, however, see fig. 3.37b. At the transitional value $1/Ro^*_1$ we do not find significant changes in $|\gamma_1|$, the deviation of the two data points at $z/H = 0.287$ around that rotation rate are considered as outliers. No such decrease is found in the data for the upper part of the cell. With increased rotation rate we measure $\gamma_1 \approx 0$ for $1/Ro \geq 1/Ro^*_2 = 4$. This is the regime where we assume a fully developed BZF, where $p(\tilde{T})$ shows the bimodal distribution. The result agrees with the superposition of two Gaussian distributions, as for them the skewness is $\gamma_1 = 0$ by definition. At half-height $z/H = 0.493$ (green diamonds in fig. 3.46a), the skewness is close to zero for all $1/Ro$, since there plumes from both sides contribute equally to the temperature signal. The data shown here suggest that the signature of the thermal plumes ejected

from the bottom and the top plates are reduced even at very low rotation rates. This reduction seems to be largely uncorrelated with the onset of the BZF and its effects are not measurable in the heat transport in form of $Nu(1/Ro)$. The twisted form of the LSC at these slow rotations (sec. 3.8.1) may be the origin of this decrease in $|\gamma_1|$, as the plumes have travelled longer distances until they reach the thermistors and hence the thermal signature is partially lost.

Let us now consider the data in the bulk area $r/R = 0.73$ in figure 3.47. Unfortunately we do not have any thermistor close to $H/4$ at that radius, so close to the bottom plate we now measure at $z/H = 0.144$. γ_1 remains constant for low $1/Ro$ similar to the case discussed above. At mid-height $H/2$, we observe again $\gamma_1 \approx 0$ as expected. While the qualitative picture remains similar, $|\gamma_1|$ decreases with $1/Ro$ in the top and bottom half of the cell, we see quantitative differences. Opposite to data at $r = 0.98R$, for both $z/H = 0.144$ and $z/H = 0.75$ the decrease in amplitude sets in at $1/Ro \approx 1/Ro_1^*$. Furthermore, the de-/increase in γ_1 does not stop at $1/Ro_2^*$ but continues up to $1/Ro \approx 10$ with opposed sign. This describes an initially skewed distribution for no or slow rotation just as it was for the wall-region, which for fast rotation rates becomes an also skewed, but mirrored *pdf*, as shown in fig. 3.47(b, c). This non-zero $|\gamma_1|$ suggests the influence of thermal plumes from the bottom (top) side reaches far through the bulk until $z/H = 0.75$ ($z/H = 0.144$). Even though we are not in the regime where we expect Taylor columns (fig. 2.7b) to appear, pumping mechanism like these or Ekman-pumping could explain the strong influence of plumes from the upper/lower sides. According to Liu and Ecke [2011], the change of skewness inside the bottom boundary layer from $\gamma_1 \approx 0$ for no rotation into a slightly negatively skewed distribution for high rotation rates can be explained by Ekman suction, where cold fluid penetrates deeper into the boundary layer. While a distribution distinctly skewed towards lower temperatures was not observed outside of the boundary layer in Liu and Ecke [2011], it seems logical that the plumes which penetrate the BL have to cross also measurement points above.

For our three data points with the largest rotation rates we observe that $|\gamma_1|$ rather abruptly decreases. While we do not have a definite answer to this, we note that for the investigated $Ra = 4.7 \times 10^{13}$ at the same rotation rates the standard deviation in fig. 3.45b strongly increased. Possibly this shows influence of centrifugal forces, as for the considered points the Froude number can reach up to $Fr = 0.5$ for $1/Ro = 12.2$. In what way centrifugal buoyancy influences the flow structure and with it γ_1 demands

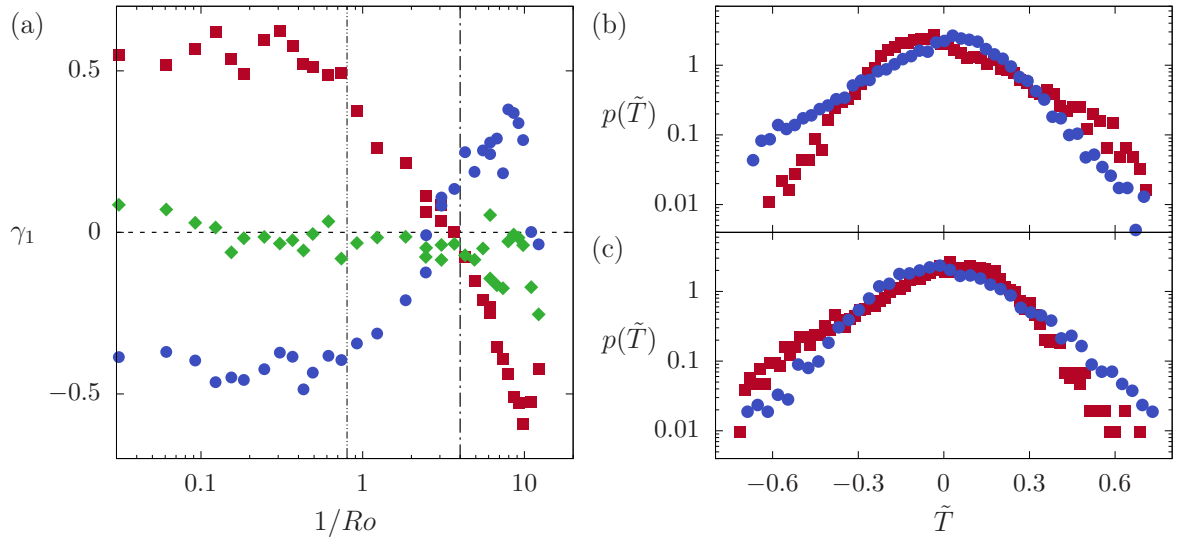

Figure 3.47: (a) skewness γ_1 as function of $1/Ro$ for $Ra = 4.7 \times 10^{13}$ at $r/R = 0.73$, red squares $z/H = 0.144$, green diamonds $z/H = 0.493$, blue bullets $z/H = 0.75$. Dashed vertical lines again show the transitional $1/Ro^*_{1,2}$. (b),(c) *pdf* of the reduced temperature $\tilde{T} = (T - \langle T \rangle)/\sigma$ at $1/Ro = 0.12$ (b) and $1/Ro = 9.8$ (c) for vertical position $z/H = 0.287$ (red squares) and $z/H = 0.75$ (blue bullets). Adapted from Wedi et al. [2021].

further investigation.

Vertical profiles for γ_1 are shown in figure 3.48 close to the wall at $r/R = 0.98$ for two Ra and a selection of $1/Ro$. We notice for no and slow rotation a maximum (minimum) in γ_1 around $z \approx H/4$ ($z \approx 3H/4$) and a vanishing skewness close to the plates. The reason for this is found in the LSC, which has an elliptical shape stretching the whole cell and carries the thermal plumes with it. Close to the plates at both sides corner rolls exist which rotate in opposite direction (Sun et al. [2005]), into which the thermal plumes do not enter. The LSC drags the signature of the plumes with it, which first hit the sidewall at $z \approx H/4$ and $3H/4$. There, γ_1 is hence strongly enhanced. For larger rotation rates, the LSC vanishes and with it, also the corner rolls. Then the maximum in γ_1 also disappears as found in fig. 3.48. The skewness remains fairly small throughout the entire vertical axis with the largest deviations close to the top and bottom plate. Once again this highlights the vertical homogeneity of the BZF with the bimodal Gaussian distribution and $\gamma_1 \approx 0$.

The decrease in skewness with rotation was observed by previous investigations, for example in a square box (Liu and Ecke [2011]), where γ_1 decreased throughout the entire vertical axis when rotation was applied. The maximum there was significantly closer at

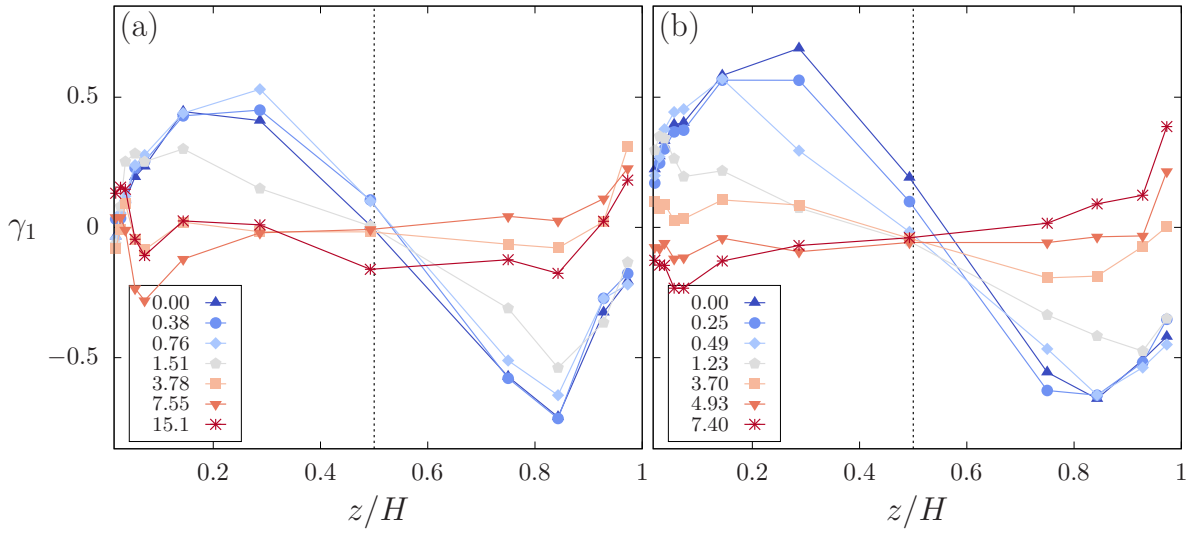

Figure 3.48: Skewness γ_1 as function of vertical position z/H for (a) $Ra = 1.9 \times 10^{11}$ and (b) $Ra = 4.7 \times 10^{13}$ for various $1/Ro$ as in the legends. Connecting lines are just guides to the eye. $r/R = 0.98$.

the plate, namely at $z/H \approx 0.1$ for $Ra = 4 \times 10^8$, $Pr \approx 6$ and without rotation. Similar decreases in γ_1 with $1/Ro$ have been found in Ding et al. [2019] in an experimental cylindrical setup at $Ra = 4.22 \times 10^9$, $Pr = 6.7$. It was suggested that with increased rotation rates the fluctuations above the thermal boundary layer vary more symmetrically. Both studies, in contrast to our measurements, exhibit a positive γ_1, i.e. a stronger influence from the plumes coming from the bottom plate, for all $1/Ro$, while for fast rotation, we measure $\gamma_1 < 0$ close to the bottom plate. Is this due to the proximity of our measurements to the sidewall? Our results at $r = 0.73R$ (fig. 3.49) do not suggest this, as the change from positive towards negative skewness is similar there. It is possible that the previous studies did not explore sufficiently high $1/Ro$ to observe this or that this is an effect of our lower investigated Prandtl number.

3.12 Conclusion of the rotating large-scale measurements

So far, we have discussed the temperature field using point-wise probes in rotating RBC at large $Ra \leq 10^{15}$ and corresponding low Ek. For this, we used a 2.24 m tall, high pressure convection facility inside the pressure vessel "U-Boot" at up to 18.7 bar with the working gas SF_6.

Vertical transport of heat in form of the Nusselt number Nu as function of Ra followed the scaling found in previous literature and models with $Nu \sim Ra^{0.315}$, fig. 3.7.

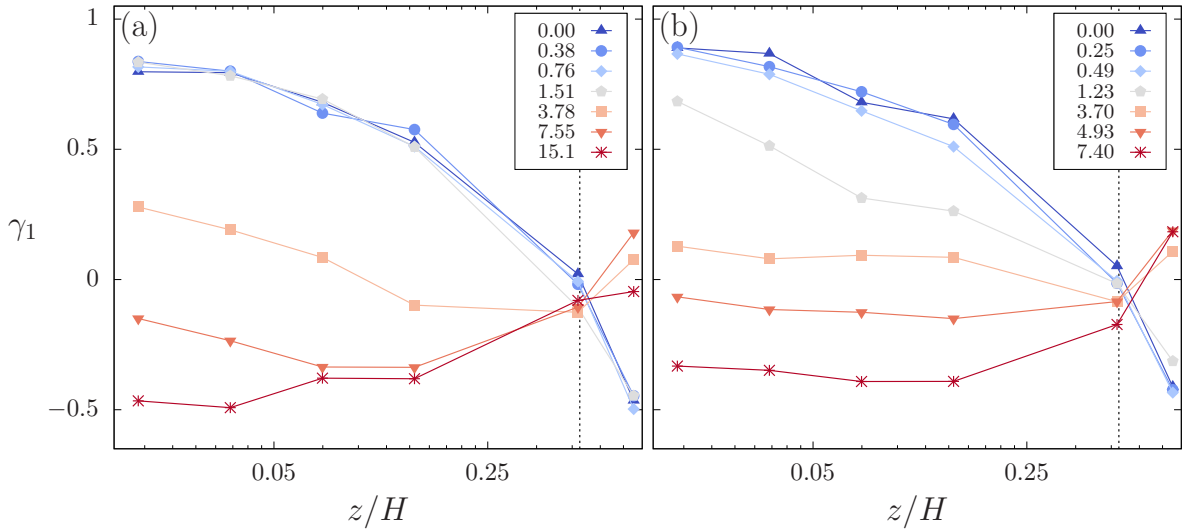

Figure 3.49: Skewness γ_1 as function of vertical position z/H at $r/R = 0.73$ for (a) $Ra = 1.9 \times 10^{11}$ and (b) $Ra = 4.7 \times 10^{13}$ for various $1/Ro$ as described in the legends. Connecting lines are just guides to the eye, dashed vertical lines mark $z/H = 0.5$.

Nu/Nu_0 collapses nicely when plotted as function of $1/Ro$, without any heat transport enhancement for moderate rotation rates. We identified two transitional $1/Ro_1^* = 0.8$ and $1/Ro_2^* = 4$, which appeared in multiple analysis. The vertical temperature profile exhibits a logarithmic shape at all depths into the bulk $r/R = 0.98, 0.96, 0.93$, and 0.73. Fits to the slopes of these profiles yield a complex behaviour on the input parameters, depending on r/R for the non-rotating case (fig. 3.13) and on $1/Ro$ for the rotating (fig. 3.15).

Most notable is the split of the *pdf* into a bimodal distribution at $1/Ro > 1/Ro_1^*$ close to the sidewalls for all Ra. We interpret this behaviour as the onset of the BZF, which consists in our $\Gamma = 1/2$ cell of a travelling wave in the temperature field with azimuthal wave number $k_{BZF} = 1$, i.e. one cold down-drafting region and one hot up-drafting region at the lateral sidewall. This is supported by the azimuthal temperature distribution and its evolution in time, fig. 3.26a. We are able to measure the drift rate of this temperature structure using both, cosine fits to the individual measurements at a given time to the eight thermistor at $z/H = const$, distributed azimuthally, or via auto- and cross-correlation of different thermistors throughout the cell. We find that the compensated drift rate depends on the inverse Rossby number as $-\omega_m/\Omega \sim 1/Ro^{-3/4}$, independent of Ra. This is a smaller exponent than observed in DNS, which suggested $\omega/\Omega \sim 1/Ro^{-5/3}$ (Zhang et al. [2021]).

3.13 Non-Oberbeck-Boussinesq effects without rotation

Almost all theoretical approaches as well as DNS in RBC are based on the assumption of Oberbeck-Boussinesq (OB) conditions, i.e. the fluid parameters do not change within the cell, except for the linear dependence of ρ on T. This leads to the simplified OB equations (2.15)-(2.17). Since in an experimental setting the fluid is physically hotter at the bottom and colder at the top and fluid parameters are in general a function of T, this assumption is always an approximation. But what if very large gradients Δ are applied, such that the difference in fluid parameters at the top and the bottom become substantial? In general, all effects that are not covered by the Boussinesq approximation are summarized as non-Oberbeck-Boussinesq (NOB) effects. Here the focus lies on large Δ and its influence on Nu and temperature distributions and how much NOB effects can influence the measurements using the HPCF setup with pressurized SF_6.

Background to NOB

NOB effects have been subject of many studies. E.g. Busse [1967] studied temperature-dependent fluid parameters and their effect on the hexagonal structures of cellular convection. He reported on non-symmetrc boundaries, which lead to a preference of certain flow states. Most experiments try to answer whether at high pressures and large Δ or close to the critical point, the resulting data are still close to the OB approximation. Wu and Libchaber [1991] reported on a similar symmetry breaking between the top and bottom half of the cell in cryogenic helium at sufficiently large Ra, where Δ becomes increasingly large. It was shown that the temperature drop over the thermal boundary layers close to the horizontal plates Δ_{top} and Δ_{bot} is not symmetric anymore, and a parameter to describe the strength of NOB effects was suggested as their ratio $x = \Delta_{top}/\Delta_{bot}$. Due to this asymmetry the temperature T_c at half-height $z = H/2$ departs from the arithmetic mean $T_m = (T_{top} + T_{bot})/2$. Depending on Pr opposite effects are induced: Urban et al. [2012] similarly to Wu and Libchaber [1991] used cryogenic helium and found an increase in $T_m - T_c$, similarly $T_c < T_m$ was reported in other studies using gases with $Pr < 1$ as working fluids, e.g. in Ahlers et al. [2007]. On the other hand, $T_c > T_m$ was found for water at $Pr = 4.38, 5.55$ Ahlers et al. [2006] or high-Pr liquids, e.g. glycerol ($Pr = 2547.9$) in Horn et al. [2013] or Zhang et al. [1997] with $300 \leq Pr \leq 7000$.

To suppress NOB effects as much as possible, most studies try to keep Δ small. A

suggestion for a phenomenological criterion to guarantee OB conditions was given in Wu and Libchaber [1991] and Urban et al. [2012] as $\alpha\Delta \leq C$, with $C \approx 0.2$. In this short section we want to investigate potential NOB effects and compare it to the approximate OB conditions at small Δ. Therefore, large temperature differences Δ are applied to the cell, while the pressure was varied between 1 and 18 bar of SF_6. At lower pressures, this lead to Δ reaching as high as 35 K, at the highest pressures either the temperature calibration range of the used thermistors were exceeded or the power input was not sufficient to reach $\Delta > 20$ K.

The answer to how to treat the NOB effects varies, a common approach is to evaluate the fluid parameters not at T_m, but at T_c. At first glance this might seem somewhat arbitrary, however, at sufficently large Ra when the bulk is at $T_c(z)|_{\text{bulk}} \approx const$, this is the temperature where the majority of the flow resides. With this approach, used for example in Urban et al. [2014], the dependence of Nu on Ra fell onto a constant power-law at higher Ra (fig. 3.51c).

Wu and Libchaber [1991] proposed a model to compensate Nu for the asymmetry based on the ratio of the temperature scales $\kappa\nu/g\alpha\delta_{BL}^3$ on the top and bottom boundary layers with thickness δ_{BL}, which were assumed to be equal. Then

$$Nu = Ra^{2/7} Pr^{-1/7} \left(\frac{2S}{S_t + S_b} \right)^{9/7}, \tag{3.20}$$

where $S = (\nu\kappa/\alpha)^{1/3}(1/\lambda)$ with λ the thermal conductivity and the subscript t, b denotes the fluid properties are evaluated at the top and bottom BL, respectively. As a first step to correct Nu at NOB conditions, Shishkina et al. [2016] suggested to calculate the conductive heat flux from the bottom to the top with a temperature dependent thermal conductivity.

Experimental NOB realizations

At high pressures of 18 bar, SF_6 begins to liquefy at ≈ 14.5°C (Scalabrin et al. [2007]). Since we wanted to investigate the NOB effects without a phase change in purely gaseous SF_6, we increased T_m to 35°C to avoid condensation at the top plate. For this investigation, during one experimental run the pressure was kept constant, hence $Pr = const$ while Δ was increased until the power for the Joule heater limited the heat input or

Run	P (bar)	Δ (K)	Pr	Ra	T_m (°C)
E1	1.0	$1.0 - 35.0$	0.781	$4.3 \times 10^{10} - 1.5 \times 10^{12}$	35.0
E2	2.0	$2.0 - 35.0$	0.784	$3.6 \times 10^{11} - 6.4 \times 10^{12}$	35.0
E3	7.0	$2.0 - 35.0$	0.803	$5.4 \times 10^{12} - 1.0 \times 10^{14}$	35.8
E4	12.0	$2.0 - 30.0$	0.831	$2.4 \times 10^{13} - 3.6 \times 10^{14}$	35.0
E5	18.5	$5.0 - 20.0$	0.889	$2.6 \times 10^{14} - 1.0 \times 10^{15}$	35.0
E6	$18.0 - 18.7$	$14.0, 15.0$	$0.889 - 0.935$	$\approx 9 \times 10^{14}$	$24.0 - 35.0$

Table 2: Overview of the conducted NOB experiments, Ra changed within a constant pressure due to increased Δ. No rotation was applied, thus $Ek = \infty$ everywhere.

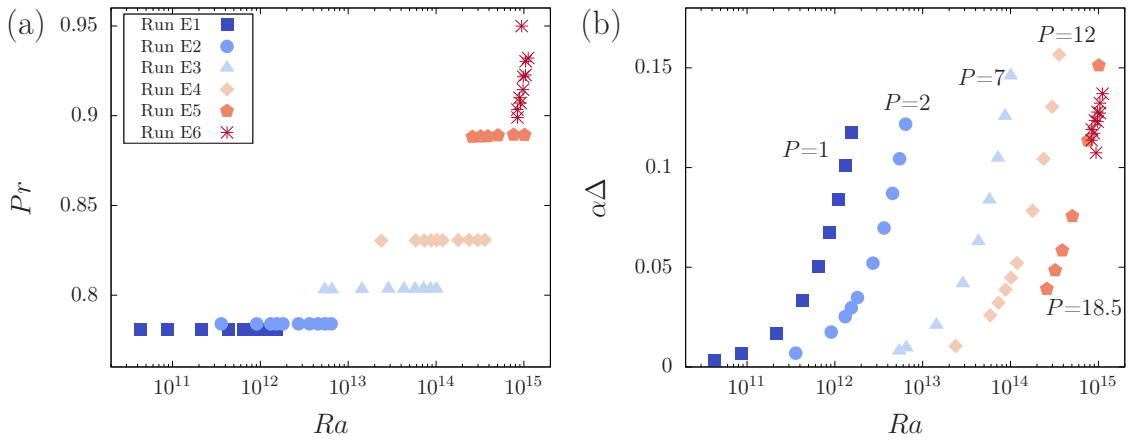

Figure 3.50: (a) Pr plotted against Ra for all measurement points. For higher pressures P (marked in (b) in bar), Pr increases. When $P = const$, $T_m = const$, thus $Pr = const$. (b) NOB criterion $\alpha\Delta$ against Ra, where α was determined at T_m. Urban et al. [2012] noted a critical value of 0.2 below which OB conditions are a valid assumption.

the thermistors measured at the limit of their calibration curve. This lead to Rayleigh numbers of $4.3 \times 10^{10} < Ra < 10^{15}$. Rotation was not applied in this stage, $Ek = \infty$. One additional run (E6) was conducted using constant $\Delta = 15\,\mathrm{K}$, with varying T_m. A list of experimental runs is given in table 2, investigated parameter combinations are given in $Ra - Pr$ in fig. 3.6b.

In fig. 3.50 we plot Pr (a) and the suggested NOB criterion $\alpha\Delta$ (b) as function of Ra, where α is evaluated at T_m. Pr changes only marginally with pressure. $\alpha\Delta$ increases within $P = const$ due to an increase in Δ, while $\alpha(P)$ of SF_6 increases rather weakly with pressure, just about a factor of ≈ 2 between 1 and 18 bar. We find $\alpha\Delta < 0.2 \forall Ra$. However, as Urban et al. [2012] have shown, this is not a necessary condition for the existence of NOB effects. The ratio of fluid properties, e.g. the thermal diffusivity κ, evaluated at T_{bot} and T_{top} can lead to NOB effects. Here, we reach ratios of up to

$\kappa_{bot}/\kappa_{top} \approx 1.3$. Vastly different Pr at the bottom and top plates lead to rather large differences in the BLs there (see, e.g. Schlichting and Gersten [2017]). Note that for all evaluations we only considered temperature dependent fluid properties, and hence neglected the effects due to hydrostatic pressure differences between the top and bottom.

Nu scaling behaviour

Analogous to section 3.2.1 we measure the heat input into the system and express it in the non-dimensional form with the Nusselt number $Nu = Q/Q_{cond}$. We here deal with rather large temperature difference Δ. Therefore, we calculate Nu by using the temperature-dependent conductive heat flux

$$Q_{cond} = 1/H \int_{T_b}^{T_t} \lambda(\hat{T}) d\hat{T}, \tag{3.21}$$

as suggested in Shishkina et al. [2016]. Since $Pr \approx const$ and $1/Ro = 0$, the assumed scaling reduces to $Nu \sim Ra^{\alpha}$. In fig. 3.51, Nu is plotted against Ra as well as its reduced value $NuRa^{-\alpha}$, where α was determined via a power-law fit to the data with $T_m = 35\,^{\circ}\mathrm{C}$, resulting in $\alpha = 0.308 \pm 0.001$. Here, we have ignored the first data point for this fit, since it visually strongly deviates from the overall trend. This exponent is very close to a similar fit the much sparser measurements in section 3.2.1 resulting in $\alpha = 0.315 \pm 0.001$ and is thus once again in good agreement to the Grossmann-Lohse theory. Looking more closely at the data in the reduced representation (fig. 3.51b), we find at large pressures some kind of "jumps" in the data, whenever the pressure was increased. Hence, data taken at similar Ra but different combinations of Δ and P do not overlap perfectly. For comparison in fig. 3.51c data from Urban et al. [2014] are plotted, which qualitatively exhibit a similar behaviour. This effect is only notable for the highest observed pressures. We note that the choice of T_m seems to have a big impact on our measured heat flux, as at comparable Ra but decreasing T_m, Nu drastically increases, arguably because we are getting closer to the liquid-vapor phase transition at the top plate, where fluid parameters sharply diverge.

All tested proposed models underestimate our observed deviations, so we need to raise the question how this can be. Certainly the environmental temperature in the U-Boot T_U plays a role, since for $T_U < T_m$, there is possibly a heat loss into the surrounding at the bottom plate even after insulation (Ahlers et al. [2009c]). The measurements at

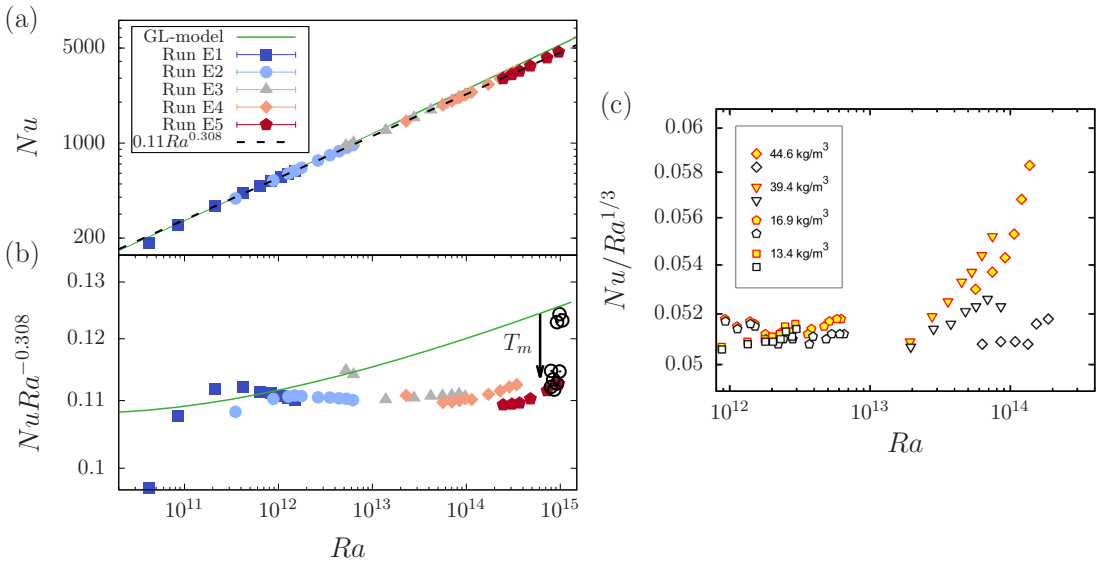

Figure 3.51: (a) Nusselt number as function of Ra in double logarithmic representation, green line curve according to Grossmann-Lohse theory (2.39,2.40). (b) Nu reduced by the fitted scaling of Ra^{α}, $\alpha = 0.308$. Every symbol represents different pressure settings with slightly deviating Pr, black open circles show run E6 with varying T_m, where in general higher T_m, marked by the black arrow, leads to lower Nu. (c) Results of the reduced $Nu/Ra^{1/3}$ against Ra from Urban et al. [2014] in cryogenic helium at different fluid densities, evaluated at T_m (red, filled symbols) and at temperature at half-height T_c (open black symbols).

$T_m = 35\,°\mathrm{C}$ for the highest Ra were taken with $T_m - T_U \approx 3\mathrm{K}$ (higher for low Ra, see below), for the lowest T_m it was $T_U - T_m \leq 2\mathrm{K}$. Assuming some additional heat $\tilde{Q}$ is lost when $T_m - T_U > 0$, which we have to compensate for in order to keep Δ constant, this would lead to a lower "true" $Nu = (Q - \tilde{Q})H/(\lambda\Delta)$, hence the opposite direction. One possible explanation can be found in the top plate, where heat from the surrounding heats up the area around $z = H$, decreasing the effective Δ, hence increasing Nu and simultaneously decreasing the effective Ra. We base our measurements on the temperature within the top plate, and T_{top} is largely unaffected from such an influence. But even then, this effect would be stronger for the measurements at smaller T_m, which actually agree better with the GL predicitions. The dependence $Nu(T_m)$ thus remains largely unanswered.

Central temperature

Due to the symmetry breaking of the boundary layers, where the majority of the temperature drop throughout the cell takes place (see e.g. fig. 3.12), the resulting temperature

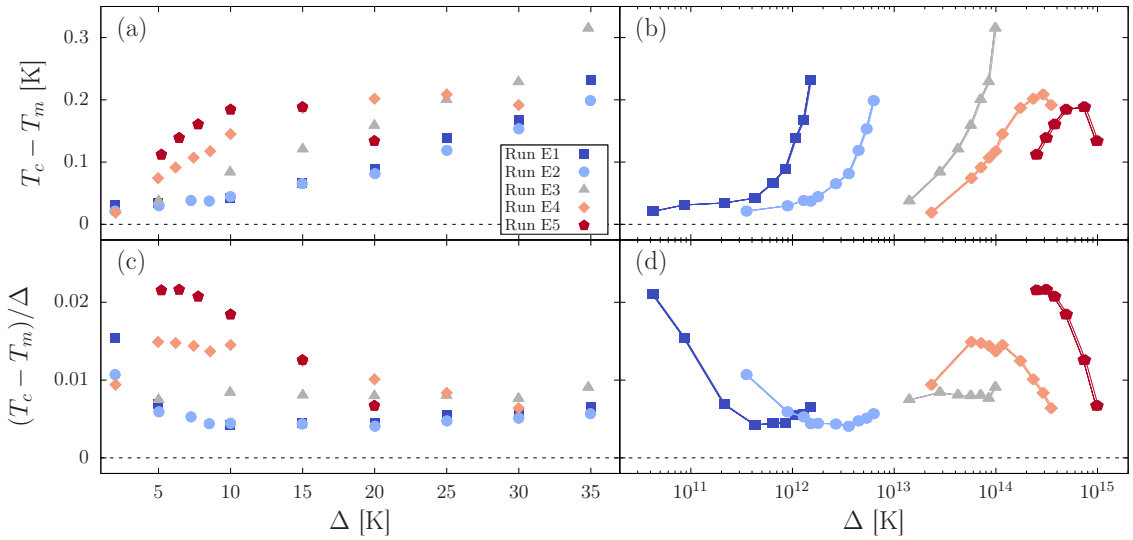

Figure 3.52: (a),(b): central temperature $(T_c - T_m)$ measured at distance $r = 0.73R$, as function of Δ (a) and Ra (b). (c) and (d) show the same data, but reduced by Δ. Colour and symbols mark the experimental runs as found in the legend, compare table 2.

profile leads to an offset in the temperature at half height $T_c = T(z = H/2) \neq T_m$. We determine T_c at different radii, due to the lack of thermistors at $r = 0$. Measurements were averaged in time over the whole experimental run, after the system has settled to a statistically steady state and over diametrically opposite sides. For this, T_c is approximated by a linear fit through the three (five for $r = 0.98R$) thermistors around $z = H/2$ as done in sec. 3.3 when available [3].

Fig. 3.52 shows $T_c - T_m$ as function of Δ (subplots a and c) and of Ra (b and d). In dimensional units, we see a clear increase in $T_c - T_m$ with increasing Δ throughout all runs. The measurements at different r/R agree with the here presented data. Only for the largest $\Delta = 20\,\mathrm{K}$ in run E5 and the largest $\Delta = 30\,\mathrm{K}$ in run E4 $T_c - T_m$ decreases with respect to the previous point, it is $T_c > T_m$ for all measurements, however. This is contrary to previous findings for experiments with $Pr < 1$.

Weiss et al. [2018] proposed a model to predict the central temperature T_c under weak NOB conditions, where the cell is divided into an upper half I_+ and a lower half I_-. Cross-over temperatures T_+ and T_- from the respective thermal boundary layer to

[3] Additional to the non-working thermistors from the previous rotating measurements, some thermistors were surprisingly unreliable at the higher working temperatures. Multiple re-calibrations were attempted, but the scatter was rather large and thus these measurements are excluded from the analysis.

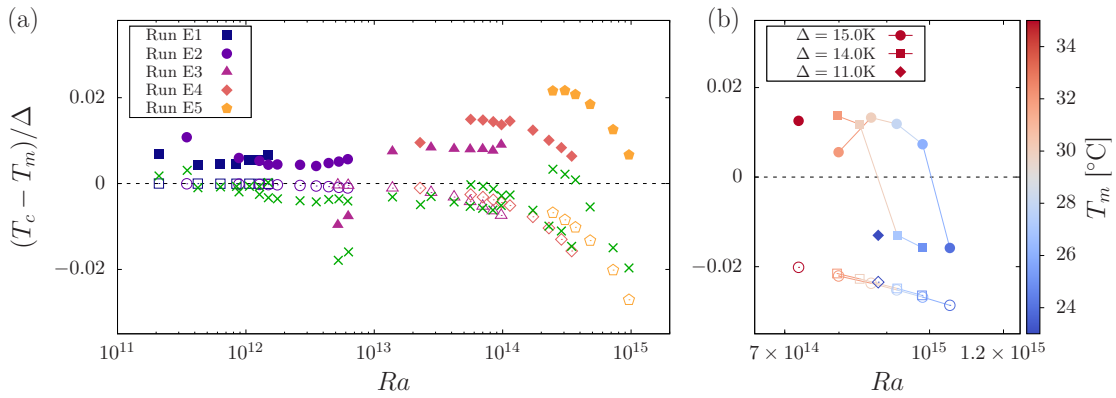

Figure 3.53: $(T_c - T_m)/\Delta$ as function of Ra at $r = 0.73R$ (closed symbols) compared to the model by Weiss et al. [2018] (open symbols) for $T_m = 35\,°\mathrm{C}$ (a) and for runs E6 and E7 with constant Δ but varying T_m (b). Green crosses in (a) show data compensated for the difference in environmental and cell temperature as discussed in the text.

the bulk are defined. From scaling arguments, the model consists of the relations

$$T_c = \frac{\delta_+^{3/4}\eta_+^{1/4}T_{bot} + \delta_-^{3/4}\eta_-^{1/4}T_{top}}{\delta_+^{3/4}\eta_+^{1/4} + \delta_-^{3/4}\eta_-^{1/4}} \tag{3.22}$$

$$T_+ = \beta T_{bot} + (1-\beta)T_c \tag{3.23}$$

$$T_- = \beta T_{top} + (1-\beta)T_c \tag{3.24}$$

with $\eta_\pm = \eta(T_\pm)$ and $\eta = \alpha g/(\kappa\nu)$. Solving this iteratively leads to fig. 3.53. Here the measurements from before (runs E1-E5) are plotted as function of Ra. Open symbols mark the estimates based on the model. As seen before, in disagreement with other studies our data show $T_c > T_m$, while the model suggests $T_c < T_m$. At least for the high pressures, we recapture the trend towards lower $(T_c - T_m)/Ra$ with increased Δ. In fig. 3.53b the same quantity is shown, this time the data with varying T_m (run E6). Surprisingly, for small T_m, we indeed see $T_c < T_m$. It appears as if the lower T_m, the lower also $(T_c - T_m)/\Delta$ and we are close to the predicted values.

All results shown here suggest a systematic measurement error which is larger than the actual NOB effects. We find a candidate in the different temperatures in the cell itself and the environment. We measured at large mean temperatures $T_m = 35\,°\mathrm{C}$. The U-Boot, although thermally shielded with porous foam, is thermally coupled to the experimental hall at $\approx 20\,°\mathrm{C}$. Without additional heating inside the U-Boot, this leads to an inevitable temperature difference compared to the cell, which decreases with

increased heat input into the bottom plate. Thus, measurements at small Ra have a rather large temperature difference $T_m - T_U \geq 5\,\mathrm{K}$, whereas measurements at larger Ra see a decreased $T_m - T_U$. This increases the measured temperature close to the sidewall within the cell with increased Ra, which likely explains the general trend of $(T_c - T_m)/\Delta$ in fig. 3.53. Seemingly, the thermal shield and the additional foam around the cell were not sufficient to suppress this influence.

Of course, this does not immediately explain why we observe $T_c > T_m$, since T_c in this picture should decrease due to thermal losses to the side. However, the calibration measurements of the thermistors inside the cell were taken within the finished setup. For those, to achieve a uniform temperature distribution, Δ was set to very low values $\approx 0.1\,\mathrm{K}$. At large T_m, this hence creates a large calibration error, as for the low heating power required to sustain these Δ, we also expect $T_m - T_U$ to be large. This is an inherent problem with the setup. To compensate, one should have heated up the U-Boot with additional heating from within or increased the thermal shielding around the sidewall.

A quick test can show this. We assume the measurements at $P = 1\,\mathrm{bar}$ and $\Delta \leq 20\,\mathrm{K}$ (excluding the $\Delta = 1\,\mathrm{K}$ measurement, as it is regarded an outlier) as Oberbeck-Boussinesq measurements. We thus shift the temperature measured at $r = 0.73R$ (as seen in fig. 3.53) to $T_c = T_m$. We further assume the influence of the environmental temperature to be approximately proportional to $T_m - T_U$, since it should be dominated by conduction through the sidewall. Therefore, data at higher Ra is shifted by the inital offset at OB conditions, multiplied by $(T_m - T_U)|_{OB}/(T_m - T_U)$. This is shown in fig. 3.53a as cross-shaped symbols. The data more or less follow $(T_c - T_m)/\Delta$ as suggested by Weiss et al. [2018]. We note that this is a mere qualitative approximation to check whether the large differences in environmental and cell temperature are the cause of this mismatch. While clearly not a quantitative analysis, this result underlines that the observed deviations are predominantly a systematic error of the setup.

4 Velocity measurements at moderate Pr and Ra

In the optically non-accessible HPCF cell measurements of the previously introduced boundary zonal flow (BZF), based on sparse point-wise temperature measurements, were difficult to perform. For direct velocity measurements we have built a transparent rotating RBC setup in order to measure the horizontal velocity field and to investigate the BZF features. Some results, especially sec. 4.3, of this chapter have been published in the Journal of Fluid Mechanics (Wedi et al. [2022]). It also includes a short description of the setup.

4.1 The small convection apparatus

In this section, the setup of the small convection cell and its operation are explained. It is followed by a description of particle image velocimetry (PIV) in sec. 4.1.2 and and a short test of the heat transport in form of the Nusselt number Nu.

4.1.1 Experimental setup

The experimental setup for PIV needs to be optically accessible from at least two sides for illumination and image recording. Therefore, the cylindrical cell consists of acrylic glass. Its height equals the diameter of 196 mm results in an aspect ratio of $\Gamma = 1$. The bottom plate is 15 mm thick and made out of copper with a heat conductivity of 394 W/m·K. An electrical high-resistance wire with a resistance of $r = 18\Omega/\mathrm{m}$ is embedded in grooves at the bottom of the plate. Neighbouring grooves are 6 mm apart to enable a uniform heating. Opposing to the sandwich method in the HPCF-II cell, no secondary plate is used, which limits the quantitative measurements of Nu due to heat losses to the side and bottom and thus larger measurement errors. Two thermistors are inserted into the plate to measure the temperature approximately 3 mm below ts upper surface. A 5 mm thick highly conductive sapphire is used as a top plate, which is cooled by a temperature controlled water bath. The water temperature is measured with two thermistors close to the inflow and kept at a desired temperature to within roughly ± 0.02 K via a Huber Ministat 240. All thermistors are read out using Keithley 2001 multiplexer; conversion to temperature was done using individual calibration curves based on the fit function eq. (3.2).

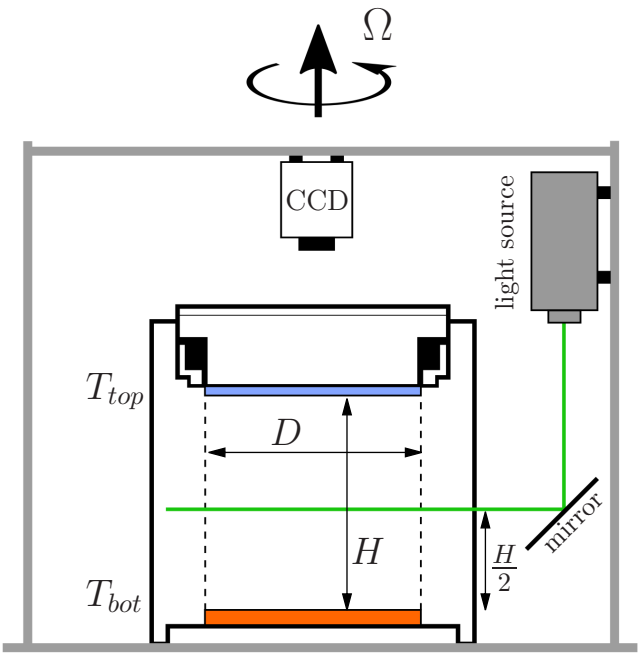

Figure 4.1: Schematic of the experimental setup. In orange the copper bottom plate, in blue the sapphire top plate. The light source and the CCD camera are attached to the rotating structure. The whole system rotates around its vertical axis with a rotation rate Ω. Adapted from Wedi et al. [2022].

(a)

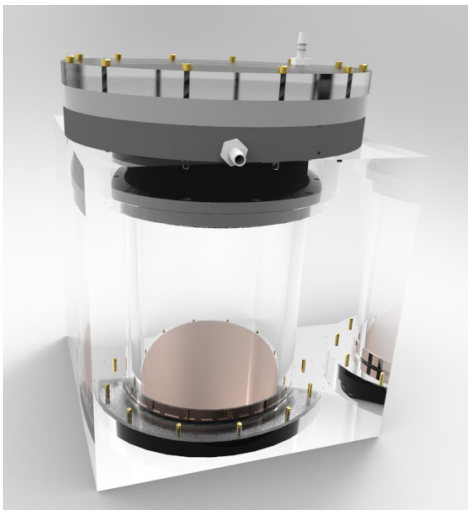

(b)

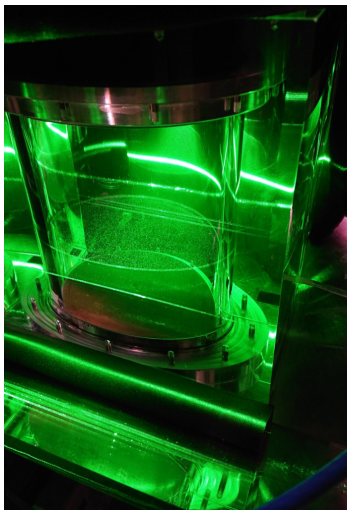

Figure 4.2: (a) Rendering of the experimental plexiglas setup. The tubings at the top part show the inlet and outlet of the cooling water. (b) Photo of the illuminated cell. A mirror redirects a laser sheet coming from the top into the cell at half height.

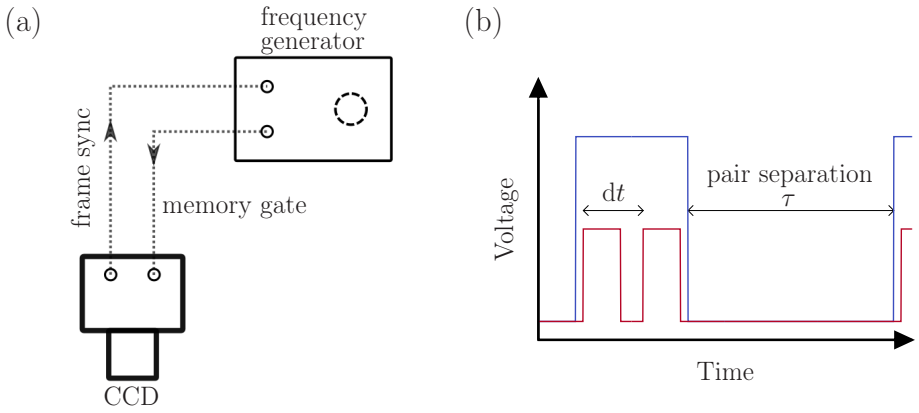

Figure 4.3: (a): Schematic of the camera and frequency generator. The camera sends a pulse when it saves an image, triggering the frequency generator to give a pulse of a width of 2 times the exposure time. (b) Voltage of the memory gate signal from the frequency generator (blue), during which time images are taken and saved to the camera's RAM (red). In between image pairs with a separation time τ no images are saved.

The entire setup was mounted on a rotating table with a frame built on top of it (fig. 4.1). The entire frame was driven by a Nanotec PD4-C stepper motor. All necessary electrical connections from the lab into the rotating frame were achieved via sliprings at the top and bottom of the rotating frame. At the top, water feedthroughs were installed to supply water to the cooling water bath.

The cooling water bath on top of the top plate consists of PVC sides and has itself a transparent top cover of acrylic glass. A Dantec RayPower 2000 laser with sheet optics is attached inside the rotating structure of the setup as shown in fig. 4.1. The light sheet is redirected using a mirror from the side in such a way that it illuminates a horizontal cross section of the cell at midheight. A high speed camera (Phantom VEO4K 990-L) with a set resolution of 2048x2048 px is mounted inside the rotating frame above the cell. Images were taken until the RAM of the camera (72 GByte) was filled. We took pairs of images with a separation time larger than the time between the two consecutive images. For this, we used a frequency generator which triggers the camera. This is realized with the *Memory gate* signal input of the Phantom camera, controlled by its Phantom Camera Control (PCC) software, as shown in fig. 4.3.

As working fluid we use various mixtures of deionized water with glycerol. For most experiments, we kept the temperature constant at $T_m = (T_{bot} + T_{top})/2 = 22.5°\mathrm{C}$, i.e., close to room temperature, in order to minimize heat flux to or from the sides. Different

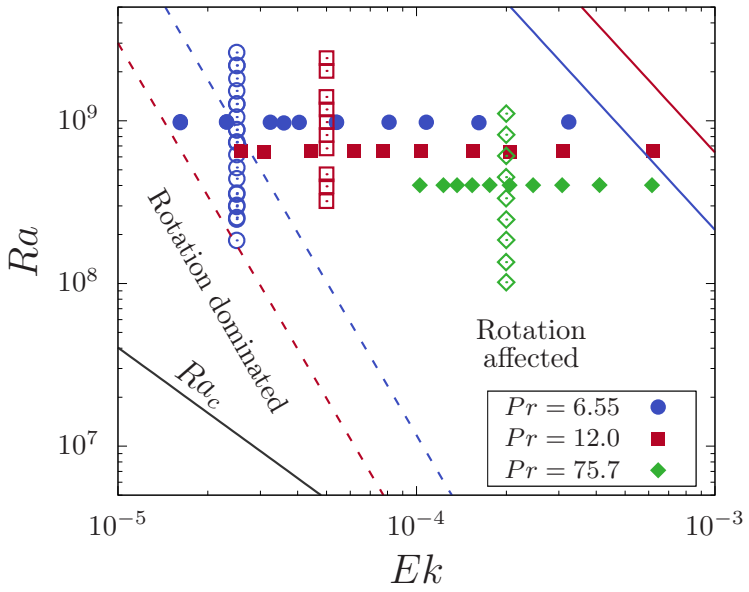

Figure 4.4: Investigated parameter space in a *Ra*-*Ek* plot. Grey line marks the onset of bulk convection (2.61) according to Chandrasekhar [1961], coloured symbols show different Pr as in the legend. Closed symbols mark the measurements taken at $Ra = const$ (datasets R1, R2, R3), while open ones mark measurements at $Ek = const$ (datasets E1, E2, E3). Red and blue lines show the change from buoyancy dominated to rotation affected regime for $Pr = 6.55$ and 12, respectively. Dashed lines correspondingly mark the transition from the rotation affected to the rotation dominated regime. From Wedi et al. [2022].

Pr were achieved by using different mass concentrations of glycerol in water. Here we investigated three different Pr namely $Pr = 6.55$ (pure water), $Pr = 12.0$ (20% glycerol) and $Pr \approx 76$ (60% Glycerol). By changing the temperature difference Δ we control Ra. Solely for the experimental runs P1 and P2, where we explored the Pr dependency of the BZF, we also changed T_m to easily adjust Pr.

Figure 4.4b and table 3 show an overview of the performed experiments. For each Pr we performed measurements at fixed Ek and various Ra (E1, E2, E3) as well as measurements with one fixed Ra and varying Ek (R1, R2, R3), respectively. Due to experimental constrains, different combinations of Ek and Ra were chosen for different Pr. In all measurements, we are far away from the onset of convection ($Ra \gg Ra_c$) as shown in fig. 4.4b. Hence, the observed structures close to the walls are results of strongly nonlinear interactions, in contrast to the linear wall modes.

Data set	Pr	Ra	Ek
R1	6.55	9.8×10^8	$1.6 \times 10^{-5} - 3.2 \times 10^{-4}$
R2	12.0	6.5×10^8	$2.6 \times 10^{-5} - 6.2 \times 10^{-4}$
R3	76	4.0×10^8	$1.0 \times 10^{-4} - 1.2 \times 10^{-3}$
E1	6.55	$1.8 \times 10^8 - 1.8 \times 10^9$	2.5×10^{-5}
E2	12.0	$3.2 \times 10^8 - 2.4 \times 10^9$	5.0×10^{-5}
E3	76	$1.0 \times 10^8 - 1.1 \times 10^9$	2.0×10^{-4}
P1	5.4 - 83.3	5.8×10^8	1.0×10^{-4}
P2	9.8 - 83.3	5.9×10^8	$5.1 \times 10^{-5} - 1.5 \times 10^{-4}$

Table 3: Overview of the conducted PIV experiments at a layer at half height $z = H/2$.

4.1.2 Particle Image Velocimetry

Single point measurements such as temperature readouts or Laser Doppler Velocimetry (LDV), that records the velocity of particles at one point, can not provide a detailed and comprehensive image of the flow morphology. This can be in parts complemented by techniques such as cross-correlations that combine multiple one dimensional measurements. However, the underlying mathematical description of the flow is elliptic (Batchelor [2000]) and thus for a complete understanding, we need to measure the entire flow field rather than local points. Particle Image Velocimetry (PIV) has become one of the standard techniques in flow visualization. An introduction into the basics of PIV is given for example in Westerweel [1997]. We here utilize the most basic, two-dimensional planar PIV, where usually a double-pulsed laser is used to illuminate fast moving flows. The flow is seeded with tracer particles which reflect the incoming light onto a digital CCD camera. The simplified idea consists of a pair of images taken with little time separation $t'' - t'$, small enough that the tracer particles do not exit a small interrogation area, but sufficiently large that particles move to a distinguishable position. Then the displacement of the tracers is followed, yielding the velocity of the flow (fig. 4.5a). The velocity field is calculated from the average displacement D of the particles in between the two images

$$D(\boldsymbol{x}, t'', t') = \int_{t'}^{t''} \boldsymbol{v}(\boldsymbol{x}(t), t) dt. \tag{4.1}$$

The first reported measurements using velocity measurements by tracking particle movements are from the late 70s, conducted by Barker and Fourney [1977], Dudderar and Simpkins [1977] as well as Grousson and Mallick [1977]. Over the years and decades, PIV became more and more popular and technical developments made it more accessi-

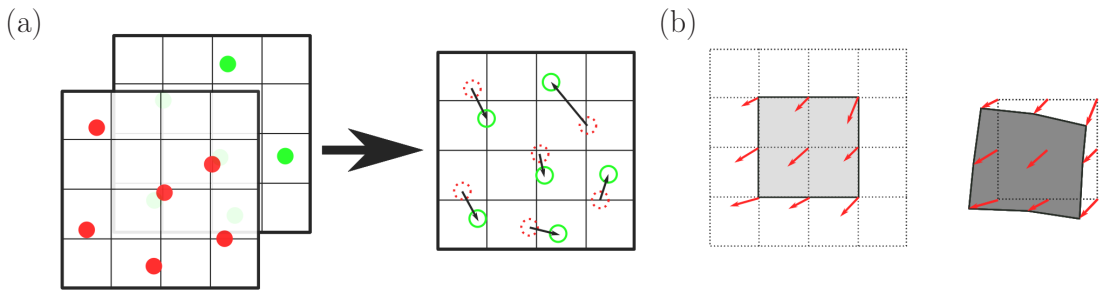

Figure 4.5: Functionality of particle image velocimetry. (a) two images are taken with small time separation $t'' - t'$, the change of the average position of the particles is calculated by spatial cross-correlation. (b) window deformation technique, adapted from Thielicke and Stamhuis [2014]. For one interrogation area, nine deformation points are calculated, shifting the interrogation area for the subsequent passes to enhance the resolution.

ble. The introduction of double-pulsed solid state lasers solved issues with insufficient lighting for high-turbulence environments, with the first published use of a Nd:Yag laser in Kompenhans and Reichmuth [1986]. Digital recordings and ever more powerful hardware made way for the widespread adoption of PIV and its variants in todays research of flows. A short review of the early history of PIV can be found in Adrian [2005], while e.g. Adrian and Westerweel [2011] serve as a comprehensive introduction of the technique.

If the particles are perfect tracer particles, i.e. follow the flow accurately, the flow velocity of the particles $\boldsymbol{v}(\boldsymbol{x}, t)$ is exactly the flow velocity $\boldsymbol{u}$. Of course, we only know the start and end point of each particle, not the steps between t' and t''. What we obtain is thus the average velocity in that time step, which inevitably leads to errors in the estimation for curved streamlines. Therefore, $t'' - t'$ should be chosen as small as possible. On the other hand we are limited by the resolution of the recording, for example by the pixel density of the CCD camera. If $t'' - t'$ is chosen too short, particles are recorded at the same pixel locations and the velocity is calculated as zero. As opposed to particle tracking velocimetry, where single particles are followed, in PIV one obtains the flow field by averaging over a larger window and hence over multiple particles. If the two snapshots taken are I' and I'', then the spatial averaging is done with window functions W' and W'' with the spatial correlation (Westerweel [1997])

$$C(s) = \int \int W'(\boldsymbol{x}) I'(\boldsymbol{x}) W''(\boldsymbol{x} + \boldsymbol{s}) I''(\boldsymbol{x} + \boldsymbol{s}) d\boldsymbol{x}. \tag{4.2}$$

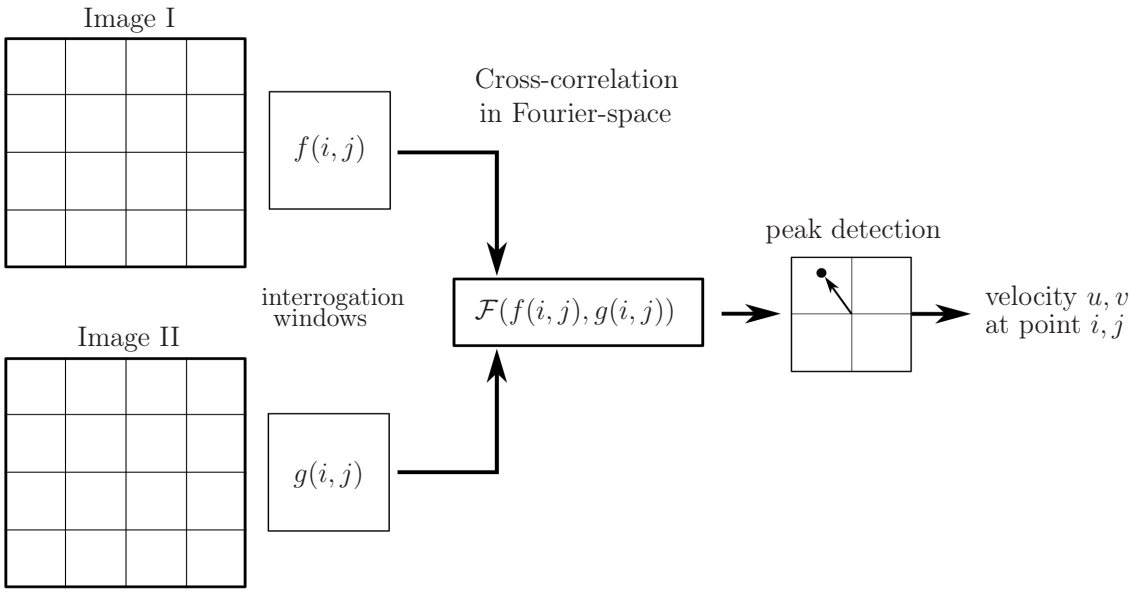

Figure 4.6: Simplified flow chart of the PIV algorithm. Two images are taken with separation $t'' - t'$, out of which interrogation windows are tranferred into Fourier space via a FFT and cross-correlation is performed. After transforming it back into real space, the peak of the correlation is found, yielding the displacement dx, dy. With the time separation, the velocity u, v is calculated.

W', W'' are the interrogation windows in the two images, typically a square of some $2^n \times 2^n$ pixels. In our case, the PIV software provides us with optional additional passes, enhancing the resolution, where the interrogation area is shifted by the previous pass (see fig. 4.5b). The nine grid points of the first, coarse interrogation window are displaced. Afterwards, finer interrogation windows are chosen, now looking for the correlation peaks in the previously found shifted area. We use a Fast Fourier Transform (FFT) approach as included in the implementation of the PIV algorithm ParaPIV (Wang [2021]), based on PIVlab (Thielicke and Stamhuis [2014]). The correlation matrix is calculated not by a convolution in spatial space, but by a multiplication in the frequency domain as shown in the flow chart of the algorithm in fig. 4.6. This approach is generally much faster than a direct cross-correlation of the images. The peak of the cross-correlation is estimated by a Gaussian fit to the values of neighbouring pixels, yielding a sub-pixel resolution of the displacement. From the PIV algorithm on our particle-filled flow field with a resolution of 2048×2048 pixel we obtain velocity fields with 240×240 grid points in three interrogation passes. A vector plot 4.7 shows the resulting velocity vectors in cartesian coordinates $\boldsymbol{u} = (u_x, u_y)$. Displayed is the resulting field after the first FFT

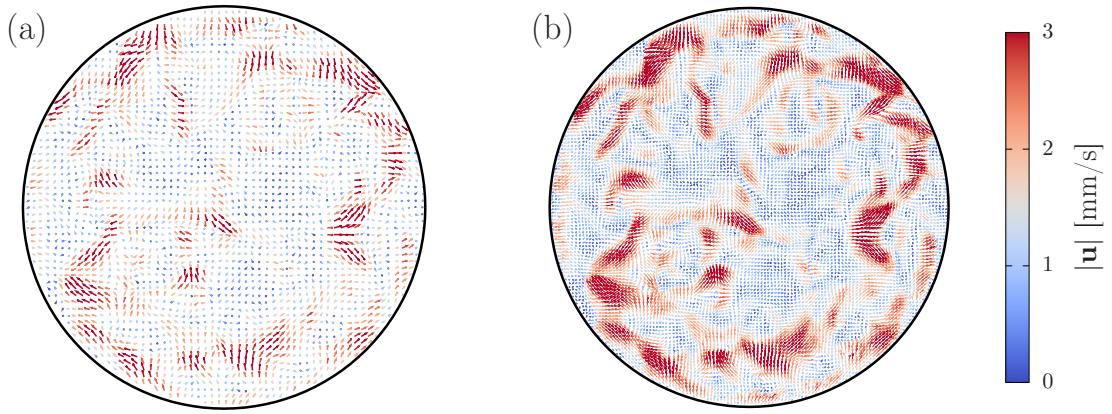

Figure 4.7: Velocity vectors $\boldsymbol{u} = (u_x, u_y)$ for a snapshot $Ra = 1.27 \times 10^9$, $Ek = 2.5 \times 10^{-5}$, $Pr = 6.55$. Colour marks the absolute velocity magnitude. (a) after the first pass with an interrogation window of 64×64 pixel. (b) After the second pass with the subsequent smaller interrogation window, here with 32×32 pixel.

pass with an interrogation area of 64×64 pixel (fig. 4.7a), and in (b) after two passes with an area of 32×32 pixel. At all times, an overlap of 50% is used as step width.

Tracer particles

In PIV, we need to seed the working fluid with tracer particles suitable for the setup. They have to have a density close to the density of the fluid as well as a size small enough, such that the particles have small inertia and follow the fluid's streamlines. A dimensionless number to describe this ability is the *Stokes number St*. It compares the particle's momentum response time due to drag t_0, also called the relaxation time, with the typical time scale of the flow. Assuming a particle Reynolds number of $\ll 1$, which for the small size of $\approx 10\,\mu$m and the low velocities in the flow is valid, we assume a Stokes flow, in which the convective term as well as the time derivative in eq. (2.6) are neglected. The momentum equation is written as:

$$\nu \nabla^2 \boldsymbol{u} - \frac{1}{\rho} \nabla p = 0. \tag{4.3}$$

Within this flow, viscous forces dominate over the inertial forces. From the Stoke's equation, the acting drag force onto a sphere with radius r_p can be calculated analytically. With a flow velocity u and μ the dynamic viscosity of the fluid, one obtains $F = 6\pi\mu r_p u$ (Stokes [1851]). As the typical time scale we use the Kolmogorov time scale

$\tau_K = (\nu/\epsilon)^{1/2}$, which in a turbulent system is the smallest relevant time scale. The kinetic energy dissipation rate ϵ_u is calculated using the exact relation eq. (2.26), $\epsilon_u = \nu^3 H^4 (Nu - 1) Ra Pr^{-2}$. The relaxation time of the particle is obtained by rewriting $F = m_p \dot{u}$:

$$\frac{u}{\dot{u}} \sim t_0 = \frac{\rho_p d_p^2}{18\mu}. \tag{4.4}$$

Therefore, the Stokes number is

$$St = \frac{\rho_p d_p^2}{\tau_K 18\mu} = \frac{\rho_p d_p^2}{18\mu} \frac{\nu H^2}{Pr} \sqrt{(Nu - 1) Ra}. \tag{4.5}$$

We use silver-coated hollow glass spheres with a diameter of $10\,\mu$m and a density of $\approx 1.4\,\mathrm{g/cm^3}$. For our control parameters and measured Nu, we yield $St \leq 1.25 \times 10^{-5} \ll 1$. For values $St \ll 1$, particles follow the streamlines of the flow with very high accuracy, thus we conclude that the particles are suitable for our application.

4.1.3 Heat flux measurements

Even though the design of the cell does not provide us with highly accurate Nu measurements due to potential heat losses towards the bottom or the sides, we nevertheless do a short analysis of the heat flux. The power input into the cell is taken as the heating power required to sustain the bottom plate at T_{BP}. Each experiment was conducted after an equilibration time and then continued for the measurement duration, which was about 20 minutes. With a low temporal resolution in temperature measurements, this leads to few data points also for the Nu measurements, with a rather large statistical error.

To obtain the heat flux Q, both the current and voltage drop across the bottom plate are measured at each time step. Due to the temperature drop across the top sapphire plate, the effective Δ is somewhat lower than the measured one by

$$T_{drop,TP} = \frac{Q d_{top}}{\lambda_{top} A} \tag{4.6}$$

with Q the total heat flux through the cell, d_{top}, λ_{top} the thickness and heat conductivity of the top plate and A the area of the cell. However, also the heat flux Q needs to be corrected for conductive heat flux through the sides and the bottom. Correction

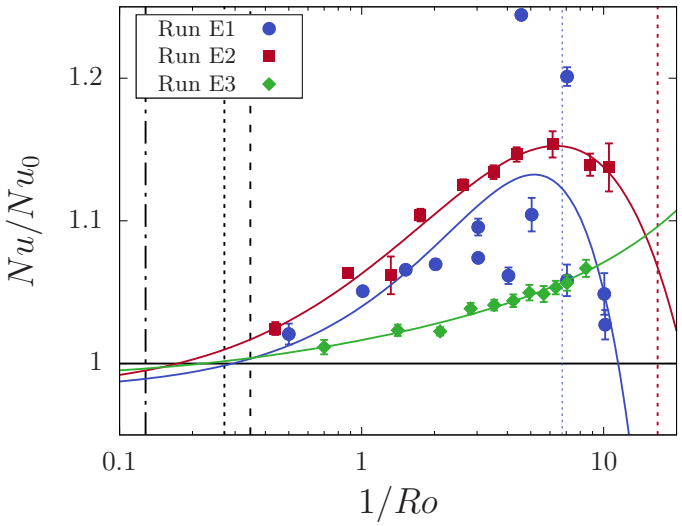

Figure 4.8: Nusselt number normalized by the value for no rotation Nu_0 for data with $Ek = const$ as function of $1/Ro$ to highlight the heat transport enhancement. Vertical black lines show the expected onset of heat transport enhancement by Weiss et al. [2016]: dashed-dotted $1/Ro_c(Pr = 76) = 0.128$, dotted $1/Ro_c(Pr = 12) = 0.271$, dashed $1/Ro_c(Pr = 6.55) = 0.347$. Dashed blue and red lines show the expected maximal heat transport enhancement suggested by Weiss et al. [2016]. Fitted curves are of the form $A \cdot \log(1/Ro - B) + C/Ro + D$ and serve just as guides to the eye. Error bars show the resulting error from the statistical uncertainty of the power input measurements.

measurements were conducted with an empty cell, which was filled with foam to suppress convection. These measurements show that the majority of the heat is lost to the bottom, and mostly depends on the difference of environmental temperature T_E and the bottom plate temperature T_{BP}. We determine a correction term on the input power of $P_{loss} = (0.25 \cdot (T_{BP} - T_E) + 0.03\Delta)\mathrm{W}$. The small influence of the heat transport through the sides can be estimated by a simplistic model, where heat is conducted from the bottom to the top inside a ring of a 5 cm thickness, the largest full circle in the acrylic square cross section. Imagine at the bottom the inner part of the acrylic glass to be at T_{BP} and the outer to be at T_E. Then the total heat conducted to the top part (at constant T_{TP}) is (while neglecting heat flux to the side in lateral direction)

$$Q_{side} = \int_{r_i}^{r_o} 2\pi \frac{\Delta T(r)\lambda_{ac}}{H} r \mathrm{d}r = \int_{r_i}^{r_o} 2\pi \frac{\lambda_{ac}}{H} \left(\Delta T + \frac{T_E - T_{BP}}{r_o - r_i}(r - r_i) \right) r \mathrm{d}r. \qquad (4.7)$$

The solution of Q_{side} for our settings agrees with the calibration measurements very well.

Weiss et al. [2016] suggested a critical value for $1/Ro$ for the onset of heat transport enhancement due to rotation that depends on the Prandtl number with $1/Ro_c = K_1 Pr^{\alpha}$, where $\alpha = -0.41$, $K_1 = 0.75$. The expected values for this are shown in fig. 4.8. Even

though we have no measurements at sufficiently small $1/Ro$ for a quantitative comparison to the suggested $1/Ro_c$, our data are consistent with these predictions. The same study found the rotation rate for the maximum heat transport enhancement to depend on Pr and Ra, as $1/Ro_{max} = N_{Ro} Pr^{\epsilon_1} Ra^{\epsilon_2}$, with $\epsilon_1 = 1.37$, $\epsilon_2 = -0.18$, $N_{Ro} = 21.4$. This leads for our measurements to $1/Ro_{max}(Pr = 6.55) = 6.74$, $1/Ro_{max}(Pr = 12) = 16.7$ and $1/Ro_{max}(Pr = 76) = 224$. These values mark the onset of the rotation-dominated regime and are shown as dashed vertical lines in fig. 4.8. We see that we have just entered the rotation-dominated regime for $Pr = 6.55$ and maybe for $Pr = 12$, but are still away from it for the largest $Pr = 76$. For that case, $1/Ro_c$ is actually outside of the shown $1/Ro$-range.

These rather crude Nu measurements are not very precise and just serve as a sanity-check for the setup. Nevertheless, we observe behaviours in agreement with previous studies, i.e. a heat transport enhancement at moderate $1/Ro$.

4.1.4 Correcting deviations in the vertical alignment

Due to imperfect vertical alignment in early measurements, we observed a small periodic movement in the camera images under rotation. The shift was small, i.e. approx. 1 mm, but noticeable in the resulting image and would have led to faulty velocity measurements. In order to correct for this movement and to improve spatial resolution, we did the following (compare fig. 4.9):

1. We define a circle with a large radius that includes the entire circular interrogation area. This radius is decreased by one pixel step by step, each time the position is updated such that the sum of brightness in the image is at maximum within the circle. If the radius of the fitted circle becomes smaller than that of the interrogation area r_{circ}, the sum of brightness decreases sharply.

2. The radius r_{circ} within one run remains constant and for every image in the data set, the position of the circle is fitted to the interrogation area by again maximising the sum of brightness within. It is written out and the image is cropped to just contain the interrogation area. Between different data sets, r_{circ} is expected to remain constant since the camera and the interrogation area were fixed. Still, it could vary by a pixel or two due to changes in the setup.

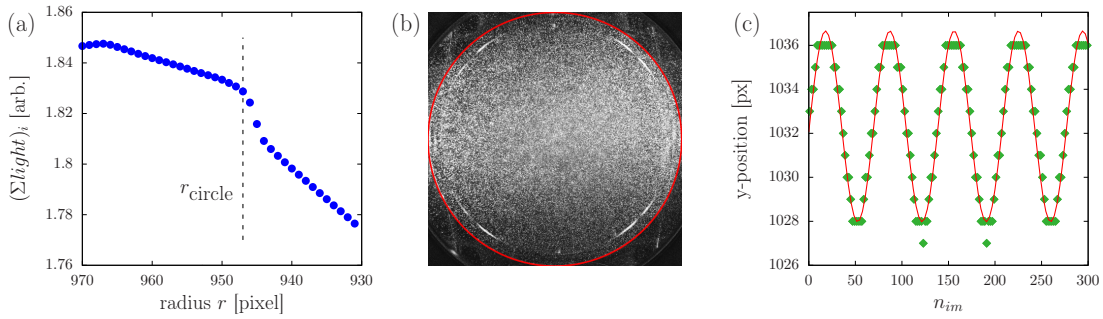

Figure 4.9: Example for the correction of the moving position of the interrogation area. (a) Maximized sum of brightness (y-axis) within a circle of radius r (x-axis). (b) Example of a cropped image with the interrogation area, which is highlighted with a red circle at its boundary. Note that the image is altered to highlight the features. (c) y-component of the interrogation area (green bullets) with a fitted sinus curve in red as function of image number.

3. The position of the circle describes a sinusoidal movement, which can be fitted with four fitting parameters a_i: $a_0 + a_1 \times \sin(a_2 \times n_{im} + a_3)$ for both x and y directions. After the PIV evalutation, the velocities u_x, u_y are corrected by the shift velocity as the derivative of the position function. This assumes the precession is small enough that any radial accelerations are negligible.

4.2 The velocity field in the horizontal layer at mid-height

From two consecutive images we can now obtain instantaneous velocity fields in two dimensions through PIV, where we focus on the x, y plane at half height $z = H/2$ (compare fig. 4.1). The horizontal velocity in cartesian coordinates (u_x, u_y) is first transformed into polar coordinates $u_r = u_x \cos(\phi) + u_y \sin(\phi)$ and $u_\phi = -u_x \sin(\phi) + u_y \cos(\phi)$. Here, r is the radial distance from the cell center and ϕ the polar angle. To give some impression of the resulting velocity, an example of such a snapshot is given in fig. 4.10 for $Ra = 9.8 \times 10^8, Ek = 5.4 \times 10^{-5}, Pr = 6.55$. There, we show the measured radial velocity u_r and azimuthal velocity u_ϕ in physical units, as well as the vorticity ω, which is defined as the curl of the velocity vector $\boldsymbol{u}$:

$$\omega = \nabla \times \boldsymbol{u}.$$

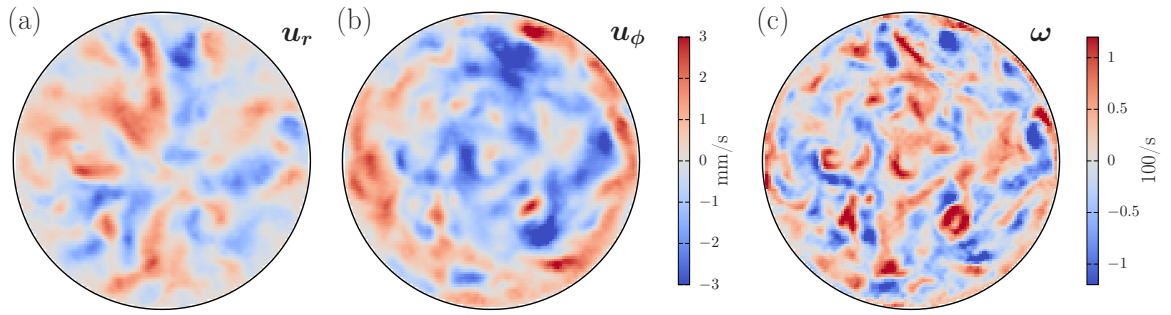

Figure 4.10: Snapshot of the velocity field for $Ra = 9.8 \times 10^8, Ek = 5.4 \times 10^{-5}, Pr = 6.55$. (a) radial velocity u_r, (b) azimuthal velocity u_ϕ, (c) resulting vorticity ω.

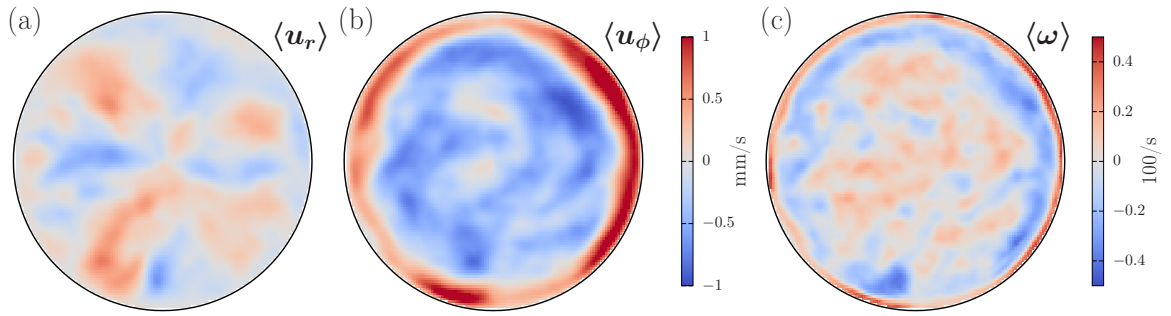

Figure 4.11: Averaged velocity fields $\langle u_r \rangle$ (a), $\langle u_\phi \rangle$ (b) and vorticity $\langle \omega \rangle$ (c) for $Ra = 9.8 \times 10^8, Ek = 5.4 \times 10^{-5}, Pr = 6.55$.

For a quantisized velocity field $\boldsymbol{u} = (u_x, u_y)^T$ in (x, y) direction, vorticity is calculated for every grid point k, l via the Jacobi matrix

$$J = \begin{bmatrix} \partial_x u_x & \partial_y u_x \\ \partial_x u_y & \partial_y u_y \end{bmatrix} = \begin{bmatrix} (u_{x,k} - u_{x,k+1})/dx & (u_{x,l} - u_{x,l+1})/dy \\ (u_{y,k} - u_{y,k+1})/dx & (u_{y,k} - u_{y,k+1})/dy \end{bmatrix}, \tag{4.8}$$

where $dx = dy$ denotes the spatial size of the grid points. For the two-dimensional velocity field, vorticity then becomes $\omega = (0, 0, \partial_x u_y - \partial_y u_x)^T = J_{21} - J_{12}$. In the snapshots, we find a rather unordered distribution of velocities and vorticity. In the latter case, regions with high vorticity can be regarded as cyclones ($\omega > 0$) or anti-cyclones ($\omega < 0$).

For our analysis, we are most interested in the time-averaged quantities of $\boldsymbol{u}$ and ω. Therefore, temporal averaging over the whole experimental time yields the field for $\langle u_r \rangle$, $\langle u_\phi \rangle$ and $\langle \omega \rangle$ (fig. 4.11).

4.3 The BZF as function of *Ra*, *Ek*, *Pr*

One of the major goals with this optical experiment was the investigation of the development of the boundary zonal flow (BZF) with rotation and Ra. We wrote the results and comparison with previous findings into a publication, which is published in *Journal of Fluid Mechanics* (Wedi et al. [2022]) and inserted in the following sections. The notation and the figures were changed where needed to be consistent with the sections above.

4.3.1 Radial velocity profile

We show in fig. 4.12(a-d) time averaged azimuthal velocity fields $\langle u_\phi(r,\phi)\rangle_t$ for different Ek. One can see how the structure of the flow changes qualitatively. In the non-rotating case ($Ek = \infty$), the flow field does not show a clear difference between the radial center and the regions close to the sidewall. Instead, the distribution of the red ($\langle u_\phi\rangle_t > 0$) and blue ($\langle u_\phi\rangle_t < 0$) is orderless. In fact one would expect in this case that due to the turbulent motion, the time averaged azimuthal velocity to be very small. This is, however, not the case, since there is a rather persistent large scale motion, i.e., the LSC, which is steady over the time duration of our measurement. Under rotation (fig. 4.12b-d), the characteristic features of the BZF become clearly visible, namely a red ring ($\langle u_\phi\rangle_t > 0$) surrounding a blue ($\langle u_\phi\rangle_t < 0$) central region. It can be observed that with increasing rotation rates, the width of the red cyclonic zone decreases as well as the strength of the flow.

For a more quantitative analysis, we average the velocity in azimuthal direction. For this, we sum over all velocity vectors at radial distances between r and $r+dr$ away from the center, and divide this sum by the number of voxels in this range (N_r)

$$\langle u_\phi\rangle(r) = \frac{1}{N_r}\sum_{r}^{r+dr}\langle u_\phi\rangle_t.$$

As an example, we show in fig. 4.12e $\langle u_\phi\rangle$ calculated from the field in fig. 4.12c. The red points show the calculated velocities. The blue line is a polynomial fit of degree 10 to these points that allows quantitative analysis. We also show for comparison, in the inset of fig. 4.12e, results from simulations at very similar Ra and Ro but smaller $Pr = 0.8$ (Zhang et al. [2021]). At first glance, our radial profile of $\langle u_\phi\rangle$ looks qualitatively very similar to the results from DNS. But on a closer look, quantitative differences become visible. The most obvious is the width of the BZF, i.e., the distance δ_0 from the wall,

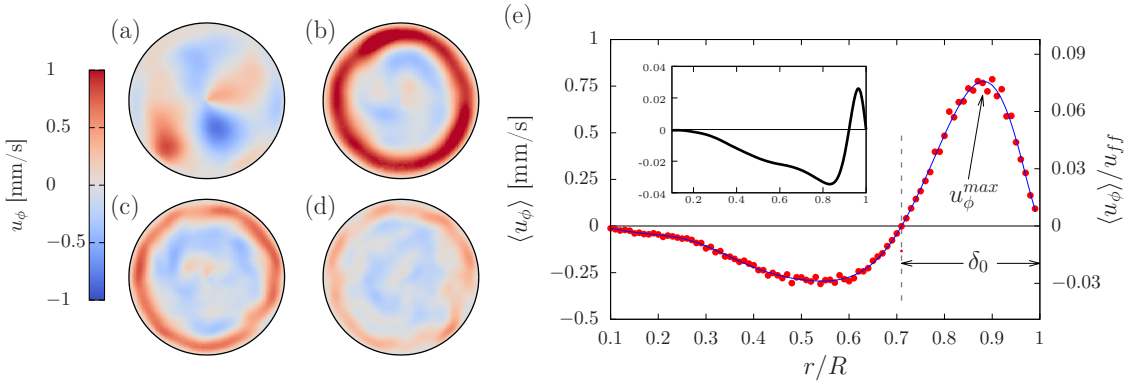

Figure 4.12: (a-d) Time averaged u_ϕ measured at midheight for $Ra = 4 \times 10^8$, $Pr \approx 76$, and $Ek = \infty$ (a), $Ek = 6.2 \times 10^{-4}$ (b), $Ek = 1.5 \times 10^{-4}$ (c), and $Ek = 1.0 \times 10^{-4}$ (d). (e): Red bullets show the azimuthal average of (c) in physical units (left y-axis) and normalized by the free-fall time (right y-axis). Blue solid line is a fit of a high-order polynomial. The dashed vertical line marks the BZF thickness δ_0, at which $\langle u_\phi \rangle$ crosses 0, the arrow points to the maximum velocity $u_\phi^{\max}$ within the BZF. The inset shows results from DNS of the azimuthal velocity normalized by the free-fall velocity $\langle u_\phi \rangle / u_{ff}$ for $Ra = 10^8, 1/Ro = 10, Pr = 0.8$.

where $\langle u_\phi \rangle$ switches sign, is much smaller in the DNS than in our case. This discrepancy is most likely due to the difference in Ek (1.8×10^{-5} compared to 1.5×10^{-4} for our measurement). While DNS was conducted within the rotation-dominated regime, our measurements were acquired in the rotation-affected regime. Even though Pr is different between DNS and our simulation by a factor of 10, from Zhang et al. [2021] we expect no, or only a very small Pr dependency of δ_0 in the investigated Pr-range.

In the following, we will analyse some features of the radial profile as functions of the dimensionless control parameters. One of these features is the radial position r_0, where $\langle u_\phi \rangle$ switches sign, i.e. where the BZF and the bulk flow separate. To be in agreement with previous publications (Zhang et al. [2020, 2021]), we define the width of the BZF as $\delta_0 = (R - r_0)/R$.

Figure 4.13 shows various time- and azimuthally-averaged velocity profiles for different control parameters. To compare with DNS, the velocity profiles are normalized by the free-fall velocity $u_{ff} = \sqrt{\alpha g H \Delta}$. In fig. 4.13(a and c), Ra was kept constant and Ek was changed. The azimuthal velocity amplitude inside the BZF decreases with increasing rotation rate (decreasing Ek). This decrease with decreasing Ek is by no means obvious. On one hand, we know that increasing rotation suppresses fluid motion, hence a reduced velocity is expected. While this is certainly true for sufficiently fast rotation rates, for moderate rotation rates and Pr discussed here, the heat flux (Nu) is

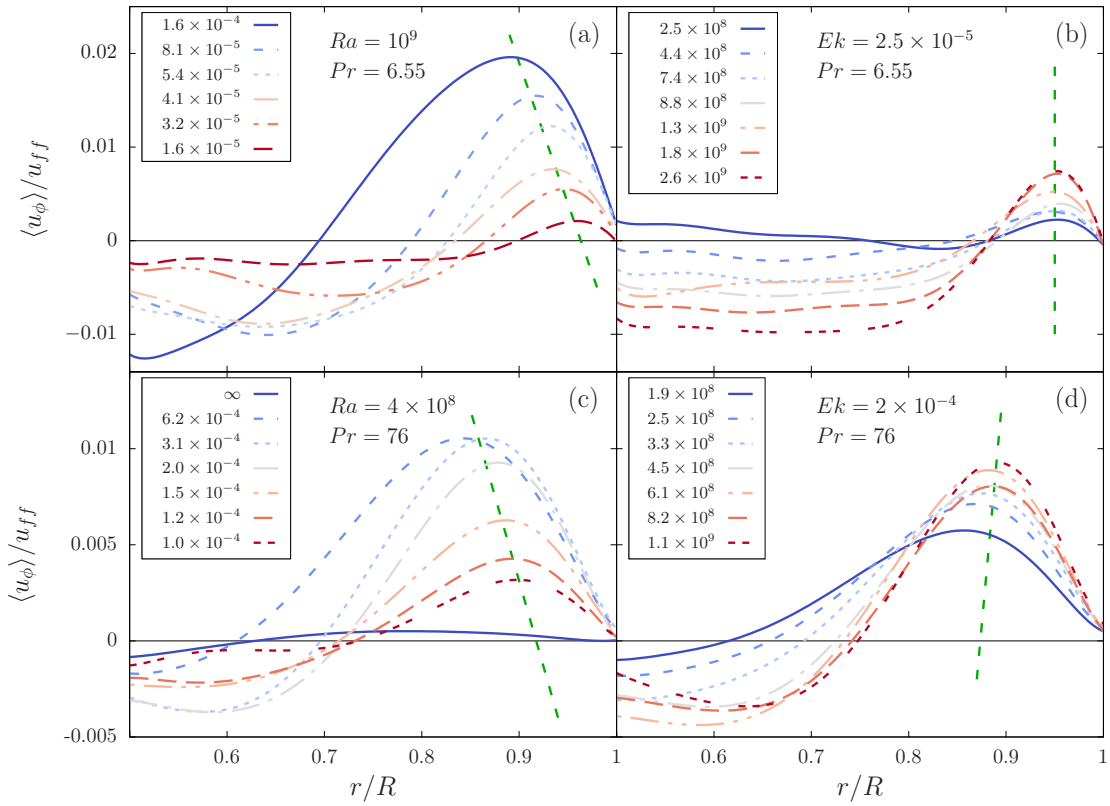

Figure 4.13: Radial profiles of $\langle u_\phi \rangle$ for $Ra = const$ and changing Ek (a and c) and changing Ra at $Ek = const$ (b and d) as in the legends, respectively. (a and b) are $Pr = 6.55$, (c and d) $Pr = 76$. Green dashed lines are guides to the eye and connect the velocity maxima inside the BZF measuring $\delta_{u_\phi^{\max}}$ (see also fig. 4.16).

enhanced, which suggests at least a faster flow in the z-direction. Also note that the rate with which potential energy is converted into kinetic energy, and finally dissipated into heat, is proportional to Nu i.e. $\epsilon_u = (\nu^3/H^4)(Nu-1)RaPr^{-2}$. Therefore, the total kinetic energy in the fluid is expected to increase with increased rotation rates first.

The fact that we nevertheless see a decrease here for all rotation rates might be because the additional kinetic energy is contributing mostly to vertical velocity. In addition, the width of the BZF becomes smaller, hence also viscous drag would lead to a further reduction of the maximal azimuthal velocity inside the BZF.

In fig. 4.13(b and d), Ek is kept constant and plots are shown for different Ra. The maximal velocities increase with increasing Ra, which can be explained with the enhanced thermal driving. However, we want to remind the reader that here, we show the azimuthal velocity normalized by the free-fall velocity $u_{ff} = \sqrt{g\alpha\Delta H} = Ra^{1/2}(\nu\kappa)^{1/2}/H$. In fact, the Reynolds number $Re = UH/\nu$, and hence also the typical velocity scale U in non-rotating RBC, scales as $Re \sim Ra^{\zeta}$ with ζ determined experimentally to be in the range $\zeta \approx 0.42 \ldots 0.5$, (see e.g., Sun and Xia [2005], Brown et al. [2007]), which would lead to $U/u_{ff} \propto Ra^{-0.08\ldots0}$, i.e. a decrease with increasing Ra. Hence the azimuthal velocity in the BZF increases significantly faster with Ra than for non-rotating RBC.

In the following, we will analyse these profiles quantitatively. Most importantly, we look at the width δ_0, as well as the maximal velocity u_ϕ^{max} and its location δ_{max}, as functions of the control parameters Ek, Ra, and Pr.

4.3.2 BZF width δ_0

We begin by calculating the zero-crossing and hence the thickness δ_0 as function of the rotation rate. These results are presented in fig. 4.14. In fig. 4.14a, we show δ_0 as a function of $1/Ro$ for three different Ra. Note that here we have chosen to plot $1/Ro$ on the x-axis, because as was shown in previous studies, different features of the heat transport seem to depend predominantly on $1/Ro$ and depend only weakly on Ra, such as the onset of heat transport enhancement in large Pr fluids (Weiss et al. [2016]) or the decrease of Nu in small Pr fluids (Wedi et al. [2021]).

We see in fig. 4.14a that δ_0 decreases with increasing $1/Ro$ for all three datasets. We have seen in fig. 4.4b that our data are in the rotation-affected but not in the rotation-dominated regime, and that we are particularly far from the geostrophic regime for Pr=76. Also considering the trend of the green data points, we decide to set a somehow arbitrary threshold for the rotation rate which is $1/Ro_t = 1$ for Pr=6.55 and Pr= 12.0

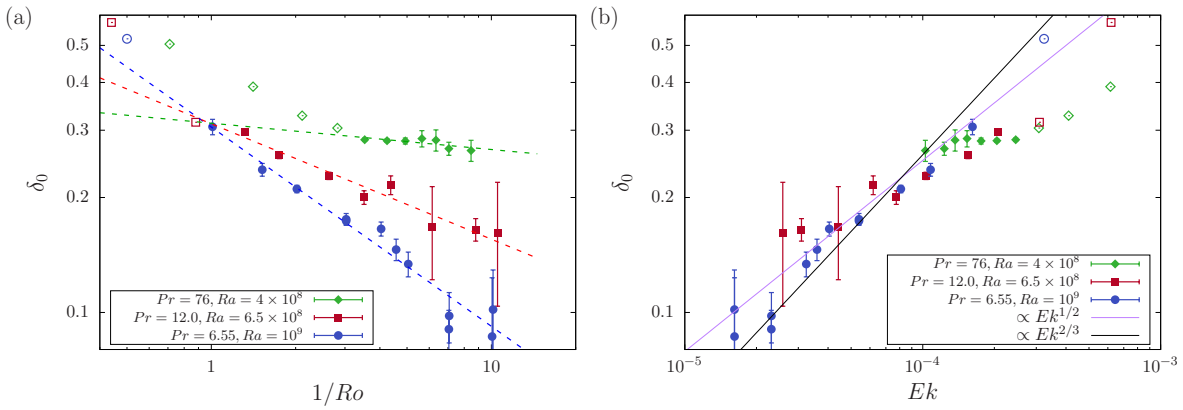

Figure 4.14: BZF width δ_0 as function of the rotation rate for datasets E1 (blue circles, E2 (red squares) and E3 (green diamonds). Open symbols mark data with $1/Ro < 1/Ro_c$. Closed symbols mark data with $1/Ro \geq 1/Ro_c$ (see text for further information). The error bars were estimated from the scatter of the data points around the fitted polynomial close to δ_0. Panel (a) shows δ_0 as a function of $1/Ro$ on a log-log plot. The dashed lines are power-law fits to the solid symbols ($1/Ro \geq 1/Ro_c$). Panel (b) shows the same data plotted against Ek. The black line is a power law $\propto Ek^{2/3}$ as suggested by Zhang et al. [2021]. The purple line is power law with $\propto Ek^{1/2}$.

and $1/Ro_t = 3$ for Pr=76. In the following, we will mark data points at small and larger $1/Ro \geq 1/Ro_t$ with open and closed symbols, respectively, and will use only the closed symbols for scaling analysis. While this decision is somewhat arbitrary, we will see below that solid symbols often follow certain scaling relations from which the open symbols diverge. Now we fit power laws of the form $\delta_0 \sim (1/Ro)^{-\alpha}$ to the data for which $1/Ro \geq 1/Ro_t$ (solid symbols in fig. 4.14).

The resulting power laws are shown as dashed lines in fig. 4.14a and have exponents $\alpha_{6.55} = 0.52 \pm 0.03$, $\alpha_{12} = 0.30 \pm 0.02$, $\alpha_{76} = 0.07 \pm 0.03$ with the subscript being Pr. At first glance, these three different power laws suggest that the exponent α is itself dependent on Ra and/or Pr and that no simple scaling law of the form

$$\delta_0 = AEk^{\alpha} Ra^{\beta} Pr^{\gamma} = 2^{\alpha} A \cdot Ro^{\alpha} Ra^{\beta-\alpha/2} Pr^{\gamma+\alpha/2}, \tag{4.9}$$

can be found, even though such simple scalings have been suggested recently based on numerical simulations (Zhang et al. [2021]), namely (for $Pr > 1$):

$$\delta_0 \propto \Gamma^0 Pr^0 Ra^{1/4} Ek^{2/3}. \tag{4.10}$$

For comparison with data from simulations, we plot in fig. 4.14b the same measured data but now as function of their respective Ek. Now the data for very different Ra and

Pr overlap surprisingly well, for a given Ek. The black solid line in fig. 4.14b is $\propto Ek^{2/3}$ as found in simulations by Zhang et al. [2021], but is ignoring the Ra-dependency. We also show by a purple line a scaling $\propto Ek^{1/2}$ for comparison. Here, our data seem to agree better with the purple line ($\propto Ek^{1/2}$), in particular for larger Ek. However, we also note that the data scatter significantly and have rather large error bars, in particular for small Ek, where the influence of buoyancy is small. Deviations from either power law mostly occur for larger Ek, where also the buoyancy becomes more important. A firm conclusion on which exponent represents the data better cannot be drawn from these data.

Clearly, there is either a simple power-law relation as in eq. 4.9, or something more complicated as fig. 4.14a suggests. In the case of a simple power-law relation (as in eq. 4.9), we can at least state from fig. 4.14b that δ_0 might depend predominantly on Ek, but is otherwise at most very weakly dependent on Ra and Pr, at least in the range of our investigation.

Observations from DNS (eq. 4.10) indeed suggest an independence from Pr, but also found a Ra-dependency $\delta_0 \propto Ra^{1/4}$. Let us have a closer look what our data have to say. Figure 4.15a shows δ_0 as function of Ra for three different Pr and different but constant Ek. While the data with $Pr = 76$ (largest Ek) suggest a scaling of the BZF width $\delta_0 \sim Ra^{\beta}$ with $\beta = -0.19 \pm 0.01$, for smaller Pr (and also smaller Ek), δ_0 seems to be unaffected by Ra, i.e., $\beta \approx 0$. As before, the error bars are estimates from the scatter of the velocity data points around the fitted polynomial close to δ_0. Again here, it seems that the exponent β is a function of Pr. Note in particular that for Pr=76, δ_0 decreases with increasing Ra, which is in disagreement with the results of DNS.

In fig. 4.15(b and c) we show δ_0 as function of Pr for constant Ra. Experimentally, Pr was varied by changing either T_m or by changing the concentration of glycerol in the aqueous working fluid. While it is trivial to set the system to the desired Ra by changing Δ accordingly, the rotation rate Ω needed to be adjusted to keep either Ek or Ro constant. We did both.

Let us first have a look at fig. 4.15b, where $1/Ro = 5$. As can be seen, the data are rather noisy and do not increase strictly monotonically with Pr. There is, however, a clear trend that δ_0 increases with increasing Pr, as suggested by the previous measurements. Fitting a power law of the form $\delta_0 \sim Pr^{\gamma_1}$ to the data yields $\gamma_1 = 0.2 \pm 0.05$.

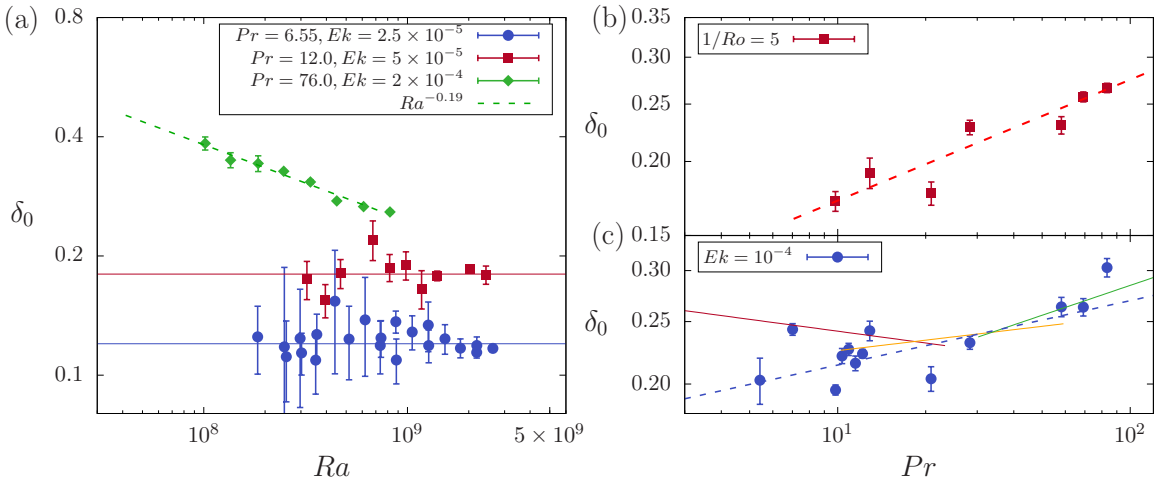

Figure 4.15: (a): Thickness δ_0 as a function of Ra for three different datasets: E1 (Pr=6.55, Ek=2.5 $\times$ 10^{-5}, blue circles), E2 (Pr=12.0, Ek=5 $\times$ 10^{-5}, red squares) and E3 (Pr=76, Ek=2 $\times$ 10^{-4}, green diamonds). The error bars were estimated from the scatter of the data points around the fitted polynomial close to δ_0. The green dashed line is a power law with exponent $\gamma = -0.19 \pm 0.01$. The red and blue horizontal lines are constants with $\delta_0 = 0.18$ and 0.12. (b): δ_0 as function of Pr for $Ra = 6 \times 10^8$ and $1/Ro = 5$ (dataset P2). The red dashed line is a power-law fit with $\sim Pr^{0.20\pm0.05}$. (c): δ_0 as function of Pr for $Ra = 6 \times 10^8$ and $Ek = 10^{-4}$ (dataset P1). The red, orange and green lines are functions $A_1 Pr^\gamma$ with the values listed in table 4. The dashed blue line marks a power law $\propto Pr^{0.1}$.

We show in fig. 4.15c values of δ_0 that were acquired at constant Ra, constant Ek and varying Pr. The data scatter significantly and no clear trend is obvious. Here, δ_0 looks rather constant for small Pr, and seems to increase for larger Pr. While the red squares in fig. 4.15b and the blue bullets in fig. 4.15c show different datasets, the data are related via eq. 4.9. In particular, we see from eq. 4.9 that $\gamma_1 = \gamma + \alpha/2$.

We assume for a moment that δ_0 can be represented by simple power laws as in eq. 4.9, but that the exponents α, β, and γ are different for the three different Pr-ranges, as observed in fig. 4.14a and fig. 4.15a. We list in table 4 the fitted parameters from fig. 4.14a as well as fig. 4.15(a and b). With this, we can calculate the expected power laws $A_1 Pr^\gamma$, with $A_1 = A Ek^\alpha Ra^\beta$, for all three Pr ranges, which we show in fig. 4.15c as solid lines. Due to the different exponents α for different Pr, we also get different exponents γ, which would explain the somewhat non-monotonic behaviour of the data points in fig. 4.15c. Indeed, the lines represent somehow the non-monotonic behaviours of the data points. Of course, assuming a power law with a varying exponent means that there is no real power law in the investigated range. However, this approach shows that the two different datasets are consistent with each other. We note that one

Table 4: Coefficient and power-law exponent estimates from eq. 4.9. The α values were estimated based on the data in fig. 4.14a. A and β are estimates from fig. 4.15a and γ was estimated from fig. 4.15b.

Pr	A	α	β	$\beta - \alpha/2$	$\gamma + \alpha/2$	A_1	γ
6.55	34.0	0.522	0	-0.261	0.20	0.278	-0.061
12.0	2.93	0.292	0	-0.146	0.20	0.199	0.054
76	15.23	0.092	-0.19	-0.236	0.20	0.140	0.154

could have also fitted a power law through the blue points in fig. 4.15c, resulting in a single exponent $\propto Pr^{0.1\pm0.03}$ (blue dashed line) over the entire range. One could then represent the data in fig. 4.15b with different power laws for different Pr ranges. In any case, we have learned from fig. 4.15c that (i) the Pr dependency is rather small when Ek is kept constant, and (ii) the Ra, Pr and Ek dependencies of δ_0 cannot be written by simple power laws in the parameter range that we are investigating here (i.e. the rotation-affected regime).

So far we have analysed δ_0, the width of the BZF, as it can be measured easily in the time-averaged two-dimensional velocity field shown in fig. 4.12(a-d). However, the strength of the flow, represented by the maximal averaged azimuthal velocity $u_\phi^{\max}$, is another quantity characteristic for the BZF, which can help to reveal the mechanisms leading to this zonal flow. Therefore, we show in fig. 4.16(a and b), the compensated time-averaged maximal velocity $u^*_{max} = u_\phi^{\max} RaPr^{0.8}$, and in fig. 4.16(c and d) its location measured as the distance from the sidewall δ_{max}. These data are plotted against $RaEk$ on the x-axis, as this represents the Rayleigh number compared to its critical value for the onset of wall modes ($Ra_w \propto Ek^{-1}$). We show in fig. 4.16(a and c) data that were acquired at constant Ek for a given Pr and varying Ra, whereas fig. 4.16(b and d) show data with constant Ra and different Ek.

Let us first have a look at the compensated maximal averaged azimuthal velocity $u^*_{\max}$ shown in fig. 4.16a. Note that the definition of $u^*_{\max}$ is not based on scaling arguments, but is rather an empirical relation that provides a very good collapse of data onto a single power law for all three Pr, with each having a different Ek. The black solid line marks $u^*_{\max} = 4.7(EkRa)^{3/2}$ (or equivalently $u_\phi^{\max} = 4.7Ek^{3/2}Ra^{1/2}Pr^{-0.8}$), which represents the data fairly well.

We show the same function as a black line also in fig. 4.16b, but now compare it with

measurements that were acquired at constant Ra but varying Ek. We see that data for small values of $EkRa$ follow this law, but data for large values of $EkRa$ diverge from the straight line. For a better visual separation, data with $1/Ro \geq 1/Ro_t$ were plotted with solid symbols, whereas data for which $1/Ro < 1/Ro_t$ were plotted with open symbols. As mentioned previously, we assumed $1/Ro_t = 1$ for the two smaller Pr and $1/Ro_t = 3$ for Pr=76.

Since data for varying Ra follow the mentioned power law for nearly two decades, we are confident this power law also holds for smaller Ek, at least as long buoyancy plays a significant role. Whether this scaling holds even in the rotation-dominated regime, however, remains unclear.

Figure 4.16(c and d) show the distance from the wall to the maximal velocity δ_{max}, normalized by $\sqrt{Ek}$ and plotted against $EkRa$. Measurements are the same as for fig. 4.16(a and b), which means constant Ek for (c) and constant Ra for (d). We see that the data collapse fairly well on a constant $\delta_{max}/\sqrt{Ek} \approx 10$ or so. The inset in fig. 4.16c shows that data do not collapse on top of each other without this normalization. However, the green data points (Pr=76) seem to decrease slightly for larger $EkRa$, which might hint at the fact that buoyancy becomes too strong compared to Coriolis forces.

In fig. 4.16d the same quantity is plotted but from data where Ra was constant (for a given Pr) and Ek was varied. We again plot with solid symbols data with $1/Ro \geq 1/Ro_t$ and use open symbols for data with $1/Ro < 1/Ro_t$. Clearly, the overlap of data with different Pr is rather good only for sufficiently large $1/Ro$ (solid symbols) and less good for the open symbols.

Data plotted as $\delta_{max}/\sqrt{Ek}$ (see fig. 4.16(c and d)) collapse onto a single flat line, suggesting that $\delta_{max} \propto Ek^{1/2}$ and δ_{max} otherwise independent of Ra and Pr. We have already seen above (fig. 4.14) that a similar scaling might also be visible in the data for δ_0, the thickness of the BZF. In fact, in fig. 4.14b, we have plotted already a purple line marking a power law $\delta_0 \propto Ek^{1/2}$. Now, for a better comparison, we plot in fig. 4.17a both $\delta_{max}/\sqrt{Ek}$ and $\delta_0/\sqrt{Ek}$ as open and solid symbols inside the same graph. Clearly, the scatter of the data for δ_0 is much larger, but both follow straight lines over more than a decade in $EkRa$. However, in both cases, the green data (Pr=76) for the largest

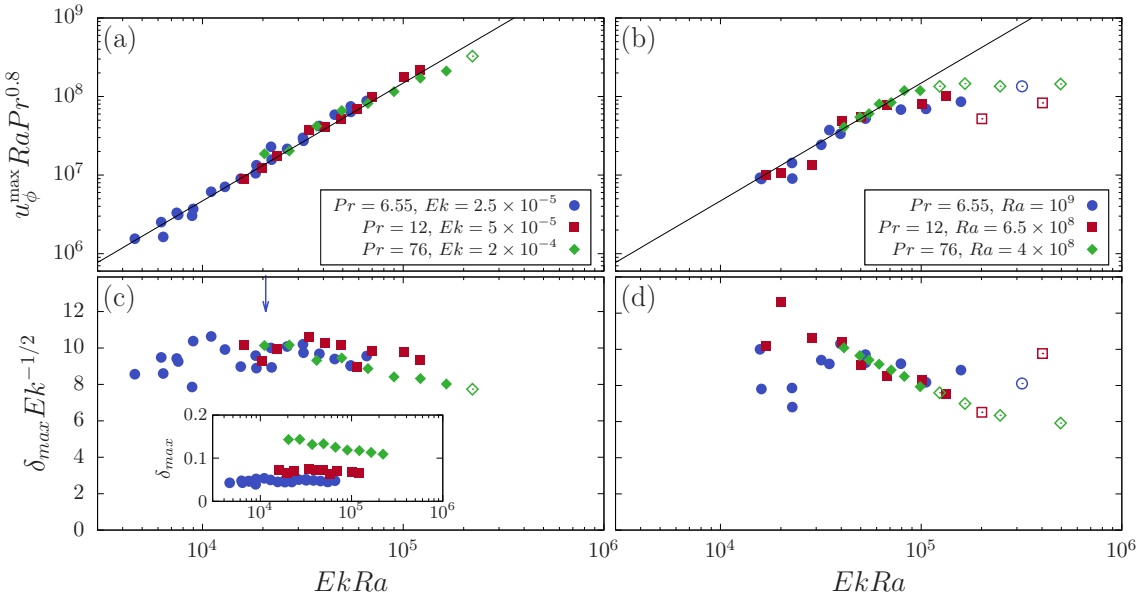

Figure 4.16: (a and b): Compensated maximal averaged azimuthal velocity $u_\phi^{\max} RaPr^{0.8}$ as a function of $EkRa$. (a) Data acquired at constant Ek (datasets E1, E2, E3). (b) Data acquired at constant Ra (datasets R1, R2, R3). The solid black lines in (a) and (b) mark the same power-law $\propto (EkRa)^{3/2}$. (c and d) show the distance between the sidewall and the location of the azimuthal velocity maximum $\delta_{u_\phi^{\max}}$. (c) Datasets E1, E2, E3 with constant Ek. (d) Datasets R1, R2, R3 taken at constant Ra. Open symbols in (b) and (d) mark data with $1/Ro < 1/Ro_t$ (see text). The inset in (c) shows the same data but plotted without the normalization $Ek^{-1/2}$. One sees that the data do not collapse on top of each other. The blue arrow in (c) marks the estimated location of the maximal heat transport for dataset E1.

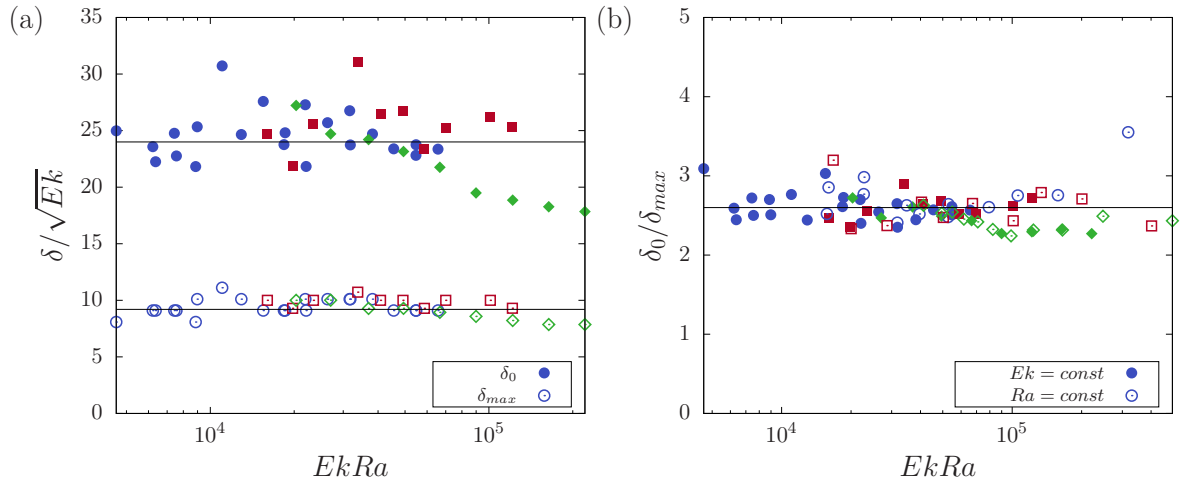

Figure 4.17: (a): Normalized length scales $\delta_0/\sqrt{Ek}$ (closed symbols) and $\delta_{max}/\sqrt{Ek}$ (open symbols) as function of $EkRa$. Note that data are presented for datasets E1, E2 and E3, where in fact only Ra was varied. The straight black lines mark $\delta_0/\sqrt{Ek} = 24.0$ and $\delta_{max}/\sqrt{Ek} = 9.2$. (b): Ratio δ_0/δ_{max} as function of $EkRa$. Here, the open (closed) symbols are datasets with constant (varying) Ra and varying (constant) Ek. The different colours denote the different Prandtl numbers Pr=6.55 (blue circles), 12 (red squares), 76 (green diamonds). Straight black line marks $\delta_0/\delta_{max} = 2.6$.

$EkRa$ clearly decrease.

Figure 4.17b shows the ratio δ_0/δ_{max} as a function of $EkRa$. For this we have used all available data and show data with constant Ek as open symbols, and data with constant Ra as solid symbols. The colour marks Pr. It becomes evident that the ratio $\delta_0/\delta_{max} \approx 2.6$ is a constant, therefore both δ_0 and δ_{max} should exhibit the same scaling relations with the control parameters. However, we note that due to the rather large scattering of the data, small differences in the scaling exponents cannot be ruled out.

4.3.3 Discussion of the BZF measurements in the velocity field

Here, we have presented measurements of the horizontal velocity at midheight in a rotating Rayleigh-Bénard cell of aspect ratio $\Gamma = 1$ for various Ra, Ek, and Pr using planar PIV. In these measurements we could observe the boundary zonal flow (BZF) for the first time in an experiment, as a ring with positive average azimuthal velocity $\langle u_\phi \rangle > 0$ (cyclonic motion) surrounding a central region with $\langle u_\phi \rangle < 0$ (anticyclonic motion) as reported in Zhang et al. [2020, 2021].

We studied the thickness of this zone (δ_0) as function of Ek, Ra, and Pr. Inter-

pretation of the measured data is a somewhat difficult task, because on the one hand, the available parameter ranges cover no more than a decade, but also because we cover mainly small rotation rates, where the system is in the rotation affected-regime, where buoyancy is of similar magnitude as Coriolis forces. Hence it is unclear, whether simple scaling laws are even expected in this regime and whether they will hold also in the rotation dominated (geostrophic) regime.

For example, for sufficiently large rotation rates (i.e., $1/Ro > 1/Ro_t$), δ_0 seems to follow $\propto 1/Ro^{\alpha}$, with $\alpha(Pr)$ being a function of Pr. While such a relation is possible (see e.g., Grossmann and Lohse [2000, 2001]), finding the correct function $\alpha(Pr)$ is a difficult task for which many more data points over a much larger range need to be acquired to get reliable results.

Furthermore, we know that the rotation-affected as well as the rotation-dominated regime consist of smaller sub-regimes with transitions between them, as has been observed in measurements of the vertical heat flux (see e.g., Zhong and Ahlers [2010], Wei et al. [2015]) and the flow configuration in the bulk (e.g., Stellmach et al. [2014], Plumley et al. [2016]). In which way these regimes affect properties of the BZF is currently unclear.

While it is somehow expected that transitions in the bulk from one regime to another also change how the BZF properties depend on Ra, Ek, and Pr, it is also possible that the BZF is decoupled from the dynamics in the bulk for sufficiently large rotation rates. As a result, scaling relations of its properties could hold in both, the rotation-affected and the rotation-dominated regimes. In this context, we want to remind the reader that data for Pr=6.55 (datasets E1 and R1) cover not only parameter ranges, where a heat transport enhancement has been observed, but also ranges where a heat transport reduction is expected (see Zhong and Ahlers [2010], Weiss et al. [2016]). In fact, the location of maximal heat transport enhancement for dataset E1 is marked with a blue arrow in fig. 4.16c. The trends of both u_{ϕ}^{max} and δ_{max} do not show significant differences at the left (Nu reduction) and the right (Nu enhancement) of this arrow.

Under the assumption of a simple power-law relationship of the form $\delta_0 \propto Ek^{\alpha} Ra^{\beta} Pr^{\gamma}$, our data suggest $\beta \approx 0$ or close by. In fact, only for the largest Pr=76, do we find a slight decrease of δ_0 with increasing Ra, which might be due to insufficient rotation

rates. This exponent is in contrast to $\beta = 1/4$, as found in numerical simulations by Zhang et al. [2021]. The exponent γ is around zero, or at least very small, which is in agreement with the scaling found in DNS, at least in the same Pr-range (Zhang et al. [2021]).

Regarding the Ek scaling, our data suggest $\alpha \approx 1/2$, again in contrast to DNS (Zhang et al. [2021]), where $\alpha = 2/3$ was suggested. A possible explanation for the difference between DNS and our experiment is the different parameter ranges. In fact, Zhang et al. [2021] report results for $Pr > 1$ only for cylinders of aspect ratio $\Gamma = 1/2$. However, probably more important for the datasets of comparable Pr is that Ek in DNS is at least an order of magnitude smaller, and therefore, Coriolis forces are much stronger compared to buoyancy in the simulation. It is indeed possible that the scaling relations that we find change for faster rotation and converge towards the findings in DNS.

In this respect, we note that in DNS, different scaling relations were found for δ_0 and δ_{max}, i.e., the distance from the sidewall at which the averaged azimuthal velocity is maximal. Here we find that both scale similarly $\propto Ek^{1/2}$. The maximal azimuthal velocity itself is found in our measurements to scale as $u_\phi^{max} \propto Ek^{3/2} Ra^{1/2} Pr^{-0.8}$. It is interesting that both δ_{max} and δ_0 are independent of Ra, but u_ϕ^{max} is not, suggesting that different mechanisms play a role here. In particular the width is not just a result of a self-adjusting wall shear stress. Note in this respect that in this system $EkRa$ represents the amount of thermal driving, compared to the minimal buoyancy that is necessary to initiate wall modes. On the other hand, δ_{max} and δ_0 are self-adjusting purely by Coriolis forces. To investigate this problem further, more measurements and simulations are necessary that indeed cover the entire range from the onset of wall modes up to the buoyancy-dominated regime.

4.4 On Stewartson layers

We also consider the time-averaged radial velocity $\langle u_r \rangle$ and see how it changes as function of the input parameters Ra, Ek, and Pr. In fig. 4.18 we find some qualitative examples for $Pr = 6.55$ and changing Ek at $Ra = const = 10^9$ (a, b). The colourscale is the same for all cases, i.e. by its saturation we clearly see that the average radial velocity decreases with applied rotation when compared to the non-rotating case. Contrary, in fig. 4.18(c, d) we show a fixed rotation rate $Ek = 2.5 \times 10^{-5}$, but increasing Ra from

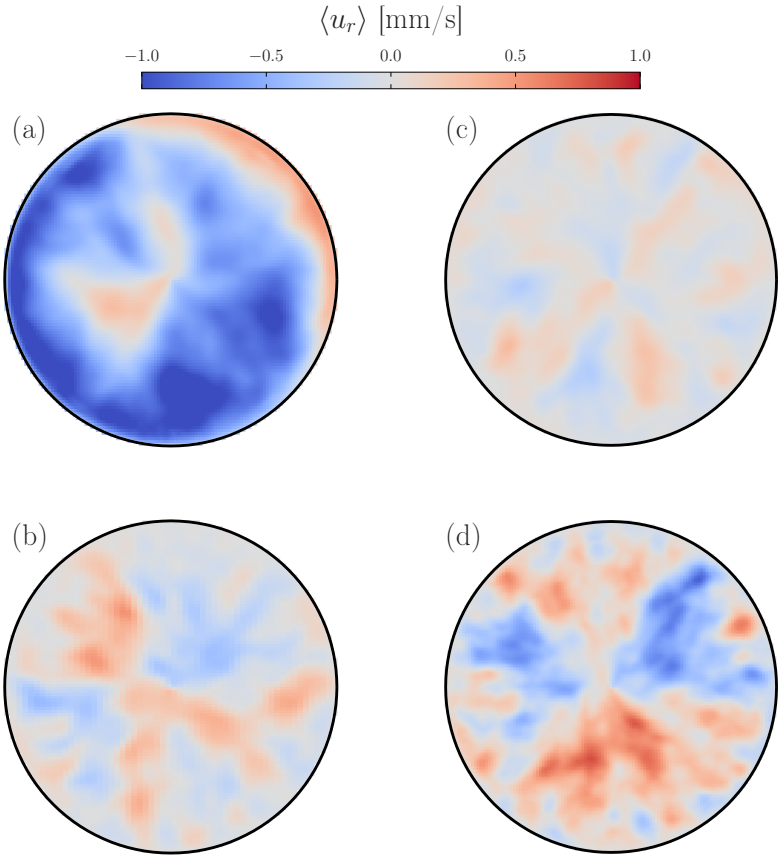

Figure 4.18: Averaged radial velocity fields $\langle u_r \rangle$ for $Ra = 10^9$ (a, b), where Ek decreases from top to bottom: $Ek = \infty$ (a), $Ek = 3.2 \times 10^{-5}$ (b). (c, d) shows $Ek = 2.5 \times 10^{-5}$, $Ra = 1.8 \times 10^8$ (c), $Ra = 2.6 \times 10^9$ (d). Prandtl number was kept at 6.55 for all cases.

top to bottom. As one would expect, larger Ra leads to higher velocity and therefore also to higher $\langle u_r \rangle$ due to the higher kinetic energy put into the system via the heating at the bottom plate. For a perfectly leveled system we expect the averaged distribution to be symmetric in azimuthal direction for the rotating case, the left-over asymmetry therefore should be remains from insufficient averaging.

From $\langle u_r \rangle$ we derive radial profiles of the radial velocity by averaging azimuthally as seen in fig. 4.19. These profiles, although somewhat erratic at $Pr = 6.55$, fig. 4.19(a and b), help to understand the dynamics in the flow at $z = H/2$. Close to the wall we mostly (low Pr) or consistently (high Pr) see $\langle u_r \rangle < 0$, i.e. an inflow of fluid from the side towards the bulk flow at half-height. For constant Ra (fig. 4.19(a, c, e)), we observe a decrease of $\langle u_r \rangle$ with increasing Ω (decreasing Ek). With higher Ra one expects an overall higher velocity in the system and therefore larger $\langle u_r \rangle$. This we observe

in fig. 4.19(d, f), at least for the higher Prandtl numbers, whereas data for $Pr = 6.55$ fluctuate quite strongly and we can not confirm the assumed increased velocities there. Comparing this to the averaged azimuthal velocity, fig. 4.13, we notice a similar decrease in u_ϕ with Ra and Ek. The location of the maxima moves towards higher radial locations r/R with decreased Ek and increased Ra for both, $\langle u_r \rangle$ and $\langle u_\phi \rangle$.

According to Greenspan and Howard [1963] this is due to the upwards-directed flow within the Stewartson layer, which leads to an internal recirculation of the fluid from the sidewall into the bulk. Coriolis force transforms this into an azimuthal velocity u_ϕ. Thus, with higher inflow velocity u_r, the resulting $|u_\phi|$ increases. Qualitatively this picture agrees with our observed radial and azimuthal velocities. The Stewartson layer thicknesses $\delta_{St} = Ek^{1/4}$ and $\delta_{St2} = Ek^{1/3}$ (Stewartson [1957]) are shown as dashed lines in fig. 4.19, where we find the majority of $\langle u_r \rangle < 0$ to be within $r/R > \delta_{St}$. Kunnen et al. [2011] conducted similar measurements on the velocity profiles in a $\Gamma = 1$ cell, and found for fast rotation a negligible averaged radial velocity. While the azimuthal velocity is about one order of magnitude larger than the radial velocity ($\langle u_\phi \rangle = \mathcal{O}(10^{-2} u_{ff})$ compared to $\langle u_r \rangle = \mathcal{O}(10^{-3} u_{ff})$) in our data, we clearly find the radial inwards directed flow also for larger rotation rates at $Pr \geq 12$. However, the study in Kunnen et al. [2011] only regarded $Pr = 6.4$ measurements. Looking at our data for the low Prandtl numbers, we find for fast rotation rates (fig. 4.19a), that there $\langle u_r \rangle \approx 0$ for all r/R.

To fully understand how the Stewartson layers interact with the radial and azimuthal velocity and its dependence on Pr, we would need to measure also the vertical velocity u_z. This was not performed in the present thesis. Note that in the study of the BZF, Zhang et al. [2021] performed DNS at various control parameters, finding that the Stewartson layers and the BZF despite their different thickness scaling $\delta_0 \sim Ra^{1/4} Ek^{2/3}$ and $\delta_{St} \sim Ek^{1/3}$, never cross. The BZF always reaches further into the bulk flow.

4.5 Vortex tracking

Rotating turbulent flows lead to coherent vortex structures, which dynamics are important, e.g. for the heat transport, as seen in Ekman pumping (sec. 2.6). For rapid rotation the flow exhibits steady columns (as seen above in fig. 2.7), which are rather fixed in place. With increased buoyancy, the vortices move around the horizontal plane, influenced by the interaction with neighbouring vortices, as well as with the turbulent

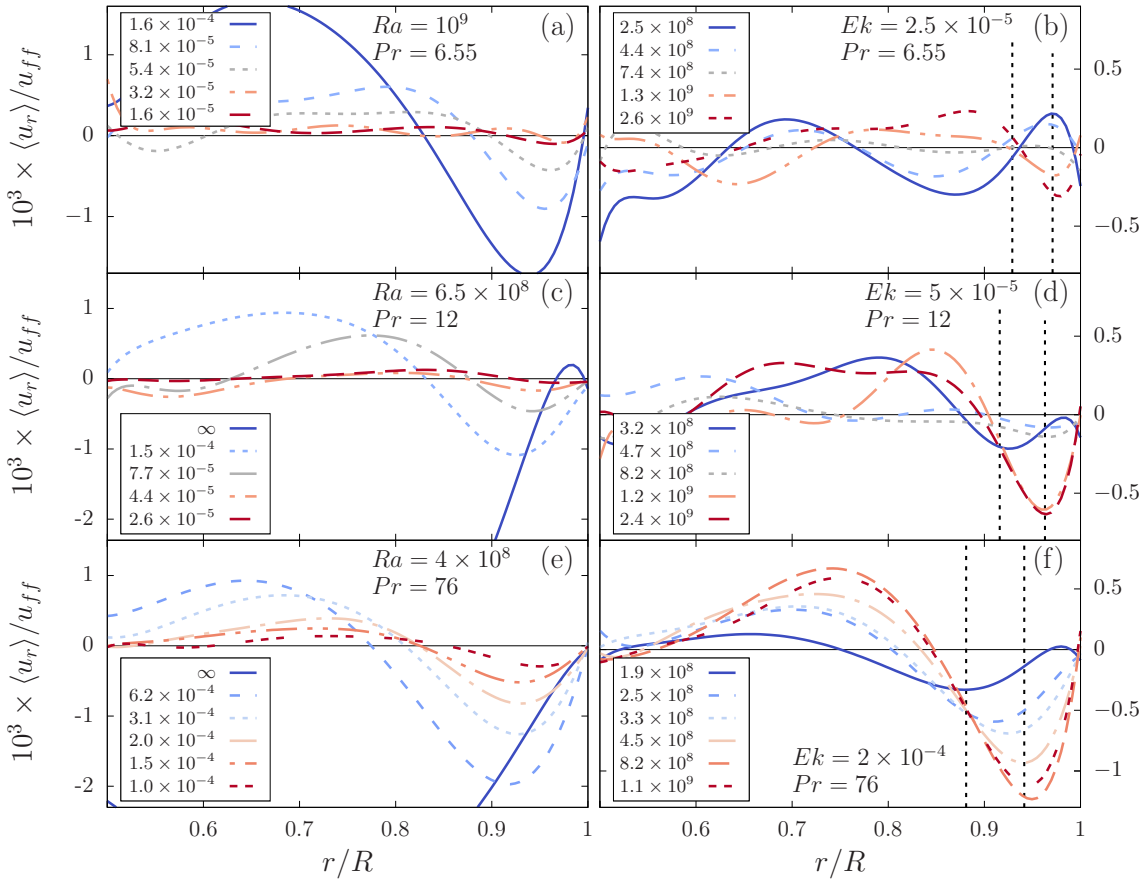

Figure 4.19: Radial profiles of $\langle u_r \rangle$ for $Ra = const$ and changing Ek (a, c, e) and changing Ra at $Ek = const$ (b, d, f) as in the legends, respectively. (a and b) are $Pr = 6.55$, (c and d) $Pr = 12$, (e and f) $Pr = 76$. For the cases with $Ek = const$, dashed vertical lines mark the radial position of the Stewartson layer thicknesses $\delta_{St} = Ek^{1/4}$ and $\delta_{St2} = Ek^{1/3}$.

background. In RBC, the plumes that detach from either top or bottom side are twisted in co-rotating direction. When Ekman pumping/suction occurs, the fluid is pumped in vertical columns towards the opposite side. Close to the opposite plate, the vorticity needs to be counter-rotating for Ekman suction to occur. Hence, the vorticity of such a Taylor column must be changing signs at about mid-height (Vorobieff and Ecke [2002]). For a fluid under OB conditions and not too fast rotation, the dynamics of both cyclones and anti-cyclones are of similar magnitude and motion at mid-height. At large Fr the centrifugal force influences the cold and warm plumes differently, also leading to a different motion for cyclones and anti-cyclones away from mid-height (Ding et al. [2019]). On planetary scales, stable vortices were for example observed on Jupiter around the poles Adriani et al. [2018], where on the north pole eight circumpolar vortices are arranged about one polar vortex. The dynamics of the vortices in our setup will be analysed in the following to try to answer the question how the thermal driving in form of Ra and the strength of rotation (Ek) influences the vortex movement in the horizontal plane.

For this, we first need to identify the vortices from the velocity fields. This can be done in multiple ways, we here only regard a simple vorticity ω threshold, where all areas with $|\omega| > \omega_{thresh}$ are marked as a vortex. Regardless of the selection criterion, all vortices need to be identified and tracked through the image series. Since the objects are not necessarily of good elliptic shape, a shape finding algorithm by fitting an ellipse onto the selection criterion or fitting a two-dimensional Gaussian kernel was disregarded. Instead, selection is done by connecting interrogation windows which fulfil the criterion $\omega > \omega_{thresh}$ as well as some filter criteria. For the image series the steps are performed as following:

1. The threshold ω_{thresh} is applied to the snapshot, returned voxels which obey the criterion are labeled individually, such that connected voxels obtain the same label.

2. To separate connecting vortices, which do not form a single vortex, a watershed algorithm is applied. Areas with an even larger $|\omega| > \omega_{thresh,2}$ are likely to be separated by an area with smaller ω. Based on this, connecting areas are separated.

3. Small fluctuations are filtered out by applying a minimum area threshold to the labeled areas. A shape parameter is introduced, which calculates the extend of the major and minor axis of the area. This is done via a principal components analysis, which calculates the first and second principal components. Their ratio

describes the eccentricity ϵ of the enveloping ellipse, where $1/5 \leq \epsilon \leq 5$ is chosen rather arbitrarly, which showed good results.

4. *Case a*: If close to the position of a found vortex no vortex was present in the previous snapshop, we assume it a newly emerged and store its x and y position and vorticity.
   Case b: If a vortex was already present close to the location with the fitting sign of vorticity, select the one from the list of vortices and update its location to the new x, y position and add the time step τ to its duration.

Let's first look at some exemplary tracks for (random) subsets at $Pr = 76$ and $Ra = 4 \times 10^8$, at both $Ek = 1.2 \times 10^{-3}$ as well as $Ek = 10^{-4}$ in fig. 4.20(a and b). The colour intensity marks the time duration since its first appearance, it starts at the dark colour and disappears at the light side. Cyclones with $\omega > 0$ are shown in red colour and anti-cyclones $\omega < 0$ in blue. Note that these paths are not simultaneous but randomly chosen throughout the entire run. We find here qualitatively that (i) the vortices seem to not move in a preferred radial or azimuthal direction and (ii) that for higher rotation rates the distance from start to endpoint seems to decrease.

To check how the vortices move in time, the sample-averaged distance from their origin $\tilde{r} = \langle \boldsymbol{r}(t) - \boldsymbol{r}(0) \rangle$ is shown for $Ra = 10^9$ and three Ek in fig. 4.21a. We find that the distance increases monotonically with time for all Ek. One can split the distribution into a region shortly after the origin $t \lessapprox 2\,\mathrm{s}$, where $\tilde{r}$ increases rather slowly with time, and a region at larger t, where $\tilde{r}$ increases faster. Diffusive processes such as Brownian motion exhibit a functional dependence of the displacement $\boldsymbol{r}$ on time like $\langle \boldsymbol{r}^2 \rangle \propto t$, while ballistic particles move linear in time $\boldsymbol{r} \propto t$. Power-law fits to the fastest rotating data show for the first region an exponent < 0.5 and > 0.5 for larger times.

Meanwhile, the sample averaged radial and azimuthal position mostly fluctuates around 0 as seen in fig. 4.21(b and c), i.e., the motion is not ordered and we can conclude that $\langle \partial\phi/\partial t \rangle \approx 0$ as well as $\langle \partial r/\partial t \rangle \approx 0$. This of course is not true for individual vortices, as otherwise we should observe $\boldsymbol{r}(t) = 0$ for all times. For all other regarded Pr and Ra, the qualitative result is exactly the same and not shown here.

To compare the spread of the vortices in time we investigate their displacement, i.e. the resulting distance from the vortices' origin to its current location and the velocity

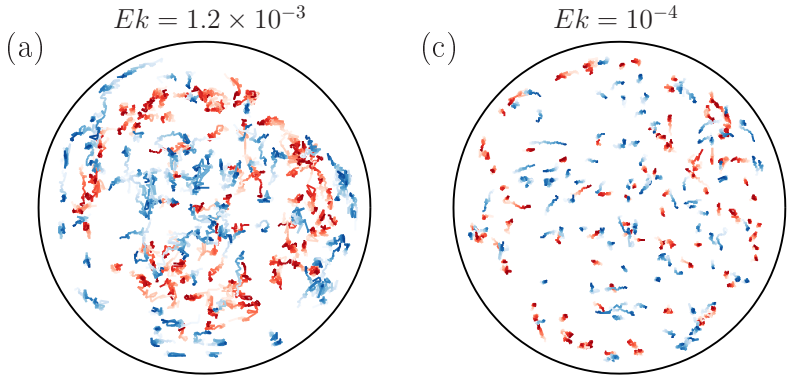

Figure 4.20: Tracks of a sample of vortices in the field of view for $Pr = 76$ and $Ra = 4 \times 10^8$ for different rotation: (a) $Ek = 1.2 \times 10^{-3}$, (b) $Ek = 10^{-4}$. Red colour are the vortices with $\omega > 0$, blue colour $\omega < 0$, where the dark side represents the origin of the trajectories and the light side the end point.

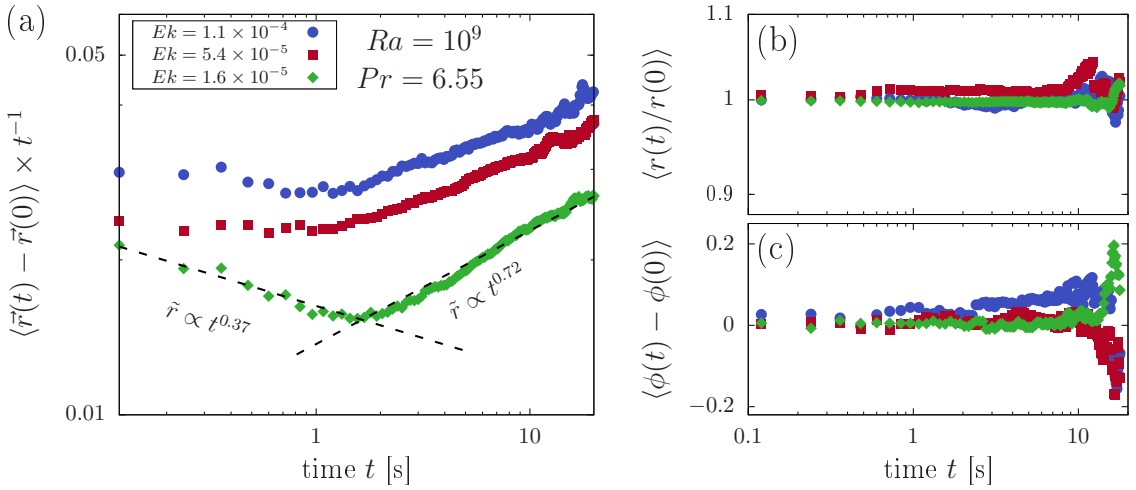

Figure 4.21: (a) distance from the origin of each vortex, reduced by t^{-1} as function of time t. To the fastest rotating data, power-laws are fitted to data with either $t < 1\,\mathrm{s}$ and $t > 3\,\mathrm{s}$. (b): ratio between the radius at each time and the radius at $t = 0$. (c) angle at time t, subtracted by the angle at $t = 0$. Each plot shows three different rotation rates, starting with slow rotation (blue bullets), some intermediate rotation rate (red squares), and the fastest rotation rate of the set (green diamonds). For all plots $\langle \cdot \rangle$ denotes the sample average.

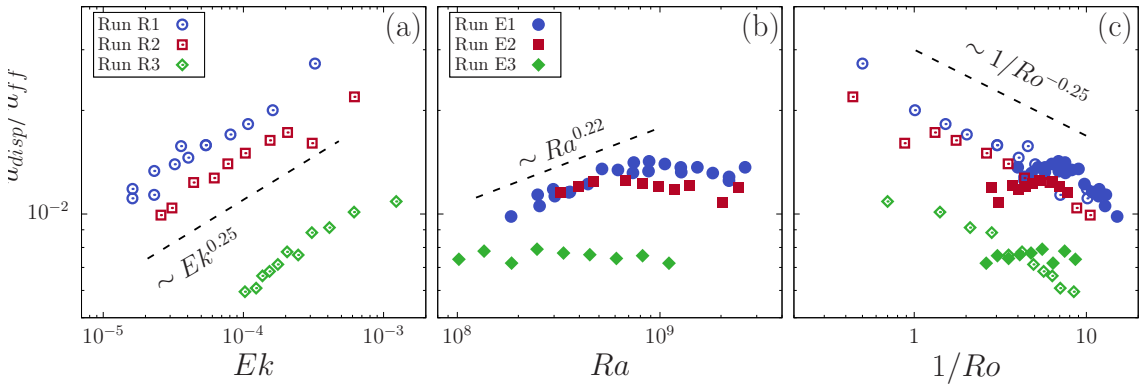

Figure 4.22: Displacement rate u_{disp} from the vortices origin as function of Ek (a) and Ra (b), normalized by u_{ff}. A fit through all the data in (a) returns a scaling $\propto Ek^{\alpha_{disp}}$ with average exponent $\alpha_{disp} = 0.25 \pm 0.02$, shown as black dashed line. Dashed line in (b) marks a fitted exponent 0.22 ± 0.03 of Ra for data with $Pr = 6.55$, $1/Ro \geq 7$. (c) shows all the data as function of $1/Ro$. Green diamonds show $Pr = 76$, red squares $Pr = 12$, and blue bullets $Pr = 6.55$.

of this distancing. It is obtained for each vortex over the entire measurement time, where the spread is simply the Euclidean norm of the distance origin-endpoint, where the vortex ceases to exist $r_{disp} = \|r_{end} - r_0\|$. Combined with the time the vortex was in existence, a spread velocity u_{disp} is calculated. In figure 4.22(a and b), u_{disp} is plotted against Ek and Ra. From the measurements at $Ra = const$, we obtain an averaged power-law scaling of the displacement velocity $u_{disp} \sim Ek^{0.23\pm0.05}$. Ra does not seem to have a large impact on u_{disp}, though for high $1/Ro \geq 7$ and the lowest $Pr = 6.55$ we find a relation $u_{disp} \sim Ra^{0.22\pm0.03}$. In fig. 4.22c, all data are shown as function of $1/Ro$, showing a consistency between the data. The spread at similar $1/Ro$ for high Pr remains way slower than for lower Pr, as expected due to the high viscosity.

A common comparison for spreading processes is the random walker. In this case, we assume a random process with a fixed step width of one in both x and y direction. A random walker with a fixed step width obeys a X^2-distribution for $k = 2$, i.e. a Rayleigh distribution for the displacement after N steps

$$p_{ra}(r, N) = 2r/N \cdot \exp\left(-r^2/N\right). \tag{4.11}$$

The Rayleigh distribution is compared to the measured data in fig. 4.23, where the probability of a drifted distance at a fixed time $\tau = 8$s is shown for a large subset of all measurements. (4.11) is fitted using the constant step width as sole fit parameter for each run. Rayleigh distributions represent the data rather well. The step width

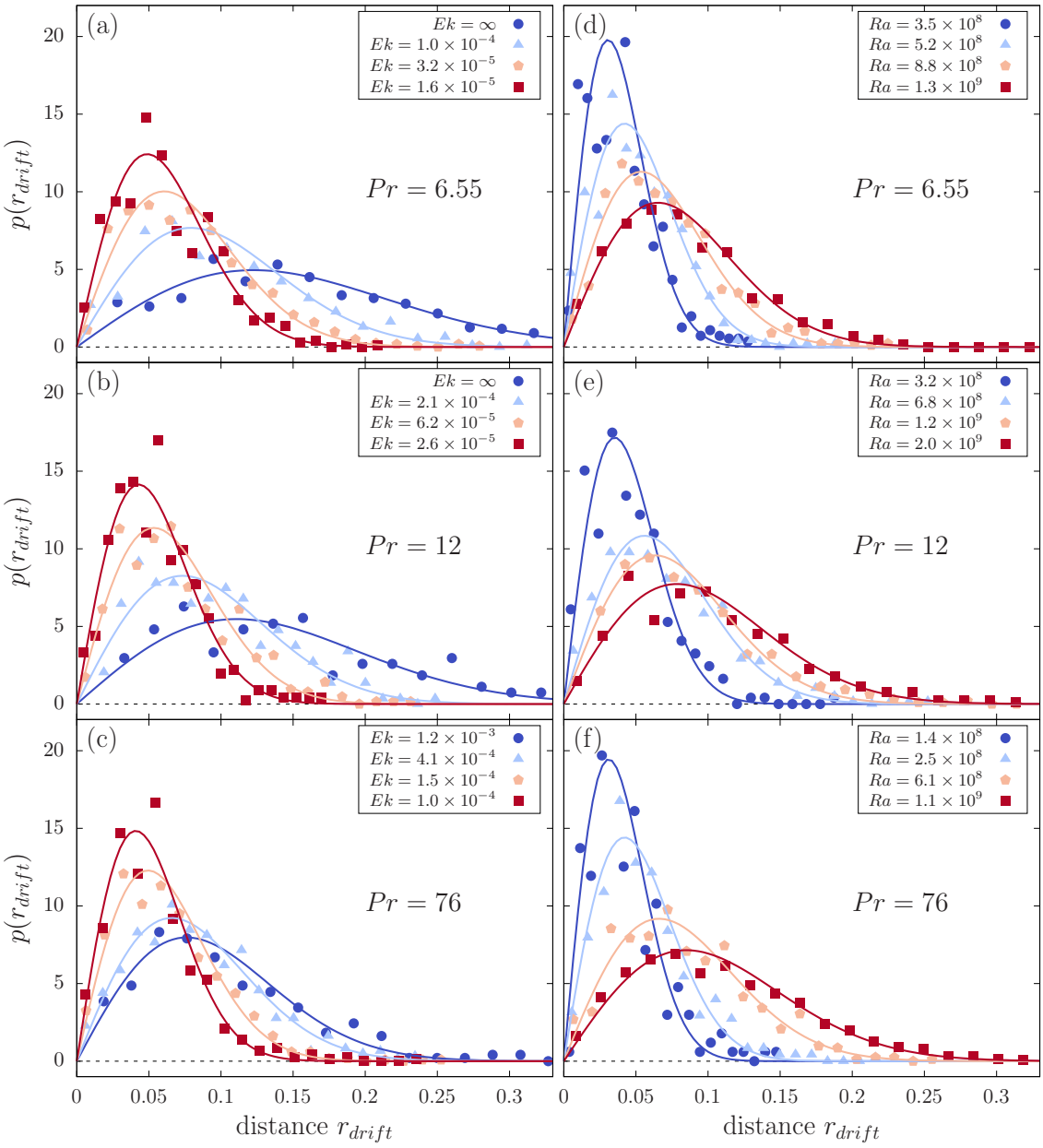

Figure 4.23: Distribution of the travelled distance of the vortices in the first 8 s. Fitted are Rayleigh distributions (4.11) with a constant step size as the only fit parameter, as would be expected in case of a random walk. (a)-(c) $Ra = const$, (d)-(f) $Ek = const$.

increases for lower rotation rates as well as lower Ra. This seems intuitive since azimuthal velocity is suppressed with increased rotation as already seen in fig. 4.22 and overall velocity decreases with decreased Ra. The results suggest the spreading of the here tracked vortices can be explained by a diffusive behaviour.

5 Discussion and outlook

In this thesis, we investigated two realizations of rotating Rayleigh-Bénard convection using very different experimental techniques. On the one hand, we analyzed pointwise temperature measurements in a large-scale $\Gamma = 1/2$ cylinder, filled with pressurized sulfur hexafluoride, which allows us to reach very large Ra and low Ek. On the other hand, we conducted planar velocity measurements in a smaller $\Gamma = 1$ setup filled with water and glycerol.

We found a heat transport scaling $Nu_0 \propto Ra^{0.315}$ over a wide range of Rayleigh numbers $10^{10} \leq Ra \leq 10^{15}$ for our non-rotating experiments. With rotation, heat transport, normalized by its value in absence of rotation, collapsed onto a single curve when plotted as function of the inverse Rossby number $1/Ro$, rather independent of Ra. Contrary to measurements in moderate to high Prandtl number fluids (say $Pr > 3$), we found no heat transport enhancement due to rotation in experiments with compressed SF_6, where Pr was in the range $0.7 \leq Pr \leq 0.96$.
We identified three regimes, buoyancy-dominated, rotation-influenced, and rotation-dominated - separated by the transitional rotation rates $1/Ro_1^* = 0.8$ and $1/Ro_2^* = 4$. The first transition appears where the large scale circulation breaks down and is replaced by an azimuthally periodic flow structure in a narrow region close to the sidewall. We termed this flow structure *boundary zonal flow* (BZF) and in the following we have investigated it comprehensively throughout this thesis.
We first noticed this new flow state in the bimodal distribution of the temperature signals close to the sidewall for rotation rates with $1/Ro \geq 1/Ro_1^*$ at all Ra. These were caused by the visible temperature bands of distinct cold and hot areas around the circumference. At each time, one side of the cell close to the sidewall was a warm upflowing region, while on the other half a cold downflow resided. We found remarkable agreement with DNS, the latter also determined the thickness δ_0 of this zone. It also highlighted the large influence on the vertical heat transport, which is strongly enhanced within the BZF. There, characteristic prograde averaged azimuthal velocities $\langle u_\phi \rangle > 0$ have been found, the bulk showed retrograde $\langle u_\phi \rangle < 0$. The temperature structure for $1/Ro > 1/Ro_1^*$ always drifted in retrograde direction close to the sidewall, azimuthal drift rates of this $k_{BZF} = 1$ temperature wave were measured as $\omega/\Omega \propto 1/Ro^{-3/4}$. We showed that this structure is seen throughout the entire vertical axis of the cell and that some previously published studies might have measured characteristics of the BZF.

The capability of the setup in combination with compressed SF_6 as a working fluid allowed us to achieve an exceptionally wide range of Ra, as well as of Ek. With our measurements we believe the potential of this cell in its current state is rather exhausted. Given the high Ra, further research on the HPCF is definitely of interest. To obtain additional valuable results, new techniques should be employed. Direct velocity measurements using hot-wire anemometers or even high density particle tracking would for example allow to determine scalings of the Reynolds number $Re(Ra, Ek)$.

To investigate the velocity field of the BZF, we performed particle image velocimetry in a smaller, transparent cell. With that, we were able to measure the characteristic $\langle u_\phi \rangle > 0$ velocities close to the sidewall. Qualitatively we see an agreement to DNS and while we do not notice a typical Stewartson layer scaling of $\delta \sim Ek^{1/3}$ or $\delta \sim Ek^{1/4}$, we can neither confirm nor reject the BZF's width scaling of $\delta_0 \sim Ek^{2/3}$ as found in DNS (Zhang et al. [2021]). We note, however, that with the current experimental setup, we only investigated the rotation-affected, but could not sufficiently enter the rotation-dominated regime. The DNS focussed solely on the latter, which makes a quantitative comparison difficult.

To perform measurements within the rotation-dominated regime using the small convection apparatus, one would need to reduce Ra by lowering the temperature difference between the bottom and the top (Δ). However, this decreases the relative precision of Δ since we measure the top plate temperature only indirectly by measuring the coolant's temperature. Since Ra depends linearly on Δ, $Ra \sim \Delta$, it would need to decrease by about one order of magnitude. Moreover, one could decrease the height of the cylinder by re-positioning the bottom plate. If one wanted to enter deeper into the rotation-dominated regime with this setup, both these changes need to be applied, additionally to an increased rotation rate with an updated rotating table. This way, wall modes close to convective onset and their transition into the BZF could be investigated. Varying Pr would still be a hard task even with these changes.

Due to its transparency, different experimental techniques could also be employed to obtain additional data. For example, we could measure the temperature field next to the velocity by laser-induced fluorescence or the three-dimensional velocity field using stereoscopic PIV or high density Lagrangian particle tracking. Further research on the

BZF is of high interest, as the large impact it has e.g. on vertical heat transport, might be crucial for rotating, slender cylinders. One could also investigate how much of the heat transport enhancement at moderate rotation rates is due to the BZF instead of Ekman pumping.

Concluding, the work presented here provided us with insights into multiple areas of rotating Rayleigh-Bénard convection. We gained knowledge about the flow structure in wall-bounded RBC far above the convective onset. The two experiments complemented each other rather well and in combination with DNS performed by our coworkers we were able to explain the phenomenon of the boundary zonal flow and its influence e.g. on the heat transport. We hope the results will also help other studies and that future research will explain some of the phenomenological observations.

6 Acknowledgements

First and foremost, I thank my supervisor, Dr. Stephan Weiss for his extensive support in all theoretical and experimental aspects regarding the scientific work. Whenever difficulties arose I was sure to be able to count on his patience, availability, and good advice. I also thank my thesis advisory committee, which includes Prof. Dr. Stefan Dreizler and Dr. Olga Shishkina for productive progress meetings and advice how to proceed with my project. Also I thank the technicians Andreas Renner, Andreas Kopp, and Dr. Artur Kubitzek and the mechanical and electrical workshops for technical support in creating and maintaining the experiments. Especially the U-Boot provided everyone with a lot of challenges, which took at least a full day to fix. I am extremely grateful for the collaboration with Denis Funfschilling and Viswa Moturi for working on the transparent apparatus and Dr. Xuan Zhang for fruitful scientific discussions.
At this point, I also thank Prof. Dr. Eberhard Bodenschatz for creating the working group and the facilities that enabled me to perform the research. The assistance of the entire staff at the institute, especially by Angela Gremmel and Caroline Siebert, helped tremendously over the years. Outside of the institute, I want to thank the PBCS office of the GGNB, in particular Frauke Bergmann and Antje Erdmann, for their extensive support for everything regarding the Ph.D. outside of the scientific work. As well, a special thank-you to all the colleagues and other Ph.D. students who worked with me on the project, discussed scientific problems, gave moral support and called for coffee breaks. These include, amongst others, Dr. Guus Bertens, Dr. Gerrit Green, Aina Gallemí Pérez, Antonio Ibáñez Landeta, Torben Neumann, Dr. Gabriele Nunnari, Philipp Reiter, Marcel Schröder, Dr. Christian Westendorf, and Hiu Fai Yik.

I acknowledge financial funding from the Deutsche Forschungsgemeinschaft (DFG) through grant WE 5011/4-1 as well as travel grants from the International Max Planck Research School for Physics of Biological and Complex Systems (IMPRS-PBCS) to attend scientific conferences.

References

Ronald J Adrian. Twenty years of particle image velocimetry. *Experiments in fluids*, 39(2):159–169, 2005.

Ronald J Adrian and Jerry Westerweel. *Particle image velocimetry*. Number 30. Cambridge university press, 2011.

Alberto Adriani, Alessandro Mura, G Orton, C Hansen, Francesca Altieri, ML Moriconi, J Rogers, G Eichstädt, T Momary, Andrew P Ingersoll, et al. Clusters of cyclones encircling Jupiter's poles. *Nature*, 555(7695):216–219, 2018.

Andrés J. Aguirre Guzmán, Matteo Madonia, Jonathan S. Cheng, Rodolfo Ostilla-Mónico, Herman J.H. Clercx, and Rudie P.J. Kunnen. Force balance in rapidly rotating Rayleigh-Bénard convection. *Journal of Fluid Mechanics*, 928:A16, 2021. doi: 10.1017/jfm.2021.802.

G. Ahlers. Effect of sidewall conductance on heat-transport measurements for turbulent Rayleigh-Bénard convection. *Phys. Rev. E*, 63:015303, 2000.

G. Ahlers, E. Brown, F. Fontenele Araujo, D. Funfschilling, S. Grossmann, and D. Lohse. Non-Oberbeck-Boussinesq effects in strongly turbulent Rayleigh-Bénard convection. *J. Fluid Mech.*, 569: 409–445, 2006.

G. Ahlers, D. Funfschilling, and E. Bodenschatz. Transitions in heat transport by turbulent convection for $Pr = 0.8$ and $10^{11} \leq Ra \leq 10^{15}$. *New J. Phys.*, 11:123001–1–18, 2009a.

G. Ahlers, S. Grossmann, and D. Lohse. Heat transfer and large scale dynamics in turbulent Rayleigh-Bénard convection. *Rev. Mod. Phys.*, 81:503–538, 2009b.

G. Ahlers et al. Transitions in heat transport by turbulent convection at Rayleigh numbers up to 10^{15}. *New J. Phys.*, 11, 2009c.

Guenter Ahlers, Francisco Fontenele Araujo, Denis Funfschilling, Siegfried Grossmann, and Detlef Lohse. Non-Oberbeck-Boussinesq Effects in Gaseous Rayleigh-Bénard Convection. *Phys. Rev. Lett.*, 98:054501, Jan 2007. doi: 10.1103/PhysRevLett.98.054501. URL `https://link.aps.org/doi/10.1103/PhysRevLett.98.054501`.

Guenter Ahlers, Eberhard Bodenschatz, and Xiaozhou He. Logarithmic temperature profiles of turbulent Rayleigh-Bénard convection in the classical and ultimate state for a Prandtl number of 0.8. *Journal of Fluid Mechanics*, 758:436–467, 11 2014. ISSN 1469-7645. doi: 10.1017/jfm.2014.543.

Julien Aubert, Thomas Gastine, and Alexandre Fournier. Spherical convective dynamos in the rapidly rotating asymptotic regime. *Journal of Fluid Mechanics*, 813:558–593, 2017.

J. M. Aurnou and P. L. Olson. Experiments on Rayleigh-Bénard convection, magnetoconvection and rotating magnetoconvection in liquid gallium. *J. Fluid Mech.*, 430:283–307, 3 2001. ISSN 1469-7645. doi: 10.1017/S0022112000002950.

K.M.S. Bajaj, G. Ahlers, and W. Pesch. Rayleigh-Bénard convection-with rotation at small Prandtl numbers. *Phys. Rev. E*, 65:056309, 2002.

D. B. Barker and M. E. Fourney. Measuring fluid velocities with speckle patterns. *Opt. Lett.*, 1(4):135–137, Oct 1977. doi: 10.1364/OL.1.000135. URL `http://www.osapublishing.org/ol/abstract.cfm?URI=ol-1-4-135`.

G.K. Batchelor. *An introduction to fluid dynamics*. Cambridge university press, 2000.

Ian H. Bell, Jorrit Wronski, Sylvain Quoilin, and Vincent Lemort. Pure and Pseudo-pure Fluid Thermophysical Property Evaluation and the Open-Source Thermophysical Property Library CoolProp. *Industrial & Engineering Chemistry Research*, 53(6):2498–2508, 2014. doi: 10.1021/ie4033999. URL `http://pubs.acs.org/doi/abs/10.1021/ie4033999`.

H. Bénard. Les tourbillons cellularies dans une nappe liquide. *Rev. Gen. Sci. Pure Appl.*, 11:1261; 1309, 1900.

E. Bodenschatz, J.R. deBruyn, G. Ahlers, and D.S. Cannell. Transition between patterns in thermal convection. *Phys. Rev. Lett.*, 67:3078–3081, 1991.

Vincent Bouillaut, Simon Lepot, Sébastien Aumaître, and Basile Gallet. Transition to the ultimate regime in a radiatively driven convection experiment. *Journal of Fluid Mechanics*, 861, 2019.

J. Boussinesq. *Theorie analytique de la chaleur, Vol. 2.* Gauthier-Villars, Paris, 1903.

A. D. Brent, V. R. Voller, and K. J. Reid. Enthalpy-porosity technique for modeling convection-diffusion phase change - application to the melting of a pure metal. *Numer. Heat Transfer*, 13:297–318, 1988.

E. Brown and G. Ahlers. Large-scale circulation model of turbulent Rayleigh-Bénard convection. *Phys. Rev. Lett.*, 98:134501–1–4, 2007.

E. Brown, D. Funfschilling, and G. Ahlers. Anomalous Reynolds-number scaling in turbulent Rayleigh-Bénard convection. *J. Stat. Mech.*, 2007:P10005–1–22, 2007.

J. C. Buell and I. Catton. Effects of rotation on the stability of a bounded cylindrical layer of fluid heated from below. *Phys. Fluids*, 26:892, 1983a.

J. C. Buell and I. Catton. The effect of wall conduction on the stability of a fluid in a right circular cylinder heated from below. *Journal of Heat Transfer*, 105(2):255–260, 1983b. doi: 10.1115/1.3245571. URL `http://link.aip.org/link/?JHR/105/255/1`.

Bruce A. Buffett. Earth's Core and the Geodynamo. *Science*, 288(5473):2007–2012, 2000. ISSN 0036-8075. doi: 10.1126/science.288.5473.2007. URL `https://science.sciencemag.org/content/288/5473/2007`.

F. H. Busse. The stability of finite amplitude cellular convection and its relation to an extremum principle. *J. Fluid Mech.*, 30:625–649, 1967.

F. H. Busse and C.R. Carrigan. Laboratory simulation of thermal convection in rotating planets and stars. *Science*, 191:81–83, 1976.

P. Cardin and P. Olson. Chaotic thermal convection in a rapidly rotating spherical shell: consequences for flow in the outer core. *Phys. of the Earth and Planetary Interiors*, 82:235–259, 1994.

B. Castaing, G. Gunaratne, F. Heslot, L. Kadanoff, A. Libchaber, S. Thomae, X. Z. Wu, S. Zaleski, and G. Zanetti. Scaling of hard thermal turbulence in Rayleigh-Bénard convection. *J. Fluid Mech.*, 204:1–30, 1989.

F. Cattaneo, T. Emonet, and N. Weiss. On the interaction between convection and magnetic fields. *Astrophys. J.*, 588:1183–1198, 2003.

S. Chandrasekhar. *Hydrodynamic and Hydromagnetic Stability.* Dover Books on Physics. Dover Publications, New York, 1961. ISBN 9780486319209. URL `https://books.google.de/books?id=Mg3CAgAAQBAJ`.

X. Chavanne, F. Chilla, B. Castaing, B. Hebral, B. Chabaud, and J. Chaussy. Observation of the ultimate regime in Rayleigh-Bénard convection. *Phys. Rev. Lett.*, 79:3648–3651, 1997.

X. Chavanne, F. Chilla, B. Chabaud, B. Castaing, and B. Hebral. Turbulent Rayleigh-Bénard convection in gaseous and liquid He. *Phys. Fluids*, 13:1300–1320, 2001.

Jonathan S. Cheng, Matteo Madonia, Andrés J. Aguirre Guzmán, and Rudie P. J. Kunnen. Laboratory exploration of heat transfer regimes in rapidly rotating turbulent convection. *Phys. Rev. Fluids*, 5:113501, Nov 2020. doi: 10.1103/PhysRevFluids.5.113501. URL `https://link.aps.org/doi/10.1103/PhysRevFluids.5.113501`.

Emily S. C. Ching. Probabilities for temperature differences in Rayleigh-Bénard convection. *Phys. Rev. A*, 44:3622–3629, Sep 1991. doi: 10.1103/PhysRevA.44.3622. URL `https://link.aps.org/doi/10.1103/PhysRevA.44.3622`.

S Cioni, Sergio Ciliberto, and Jöel Sommeria. Strongly turbulent Rayleigh-Bénard convection in mercury: comparison with results at moderate Prandtl number. *Journal of Fluid Mechanics*, 335:111–140, 1997.

R. M. Clever. Finite amplitude longitudal convection rolls in an inclined layer. *Journal of Heat Transfer*, 95(3):407–408, 1973. doi: 10.1115/1.3450072. URL `http://link.aip.org/link/?JHR/95/407/1`.

Mark C Cross and Pierre C Hohenberg. Pattern formation outside of equilibrium. *Reviews of modern physics*, 65(3):851, 1993.

K. Daniels, B. Plapp, and E. Bodenschatz. Pattern formation in inclined layer convection. *Physical Review Letters*, 84:5320–5323, 2000.

A.H. Davis. Xxxi. natural convective cooling of wires. *The London, Edinburgh, and Dublin Philosophical Magazine and Journal of Science*, 43(254):329–339, 1922a. doi: 10.1080/14786442208565219. URL `https://doi.org/10.1080/14786442208565219`.

A.H. Davis. LXXIX. Natural convective cooling in fluids. *The London, Edinburgh, and Dublin Philosophical Magazine and Journal of Science*, 44(263):920–940, 1922b. doi: 10.1080/14786441208562566. URL `https://doi.org/10.1080/14786441208562566`.

Z. A. Daya and R. E. Ecke. Prandtl-number dependence of interior temperature and velocity fluctuations in turbulent convection. *Phys. Rev. E*, 66:045301, Oct 2002. doi: 10.1103/PhysRevE.66.045301. URL `https://link.aps.org/doi/10.1103/PhysRevE.66.045301`.

Xander M. de Wit, Andrés J. Aguirre Guzmán, Matteo Madonia, Jonathan S. Cheng, Herman J. H. Clercx, and Rudie P. J. Kunnen. Turbulent rotating convection confined in a slender cylinder: The sidewall circulation. *Phys. Rev. Fluids*, 5:023502, Feb 2020. doi: 10.1103/PhysRevFluids.5.023502. URL `https://link.aps.org/doi/10.1103/PhysRevFluids.5.023502`.

James W. Deardorff. A numerical study of three-dimensional turbulent channel flow at large Reynolds numbers. *Journal of Fluid Mechanics*, 41(2):453–480, 1970. doi: 10.1017/S0022112070000691.

Shan-Shan Ding, Hui-Min Li, Wen-Dan Yan, and Jin-Qiang Zhong. Temperature fluctuations relevant to thermal-plume dynamics in turbulent rotating Rayleigh-Bénard convection. *Physical Review Fluids*, 4(2):023501, 2019.

TD Dudderar and PG Simpkins. Laser speckle photography in a fluid medium. *Nature*, 270(5632): 45–47, 1977.

Robert Ecke and Joseph Niemela. Heat Transport in the Geostrophic Regime of Rotating Rayleigh-Bénard Convection. *Phys. Rev. Lett.*, 113:114301, 09 2014. doi: 10.1103/PhysRevLett.113.114301. URL `http://link.aps.org/doi/10.1103/PhysRevLett.113.114301`.

V. W. Ekman. On the influence of the earth's rotation on ocean currents. *Arkiv Matem. Astr. Fysik, Stockholm*, 2-11:1–52, 1905.

Benjamin Favier and Edgar Knobloch. Robust wall states in rapidly rotating Rayleigh-Bénard convection. *Journal of Fluid Mechanics*, 895:R1, 2020. doi: 10.1017/jfm.2020.310.

D. E. Fitzjarrald. A field observation of atmospheric free convection. *Journal of Applied Meteorology and Climatology*, 15(3):259 – 263, 1976. doi: 10.1175/1520-0450(1976)015¡0259:AFOOAF¿2.0.CO;2.

A. S. Fleischer and R. J. Goldstein. High-Rayleigh-number convection of pressurized gases in a horizontal enclosure. *Journal of Fluid Mechanics*, 469:1–12, 2002. doi: 10.1017/S002211200200174X.

P. Frick, R. Khalilov, I. Kolesnichenko, A. Mamykin, V. Pakholkov, A. Pavlinov, and S. Rogozhkin. Turbulent convective heat transfer in a long cylinder with liquid sodium. *EPL (Europhysics Letters)*, 109(1):14002, jan 2015. doi: 10.1209/0295-5075/109/14002. URL `https://doi.org/10.1209/0295-5075/109/14002`.

D. Funfschilling, E. Brown, A. Nikolaenko, and G. Ahlers. Heat transport by turbulent Rayleigh-Bénard convection in cylindrical cells with aspect ratio one and larger. *J. Fluid Mech.*, 536:145–154, 2005.

J.-C. Gascard, A.J. Watson, M.-J. Messias, K.A. Olsson, T. Johannessen, and K. Simonsen. Long-lived vortices as a mode of deep ventilation in the greenland sea. *Nature (London)*, 416:525–527, 2002.

Gary A. Glatzmaier. Geodynamo simulations - how realistic are they? *Annual Review of Earth and Planetary Sciences*, 30(1):237–257, 2002. doi: 10.1146/annurev.earth.30.091201.140817. URL `http://dx.doi.org/10.1146/annurev.earth.30.091201.140817`.

G. A. Glatzmeier and P. H. Roberts. A three-dimensional self-consistent computer simulation of a geomagnetic field reversal. *Nature*, 377:203, 1995.

H. F. Goldstein, E. Knobloch, I. Mercader, and M. Net. Convection in a rotating cylinder. Part 1 Linear theory for moderate Prandtl numbers. *Journal of Fluid Mechanics*, 248:583–604, 1993. doi: 10.1017/S0022112093000928.

H. F. Goldstein, E. Knobloch, I. Mercader, and M. Net. Convection in a rotating cylinder. Part 2. Linear theory for low Prandtl numbers. *Journal of Fluid Mechanics*, 262:293–324, 1994. doi: 10.1017/S0022112094000510.

HP Greenspan and LN Howard. On a time-dependent motion of a rotating fluid. *Journal of fluid mechanics*, 17(3):385–404, 1963.

S. Grossmann and D. Lohse. Scaling in thermal convection: a unifying theory. *J. Fluid Mech.*, 407: 27–56, 2000.

S. Grossmann and D. Lohse. Thermal convection for large Prandtl number. *Phys. Rev. Lett.*, 86: 3316–3319, 2001.

Siegfried Grossmann and Detlef Lohse. Multiple scaling in the ultimate regime of thermal convection. *Physics of Fluids*, 23:045108, 2011.

R Grousson and S Mallick. Study of flow pattern in a fluid by scattered laser light. *Applied Optics*, 16 (9):2334–2336, 1977.

David Gubbins. The Rayleigh number for convection in the Earth's core. *Physics of the Earth and Planetary Interiors*, 128(1):3–12, 2001. ISSN 0031-9201. doi: https://doi.org/10.1016/S0031-9201(01)00273-4. URL https://www.sciencedirect.com/science/article/pii/S0031920101002734. Dynamics and Magnetic Fields of the Earth's and Planetary Interiors.

Xiaozhou He, Denis Funfschilling, Eberhard Bodenschatz, and Guenter Ahlers. Heat transport by turbulent Rayleigh–Bénard convection for Pr $\approx$ 0.8 and $4 \times 10^{11} < Ra < 2 \times 10^{14}$: ultimate-state transition for aspect ratio $\gamma = 1.00$. *New. J. Physics*, 14:063030, 2012a.

Xiaozhou He, Denis Funfschilling, Holger Nobach, Eberhard Bodenschatz, and Guenter Ahlers. Transition to the Ultimate State of Turbulent Rayleigh-Bénard Convection. *Phys. Rev. Lett.*, 108:024502, 01 2012b. doi: 10.1103/PhysRevLett.108.024502. URL http://link.aps.org/doi/10.1103/PhysRevLett.108.024502.

Xiaozhou He, Yin Wang, and Penger Tong. Dynamic heterogeneity and conditional statistics of non-Gaussian temperature fluctuations in turbulent thermal convection. *Physical Review Fluids*, 3(5): 052401, 2018.

Moritz Heimpel, Jonathan Aurnou, and Johannes Wicht. Simulation of equatorial and high-latitude jets on Jupiter in a deep convection model. *Nature*, 438:193, 2005.

J. Herrmann and F. H. Busse. Asymptotic theory of wall-attached convection in a rotating fluid layer. *Journal of Fluid Mechanics*, 255:183–194, 1993. doi: 10.1017/S0022112093002447.

Bradley W Hindman, Nicholas A Featherstone, and Keith Julien. Morphological classification of the convective regimes in rotating stars. *The Astrophysical Journal*, 898(2):120, 2020.

Hajo Holzmann and Sebastian Vollmer. A likelihood ratio test for bimodality in two-component mixtures with application to regional income distribution in the EU. *AStA Advances in Statistical Analysis*, 92(1):57–69, Feb 2008. ISSN 1863-818X. doi: 10.1007/s10182-008-0057-2. URL https://doi.org/10.1007/s10182-008-0057-2.

Susanne Horn and Jonathan M. Aurnou. Regimes of Coriolis-Centrifugal Convection. *Phys. Rev. Lett.*, 120:204502, May 2018. doi: 10.1103/PhysRevLett.120.204502. URL https://link.aps.org/doi/10.1103/PhysRevLett.120.204502.

Susanne Horn and Jonathan M. Aurnou. Rotating convection with centrifugal buoyancy: Numerical predictions for laboratory experiments. *Phys. Rev. Fluids*, 4:073501, Jul 2019. doi: 10.1103/PhysRevFluids.4.073501. URL https://link.aps.org/doi/10.1103/PhysRevFluids.4.073501.

Susanne Horn and Jonathan M Aurnou. Tornado-like vortices in the quasi-cyclostrophic regime of coriolis-centrifugal convection. *Journal of Turbulence*, 22(4-5):297–324, 2021.

Susanne Horn and Olga Shishkina. Rotating non-oberbeck-boussinesq rayleigh-bénard convection in water. *Physics of Fluids*, 26(5):055111, 2014. doi: http://dx.doi.org/10.1063/1.4878669. URL http://scitation.aip.org/content/aip/journal/pof2/26/5/10.1063/1.4878669.

Susanne Horn and Olga Shishkina. Toroidal and poloidal energy in rotating Rayleigh-Bénard convection. *Journal of Fluid Mechanics*, 762:232–255, 001 2015. doi: 10.1017/jfm.2014.652.

Susanne Horn, Olga Shishkina, and Claus Wagner. On non-Oberbeck-Boussinesq effects in three-dimensional Rayleigh-Bénard convection in glycerol. *Journal of Fluid Mechanics*, 724:175–202, 2013. doi: 10.1017/jfm.2013.151.

G. R. Hunt and P. F. Linden. The fluid mechanics of natural ventilation - displacement ventilation by buoyancy-driven flows assisted by wind. *Build. Environ.*, 34:707, 1999.

Jerome G Hust and Alan B Lankford. Thermal conductivity of aluminum, copper, iron, and tungsten for temperatures from 1 k to the melting point. Technical report, National Bureau of Standards, Boulder, CO (USA). Chemical Engineering Div., 1984.

Andrew P Ingersoll. Atmospheric dynamics of the outer planets. *Science*, 248(4953):308–315, 1990.

C.A. Jones. Convection-driven geodynamo models. *Phil. Trans. R. Soc. Lond. A*, 358:873–897, 2000.

K. Julien, S. Legg, J. Mcwilliams, and J. Werne. Rapidly rotating turbulent Rayleigh-Bénard convection. *Journal of Fluid Mechanics*, 322:243–273, 1996a. doi: 10.1017/S0022112096002789.

K. Julien, S. Legg, J. McWilliams, and J. Werne. Hard turbulence in rotating Rayleigh-Bénard convection. *Phys. Rev. E*, 53:R5557–R5560, 1996b.

Keith Julien, Edgar Knobloch, Antonio M. Rubio, and Geoffrey M. Vasil. Heat Transport in Low-Rossby-Number Rayleigh-Bénard Convection. *Phys. Rev. Lett.*, 109:254503, Dec 2012. doi: 10.1103/PhysRevLett.109.254503. URL `https://link.aps.org/doi/10.1103/PhysRevLett.109.254503`.

L. P. Kadanoff. Turbulent Heat Flow: Structures and Scaling. *Phys. Today*, 54(8):34–39, 2001.

B.A Kader and A.M Yaglom. Heat and mass transfer laws for fully turbulent wall flows. *International Journal of Heat and Mass Transfer*, 15(12):2329 – 2351, 1972. ISSN 0017-9310. doi: https://doi.org/10.1016/0017-9310(72)90131-7. URL `http://www.sciencedirect.com/science/article/pii/0017931072901317`.

E. King, S. Stellmach, J. Noir, U. Hansen, and J. Aurnou. Boundary layer control of rotating convection systems. *Nature*, 457:301–304, 2009.

E. M. King, S. Stellmach, and J. M. Aurnou. Heat transfer by rapidly rotating Rayleigh-Bénard convection. *J. Fluid Mech.*, 691:568–582, 2012. doi: 10.1017/jfm.2011.493.

E. M. King, S. Stellmach, and B. Buffett. Scaling behaviour in Rayleigh-Bénard convection with and without rotation. *Journal of Fluid Mechanics*, 717:449–471, 2013. doi: 10.1017/jfm.2012.586.

Eric M. King and Jonathan M. Aurnou. Thermal evidence for Taylor columns in turbulent rotating Rayleigh-Bénard convection. *Phys. Rev. E*, 85:016313, Jan 2012. doi: 10.1103/PhysRevE.85.016313. URL `https://link.aps.org/doi/10.1103/PhysRevE.85.016313`.

Andrey Nikolaevich Kolmogorov. The local structure of turbulence in incompressible viscous fluid for very large Reynolds numbers. *Cr Acad. Sci. URSS*, 30:301–305, 1941.

J Kompenhans and J Reichmuth. Particle imaging velocimetry in a low turbulent wind tunnel and other flow facilities. *Advanced Instrumentation for Aero Engine Components*, 35:2, 1986.

R.H. Kraichnan. Turbulent thermal convection at arbitrary Prandtl number. *Physics of Fluids*, 5: 1374–1389, November 1962. doi: 10.1063/1.1706533.

R. P. J. Kunnen, B. J. Geurts, and H. J. H. Clercx. Experimental and numerical investigation of turbulent convection in a rotating cylinder. *Journal of Fluid Mechanics*, 642:445–476, 2010. doi: 10.1017/S002211200999190X.

RPJ Kunnen, HJH Clercx, and Bernardus J Geurts. Breakdown of large-scale circulation in turbulent rotating convection. *Europhys. Lett.*, 84(2):24001, 2008.

Rudie PJ Kunnen, Richard JAM Stevens, Jim Overkamp, Chao Sun, GertJan F van Heijst, and Herman JH Clercx. The role of Stewartson and Ekman layers in turbulent rotating Rayleigh–Bénard convection. *J. Fluid Mech.*, 688:422–442, 2011. doi: 10.1017/jfm.2011.383. URL http://dx.doi.org/10.1017/S0022112011003831.

E. Y. Kuo and M. C. Cross. Traveling-wave wall states in rotating Rayleigh-Bénard convection. *Phys. Rev. E*, 47:R2245–R2248, Apr 1993. doi: 10.1103/PhysRevE.47.R2245. URL https://link.aps.org/doi/10.1103/PhysRevE.47.R2245.

S. Lam, X. D. Shang, S. Q. Zhou, and K.-Q. Xia. Prandtl-number dependence of the viscous boundary layer and the Reynolds-number in Rayleigh-Bénard convection. *Phys. Rev. E*, 65:066306, 2002.

L. D. Landau and E. M. Lifshitz. *Fluid Mechanics*, volume 6. Pergamon Press, 1959.

Y. Liu and R.E. Ecke. Heat Transport Scaling in Turbulent Rayleigh-Bénard Convection: Effects of Rotation and Prandtl Number. *Physical Review Letters*, 79:2257–2260, September 1997. doi: 10.1103/PhysRevLett.79.2257.

Yuanming Liu and Robert E Ecke. Local temperature measurements in turbulent rotating Rayleigh-Bénard convection. *Physical Review E*, 84(1):016311, 2011.

Robert A. Maddox. Mesoscale Convective Complexes. *Bulletin of the American Meteorological Society*, 61(11):1374–1387, 1980. ISSN 00030007, 15200477. URL http://www.jstor.org/stable/26221473.

W. V. R. Malkus. The heat transport and spectrum of thermal turbulence. *Proceedings of the Royal Society of London A: Mathematical, Physical and Engineering Sciences*, 225(1161):196–212, 1954. doi: 10.1098/rspa.1954.0197. URL http://rspa.royalsocietypublishing.org/content/225/1161/196.

W. V. R. Malkus and G. Veronis. Finite amplitude cellular convection. *Journal of Fluid Mechanics*, 4 (3):225–260, 1958. doi: 10.1017/S0022112058000410.

Michael Manga and Dayanthie Weeraratne. Experimental study of non-Boussinesq Rayleigh-Bénard convection at high Rayleigh and Prandtl numbers. *Physics of Fluids*, 11(10):2969–2976, 1999. doi: 10.1063/1.870156. URL https://doi.org/10.1063/1.870156.

J. Marshall and F. Schott. Open-ocean convection: Observations, theory, and models. *Rev. Geophys.*, 37:1–64, 1999.

Chester W. Newton. *Dynamics of Severe Convective Storms*, pages 33–58. American Meteorological Society, Boston, MA, 1963. ISBN 978-1-940033-56-3. doi: 10.1007/978-1-940033-56-3_2. URL https://doi.org/10.1007/978-1-940033-56-3_2.

J. J. Niemela and K. R. Sreenivasan. Confined turbulent convection. *J. Fluid Mech.*, 481:355–384, 2003.

J. J. Niemela and K. R. Sreenivasan. The use of cryogenic helium for classical turbulence: Promises and hurdles. *J. Low Temp. Phys.*, 143:163–212, 2006.

J.J. Niemela, L Skrbek, K.R. Sreenivasan, and R.J. Donnelly. Turbulent convection at very high Rayleigh numbers. *Nature*, 404:837–840, 04 2000.

A. Nikolaenko, E. Brown, D. Funfschilling, and G. Ahlers. Heat transport by turbulent Rayleigh-Bénard convection in cylindrical cells with aspect ratio one and less. *J. Fluid Mech.*, 523:251–260, January 2005. doi: 10.1017/S0022112004002289.

A. Oberbeck. Über die Wärmeleitung der Flüssigkeiten bei Berücksichtigung der Strömungen infolge von Temperaturdifferenzen. *Ann. Phys. Chem.*, 243:271–292, 1879.

Anne Pellew and Richard Vynne Southwell. On maintained convective motion in a fluid heated from below. *Proceedings of the Royal Society of London. Series A. Mathematical and Physical Sciences*, 176(966):312–343, 1940.

Meredith Plumley, Keith Julien, Philippe Marti, and Stephan Stellmach. The effects of Ekman pumping on quasi-geostrophic Rayleigh-Bénard convection. *Journal of Fluid Mechanics*, 803:51–71, 2016. doi: 10.1017/jfm.2016.452.

S. B. Pope. *Turbulent Flow*. Cambridge University Press, Cambridge, 2000.

Dagmar Popke, Bjoern Stevens, and Aiko Voigt. Climate and climate change in a radiative-convective equilibrium version of echam6. *Journal of Advances in Modeling Earth Systems*, 5(1):1–14, 2013.

L. Prandtl. Bericht über Untersuchungen zur ausgebildeten Turbulenz. *Z. Angew. Math. Mech.*, 5: 136–139, 1925.

X. L. Qiu and P. Tong. Temperature oscillations in turbulent Rayleigh-Bénard convection. *Phys. Rev. E*, 66:026308–1–12, 2002.

Xin-Liang Qiu and Ke-Qing Xia. Viscous boundary layers at the sidewall of a convection cell. *Physical Review E*, 58(1):486, 1998.

S. Rahmstorf. The thermohaline ocean circulation: A system with dangerous thresholds? *Climate Change*, 46:247–256, 2000.

Lord Rayleigh. On Convection Currents in a Horizontal Layer of Fluid, when the Higher Temperature is on the Under Side. *The London, Edinburgh, and Dublin Philosophical Magazine and Journal of Science*, 32(192):529–546, 1916.

Nilton O Renno, Vincent J Abreu, Jacquelin Koch, Peter H Smith, Oscar K Hartogensis, Henk AR De Bruin, Dirk Burose, Gregory T Delory, William M Farrell, Christopher J Watts, et al. Matador 2002: A pilot field experiment on convective plumes and dust devils. *Journal of Geophysical Research: Planets*, 109(E7), 2004.

DC Reuter, AA Simon-Miller, A Lunsford, KH Baines, AF Cheng, DE Jennings, CB Olkin, JR Spencer, SA Stern, HA Weaver, et al. Jupiter cloud composition, stratification, convection, and wave motion: A view from new horizons. *Science*, 318(5848):223–225, 2007.

Lewis Fry Richardson. I. some measurements of atmospheric turbulence. *Philosophical Transactions of the Royal Society of London. Series A, Containing Papers of a Mathematical or Physical Character*, 221(582-593):1–28, 1921.

H. T. Rossby. A study of Bénard convection with and without rotation. *J. Fluid Mech.*, 36:309–335, 1969.

Matthias Roth. Review of atmospheric turbulence over cities. *Quarterly Journal of the Royal Meteorological Society*, 126(564):941–990, 2000.

Christopher S Ruf, Robert Atlas, Paul S Chang, Maria Paola Clarizia, James L Garrison, Scott Gleason, Stephen J Katzberg, Zorana Jelenak, Joel T Johnson, Sharanya J Majumdar, et al. New ocean winds satellite mission to probe hurricanes and tropical convection. *Bulletin of the American Meteorological Society*, 97(3):385–395, 2016.

Agustın Sanchez-Lavega, José F Rojas, and Pedro V Sada. Saturn's zonal winds at cloud level. *Icarus*, 147(2):405–420, 2000.

Giancarlo Scalabrin, Luigi Bettio, Paolo Marchi, and Paolo Stringari. A Fundamental Equation of State for Sulfur Hexafluoride (SF6) in Extended Equation of State Format. *Journal of Physical and Chemical Reference Data*, 36(2):617–662, 2007. doi: 10.1063/1.2716004. URL `https://doi.org/10.1063/1.2716004`.

H. Schlichting and K. Gersten. *Boundary layer theory*. Springer Verlag, Berlin, 9th edition, 2017.

G. Schubert and K.M. Soderlund. Planetary magnetic fields: Observations and models. *Physics of the Earth and Planetary Interiors*, 187(3):92–108, 2011. ISSN 0031-9201. doi: https://doi.org/10.1016/j.pepi.2011.05.013. URL `https://www.sciencedirect.com/science/article/pii/S0031920111001129`. Special Issue: Planetary Magnetism, Dynamo and Dynamics.

Jörg Schumacher, Ambrish Pandey, Victor Yakhot, and Katepalli R Sreenivasan. Transition to turbulence scaling in rayleigh-bénard convection. *Physical Review E*, 98(3):033120, 2018.

Olga Shishkina, Stephan Weiss, and Eberhard Bodenschatz. Conductive heat flux in measurements of the Nusselt number in turbulent Rayleigh-Bénard convection. *Phys. Rev. Fluids*, 1:062301, Oct 2016. doi: 10.1103/PhysRevFluids.1.062301. URL `https://link.aps.org/doi/10.1103/PhysRevFluids.1.062301`.

B. I. Shraiman and E. D. Siggia. Heat transport in high-Rayleigh number convection. *Phys. Rev. A*, 42:3650–3653, 1990.

E. D. Siggia. High Rayleigh number convection. *Annu. Rev. Fluid Mech.*, 26:137–168, 1994.

Roger K Smith. The role of cumulus convection in hurricanes and its representation in hurricane models. *Reviews of Geophysics*, 38(4):465–489, 2000.

E. A. Spiegel. Convection in stars. *Ann. Rev. Astron. Astrophys.*, 9:323–352, 1971.

S. Stellmach, M. Lischper, K. Julien, G. Vasil, J. S. Cheng, A. Ribeiro, E. M. King, and J. M. Aurnou. Approaching the asymptotic regime of rapidly rotating convection: Boundary layers versus interior dynamics. *Phys. Rev. Lett.*, 113:254501, Dec 2014. doi: 10.1103/PhysRevLett.113.254501. URL `http://link.aps.org/doi/10.1103/PhysRevLett.113.254501`.

Richard Stevens, Herman Clercx, and D Lohse. Optimal Prandtl number for heat transfer in rotating Rayleigh-Bénard convection. *New J. Phys.*, 12, 12 2010a. doi: 10.1088/1367-2630/12/7/075005.

Richard Stevens, Erwin P. van der Poel, Siegfried Grossmann, and D Lohse. The unifying theory of scaling in thermal convection: The updated prefactors. *Journal of Fluid Mechanics*, 730:295–308, 01 2013.

Richard J. A. M. Stevens, Roberto Verzicco, and Detlef Lohse. Radial boundary layer structure and Nusselt number in Rayleigh-Bénard convection. *Journal of Fluid Mechanics*, 643:495–507, 2010b. doi: 10.1017/S0022112009992461. URL `http://dx.doi.org/10.1017/S0022112009992461`.

Richard J. A. M. Stevens, Detlef Lohse, and Roberto Verzicco. Prandtl and Rayleigh number dependence of heat transport in high Rayleigh number thermal convection. *Journal of Fluid Mechanics*, 688:31–43, 12 2011. ISSN 1469-7645. doi: 10.1017/jfm.2011.354.

Richard J. A. M. Stevens, Detlef Lohse, and Roberto Verzicco. Sidewall effects in Rayleigh-Bénard convection. *Journal of Fluid Mechanics*, 741:1–27, 01 2014. doi: 10.1017/jfm.2013.664.

Richard J. A. M. Stevens, Alexander Blass, Xiaojue Zhu, Roberto Verzicco, and Detlef Lohse. Turbulent thermal superstructures in rayleigh-bénard convection. *Phys. Rev. Fluids*, 3:041501, Apr 2018. doi: 10.1103/PhysRevFluids.3.041501. URL `https://link.aps.org/doi/10.1103/PhysRevFluids.3.041501`.

R.J.A.M. Stevens, J.-Q. Zhong, H.J.H. Clercx, G. Ahlers, and D. Lohse. Transitions between turbulent states in rotating Rayleigh-Bénard convection. *Phys. Rev. Lett.*, 103:024503, 2009.

K. Stewartson. On almost rigid rotations. *Journal of Fluid Mechanics*, 3:17 – 26, 10 1957.

K. Stewartson. On almost rigid rotations. part 2. *Journal of Fluid Mechanics*, 26(1):131–144, 1966. doi: 10.1017/S0022112066001137.

George Gabriel Stokes. On the effect of the internal friction of fluids on the motion of pendulums. *Transactions of the Cambridge Philosophical Society*, 8, 1851.

K. Sugiyama, E. Calzavarini, S. Grossmann, and D. Lohse. Non-Oberbeck-Boussinesq effects in two-dimensional Rayleigh-Bénard convection in glycerol. *Europhys. Lett.*, submitted:[Arxiv: physics/0707.0116], 2007.

C. Sun and K.-Q. Xia. Scaling of the Reynolds number in turbulent thermal convection. *Phys. Rev. E*, 72:067302–1–4, 2005.

C. Sun, H. D. Xi, and K. Q. Xia. Azimuthal symmetry, flow dynamics, and heat transport in turbulent thermal convection in a cylinder with an aspect ratio of 0.5. *Phys. Rev. Lett.*, 95:074502, 2005.

G. I. Taylor. Stability of a viscous liquid contained between two rotating cylinders. *Philosophical Transactions of the Royal Society of London A: Mathematical, Physical and Engineering Sciences*, 223(605-615):289–343, 1923. ISSN 0264-3952. doi: 10.1098/rsta.1923.0008. URL `http://rsta.royalsocietypublishing.org/content/223/605-615/289`.

William Thielicke and Eize Stamhuis. PIVlab – Towards User-friendly, Affordable and Accurate Digital Particle Image Velocimetry in MATLAB. *Journal of Open Research Software*, 2(1), 2014. doi: http://doi.org/10.5334/jors.bl.

P. Urban, P. Hanzelka, T. Kralik, V. Musilova, A. Srnka, and L. Skrbek. Effect of Boundary Layers Asymmetry on Heat Transfer Efficiency in Turbulent Rayleigh-Bénard Convection at Very High Rayleigh Numbers. *Phys. Rev. Lett.*, 109:154301, Oct 2012. doi: 10.1103/PhysRevLett.109.154301. URL `https://link.aps.org/doi/10.1103/PhysRevLett.109.154301`.

P. Urban, P. Hanzelka, V. Musilová, T. Králík, M. La Mantia, A. Srnka, and L. Skrbek. Heat transfer in cryogenic helium gas by turbulent Rayleigh-Bénard convection in a cylindrical cell of aspect ratio 1. *New Journal of Physics*, 16(5):053042, 2014. URL `http://stacks.iop.org/1367-2630/16/i=5/a=053042`.

Geoffrey K. Vallis. *Atmospheric and Oceanic Fluid Dynamics: Fundamentals and Large-Scale Circulation*. Cambridge University Press, 2 edition, 2017. doi: 10.1017/9781107588417.

Roberto Verzicco and Roberto Camussi. Numerical experiments on strongly turbulent thermal convection in a slender cylindrical cell. *J. Fluid Mech.*, 477:19–49, 2003. doi: 10.1017/S0022112002003063.

Th von Kármán. Mechanische Ähnlichkeit und Turbulenz. *Math.-Phys. Klasse*, 1930.

P. Vorobieff and R. E. Ecke. Turbulent rotating convection: an experimental study. *J. Fluid Mech.*, 458:191–218, 2002.

Chun-Sheng Wang. ParaPIV, 2021. Retrieved October 7, 2021.

Yin Wang, Xiaozhou He, and Penger Tong. Turbulent temperature fluctuations in a closed Rayleigh–Bénard convection cell. *Journal of Fluid Mechanics*, 874:263–284, 2019. doi: 10.1017/jfm.2019.405.

Marcel Wedi. Effects of rotation on the Nusselt number in large-scale Rayleigh-Bénard convection. Master's thesis, Georg-August-Universität Göttingen, 2018.

Marcel Wedi, Dennis P.M. van Gils, Eberhard Bodenschatz, and Stephan Weiss. Rotating turbulent thermal convection at very large Rayleigh numbers. *Journal of Fluid Mechanics*, 912:A30, 2021. doi: 10.1017/jfm.2020.1149.

Marcel Wedi, Viswa M. Moturi, Denis Funfschilling, and Stephan Weiss. Experimental evidence for the boundary zonal flow in rotating Rayleigh-Bénard convection. *Journal of Fluid Mechanics*, 939, 2022.

Ping Wei, Stephan Weiss, and Guenter Ahlers. Multiple transitions in rotating turbulent Rayleigh-Bénard convection. *Phys. Rev. Lett*, 114:114506, 2015.

S. Weiss and G. Ahlers. Turbulent Rayleigh-Bénard convection in a cylindrical container with aspect ratio $\Gamma = 0.50$ and Prandtl number Pr=4.38. *J. Fluid Mech.*, 676:5–40, 2011a.

S. Weiss and G. Ahlers. The large-scale flow structure in turbulent rotating Rayleigh-Bénard convection. *J. Fluid Mech.*, 688:461–492, 2011b.

Stephan Weiss, Richard J. A. M. Stevens, Jin-Qiang Zhong, Herman J. H. Clercx, Detlef Lohse, and Guenter Ahlers. Finite-Size Effects Lead to Supercritical Bifurcations in Turbulent Rotating Rayleigh-Bénard Convection. *Phys. Rev. Lett.*, 105(22):224501, Nov 2010. doi: 10.1103/PhysRevLett.105.224501. URL `https://link.aps.org/doi/10.1103/PhysRevLett.105.224501`.

Stephan Weiss, Ping Wei, and Guenter Ahlers. Heat-transport enhancement in rotating turbulent Rayleigh-Bénard convection. *Phys. Rev. E*, 93(4):043102, Apr 2016. doi: 10.1103/PhysRevE.93.043102. URL `https://link.aps.org/doi/10.1103/PhysRevE.93.043102`.

Stephan Weiss, Xiaozhou He, Guenter Ahlers, Eberhard Bodenschatz, and Olga Shishkina. Bulk temperature and heat transport in turbulent Rayleigh-Bénard convection of fluids with temperature-dependent properties. *Journal of Fluid Mechanics*, 851:374–390, 09 2018. doi: 10.1017/jfm.2018.507.

Jerry Westerweel. Fundamentals of digital particle image velocimetry. *Measurement science and technology*, 8(12):1379, 1997.

K. Wieghardt. *Theoretische Strömungslehre*. Göttinger Klassiker der Strömungsmechanik. Univ.-Verlag Göttingen, 2005. ISBN 9783938616338.

Wikimedia. Estrellatipos, 2005. URL `https://commons.wikimedia.org/wiki/File:Estrella-tipos.png`. Original upload by Xenoforme.

X. Z. Wu and A. Libchaber. Non-Boussinesq effects in free thermal convection. *Phys. Rev. A*, 43: 2833–2839, 1991.

J. Zhang, S. Childress, and A. Libchaber. Non-Boussinesq effect: Thermal convection with broken symmetry. *Phys. Fluids*, 9:1034–1042, 1997.

Keke Zhang and Xinhao Liao. The onset of convection in rotating circular cylinders with experimental boundary conditions. *Journal of Fluid Mechanics*, 622:63–73, 2009. doi: 10.1017/S002211200800517X.

Xuan Zhang, Dennis P. M. van Gils, Susanne Horn, Marcel Wedi, Lukas Zwirner, Guenter Ahlers, Robert E. Ecke, Stephan Weiss, Eberhard Bodenschatz, and Olga Shishkina. Boundary Zonal Flow in Rotating Turbulent Rayleigh-Bénard Convection. *Phys. Rev. Lett.*, 124:084505, Feb 2020. doi: 10.1103/PhysRevLett.124.084505. URL `https://link.aps.org/doi/10.1103/PhysRevLett.124.084505`.

Xuan Zhang, Robert E. Ecke, and Olga Shishkina. Boundary zonal flows in rapidly rotating turbulent thermal convection. *Journal of Fluid Mechanics*, 915:A62, 2021. doi: 10.1017/jfm.2021.74.

F. Zhong, R. Ecke, and V. Steinberg. Rotating Rayleigh-Bénard convection: asymmetric modes and vortex states. *J. Fluid Mech.*, 249:135, 1993.

Fang Zhong, Robert Ecke, and Victor Steinberg. Asymmetric modes and the transition to vortex structures in rotating Rayleigh-Bénard convection. *Physical review letters*, 67(18):2473, 1991.

J.-Q. Zhong, R. J. A. M. Stevens, H. J. H. Clercx, R. Verzicco, D. Lohse, and G. Ahlers. Prandtl-, Rayleigh-, and Rossby-Number Dependence of Heat Transport in Turbulent Rotating Rayleigh-Bénard Convection. *Physical Review Letters*, 102(4):044502, January 2009. doi: 10.1103/PhysRevLett.102.044502.

Jin-Qiang Zhong and Guenter Ahlers. Heat transport and the large-scale circulation in rotating turbulent Rayleigh-Bénard convection. *J. Fluid Mech.*, 665:300–333, 2010. doi: 10.1017/S002211201000399X.

Xiaojue Zhu, Varghese Mathai, Richard J. A. M. Stevens, Roberto Verzicco, and Detlef Lohse. Transition to the Ultimate Regime in Two-Dimensional Rayleigh-Bénard Convection. *Phys. Rev. Lett.*, 120:144502, Apr 2018. doi: 10.1103/PhysRevLett.120.144502. URL `https://link.aps.org/doi/10.1103/PhysRevLett.120.144502`.

Lukas Zwirner and Olga Shishkina. Confined inclined thermal convection in low-Prandtl-number fluids. *Journal of Fluid Mechanics*, 850:984–1008, 2018. doi: 10.1017/jfm.2018.477.

Appendix

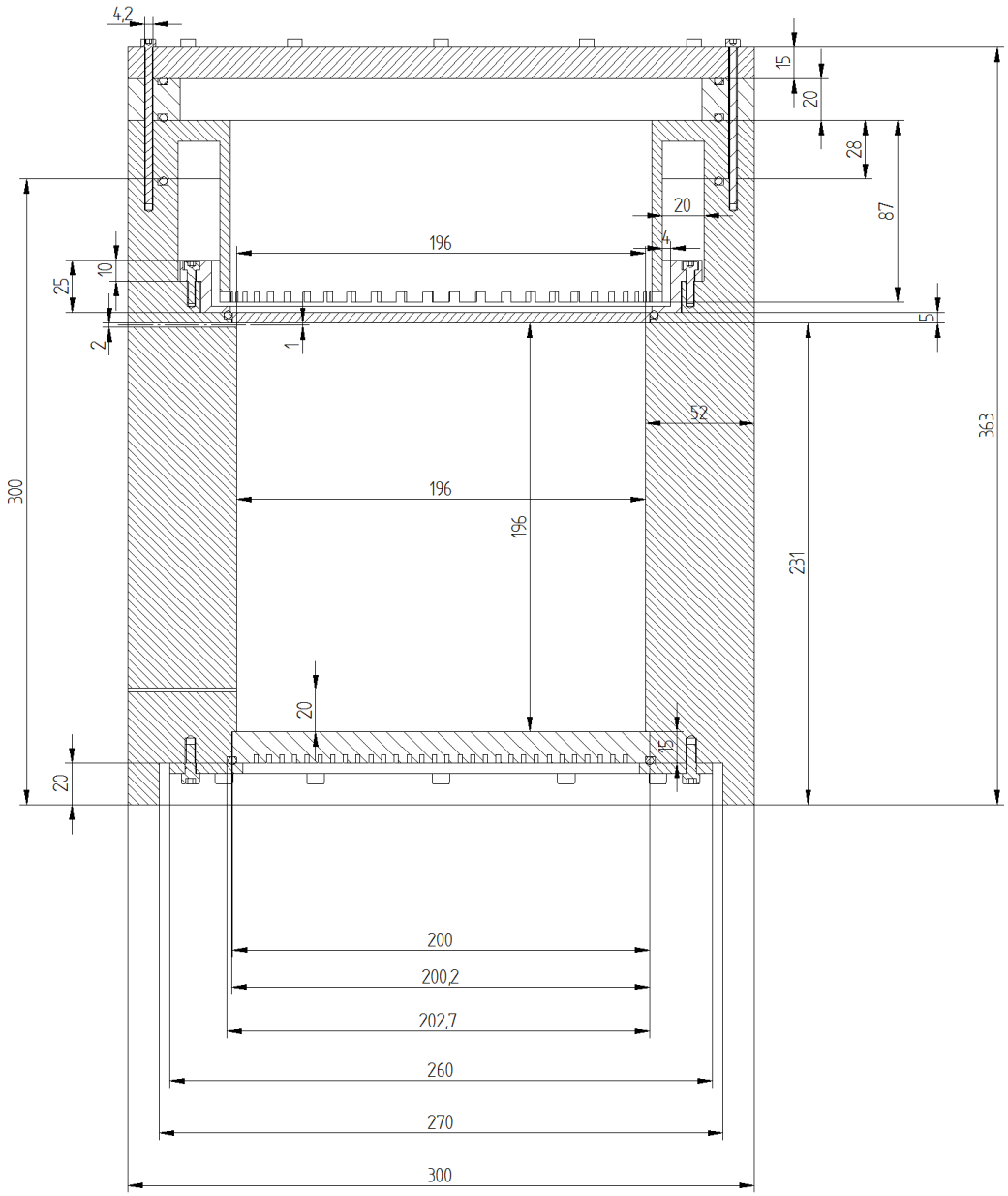

Figure 6.1: Technical drawing of the plexiglas cell, cut at the center $r = D/2$.

Curriculum Vitae

Education:

07/2018 –02/2022	Ph.D. student at the Max-Planck-Institute for Dynamics and Self-Organization, Project title "Heat transport and flow structure in rapidly rotating thermal convection"
10/2015–05/2018	M.Sc. of Astro- and Geophysics at the Georg-August-Universität Göttingen, Master's thesis "Effects of rotation on the Nusselt number in large-scale Rayleigh-Bénard convection", Grade "very good"
09/2016–02/2017	Studies of Astro- and High Energy Physics, Universitat Autònoma de Barcelona
10/2012–09/2015	B.Sc. of Physics "with distinction" at the Georg-August-Universität Göttingen, Bachelor's thesis "Dynamic Evolution of Circumbinary Planets", Grade "good"

Teaching experience:

2020-2021	Teaching assistant in lecture "Physics for medical students"
2020	Teacher for introductory Python programming course
	Teaching assistant for laboratory course "Experimental physics - Waves and Optics"
2019	Teaching assistant in lecture "Experimental physics - Electricity"
2015–2017	Teaching assistant for laboratory courses "Experimental physics - Mechanics" and "Experimental physics - Electricity"

Publications:

- **M. Wedi**, D. van Gils, E. Bodenschatz, and S. Weiss, *Rotating turbulent thermal convection at very large Rayleigh numbers* (2021), Journal of Fluid Mechanics, 912, A30
- **M. Wedi**, V. Moturi, D. Funfschilling, and S. Weiss, *Experimental evidence for the boundary zonal flow in rotating Rayleigh-Bénard convection* (2022), Journal of Fluid Mechanics, 939, A14
- X. Zhang, D. van Gils, S. Horn, **M. Wedi**, L. Zwirner, G. Ahlers, R. Ecke, S. Weiss, E. Bodenschatz, and O. Shishkina, *Boundary Zonal Flow in Rotating Turbulent Rayleigh-Bénard Convection* (2020), Physical Review Letters, 124, 084505
- G. Ahlers, E. Bodenschatz, R. Hartmann, X. He, D. Lohse, P. Reiter, R. Stevens, R. Verzicco, **M. Wedi**, S. Weiss, X. Zhang, L. Zwirner, and O. Shishkina, *Aspect Ratio Dependence of Heat Transfer in a Cylindrical Rayleigh-Bénard Cell* (2022), Physical Review Letters, 128, 084501

Presentations at international conferences:

- 74th Annual Meeting of the APS Division of Fluid Dynamics, November 2021

- German Physical Society (DPG) virtual spring meeting, March 2021
- 91st Annual Meeting of the International Association of Applied Mathematics and Mechanics, March 2021
- 73th Annual Meeting of the APS Division of Fluid Dynamics, November 2020
- European Geosciences Union (EGU) General Assembly, May 2020
- European Turbulence Conference 17 in Turino, September 2019
- DPG spring meeting in Regensburg, March 2019
- Workshop "Rotating Convection: from the Lab to the Stars" in Leiden, May 2018
- DPG spring meeting in Berlin, March 2018